PROTOSTELLAR INFALL: MODELLING SUBMILLIMETRE SPECTRAL LINE OBSERVATIONS

Henry David Buckley

Presented for the Degree of Doctor of Philosophy
The University of Edinburgh
1997

Abstract

In this thesis we study the problem of how to identify, and measure the properties of, infalling protostellar envelopes, through radiative transfer modelling of submillimetre spectral line observations. The densities and temperatures in the gas envelopes surrounding the youngest protostars are favourable for exciting a number of rotational molecular transitions, observable in the submillimetre waveband. The line profiles of these transitions contain information about both the physical state and dynamics of the envelope gas, and may potentially be used to test theoretical models of star formation. We review the observational and theoretical background to the current picture of star formation and protostellar evolution, and the previous molecular line studies of infall in molecular clouds and protostellar envelopes.

The physical concepts and assumptions used in radiative transfer modelling of rotational molecular lines are discussed. The observations of this thesis are modelled using an exact, non-LTE, spherically symmetric radiative transfer code (STENHOLM), which numerically solves the radiative transfer problem using the Λ-iteration method. A detailed description of the code is given, including a number of new modifications. To test the performance of the code, comparisons are shown between the line profiles produced by STENHOLM and independent analytical and numerical calculations.

Observations are presented of a sample of protostellar candidates (mainly Class 0 sources), in transitions of HCO^+, $H^{13}CO^+$, CS, CO, and $C^{18}O$. The HCO^+ and CS transitions preferentially trace high density gas, whereas CO traces a much wider range of gas densities. A complex dynamical picture emerges, involving infall, rotation, and outflow. Of the ten objects included in our sample, five show qualitative signatures of infall (i.e. blue-skewed line profiles) in the high critical density tracers, CS and HCO^+ . Of the remaining objects, four show either no signature of infall or conflicting

signatures in different tracers, and one (L483) show red-skewed line profiles, in direct conflict with the infall expectation. We examine the evidence that the line profiles of the HCO^+ and CS transitions observed towards each of the objects are confused by emission from outflows, by comparing, wherever possible, the morphology and centroid velocity gradients found in maps of these transitions with CO outflow maps. We find that the CS and HCO^+ submillimetre transitions, which are usually thought of as good tracers of protostellar envelope gas by virtue of their large critical densities, are often significantly contaminated by outflow emission. For the three objects which show the strongest evidence for infall (NGC1333-IRAS2, IRAS 16293-2422 and Serpens SMM4) strong centroid velocity gradients are measured in the CS and HCO^+ maps. We examine whether these velocity gradients are caused by outflow or rotation, and conclude that in the case of NGC1333-IRAS2, the outflow dominates the velocity gradient, whereas we find strong evidence that the IRAS 16293-2422 and Serpens SMM4 velocity gradients are due to rotation. Both these latter objects show evidence for elongation of their envelopes perpendicular to the rotation axis, suggesting they may be partially centrifugally supported.

We examine the physical constraints which can be used to limit the number and range of parameters used in protostellar envelope models, and identify the turbulent velocity and tracer molecule abundance as the principle sources of uncertainty in the radiative transfer modelling. We explore the trends in the appearance of the predicted line profiles as certain key parameters in the models are varied. The formation of the characteristic asymmetric double-peaked line profile in infalling envelopes is discussed in detail, and some previous misconceptions concerning this problem are highlighted. Radiative transfer modelling is carried out on HCO^+ and CS observations of NGC1333-IRAS2 and Serpens SMM4, using the STENHOLM radiative transfer code. Adequate fits are found for most of the observed line profiles using plausible infall model parameters, and possible reasons for the discrepancies are suggested. The density and velocity profiles in our best fit models are inconsistent with the Shu model, since for both objects modelled, the infall velocities appear further advanced than the Shu model would predict, given the density profile. We find better agreement with a form of col-

lapse which assumes non-static initial conditions than with a static singular isothermal sphere. We also find tentative evidence that the infall velocity is retarded from free-fall towards the centre of the cloud.

ACKNOWLEDGEMENTS

Most PhD's are collaborations, and this is no exception. First and foremost, I would like to thank Derek Ward-Thompson, for taking me on as his first PhD student, and being an extremely patient and supportive supervisor. I have had an invaluable apprenticeship in research and whiskey appreciation. Many thanks to Peter Brand for his inspirational enthusiasm for physics, for providing a compass when I occasionally felt lost at sea, and for remaining enigmatic to the last. The most enjoyable part of a PhD for me (apart from completing it) is debating the subject with others. For being game opponents, I thank Phillipe André, Bill Ballinger, Andrew Harrison, Nick Jessop, Mike McCartney, Gopal Narayanan, Jonathon Rawlings, Frank Shu, Jonathon Tedds, and Jeremy Yates, among others.

Special thanks go to Andy Gibb, Les Little, and Robin Phillips, who gave me access to their radiative transfer code, and patiently answered all my queries. I first found out about the code through the CCP7 project.

Many people have supported me, in word and deed, during the past few years. Jennifer Mair mopped my brow and kept the batteries on my life support machine charged. No greater devotion hath any woman than to proof-read the thesis of her beloved. Robert, Jay, Michael and Valentina Mair provided welcome retreats on many occasions. Thanks to Jane Ward-Thompson for all the meals and some last minute photocopying.

The final word goes to my Mum and Dad, who have been a continual source of encouragement.

This thesis is my own composition except where indicated in the text.

December 17, 1997

This thesis is dedicated to Mum, Dad, and Jennifer

Contents

Chapter 1

Introduction

The problem of how stars form is one of the most fundamental areas of study in astronomy, with far-reaching implications for many branches of the subject. In particular, a theory of star formation is a prerequisite for a proper understanding of the origin of the Solar System, the structure of the Milky Way, and the formation and evolution of galaxies. Some of the questions the work in this field aims to answer are:

- Under what conditions can star formation take place, and how do these conditions arise?
- What are the processes which initiate, regulate and eventually terminate the accumulation of material onto the forming star, and what determines the final mass of the star?
- How did the first stars form in the early universe?
- What does the study of star formation tell us about the origin of our own Solar System?

Definitive answers to these questions have not yet been found. The problem is extremely complicated, encompassing around ten orders of magnitude in scale, from a molecular cloud to a hydrostatic protostar. Phenomena originating at the smallest scales influence events at the largest scales, and vice-versa – for example, the stability of

molecular clouds may depend on the turbulent support provided by both outflows from protostars and differential rotation of the cloud about the galactic centre (e.g. Norman & Silk 1980; McKee 1989; Silk 1995; Fleck 1980, 1981). Even chemical processes may have an important influence on the dynamics of protostellar envelopes, through the support provided by the 'freezing' of ionised particles to magnetic field lines. The study of star formation also presents huge observational challenges. The rapid advance of long wavelength astronomy in the past few decades, combined with increasingly sophisticated numerical modelling tools, has made star formation one of the most exciting and rapidly evolving fields in astronomy.

1.1 Theory of Protostars

1.1.1 Gravitational instability

It is observationally well established that stars are formed by the gravitational collapse of interstellar molecular gas clouds (see section 1.2). An approximate criterion for a cloud to be gravitationally unstable is that the absolute magnitude of the gravitational potential energy must exceed the combined thermal, rotational, turbulent and magnetic energies.[1] For the idealised case of a uniform spherical isothermal cloud, where the gas has no internal degrees of freedom, the gravitational and thermal energies are given by

$$|E_{\rm grav}| = \frac{3GM^2}{5R} \tag{1.1}$$

$$E_{\rm th} = \frac{3MkT}{2\bar{m}} = \frac{3Ma^2}{2}, \tag{1.2}$$

where M and R are the mass and radius of the cloud respectively, T is the temperature, k is Boltzmann's constant, G is the gravitational constant, $\bar{m}$ is the mean molecular weight, and $a \equiv \sqrt{kT/\bar{m}}$ is the isothermal sound speed. Turbulent energy may be ac-

[1] Strictly speaking, the role of each energy in the *support* of the cloud must be taken into consideration, e.g. a uniform unidirectional magnetic field would contribute to the magnetic energy in the cloud, but would not support it against collapse unless the field lines became distorted, and then only if the cloud is sufficiently ionised to couple well to the magnetic field. Also, in the full virial theorem the surface boundary conditions may be important, e.g. if there is an externally applied pressure (McCrea 1957).

counted for in Equation 1.2 by replacing the isothermal sound speed a, by the 'effective sound speed', $a_{\rm eff}$, where

$$a_{\rm eff}^2 = \frac{kT}{\bar{m}} + \sigma_{\rm tb}^2, \tag{1.3}$$

where $\sigma_{\rm tb}$ is the turbulent velocity dispersion (i.e. the $e^{-1/2}$ half-width, assuming the turbulent velocity follows a gaussian distribution).

Equating $E_{\rm th}$ and $E_{\rm grav}$ gives an expression for the maximum radius of the cloud such that it is gravitationally bound, when supported only by thermal pressure. This radius is commonly referred to as the **Jeans length**, and is given by

$$R_{\rm J} = \frac{2}{5}\frac{GM}{a_{\rm eff}^2}, \tag{1.4}$$

$$\simeq 0.043 \left(\frac{M}{\rm M_\odot}\right) \cdot \left(\frac{a_{\rm eff}}{0.2\,{\rm km\,s^{-1}}}\right)^2 {\rm pc}. \tag{1.5}$$

A uniform cloud of fixed mass will be unstable to gravitational collapse if its outer radius is *less* than the Jeans length. In the exact treatment of the gravitational stability of self-gravitating, hydrostatic isothermal spheres (Ebert 1955; Bonnor 1956; see appendix) the numerical coefficient in Equation 1.4 is only changed to 0.41.

Eliminating R for ρ in Equation 1.4, using $M = 4\pi R^3\rho/3$, and rearranging, we obtain the following expression for the maximum stable mass at fixed density:

$$M_{\rm J} = \left(\frac{5a_{\rm eff}^2}{2G}\right)^{3/2} \left(\frac{4\pi}{3}\rho\right)^{-\frac{1}{2}}. \tag{1.6}$$

$$\simeq 2.1 \left(\frac{a_{\rm eff}}{0.2\,{\rm km\,s^{-1}}}\right)^3 \cdot \left(\frac{n_{\rm H_2}}{10^4\,{\rm cm^{-3}}}\right)^{-\frac{1}{2}} {\rm M_\odot}. \tag{1.7}$$

If the cloud is rotating with a solid body angular velocity Ω, the Jeans criterion becomes:

$$M_{\rm J} = \frac{5a_{\rm eff}^2 R + 2\Omega^2 R^3/3}{2G}, \tag{1.8}$$

$$\simeq M_J^{\rm th} + 0.08 \left(\frac{\Omega}{\rm km\,s^{-1}\,pc^{-1}}\right)^2 \cdot \left(\frac{R}{0.1\,{\rm pc}}\right)^3 {\rm M_\odot}. \tag{1.9}$$

where $M_J^{\rm th}$ is the Jeans mass for purely thermal support, given by Equation 1.7.

For a magnetically supported cloud, in the absence of thermal pressure support, the collapse criterion may be expressed as a critical value for the mass to flux ratio (Mouschovias & Spitzer 1976; Tomisaka, Ikeuchi & Nakamura 1988):

$$M_{\rm crit} \simeq 0.12 \left(\frac{\Phi}{G^{\frac{1}{2}}}\right), \tag{1.10}$$

$$\simeq 0.054 \left(\frac{B}{G^{\frac{1}{2}}}\right)^3 \left(\frac{3}{4\pi\rho}\right)^2, \tag{1.11}$$

$$\simeq 1.1 \left(\frac{B}{30\,\mu G}\right)^3 \cdot \left(\frac{n_{\rm H_2}}{10^4\,{\rm cm}^{-3}}\right)^{-2} {\rm M}_\odot \tag{1.12}$$

where $\Phi \simeq \pi R^2 B$ is the magnetic flux threading the cloud and B is the magnetic field (in gaussian units). Magnetically subcritical clouds may evolve towards a critical configuration through **ambipolar diffusion** (Mestel & Spitzer 1956), which describes the inhibited flow of neutral particles relative to the ionised particles in the gas, when the latter are supported by the magnetic field.

Protostellar collapse

Much of the current theoretical picture of early protostellar evolution is from the pioneering hydrodynamical simulations of Larson (1969, 1972), which demonstrated for the first time that Jeans-unstable gas clouds with typical molecular cloud densities could evolve to form pre-main sequence stars on the Hayashi pre-main sequence track (see also Bodenheimer & Sweigart 1968). It also highlighted the essentially non-homologous nature of protostellar collapse. Previous theoretical treatments had assumed a homologous contraction of the cloud, preserving a uniform or polytropic density profile throughout the collapse (e.g. Gaustad 1963; Hayashi 1966).

Larson (1969) modelled the collapse of a marginally Jeans unstable $\sim 1\,{\rm M}_\odot$ spherical cloud of molecular gas, with an initially uniform density ($\sim 10^{-19}\,{\rm g\,cm}^{-3}$, $n_{H_2} \sim 10^4\,{\rm cm}^{-3}$), and temperature (10K), which serves as a good illustration of the evolution of a protostar for a wide range of cloud masses (e.g. Larson 1972), at least for the idealised case of spherically symmetric purely hydrodynamic collapse. Subsequent

studies have confirmed this qualitative picture (e.g. Tscharnuter 1989). The collapse takes place in several stages, which are now outlined.

Initially, the collapse is isothermal, since at these densities the gas is reasonably well coupled to the dust, which can efficiently radiate away the compressional heat energy generated by the collapse as long as the cloud remains optically thin to far-infrared radiation. As the initial density profile is uniform, there is no initial pressure gradient and the whole cloud begins to collapse in freefall. In the absence of pressure gradients, the whole cloud would collapse homologously, maintaining a uniform density, on the free fall timescale:

$$t_{ff} = \sqrt{\frac{3\pi}{32G\rho}}, \tag{1.13}$$

which for the initial density stated above is $\sim 2 \times 10^5$ yr. This does not happen, however, since the pressure and density at the outer boundary of the cloud are constrained by the external boundary conditions, and cannot keep in step with the rapidly rising density in the inner regions. Initially the central regions collapse homologously, while in the outer parts of the cloud a pressure gradient is set up, which retards the collapse of the outer layers, and propagates inwards at the sound speed. The density profile becomes centrally peaked, which decreases the free-fall time in the centre relative to the envelope, resulting in an extremely non-homologous collapse with the central regions evolving on a much shorter timescale than the outer parts. The density profile changes from a flat distribution to a $\rho \propto r^{-2}$ power law, in about one free-fall time.

The purely isothermal collapse phase ends when a small region at the centre of the cloud becomes opaque. This happens when the central density reaches $\sim 10^{-13}\,\mathrm{g\,cm^{-3}}$ ($n_{H_2} \sim 10^{10}\,\mathrm{cm^{-3}}$). The heat generated by the collapse is no longer freely radiated away in this region, and the gas temperature rises as the compression becomes approximately adiabatic. In this regime, the density and pressure are related by

$$P \propto \rho^{\gamma}, \tag{1.14}$$

where γ is the ratio of specific heats, which for molecular hydrogen at these tempera-

tures is $\simeq$1.4. In this case the dependence of the Jeans mass on density goes as

$$M_{\rm J} \propto \rho^{(3\gamma-4)/2}. \tag{1.15}$$

The exponent is positive for $\gamma > 4/3$, as in this case, and the Jeans mass increases with increasing density. The collapse in the opaque core is therefore rapidly halted, and the gas approaches hydrostatic equilibrium. At this stage the gas temperature in the core is $\sim 200K$. The gas further out continues to fall inwards, and intercepts the static core at a shock front.

As the mass of the static core increases by accretion, its temperature rises due to the adiabatic compression. When a temperature of 2000K is reached inside the core, molecular hydrogen begins to dissociate, and the effective value of γ drops to $\simeq$ 1.1. Gravitational instability sets in once again and a second dynamic collapse takes place inside the opaque core. When all of the molecular hydrogen in the infalling stream is dissociated γ rises to 5/3 and the collapse is again halted. A second static core is formed with a temperature of $\sim 2000K$, a mass of a few tenths of a solar mass, and a radius of a few solar radii. This stellar core is usually referred to as the 'protostar', and the surrounding infalling cloud is the 'protostellar envelope'. The original core and its associated shock front are rapidly dissipated from within, and a new shock front is set up at the interface of the protostar and the infalling envelope.

The protostar initially contains only a very small fraction of the total cloud mass. Most of the eventual stellar mass is acquired by infall of the envelope over a further freefall time. This is known as the main accretion phase. Towards the end of this stage the extinction of the envelope in the near infrared and the optical drops sufficiently for the central protostar to become visible as a pre-main sequence star on the Hayashi track.

1.1.2 The Shu Model

The so-called 'standard model' or 'Shu model' of protostellar evolution was first expounded in the seminal paper of Shu (1977), and elaborated upon over the two decades following. Shu discovered an exact similarity solution for the idealised problem of spherically symmetric, isothermal hydrodynamic collapse. The solution is self-similar in the sense that the density and velocity profiles at different times differ only by a normalisation factor and a constant spatial scaling factor, both of which are well-defined functions of the collapse age. The original motivation for the Shu model was to decouple the problems of the dynamical evolution of the infalling envelope and the structure of the central hydrostatic protostar (Stahler, Shu & Taam 1980). In its various guises, the Shu model has been extremely widely used in the two decades since it was first proposed, due to its mathematical simplicity and elegance, and the lack of competing models which allow similarly detailed predictions. Recently, however, the validity of the Shu model as realistic description of protostellar evolution has been seriously questioned (e.g. Whitworth et al. 1996; Ward-Thompson 1996).

To allow a mathematically simple treatment, the details of the various collapse stages which were described in the previous section are omitted, and the gas is assumed to remain isothermal at all radii throughout the entire collapse. In the simplest version of the model (Shu 1977) the assumed initial condition is the static singular isothermal sphere (SIS), for which the dependence of the density and the enclosed mass with radius are as follows:

$$\rho(r) = \frac{a^2}{2\pi G r^2}, \tag{1.16}$$

$$M(r) = \frac{2a^2 r}{G}, \tag{1.17}$$

where a is the isothermal sound speed as before. a may be replaced by the effective sound speed, $a_{\rm eff}$, if turbulent motions are present, are spatially uniform, and behave like an isotropic pressure as far as their role in the dynamics is concerned. The thermal and gravitational energies of the SIS, when truncated at the radius R, are given by

$$E_{\rm th}(R) = \frac{3}{2} M(R) a^2, \tag{1.18}$$

$$E_{\rm grav}(R) \;=\; 2M(R)a^2, \tag{1.19}$$

hence $E_{\rm th}(R)/E_{\rm grav}(R)$ is constant and close to unity.

The collapse begins at the centre of the cloud, with the formation of a central point mass. There is no collapse phase prior to the formation of the central protostar ('core formation') in the Shu model, in contrast with the predicted collapse behaviour of clouds with flat density profiles at the origin (such as the critical Bonnor-Ebert sphere - see appendix) which evolve dynamically for about one free-fall time before core formation (e.g. Foster & Chevalier 1993).

Once the collapse has begun it progresses outwards, as the gas just outside the collapsing region loses pressure support from within and fall inwards. The spherical 'collapse front', marking the boundary between the inner collapsing region and the undisturbed outer cloud, travels outwards from the moment of initiation of the collapse, at the isothermal sound speed. The terms 'inside-out collapse' and 'collapse-expansion wave' (CEW) are frequently used to describe this behaviour. Outside the CEW, the envelope is completely unaffected by the collapse taking place inside, and maintains its initial $1/r^2$ density distribution. The boundary between these two regimes lies at the 'infall radius', $r_{\rm inf}$, where $r_{\rm inf} = at$.

When the gas at a particular radius is overtaken by the CEW, it begins to accelerate inwards, although it is initially retarded from pure free-fall collapse by the pressure gradient in the infalling region. As the gas falls towards the centre, gravitational forces become dominant, and the density and (outward) radial velocity profiles asymptotically approach 'free-fall' $r^{-\frac{3}{2}}$ and $r^{-\frac{1}{2}}$ profiles respectively:

$$v(r,t) \;\simeq\; -1.40\,(GM_\star)^{1/2}\,r^{-1/2}, \tag{1.20}$$

$$\rho(r,t) \;\simeq\; 0.056\left(\frac{a^6}{G^3M_\star}\right)^{1/2} r^{-3/2}, \tag{1.21}$$

where $M_\star$ is the mass of the central protostar. Note that as the collapse proceeds and $M_\star$ increases, the infall velocity at fixed radius increases and the density at fixed radius

decreases. Only two parameters are required to specify any Shu model solution: the isothermal sound speed of the gas, and the infall radius (i.e. the radius of the head of the CEW).

The mass accretion rate of the protostar is given by:

$$\dot{M}_\star = \lim_{r\to 0} -4\pi r^2 \rho v, \tag{1.22}$$

$$= 0.975 \frac{a^3}{G}, \tag{1.23}$$

$$= 1.8 \left(\frac{a}{0.2\mathrm{km\,s^{-1}}}\right)^3 \mathrm{M_\odot\,Myr^{-1}} \tag{1.24}$$

and remains constant as the collapse proceeds. The total mass accreted by the protostar at any given instant may be written as:

$$M_\star = \dot{M}_\star t = 0.975 \left(\frac{a^2 r_{\mathrm{inf}}}{G}\right), \tag{1.25}$$

$$= 0.22 \left(\frac{a}{0.2\,\mathrm{km\,s^{-1}}}\right)^2 \cdot \left(\frac{r_{\mathrm{inf}}}{5000\,\mathrm{AU}}\right) \mathrm{M_\odot}. \tag{1.26}$$

Because the Shu model solution is self-similar by assumption, the density and velocity profiles at different times during the collapse can be mapped onto one another by applying simple scaling factors to both the radial and velocity/density axes. Figures 1.1 and 1.2 show the Shu model predictions for the normalised density and velocity profiles, which are satisfied at all times following the initiation of collapse. The model does not predict a final protostellar mass, however, since there is nothing inherent in the model which leads to a cutoff or lessening of the mass accretion rate as given by Equation 1.23. In practice, the singular isothermal sphere must be truncated at some finite radius, and the self-similarity therefore breaks down when the collapse-expansion wave reaches the outer boundary of the cloud.

The singular initial state assumed by the Shu model represents the extreme unstable limit of the family of hydrostatic, isothermal, pressure-bounded spheres, known as Bonnor-Ebert spheres (e.g. Ebert 1955; Bonnor 1956; see appendix). Although all Bonnor-Ebert spheres are in precise hydrostatic equilibrium, they may be unstable to

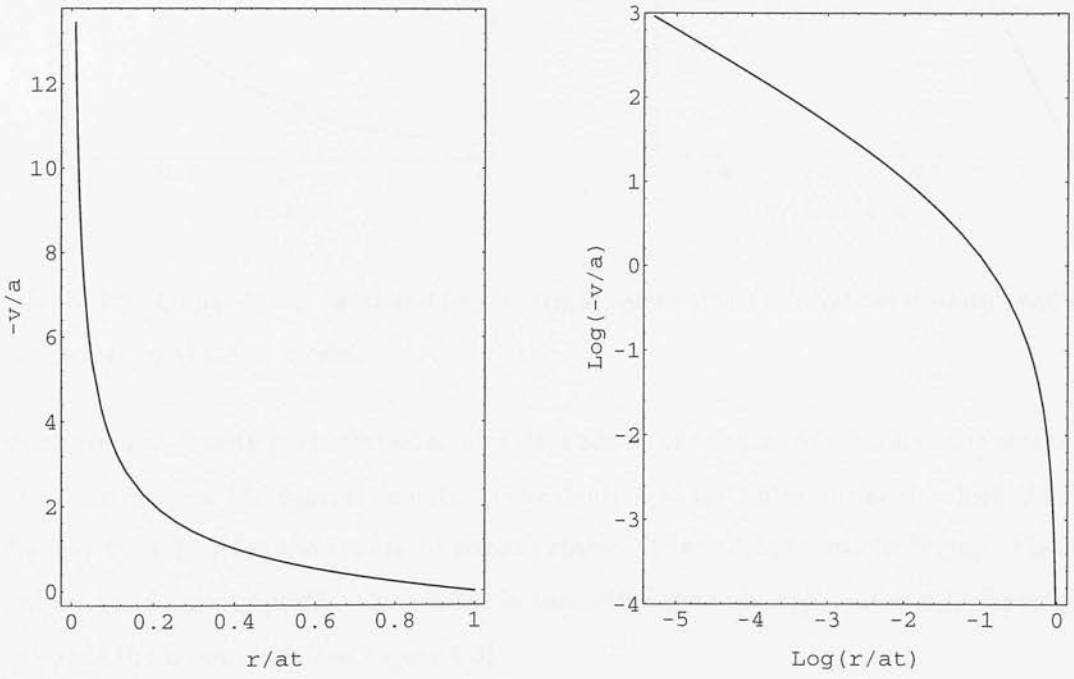

Figure 1.1: Linear-linear (left) and log-log (right) plots of the normalised velocity profile predicted by the Shu model. a is the isothermal sound speed, and t is the time since the onset of collapse. The head of the collapse expansion wave lies at $r/at = 1$.

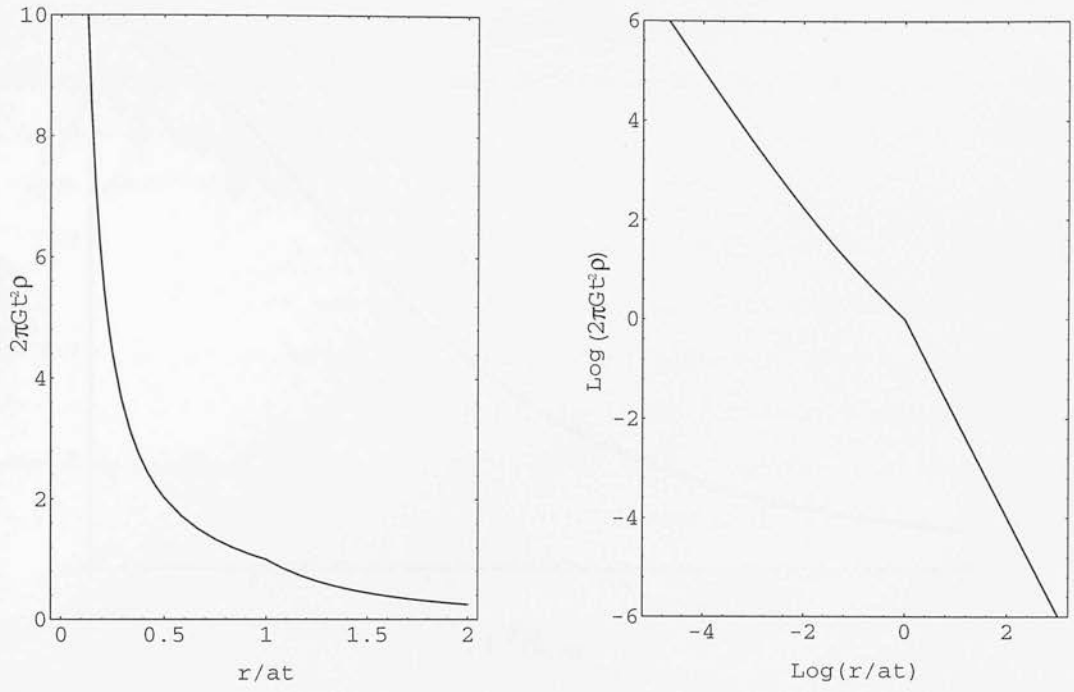

Figure 1.2: Linear-linear (left) and log-log (right) plots of the normalised density profile predicted by the Shu model.

pressure and density perturbations. This depends on the degree of central condensation (i.e. the ratio of the central density to the density at the outer surface), which must be less than 14.1 for the sphere to remain stable. The critically stable Bonnor-Ebert sphere has a density profile which is flat in the centre and only approaches a $1/r^2$ profile towards the outer edge (see Figure 1.3).

Shu (1977) argued that the hydrodynamical collapse of the critical Bonnor-Ebert sphere should closely resemble the collapse of the SIS, claiming that the density profile would subsonically readjust to an approximate $1/r^2$ configuration only a short time after the beginning of the collapse. Hunter (1977) and Foster & Chevalier (1993) tested this assertion using numerical hydrodynamic calculations to follow the collapse of a marginally supercritical Bonnor-Ebert sphere. Surprisingly, it was found that by the time a central protostar has formed, at which time the density profile approaches a $1/r^2$ configuration, a significant fraction of the gas is infalling at supersonic velocities, which contrasts with the static initial condition assumed in the Shu model. The evolution of

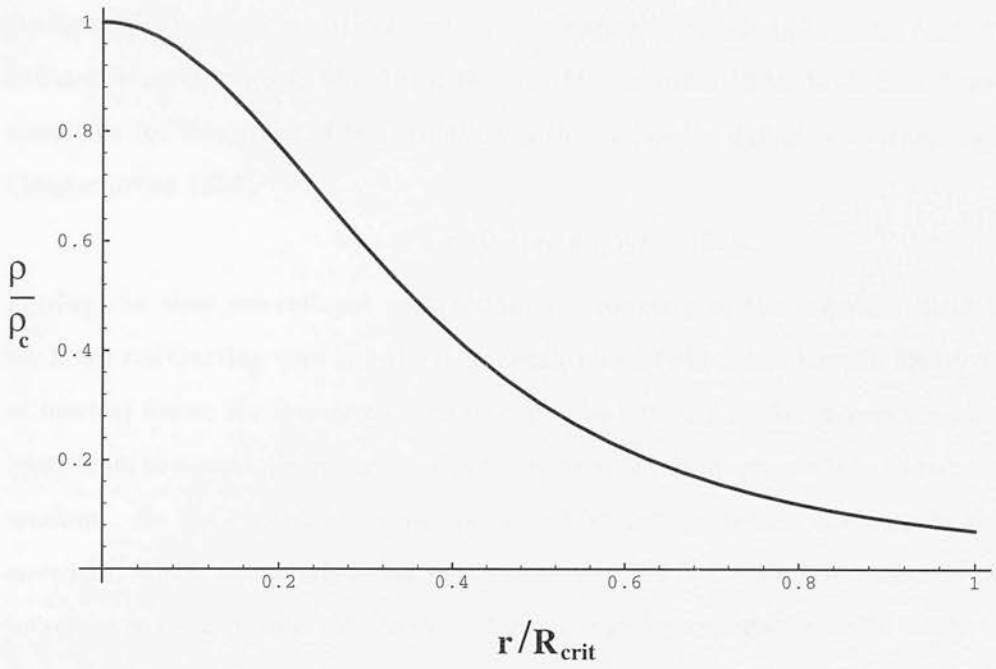

Figure 1.3: Normalised density profile of the critical Bonnor-Ebert sphere. The critical radius is given by $R_{\rm crit} \simeq 6.451(a^2/4\pi G\rho_c)^{\frac{1}{2}}$.

the collapse beyond the formation of a central protostar also differs markedly from the Shu model, particularly with regard to the mass accretion rate, which reaches an early peak at $\sim$8 times the Shu model prediction (Equation 1.23), and decreases steadily until it falls below the Shu model prediction after $\simeq 2t_{ff}$. Numerical hydrodynamic simulations have also established that fragmentation is strongly suppressed during the collapse of a singular $1/r^2$ density profile (e.g. Burkert, Bate& Bodenheimer 1997), which makes it difficult to account for the the very large binary frequency among pre-main sequence stars (e.g. Simon et al. 1995). By contrast, binary formation appears to take place much more readily for initial conditions resembling the critical Bonnor-Ebert sphere (Boss & Myhill 1995).

The preceding discussion removes much of the theoretical justification for the Shu model in the case of purely hydrodynamic collapse. If magnetic fields play a significant role in supporting the cloud, however, then the question of gravitational stability needs to be re-examined. Theoretical studies have shown that magnetically supported clouds may evolve through ambipolar diffusion towards much more centrally condensed

configurations than the critical Bonnor-Ebert sphere, before undergoing fully dynamic collapse (e.g. Lizano & Shu 1989; Basu & Mouschovias 1994; Li & Shu 1996). The timescale for this stage of the evolution is the *ambipolar diffusion timescale*, given by (Mouschovias 1991)

$$\tau_{\rm AD} = 2 \times 10^{13} (n_{\rm i}/n_{\rm H_2}) {\rm yr} \sim 10 t_{ff}. \qquad (1.27)$$

During the slow pre-collapse contraction, the coupling of the magnetic field lines to both the contracting core and the larger scale cloud (which has a much higher moment of inertia) forces the former to corotate with the latter. Angular momentum is carried away from the envelope by torsional Alfvén waves which propagate into the surrounding medium. As the contraction proceeds, a $\sim 1/r^2$ density profile is set up in the outer envelope, which surrounds a flat central region. The flat region decreases in size and increases in density with time, and contains a mass approximately equal to the thermal Jeans mass for the instantaneous value of the central density (see Figure 1.4). At some point, the gravitational force completely overwhelms the magnetic force in the centre of the cloud, and fully dynamical collapse ensues, leading to the rapid formation of a central protostar (termed 'core formation'), broadly along the route described in the previous section.

There is a lack of consensus among workers in the field about how the collapse evolves beyond core formation. There are two main areas of disagreement, relating to the velocity field in the envelope at the time the central protostar is formed, and the degree to which the outer envelope remains supported by the magnetic field during the collapse.

On the first point, Shu and co-workers argue that the velocity field which develops prior to protostar formation has a negligible effect on the subsequent dynamical evolution of the envelope, and the quasi-static approximation is assumed to hold with reasonable accuracy right up to the moment the protostar is formed (e.g. Lizano & Shu 1989; Shu et al. 1993; Galli & Shu 1993; Li & Shu 1996). The numerical simulations of Mouschovias and coworkers, however, show that at the time of protostar formation, a significant fraction of the contracting core is infalling with a speed comparable to the

isothermal sound speed. These motions are likely to radically alter the the subsequent dynamical evolution compared with the predictions of models which assume a static envelope at the time of protostar formation.

On the second point, Shu and coworkers argue that even in the magnetic case, the envelope evolves according to a modified version of the self-similar, inside-out collapse of the hydrodynamical Shu model, and at no point is there a natural cutoff in the infall rate (e.g. Shu et al. 1993; Galli & Shu 1993; Li & Shu 1997). Processes not included in the model, such as a protostellar wind, have to be invoked to terminate the accretion and decide the final stellar mass. On the other hand, Mouschovias and others have argued that the problem is intrinsically non-self-similar. The mass rate is cut off beyond a certain radius due to the increased magnetic support of the outer regions, resulting from more effective ionisation of the gas by cosmic rays and ultraviolet radiation (e.g. Mouschovias 1991; Ciolek & Mouschovias 1995). This in turn sets a natural limit for the final protostellar mass.

Safier, McKee & Stahler (1997) recently followed the evolution of a contracting, magnetically supported cloud through the core formation stage, using a simplified analytical treatment which assumed that pressure support of the cloud is negligible compared with the magnetic support. As with the collapse of the critical Bonnor-Ebert sphere, significant deparatures from the Shu model prior to and immediately following core formation were found. In the later infall stages, however, the mass infall rate approached a constant value similar to the Shu model prediction. More work needs to be carried out in this area, however. The post-core formation evolution of a collapsing, magnetically supported protostellar envelope remains one of the most important unresolved issues in theoretical star formation.

The collapse of a hydrostatic singular isothermal sphere with a small initial solid-body rotation was studied by Terebey, Cassen & Shu (1984) (see also Zhou 1995). The solutions are parameterised by the isothermal sound speed a, the infall radius, and the

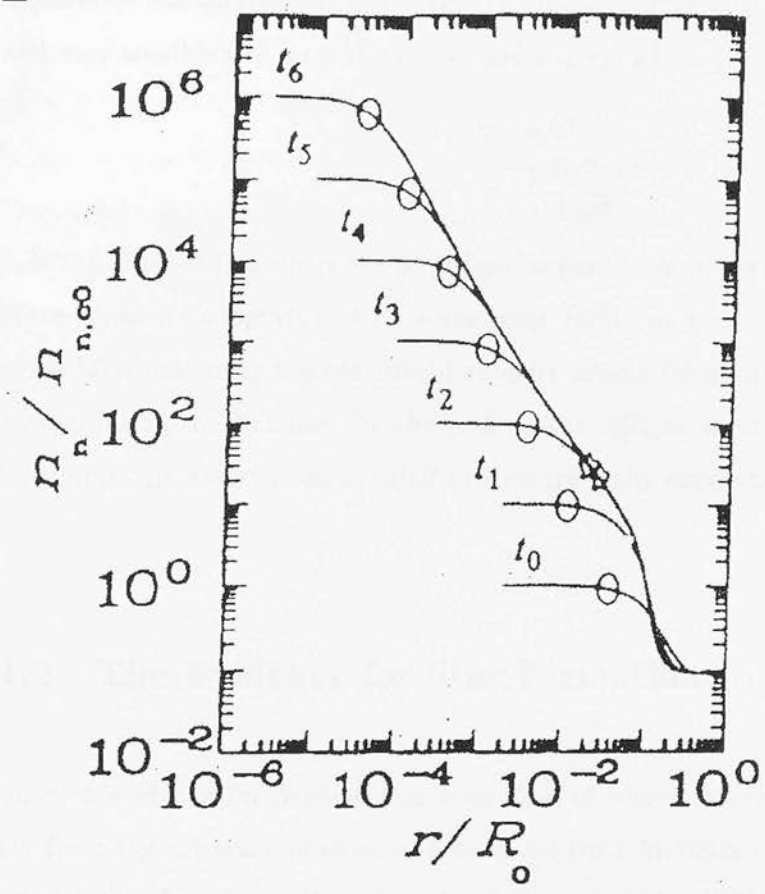

Figure 1.4: Evolution of the radial density profile in a magnetically supported envelope during the ambipolar diffusion phase (Mouschovias 1994). The number density of neutral particles is normalised to the initial central value of $n_{\mathrm{n,c0}} = 2.60 \times 10^3\,\mathrm{cm}^{-3}$, and the radius is normalised to $R_0 = 4.29\mathrm{pc}$. The density profile is plotted at times 0, 14.2, 17.7, 18.10, 18.16, 18.178 and 18.182 Myr from the start of the simulation (t_0). The open circles mark the radii which enclose one Jeans mass.

initial solid body rotation rate Ω. The rotation distorts the spherical CEW, flattens the density profile, modifies the radial velocity profile, and introduces azimuthal and polar components to the velocity field. For small rotation rates and at early times, the collapse proceeds in a similar fashion to the standard Shu model (Shu 1977). Large departures from purely radial collapse of the standard model occur on both very large and very small scales, i.e when $r > r_c$ and $r < r_d$, where

$$r_c = a/\Omega, \tag{1.28}$$

$$r_d = \frac{\Omega^2 G^3 M^3}{16 a^8}. \tag{1.29}$$

r_c is the outer radius where the centrifugal support due to the solid-body rotation dominates pressure support, and r_d is the inner radius at which the collapse of a central mass M is halted by the centrifugal support arising from angular momentum conservation during the collapse. On the scale r_d the collapse solution qualitatively changes from approximately spherical infall to a centrifugally supported flattened disk.

1.2 The Evidence for Star Formation

Indirect evidence for ongoing star formation of some kind in our galaxy comes simply from the existence of stars with main-sequence lifetimes of $<\sim 10^7$ years ($M_\star >\sim 15\,M_\odot$), much younger than the age of the galaxy ($\sim 10^{10}$ yr). Over the past few decades, the observational evidence for star formation in interstellar molecular clouds has become overwhelming. Most of these observations have, for practical reasons, concentrated on the later stages or by-products of the star formation process, e.g. ultracompact HII regions (e.g. Welch et al. 1987), T-Tauri stars (e.g Bertout 1989), and bipolar outflows (e.g. Lada 1985). Only relatively recently has it been possible to directly observe star-formation in progress.

This thesis is primarily concerned with the field of low mass star formation ($M_\star <\sim 3M_\odot$). High mass protostars are expected on theoretical grounds to evolve more rapidly than low mass protostars, reaching the main sequence even before they emerge from

the gas cloud which forms them (e.g. Yorke 1986; Palla & Stahler 1990). Low mass protostars are predicted to be more slowly evolving and more numerous than high mass protostars, allowing a better determination of their statistical properties, and making it more likely that the full range of evolutionary stages will be represented. The strong interaction of high mass stars with their environment, and the violent global disruption often associated with high mass star forming regions (e.g. cloud-cloud collision – Serabyn, Güsten & Schultz (1993)) also complicates the study of high mass star formation. A final reason for focusing on low mass star formation is that the nearest star forming clouds fall into this category, and therefore maximum advantage is gained from the resolution and sensitivity of the observational instruments.

Myers & Benson (1983) and Myers, Linke & Benson (1983) carried out the groundbreaking observational studies which linked low mass star-formation to 'dense cores' – isolated density condensations, with characteristic properties similar to Bok Globules: size, $\sim 0.1\,\mathrm{pc}$; mass, $\sim 30\,\mathrm{M}_{\odot}$; hydrogen number density, $\sim 10^4\ \mathrm{cm}^{-3}$; and temperature $\sim 10K$ (see also Benson & Myers 1989). Assuming the broader than thermal linewidths measured in these cores could be attributed to cloud-supporting turbulent motions, the cores were inferred to be close to virial equilibrium. Beichman et al. (1986) found that $\sim 50\%$ of a sample of 97 dense cores were associated with IRAS far-infrared point sources with non-main sequence colours. The detection rate was around 20 times greater than expected from the chance overlap of background galaxies. About half of these infrared sources had no optical counterpart, and were suggested to be embedded protostars.

Myers et al. (1987) presented near-infrared observations which confirmed the protostellar nature of the optically invisible IRAS sources. Self-consistent modelling of the dust extinction and far-infrared continuum emission (Adams & Shu 1986; Myers et al. 1987; Adams, Lada & Shu 1987) suggested that most of the extinction towards the objects was produced by surrounding dust (and gas) envelopes, of size $<\sim 0.1\,\mathrm{pc}$. The central radiation sources were inferred to have a lower effective temperature than expected from a bare protostellar photosphere, however. Circumstellar disks of size

10-100 AU, which had been predicted by theoretical models of rotating, collapsing protostellar envelopes (e.g. Terebey, Cassen & Shu 1984), were invoked to explain this discrepancy. This picture has been supported by a number of subsequent investigations (e.g. Adams, Lada & Shu 1987, 1988; Ladd et al. 1991; Kenyon, Calvet & Hartmann 1993; Lay et al. 1994; McCaughrean & O'Dell 1996). Initially these objects (known as 'Class I' objects – see below) were thought to represent the phase of evolution where most of the material of the star was accumulated onto the hydrostatic core. Recent observational evidence suggests, however, that these objects only represent the later stages of envelope accretion. In the following section we summarise the different stages of protostellar evolution from an observational point of view.

1.2.1 Young stellar objects

'Young stellar object' is the generic term encompassing all phases of protostellar evolution, following the actual formation of the protostar. At the time of its formation, a protostar is surrounded by a dense and massive gas and dust envelope, which absorbs the optical and ultraviolet radiation emitted from the photosphere and accretion shock of the central protostar, and re-emits it at infrared wavelengths. Over time, the extinction and infrared emission from the envelope diminishes, as it accretes onto the protostar and surrounding centrifugally supported gaseous disk (if present), or is dispersed by protostellar winds. The circumstellar disk evolves over a much longer timescale, by accretion onto the star, and by coagulation into large dense bodies (e.g. planets). The continuum spectrum of a young stellar object (YSO) is dominated by far-infrared emission from the envelope in the early stages (e.g. Larson 1972; Adams & Shu 1985), but as the object evolves, the spectrum approaches that of the bare protostar, on a Hayashi convective track (e.g. D'Antona & Mazzitelli 1994).

Drawing on infrared observations of young stellar objects in the Ophiuchus star forming region (Lada & Wilking 1984), Lada (1987) proposed an empirical infrared YSO classification scheme. Recently, small improvements to this scheme have been

suggested to give better correspondence with the physical stages of YSO evolution (André & Montmerle 1994, hereafter AM; Greene et al. 1994). These are adopted in the following description of the scheme.

The YSO classes are defined according to the slope of their spectral energy distributions between 2.2 μm and 25 μm, as measured by the spectral index, α:

$$\alpha = \frac{d\,\log(\lambda F_\lambda)}{d\,\log\lambda} \equiv -\frac{d\,\log(\nu F_\nu)}{d\,\log\nu}. \tag{1.30}$$

The value of α may be obtained by least-squares fitting to all photometric measurements in the wavelength range quoted above. In order of decreasing α (i.e. decreasing infrared excess relative to stellar blackbodies), the three classes are labelled Class I, Class II and Class III, as detailed in Table 1.1. Also listed in the table is the 'Flat-Spectrum' category. As discussed below, Flat Spectrum sources probably do not represent a physically distinct class of object, and orientation effects may account for their unusual spectral energy distributions. Since the sequence from Class I to Class III is one of decreasing far-infrared emission and circumstellar material, it is natural to suppose that it forms an evolutionary sequence, tracing the gradual emergence of a newly born star from its nascent gas cloud (AM; Kenyon & Hartmann 1995, hereafter KH). Although this is on the whole supported by observations, there is evidence that the Class II and III stages may be coeval in some YSO populations (see below), which if confirmed may complicate this evolutionary scenario.

In an extension to this scheme, André, Ward-Thompson & Barsony (1993, hereafter AWB) introduced the 'Class 0' category, suggesting that it represents the precursor to the Class I phase. Class 0 sources have bright, compact submillimetre continuum emission, and show indirect evidence for a central embedded YSO, such as very compact centimetre continuum emission, or a collimated CO outflow (e.g. Dent, Matthews & Walther 1995; Bontemps, André & Ward-Thompson 1995). The continuum spectra of Class 0 sources are usually well fitted by a single temperature 15-30 K 'greybody', and they are normally undetected at wavelengths shorter than $\sim 10\,\mu$m (André 1995). AWB used the criterion $L_{\rm submm}/L_{\rm bol} > 1/200$ to define Class 0 sources, where $L_{\rm submm}$

is the integrated luminosity at wavelengths longward of 350μm, and $L_{\rm bol}$ is the total luminosity. The submillimetre luminosity mainly arises from dust in the protostellar envelope, and the bolometric luminosity, which is mainly derived from accretion, is expected to be roughly proportional to the mass of the central protostar (e.g. Stahler, Shu & Taam 1980). The ratio $L_{\rm submm}/L_{\rm bol}$ should therefore be approximately proportional to the fraction of the total mass contained in the protostellar envelope. The Class 0 threshold is set such that, under certain assumptions, the envelope contains approximately half the total mass of the system or greater (AWB). The lack of optical and near-infrared emission in Class 0 sources is due to the very large extinction from this envelope.

Ward-Thompson et al. (1994) and André, Ward-Thompson & Motte (1996) have carried out detailed dust-continuum studies of a number of starless dense cores, which they labelled 'pre-stellar cores'. It was argued that these were evolving towards a gravitationally unstable configuration via ambipolar diffusion, and may therefore be precursors to the Class 0 phase. These cores provide the best means of investigating the initial conditions for protostellar collapse, and are therefore of great observational and theoretical interest.

An alternative measure of the shape of YSO spectral energy distributions, is the bolometric temperature, which has the advantage that it may be applied to sources which are not detected in the near and mid-infrared. Myers & Ladd (1993) defined the bolometric temperature, $T_{\rm bol}$, of a spectrum F_ν, to be the temperature of a blackbody having the same mean frequency, $\bar{\nu}$ (Ladd et al. 1991), where

$$\bar{\nu} \equiv \frac{\int_0^\infty \nu F_\nu \, d\nu}{\int_0^\infty F_\nu \, d\nu}. \tag{1.31}$$

In practice, the integrals in the above equation are estimated by piecewise linear integration between the observed photometric measurements, which should span the frequency range over which most of the luminosity is emitted. $T_{\rm bol}$ is then given by (Myers & Ladd 1993):

$$T_{\rm bol} = 1.25 \times 10^{-11} \bar{\nu} \, {\rm K \, Hz^{-1}}. \tag{1.32}$$

$T_{\rm bol}$ is expected to increase with evolutionary age, as the central stellar object becomes less obscured and the emergent spectrum shifts towards shorter wavelengths. The approximate range of $T_{\rm bol}$ for each YSO class, adapted from Chen et al. (1995), is given in Table 1.1. Apart from the flat-spectrum sources (which as stated above probably do not define a distinct class), the YSO classes correspond to well defined ranges of $T_{\rm bol}$.

1.2.2 The empirical picture of low mass star formation

The YSO populations of the nearby Ophiuchus and Taurus star-forming regions have been the most comprehensively studied to date (e.g. AM; Greene et al. 1994; Kenyon et al. 1990; KH; Chen et al. 1995; Bontemps et al. 1996). The picture of the evolutionary progression of a low mass protostar which has emerged from these studies is now described.

The Class 0 stage follows the collapse of a gravitationally unstable molecular gas cloud (prestellar core) and the formation of a small partially ionised central hydrostatic core, or protostar. It represents the *main accretion phase*, when the protostar accumulates most of the eventual mass of the star, through the infall of gas from the envelope onto the protostar. The duration of the Class 0 phase is estimated to be $\sim 10^4$ yr from their numbers relative to the later evolutionary stages (AM). Nearly all Class 0 sources drive bipolar outflows, which tend to be more energetic and well collimated than those of more evolved objects (Saraceno et al. 1996; Bontemps et al. 1996; Bachiller et al. 1990; Dent, Matthews & Walther 1995). A number of Class 0 sources show a complicated, multiple-lobed outflow structure, e.g. IRAS 16293−2422 (Walker et al. 1988); IRAS 23011 (Ladd & Hodapp 1997), NGC1333-IRAS2 (Sandell et al. 1994) and L723 (Avery et al. 1990), which may indicate that the intensity and direction of bipolar outflows can be extremely variable in their earliest stages, or that protostars tend to coexist in close pairs or groups. Class 0 sources are also frequently associated with free-free centimetre continuum emission, which may arise in shocks produced by the protostellar wind, or by the impact of infalling envelope material onto the protostar or

disk (e.g. Neufield & Hollenbach 1996). The Class 0 source VLA 1623 was inferred to have an unresolved disk with a radius of $< 175\,\mathrm{AU}$ from submillimetre interferometry measurements (Pudritz et al. 1996).

The Class I stage represents the *late accretion phase* (André 1993), with a lifetime of $\sim 2 \times 10^5\,\mathrm{yr}$ (AM; Greene et al. 1994; KH), during which the last 10–20% of the protostellar envelope is accreted onto the central protostar/disk system. Class I sources usually have outflows, but these are less energetic and collimated than Class 0 sources. There is a strong correlation between the outflow luminosity and the protostellar envelope mass, which spans both YSO classes, suggesting a link between infall and outflow (Bontemps et al. 1996; Saraceno et al. 1996).

The short lifetimes and large circumstellar masses of Class 0 sources imply that the mass accretion rate in these objects is significantly larger than Class I objects. It is therefore surprising that the bolometric luminosities of Class I and Class 0 sources appear to lie in approximately the same range. Henriksen, André & Bontemps (1997) have argued, however, that this can be explained by the fact that Class 0 sources are expected to have lower central protostellar masses and larger protostellar radii (assuming the protostellar radius, $R_\star$, obeys $R_\star \propto \dot{M}_{\mathrm{acc}}$ (Stahler 1988)), and may be expected to dissipate a larger fraction of their accretion energy in the outflow than Class I sources.

The physical nature of the flat-spectrum sources is still a subject of some debate. Flared disks (i.e. increasing disk scale height with radius) and active, self-luminous disks (Kenyon & Hartmann 1987; Adams et al. 1988) have been invoked to explain the flat spectral energy distribution. Recent work suggests that flat spectrum sources may be Class I sources oriented favourably with respect to the line of sight, such that the extinction to the central protostar is unusually low, possibly due to a cavity cleared by the outflow (e.g. Kenyon et al. 1993; Calvet et al. 1994).

Class II objects are approximately equivalent to Classical T-Tauri stars (CTTS) (Herbig & Bell 1988; Bertout 1989), which are pre-main sequence stars with surrounding compact, centrifugally supported disks (Bertout, Basri & Bouvier 1988). CTTS are identified by the strength of their Hα emission lines, which is thought to be associated with strong stellar wind. Cabrit et al. (1990) found a good correlation between the Hα line luminosity (which traces mass outflow) and excess near-infrared emission (which traces the disk) for a large sample of YSO's. There was no strong correlation between the Hα line luminosity and the total stellar luminosity, however, suggesting that the disk plays an important role in the mass loss mechanism of T-Tauri stars (see also Shu et al. 1993).

The predicted infrared spectral index for both optically thick (but spatially thin) passive disks (which reprocess incident radiation from the protostar) and actively accreting Keplerian disks, is $\alpha_{\rm disk} = -4/3$ (Lynden-Bell & Pringle 1974; Adams et al. 1988). This lies inside the Class II spectral index range (see Table 1.1). The typical Class II disk mass is ($\sim 0.02 \mathrm{M}_\odot$), similar to the disks associated with most Class I objects (Terebey, Chandler & André 1993). Unlike Class I sources, however, Class II sources are rarely associated with bipolar outflows, although when optically visible they often show evidence of mass loss in optical emission lines, particularly Hα emission. The lifetime of the Class II phase is $\sim 10^6$ yr, as determined from comparisons with theoretical pre-main sequence evolutionary tracks (e.g. KH).

Class III sources have continuum spectra similar to a reddened blackbody, and are the least obscured of the YSO classes. They are approximately equivalent to Weak Line T-Tauri Stars (WTTS) (Herbig & Bell 1988; Walter et al. 1988), which are distinguished from ordinary stars by their strong X-ray emission, and by the fact that they lie well above the main-sequence in the Hertzsprung-Russell (H-R) diagram. Although Class III sources are occasionally associated with a small amount of cold circumstellar material (AM), they do not have the massive circumstellar disk and strong mass loss associated with Class II sources.

There is a controversy about the evolutionary status of the WTTS (e.g. Alcalá et al. 1997). It was initially suggested that Class II sources/CTTS evolved into Class III sources/WTTS, after the disk had mostly dispersed, or coagulated into large bodies. In contrast to CTTS, which tend to be confined to the vicinity of dense molecular cores, WTTS are usually very widely distributed spatially (Wichmann et al. 1996; Alcalá et al. 1997). This suggests that they are older than CTTS, having had a longer time to disperse from their sites of formation. This is contradicted, however, by the fact that WTTS and CTTS are generally well mixed in the H-R diagram, suggesting that they have similar age and mass ranges.

YSO Class	α	$T_{bol}(K)$	Age(yr)	Description
Class 0	–	<70	$\sim 10^4$	Massive envelope/main accretion phase
Class I	$\alpha \geq 0.3$	70–650	$\sim 10^5$	Disk + residual envelope/late acc. ph.
Flat Spec.	$-0.3 \leq \alpha < 0.3$	500–1500	$\sim 10^5$	'Pole-on' Class I?
Class II	$-1.6 \leq \alpha < -0.3$	650–2880	$\sim 10^6$	Optically thick disk/CTTS
Class III	$\alpha < -1.6$	>2880	$\geq\sim 10^6$	Optically thin or no disk/WTTS

Table 1.1: Table outlining the different YSO classification schemes. 'CTTS' and 'WTTS' are abbreviations for 'Classical T-Tauri Star' and 'Weak Line T-Tauri Star' respectively.

1.3 Spectroscopic Evidence for Collapse and Infall

In this section we review the evidence for collapse in molecular clouds and protostellar envelopes, provided by millimetre and submillimetre spectral line observations.

1.3.1 Turbulence and collapse motions in molecular clouds

Early observations of molecular clouds in the CO($J = 1 \rightarrow 0$) rotational emission line showed several unexpected features. The velocity widths of the lines were usually many times larger than the predicted thermal velocity width corresponding to the gas temperature. The broadening could only be explained by bulk motions of the emitting

gas, although the nature of the required velocity field was uncertain. It was difficult to understand the apparent ability to 'see through' clouds in CO emission, which showed peaks towards deeply embedded heating sources, since the optically thick CO emission was only expected to probe the outer layers of the cloud. Furthermore, the general lack of self-absorption in the CO profiles was puzzling, since it was expected that the CO excitation temperature would drop significantly in the outermost cloud layers as the gas density decreased. The following account of some of the attempts made to reconcile these facts touches on many important concepts, and pitfalls, associated with the analysis of molecular line profiles.

Homologous collapse

To explain the observations in the preceding paragraph, it was proposed that molecular clouds were undergoing global homologous collapse (e.g. Goldreich & Kwan 1974; de Jong, Dalgarno & Chu 1975; Kwan 1978). A homologously contracting cloud has a ($v \propto r$) collapse velocity profile which is the predicted behaviour for a collapsing pressureless uniform density sphere. This velocity law results in a linear velocity gradient along any line of sight through the cloud. If the collapse was rapid enough that the velocity difference at the front and back of the cloud was much greater than the intrinsic velocity width of the gas (assumed to be due to microscopic random thermal motions), then different points on the observed spectra would directly sample different depth layers of the cloud, without confusion from intervening layers. As well as accounting for the large observed velocity widths, this could explain the lack of self-absorption in the line profiles, and the apparent 'transparency' of the CO emission.

Another advantage of this model was that the 'large velocity gradient' (LVG) approximation (also referred to as the Sobolev approximation) could be used to simplify the derivation of cloud properties from the observed specta (e.g. Scoville & Solomon 1974). The LVG approximation assumes that the systematic flow velocities are much larger than the local thermal and turbulent random velocities. More specifically, the

photon thermalisation length (i.e. the mean distance between the creation and destruction of a photon) must be greater than the distance over which the systematic velocity changes by an amount equal to the intrinsic velocity width of the gas. If this condition is satisfied, the mean radiation intensity at each point depends only on the line excitation temperature and the photon escape probability (i.e. the probability that a photon emitted at that point will escape from the cloud without further interaction), both of which are locally determined quantities (Castor 1970; Lucy 1971). The LVG approximation made the radiative transfer analysis of molecular clouds tractable, but was only valid for a restrictive range of possible velocity fields.

Turbulence

Objections to the collapse model were raised by Zuckerman & Evans (1974) and Zuckerman & Palmer (1974). If the collapsing material was being turned into stars at the centre of each molecular cloud, the model predicted a prohibitively high value for the galactic star formation rate. A more direct problem was the general agreement in the radial velocity of H_2CO absorption lines and CO emission lines observed towards embedded ultracompact HII (UCHII) regions in molecular clouds. If the clouds in which the HII regions were embedded were collapsing homologously, the absorption lines should be preferentially red-shifted with respect to the CO lines, unless the HII regions all happened to be situated close to the rear edge of each cloud.

Zuckerman & Evans (1974) attributed the large CO linewidths to supersonic turbulent motions. One difficulty with the latter explanation, however, was that supersonic turbulence was expected to decay on a timescale comparable to the sound crossing time of the largest turbulent eddies, and a constant replenishment of the turbulent energy was required (e.g. Lucas 1974; Field 1978). To address this problem, it was proposed that molecular clouds have a very inhomogeneous structure, with small, dense clumps moving through a more diffuse medium, interacting with each other only occasionally. In this way the predicted dissipation timescale of the supersonic random motions could

be increased to a value more compatible with molecular cloud lifetimes. Alternatively, magnetic fields could inhibit turbulent dissipation (e.g. Arons & Max 1975), or the turbulent energy could be replenished by outflows of gas from forming stars (Norman & Silk 1980; Bally & Lada 1982; McKee 1989), or by galactic rotational shear (Fleck 1980, 1981).

Several theoretical investigations have addressed the problem of line formation in turbulent gas (e.g Leung & Liszt 1976; White 1977; Leung 1978; Dickman 1985; Albrecht & Kegel 1987; Kegel, Piehler & Albrecht 1993; Piehler & Kegel 1995; Park & Hong 1995; Park, Hong & Minh 1996; Juvela 1997). Although the earliest studies predicted strongly self-absorbed line profiles (e.g Lucas 1974, 1976) which were only rarely observed, later work showed that this was largely dependent on the assumptions of *microturbulence* and a smooth density field. The microturbulent approximation (see Chapter 2) assumes that the characteristic turbulent length scale is much less than the photon mean free path, and allows the turbulence to be fully taken into account by a modification of the intrinsic line profile function of the gas (see Chapter 2). For very optically thick CO transitions, however, the photon mean free path is typically only a very small fraction of the size of the cloud, and it seems unlikely that turbulent motions would be confined to such a scale. Furthermore, there is plenty of observational evidence that molecular clouds have very inhomogeneous density structures (e.g. Falgarone, Phillips & Walker 1991).

Non-homologous collapse

A few exceptions have been found to the general rule that CO line profiles observed towards molecular clouds are not strongly self-absorbed. Snell & Loren (1977) (hereafter SL) drew attention to the double-peaked CO($J = 1 \rightarrow 0$) line profiles observed towards several molecular clouds, including NGC 1333 (see also Loren 1976) and the ρ Oph cloud. The line profiles tended to be asymmetric, with a brighter blue peak than red peak, and a red-shifted absorption minimum (relative to the systemic velocity). SL argued that the unusual line profiles could be explained if these clouds were collapsing

in a non-homologous fashion.

Hummer & Rybicki (1968) first realised that a region of gas with a systematic velocity gradient and a line excitation temperature which increases with optical depth into the cloud, could give rise to an asymmetric, double peaked (or skewed) line profile, as long as the line was reasonably optically thick and the velocity gradient was not too large. The predicted profile for a converging velocity field has a blue-shifted main peak and a red-shifted secondary peak or red 'shoulder', as observed by SL (see also Figure 1.5). The problem actually analysed by Hummer & Rybicki (1968) was an *expanding* slab of gas, for which the predicted asymmetry is reversed.

SL modelled their observations with a spherical cloud model and a $v \propto r^{-1/2}$ collapse velocity profile, using the LVG assumption. The decrease in infall speed with radius has the important consequence that distant regions of the cloud may be radiatively coupled to one another as a result of velocity projection effects, which allows for greater self-absorption. Partly for this reason, and partly because of the low velocities at large radius for a $v \propto r^{-1/2}$ velocity profile, the LVG approximation is strictly invalid in this case. This point was emphasised by Leung & Brown (1977), who remodelled some of the SL observations by solving the radiative transfer problem for a *static* cloud, and then imposed an infalling velocity field during the line profile calculation. Although self-consistency is lost in this approach, it is founded on the expectation that the solution for the equilibrium level populations in the cloud is much less sensitive to the velocity field than the prediction for the observed line profile.

Myers (1980) used a simple planar analytical radiative transfer model to fit blue-asymmetric CO line profiles observed towards several dark clouds in Taurus. The model pictured an outer gas envelope contracting onto a static central core. Myers, Linke & Benson (1983) used this model to interpret the significant excess of blue-skewed line profiles in their sample of 90 dense cores in terms of contraction motions. A similar analytical model was recently proposed by Myers et al. (1996) to analyse line profiles

observed towards infalling protostellar envelopes.

It has been claimed that the high mass star-forming regions W49N (Welch et al. 1987; Dickel & Auer 1994), and W51 (Rudolph et al. 1990) are collapsing on a global scale. In both cases, inverse P-Cygni type line profiles (i.e. blue-shifted emission and red-shifted absorption) were observed in $HCO^+(J = 1 \rightarrow 0)$ towards a number of deeply embedded UCHII regions, and were fitted using the Shu (1977) protostellar collapse model, which was assumed to be applicable on the scale of a molecular cloud. This interpretation is controversial however. There is strong evidence that the large scale dynamics of W49N is dominated by the collision of two giant molecular clouds, rather than by global collapse (Serabyn et al. 1993; Miyawaki, Hayashi & Hasegawa 1986; Buckley & Ward-Thompson 1996). Serabyn et al. (1993) argued that the cloud-cloud collision model could explain the inverse P-Cygni HCO^+ profiles, if the UCHII regions lie in the interface region between the colliding clouds. Ho & Young (1996) inferred from their VLA ammonia observations of W51 that collapse was only taking place in the direct vicinity of one of the UCHII regions, and also found evidence for two extended cloud components with rapidly converging velocities along the line of sight.

1.3.2 Observations of protostellar infall

'Protostellar infall' refers to the main and late accretion phases which follow the initial collapse of a dense core and the formation of a central hydrostatic protostar. The most convincing cases for protostellar infall to date have been made for the Class 0 sources IRAS 16293−2422, B335 and L1527. We now briefly summarise the evidence for infall in these objects.

IRAS 16293−2422

The first claimed spectroscopic detection of infall in a protostellar envelope was made by Walker et al. (1986), for the protobinary far-infrared source IRAS 16293−2422

(hereafter IRAS 16293), which was observed in the CS($J = 2 \rightarrow 1$) and ($J = 5 \rightarrow 4$) main and isotopic lines. The CS($J = 5 \rightarrow 4$) main line spectrum showed a double peaked asymmetric infall-type line profile, and the data was approximately fitted by an infalling spherical envelope model with a $v \propto r^{-1/2}$ infall velocity profile.

Menten et al. (1987) mapped the IRAS 16293 envelope in CS($J = 3 \rightarrow 2$) emission, and argued that the asymmetric self-reversed line profile was caused by absorption from a physically unrelated foreground gas layer, rather than by infall. They also found strong evidence of a rotational velocity gradient across the envelope. Subsequent spectroscopic observations have strengthened the support for both infall and rotation, and have led to the view that both kinds of motion are taking place simultaneously (Walker, Carlstrom & Bieging 1993; Walker, Narayanan & Boss 1994; Zhou 1995; Narayanan, Walker & Buckley 1997). IRAS 16293 will be discussed in greater detail when new observations of this object are presented in Chapter 3.

B335

The most convincing case for infall to date has been made for the isolated Bok Globule, B335, which contains an embedded far-infrared source (Keene et al. 1983) powering a wide angle bipolar outflow lying in the plane of the sky (e.g. Cabrit, Goldsmith & Snell 1988; Chandler & Sargent 1993).

Zhou et al. (1990) found that an approximate Shu model density profile gave a good fit to their 6 cm H_2CO map of B335, in which *absorption* against the microwave background radiation was clearly observed. The gas kinetic temperature profile was assumed to match the dust temperature profile, which was derived independently from dust radiative transfer modelling of the continuum spectral energy distribution. Zhou et al. (1993) tested the kinematic implications of this model by carrying out line-profile modelling of CS and H_2CO line profiles. In this case, the exact velocity and density

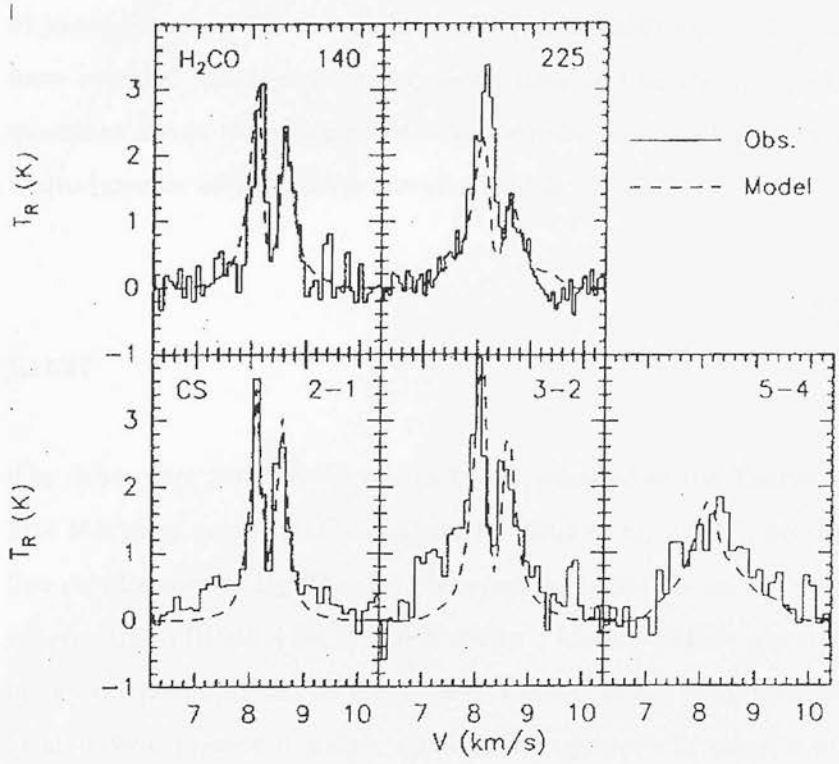

Figure 1.5: Non-LTE radiative transfer model fits to H_2CO and CS line profiles observed towards B335, using the density and velocity profiles predicted by the Shu model for an infall radius of 6200 AU and an effective sound speed of $0.23\,\mathrm{km\,s^{-1}}$(from Choi et al. 1995).

profiles predicted by the Shu model were used, and acceptable fits to most of the observations were obtained. Choi et al. (1995) later remodelled the same observations using an exact, non-LTE Monte Carlo radiative transfer code, and found an improved fit to the data (see Figure 1.5).

B335 is the only object discovered to date which is well matched to the original Shu (1977) inside out collapse model, both in its kinematics and in its density structure. This may be related to the fact that it is an isolated object, with only a small rotation ($\sim 0.4\,\mathrm{km\,s^{-1}pc^{-1}}$, Frerking, Langer & Wilson 1987). Whitworth et al. (1996) and Henriksen et al. (1997) have recently questioned the validity of the Shu model in the highly perturbing environment present in most molecular clouds. Bok globules usually provide an isolated and unperturbed environment for star formation to take place, and if the Shu model has any domain of validity at all, it is most likely to be valid in these

objects. Even so, VLA maps in H_2CO (Zhou 1992) and CCS (Velusamy et al. 1995) have revealed a rather inhomogeneous structure to the B335 envelope, which raises questions about the validity of the assumption of smooth density profiles used in both hydrodynamic and radiative transfer models.

L1527

The dense core and Class 0 source L1527, situated in the Taurus molecular cloud, was first identified as an infall candidate by Zhou et al. (1994), on the basis of infall-type line profiles seen in H_2CO and $C^{18}O$ spectra. L1527 contains an embedded far-infrared source (IRAS 04368 +2557) which drives a bipolar outflow oriented close to the plane of the sky (Zhou, Evans & Wang 1996; Tamura et al. 1996; Ohashi et al. 1996). Myers et al. (1995) presented mainly qualitative arguments in support of infall, based on the trends in the observed lineshapes with distance across the source and with increasing optical depth of the line, compared with the theoretical predictions of Adelson & Leung (1988). Zhou et al. (1996) carried out radiative transfer modelling of single dish and interferometric spectral line observations of L1527, adopting the Terebey, Shu & Cassen (1984) model of inside-out collapse with rotation. The best fit parameters for the collapse time and mass infall rate were 1.3×10^5yr and $2.9\times10^{-6}\,M_\odot\,yr^{-1}$ respectively. The rotation rate at large distance was fixed using the measured velocity gradient of $3.3\,km\,s^{-1}pc^{-1}$ in the core (Goodman et al. 1993), assuming a rotation axis in the plane of the sky, as suggested by the low inclination angle of the outflow. Ohashi et al. (1996) used a simple kinematic model of infall and rotation to fit position-velocity diagrams derived from their interferometric $C^{18}O$ observations, and found broadly similar rotation and infall parameters as Zhou et al. (1996). Figure 1.6, shows the structure of L1527 core and outflow, as revealed in the CO and $C^{18}O$ ($J = 1 \rightarrow 0$) interferometer observations of Ohashi et al. (1996).

In many respects, L1527 is quite similar to B335 – both have comparable luminosity and mass; both drive conical east-west outflows close to the plane of the sky

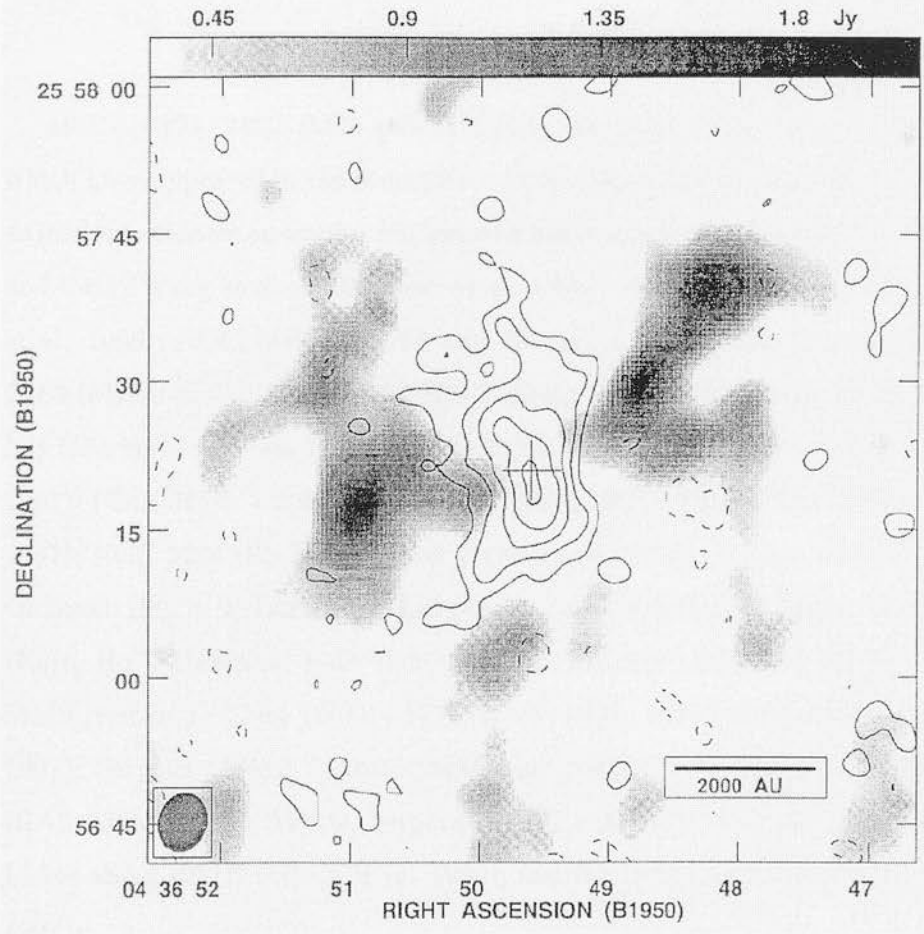

Figure 1.6: Map of L1527 in $C^{18}O(J = 1 \rightarrow 0)$ emission (contours) delineating the protostellar envelope, and high velocity red-shifted and blue-shifted $CO(J = 1 \rightarrow 0)$ emisson (greyscale), tracing the outflow (Ohashi et al. 1996). The cross marks the position of the central protostar. The envelope is rotating about its minor axis, and contains cavities evacuated by the outflow lobes.

and both have relatively narrow line profiles, which show evidence of infall motions. The principal difference between the objects is the much more rapid rotation in L1527. The poorly collimated outflows and narrow linewidths contrast markedly with several other Class 0 sources, such as VLA 1623, and L1448-C, although the reason for these differences is not clear.

IRAS 16293−2422, B335 and L1527 are the clearest examples of protostellar infall which have appeared in the literature to date. Many other objects have been suggested as infall candidates on similar but less conclusive spectroscopic evidence: CB 54, CB 244 and CB3 (Wang et al. 1995; Zhou et al. 1996); NGC 1333-IRAS 2 (Ward-Thompson et al. 1996); NGC 1333-IRAS 4A and 4B (Blake et al. 1994; Mardones et al. 1997); L483 (Myers et al. 1995); L1551-IRS 5 (Saito et al. 1996; Ohashi et al. 1996); L1551-NE (Moriarty-Schieven et al. 1995); L1524 (Zhou et al. 1994); HH 111 (Yang et al. 1997); IRAS 04169 +2702 (Ohashi et al. 1997); IRAS 0038 +6312 (Walker & Masheder 1997); NGC 2264 IRS (Wolf-Chase & Gregersen 1997); Z Canis Majoris (Liljeström & Olofsson 1997); T-Tauri (van Langevelde, van Dishoeck & Blake 1994); G10.6−0.4 (Keto, Ho & Haschick; Keto 1990); HL Tau (Hayashi, Ohashi & Miyami 1993); HH24 MMS (Krügel & Chini 1994); L1157 (Gueth et al. 1997); IRAS 13036 -7644 (Lehtinen 1997); Serpens SMM2, SMM3, SMM4 and S68N (Hurt, Barsony & Wootten 1996); IRAS 03256 +3055, WL22, Serpens SMM5 and VLA 1623 (Mardones et al. 1997); L1544 and L1251B (Myers et al. 1996); and HH25 and IRAS 20050 (Gregersen et al. 1997).

1.3.3 Infall surveys

We now summarise the results of a number of recent spectral line surveys of relevance to protostellar infall.

Zhou et al. (1994) mapped 11 dense cores in the Taurus molecular cloud in the $C^{18}O(J = 2 \rightarrow 1)$ line. In the five cores containing embedded infrared sources they measured excessive $C^{18}O$ line widths, when compared with the generic linewidth-size

relation derived by Fuller & Myers (1992). It was suggested the anomalous linewidths in the cores containing embedded objects could be due to infalling gas. The linewidths and radial $C^{18}O$ intensity distributions of these cores could not be well fitted by the Shu model however.

Moriarty-Schieven et al. (1995) observed 25 young stellar objects in Taurus (mostly Class I sources) in several transitions of the high density tracers CS and H_2CO, and used them to derive temperatures and densities of the envelope and outflow gas. Of the 25 sources observed, only 2 (L1527 and L1551-NE) showed profiles indicative of infall.

Wang et al. (1995) carried out a $C^{18}O(J = 2 \rightarrow 1)$ mapping survey of 33 Bok globules containing IRAS point sources. The IRAS sources were associated with the globules by their proximity and characteristic YSO colours (Yun & Clemens 1990). 12 globules showed $C^{18}O$ column density peaks close to the IRAS positions, and of these, nine were detected in the high critical density transition $H_2CO(J_{K_{-1}K_1} = 3_{12} \rightarrow 2_{11})$. Three of the H_2CO detections showed mild blue asymmetries, and significantly enhanced linewidths compared with $C^{18}O$. On this evidence they were suggested to be infall candidates.

Hogerheijde et al. (1997) observed most of the source sample studied by Moriarty-Schieven et al. (1995) (see above) in the $HCO^+(J = 3 \rightarrow 2)$ transition. A subsample of the nine strongest detections in this line were selected for mapping at 2.7 and 3.4 mm using the OVRO millimetre array. Two thirds of the sources showed an unresolved central component in interferometer maps, attributed to a compact circumstellar disk, and in about half of the sources an extended envelope was resolved. Single dish mapping was carried out for these nine sources in $HCO^+(J = 1 \rightarrow 0)$, $(J = 3 \rightarrow 2)$ and $(J = 4 \rightarrow 3)$ transitions. On-source spectra of the relatively optically thin $H^{13}CO^+(J = 3 \rightarrow 2)$ and $(J = 4 \rightarrow 3)$ lines were also obtained. Infall-type profiles were only found towards two objects – L1489 and L1527– similar to the result found by Moriarty-Schieven et al. (1995) for CS. It was inferred that $HCO^+(J = 3 \rightarrow 2)$ and $(J = 4 \rightarrow 3)$ were

robust tracers of the envelope, whereas the $HCO^+(J = 1 \rightarrow 0)$ line appeared to be contaminated by emission from the surrounding ambient cloud.

Comparing the $HCO^+(J = 3 \rightarrow 2)$ integrated emission with the $CS(J = 3 \rightarrow 2)$, $CS(J = 5 \rightarrow 4)$, $CS(J = 7 \rightarrow 6)$ observations of Moriarty-Schieven et al. (1995), it was concluded that HCO^+ is a better tracer of envelope mass than CS. Hogerheijde et al. (1997) also concluded that for single dish observations, HCO^+ is a better tracer of the mass in the dense protostellar envelope than the millimetre continuum flux. This is because the HCO^+ emission from the disk is too beam diluted to contribute significantly to the total, unlike the millimetre continuum flux from the disk, which stays optically thin. Hogerheijde et al. (1997) suggested that the ratio of the integrated $HCO^+(3 \rightarrow 2)$ flux to the bolometric luminosity of the source could be used as an indicator of evolutionary age. This ratio would be expected to decrease with time, as the protostellar envelope mass is depleted by accretion onto the central protostar and disk, and as the accretion luminosity rises, due to the increase in mass of the protostar.

Gregersen et al. (1997) carried out a multi-transition, multi-isotope HCO^+ survey of a near-complete sample of the known Class 0 sources. Of the 18 objects which were observed in both the $HCO^+(J = 4 \rightarrow 3)$ and $HCO^+(J = 3 \rightarrow 2)$ transitions, nine showed a blue infall asymmetry in both these lines. Three objects showed a red asymmetry in both lines, and one object (L1157) showed a blue asymmetry in $HCO^+(J = 3 \rightarrow 2)$ and a red asymmetry in $HCO^+(J = 4 \rightarrow 3)$. The remaining sources showed no significant asymmetry in either line. Hogerheijde et al. (1997) argued that these lines are particularly good tracers of envelope gas. The observed bias towards profiles which have a blue, infall-type asymmetry is consistent with the view that Class 0 sources represent protostars in the main accretion phase of their evolution, and so are better observable infall candidates than Class I sources. This statement must be qualified, however, by the small but significant number of clear counterexamples to the overall trend.

To help determine whether emission from the outflow was significantly contaminat-

ing the observed profiles, Gregersen et al. (1997) presented $HCO^+(J = 3 \rightarrow 2)$ channel maps of seven of the most promising infall candidates, which showed the spatial distributions of line core and line wing emission separately, and further separated these into their red-shifted and blue-shifted components. For a pure Shu model collapse the line wings were predicted to show a much more compact peak than the line core, since the largest systematic velocities are found close to the centre of the collapsing envelope. In both the line wings and line core, the blueshifted emission was predicted to be brighter and more extended than the redshifted emission. None of the line wing maps of the infall candidates matched the predicted behaviour. For most of the sources, the redshifted and blue shifted line wing maps showed peaks which were displaced a significant distance from the source position in opposite directions. Gregersen et al. (1997) attributed this to bipolar outflows, and for several of the objects this is supported by the agreement with the CO outflow maps. The redshifted and blue-shifted peaks in the line core maps were also displaced from one other, although by smaller distances and sometimes in different directions than seen in the line wing maps. One explanation for this could be that the line core maps are dominated by rotation of the protostellar envelope, whereas the line wings are dominated by the outflow. On the whole, the blue shifted peaks in the line core maps were brighter and more extended than the red-shifted peaks, as predicted by the model. These maps therefore suggest that outflow, infall and rotation may contribute significantly to different parts of the line profile and at different positions on the source.

Mardones et al. (1997) carried out the largest infall survey to date, observing a sample of 23 Class 0 sources and 24 Class I sources in the typically optically thick $H_2CO(J_{K_{-1}K_1} = 2_{12} \rightarrow 1_{11})$ and $CS(J = 2 \rightarrow 1)$ lines, and the optically thin $N_2H^+(J = 1 \rightarrow 0)$ lines. They used δV, defined by the following equation, to measure the line asymmetry:

$$\delta V = \frac{V_{\rm thick} - V_{\rm thin}}{\Delta V_{\rm thin}}, \tag{1.33}$$

where $V_{\rm thick}$ and $V_{\rm thin}$ are the velocities of the peak emission in the chosen optically thick and optically thin line respectively, and $\Delta V_{\rm thin}$ is the FWHM velocity width of the optically thin line. A line was considered to have no significant asymmetry for the range

$-0.25 \leq \delta V \leq 0.25$. Using this measure, a strong segregation was found between the Class 0 and Class I sources in the sample. Of the 23 Class 0 objects, 12 showed a blue asymmetry in the H_2CO line, 8 showed no asymmetry, and 3 showed a red asymmetry. Of the 24 Class I objects, only 3 showed a blue asymmetry, 19 showed no asymmetry, and 2 showed a red asymmetry. Class 0 objects therefore show a much stronger tendency towards blue-skewed profiles than Class I objects. The segregation between the Class 0 and Class I sources was found to be even stronger in the CS($J = 2 \rightarrow 1$) sample (see Figure 1.7). Addressing the possibility that emission from the outflow might somehow mimic the observed blue asymmetries, Mardones et al. (1997) tested for a correlation between asymmetrical emission in the red and blue-shifted line wings, and the asymmetries found in the line core, and found none. These results are consistent with the findings of Gregersen et al. (1997) (see above). In a few cases (L1157, VLA 1623, L1551-NE and L483), however, the two studies found contradictory directions for the prevailing line asymmetries. This reflects the different methods used to measure the line asymmetry, and is a good indication of the systematic error in the source statistics quoted by both studies.

1.4 Summary

In this introduction we have selectively reviewed the current state of theory and observations in the field of star formation, focusing particularly on the collapse and main accretion phases of protostellar evolution.

Despite the progress made in recent years, the problem of star formation remains a formidable one. Magnetic fields are now generally believed to play a pivotal role in regulating the star formation process, and provide an elegant resolution of the angular momentum problem. Magnetic fields may also be central to the mechanism behind the ubiquitous but largely unexplained bipolar outflow phenomenon. Unfortunately, the complexity of the magnetohydrodynamic collapse problem means that it can only

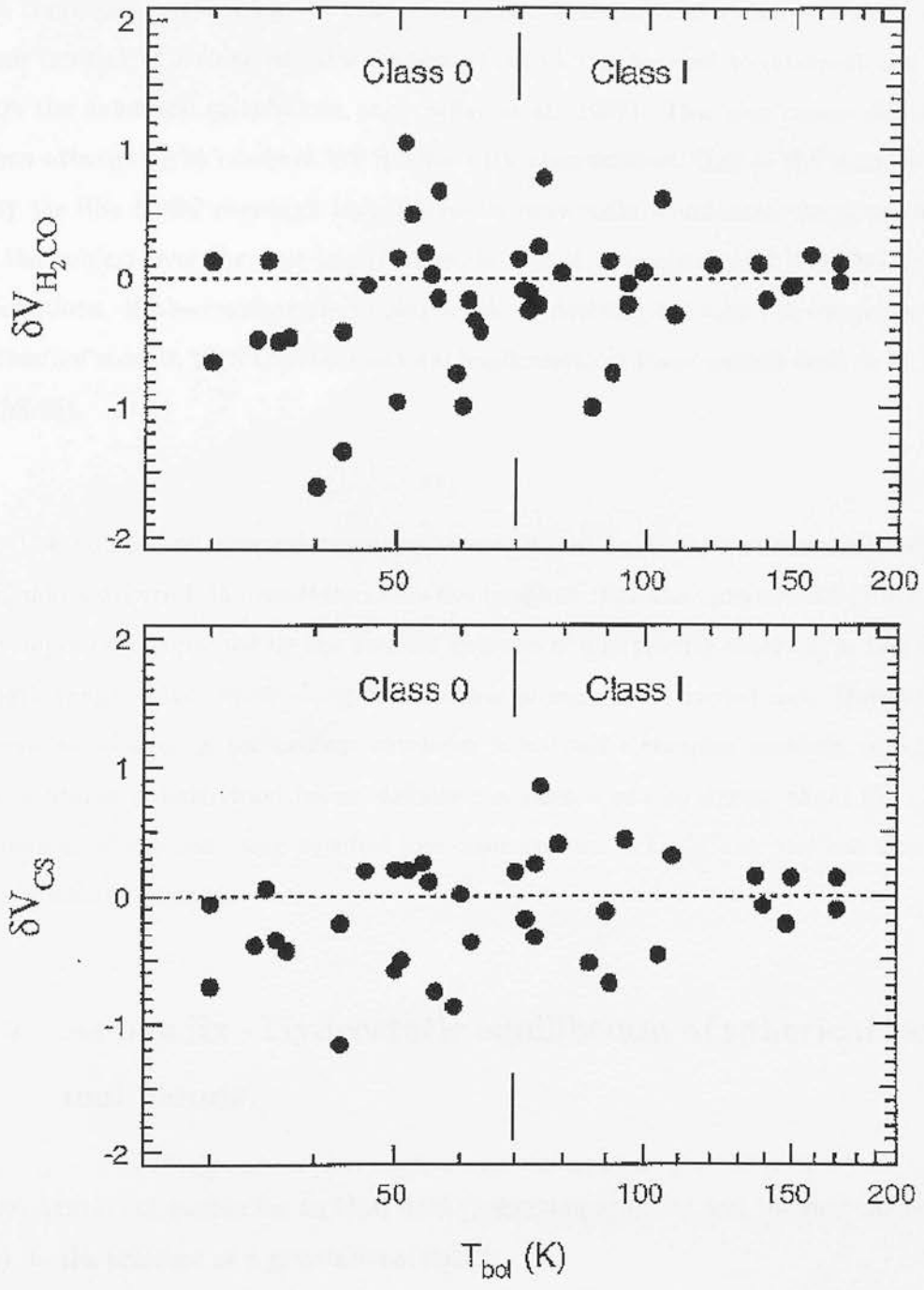

Figure 1.7: Figure showing the distribution of δV, as determined from $H_2CO(J_{K_{-1}K_1} = 2_{12} \rightarrow 1_{11}$ and $CS(J = 2 \rightarrow 1)$ spectra (see text), as function of T_{bol}, for a sample of Class 0 and Class I YSO's (Mardones et al. 1997). Negative values of δV imply blue-skewed line profiles.

be properly studied using computationally expensive numerical simulations. Much of the confusion surrounding the role of magnetic fields in protostellar evolution arises from the lack of a clear intuitive framework which can be used to interpret and compare the numerical calculations (e.g. Safier et al. 1997). This also causes difficulties when attempting to compare the models with observations. One of the main reasons why the Shu model paradigm has, despite its drawbacks, dominated the development of the subject over the past two decades, is that it is intuitive and it makes definite predictions. If observations are to play a role in deciding between the competing star formation models, then the observational implications of these models need to be made apparent.

The unmatched spectral resolving power offered by today's millimetre and submillimetre spectral line receivers offers the prospect that the dynamics of protostellar envelopes can be probed by the detailed analysis of line profiles observed in this wavelength range. Much work along this line has already been carried out. However the formation of lines in protostellar envelopes is in itself a complex problem, and needs to be properly understood before definite conclusions can be drawn about the actual dynamics of the gas using spectral line observations. This is the problem that this thesis aims to address.

1.5 Appendix - Hydrostatic equilibrium of spherical isothermal clouds.

The equation of motion for an ideal fluid (neglecting viscosity and thermal conductivity), in the presence of a gravitational field is

$$\frac{d\mathbf{v}}{dt} \equiv \frac{\partial \mathbf{v}}{dt} + (\mathbf{v} \cdot \nabla)\mathbf{v} = -\frac{\nabla P}{\rho} + \mathbf{g}, \tag{1.34}$$

e.g. Landau & Lifshitz (1959). In the equation above, $\mathbf{v}(\mathbf{r}, t)$ and $\rho(\mathbf{r}, t)$ are respectively the density and velocity fields; P is the pressure, which is related to the density by an equation of state for the fluid, and $\mathbf{g}$ is the gravitational field.

The conservation of mass in the flow is expressed by the continuity equation,

$$\frac{\partial \rho}{\partial t} + \nabla \cdot (\rho \mathbf{v}) = 0. \tag{1.35}$$

We now assume spherical symmetry, and that the gas obeys the ideal gas equation of state and remains isothermal:

$$P = \frac{\rho k T}{\mu} = \rho a^2, \tag{1.36}$$

where a is the isothermal sound speed, and is a constant. Equations 1.34 and 1.35 become

$$\frac{\partial \rho}{\partial t} + \frac{1}{r^2}\frac{\partial}{\partial r}(r^2 \rho v) = 0 \tag{1.37}$$

$$\frac{\partial v}{\partial t} + v\frac{\partial v}{\partial r} = -\frac{a^2}{\rho}\frac{\partial \rho}{\partial r} - \frac{GM}{r^2}. \tag{1.38}$$

$M(r,t)$ is the total mass inside the radius r at time t, given by

$$M(r,t) = \int_0^r 4\pi r'^2 \rho(r',t)\, dr'. \tag{1.39}$$

To find a hydrostatic solution, we set $v = 0$ in equations 1.38 and 1.38. Equation 1.38 then simply reduces to $\partial\rho/\partial t = 0$, i.e. the density profile is static, as expected. Differentiating equation 1.38 with $v = 0$, and substituting equation 1.39, we arrive at the well known Lane-Emden equation:

$$\frac{1}{r^2}\frac{d}{dr}\left(\frac{r^2}{\rho}\frac{d\rho}{dr}\right) = -\frac{4\pi G \rho}{a^2}. \tag{1.40}$$

The density ρ and the density gradient $d\rho/dr$ at the centre of the cloud may be conveniently specified as boundary conditions. In the absence of a central point mass, the gas pressure gradient at the centre must be zero, and hence from equation 1.36 we have

$$\left.\frac{d\rho}{dr}\right|_{r=0} = 0. \tag{1.41}$$

The other boundary condition (i.e. the central density) is not constrained a-priori, and may be used to parameterise the family of possible hydrostatic equilibrium configurations, which are referred to as Bonnor-Ebert spheres (Ebert 1955; Bonnor 1956). The

density profiles of all Bonnor-Ebert spheres have an identical mathematical form, as can be seen by making the following co-ordinate transformation:

$$\rho = \rho_c e^{-\varrho(x)} \tag{1.42}$$

$$r = \left(\frac{a^2}{4\pi G\rho_c}\right)^{\frac{1}{2}} x \equiv R_0 x, \tag{1.43}$$

where $\varrho(x)$ and x are dimensionless quantities, ρ_c is the central density, and $R_0 = (a^2/4\pi G\rho_c)^{1/2}$ is a constant with the dimension of length. Substituting these into equation 1.40 yields the dimensionless equation

$$\frac{d}{dx}\left(x^2\frac{d\varrho}{dx}\right) = x^2 e^{-\varrho}. \tag{1.44}$$

In these co-ordinates the boundary conditions become $\varrho = d\varrho/dx = 0$ at $x = 0$. This equation may be solved numerically for $\varrho(x)$. The density profile of the hydrostatic equilibrium configuration may then be constructed using equations 1.42–1.43, once the central density and isothermal sound speed have been specified. The entire family of Bonnor-Ebert spheres is then represented by a single mathematical form, and any two such spheres are related to each other by constant scaling factors in density and radius.

In practice the spheres must be truncated at some finite density and pressure, since the enclosed mass diverges as the radius extends to infinity. Bonnor (1956) investigated the stability of these truncated spheres, and found that there is a critical value of x, (i.e. a critical ratio of central to surface density) above which the sphere becomes unstable to external perturbations. The threshold value of x is $x_{\rm crit} \simeq 6.451$, which in physical units corresponds to

$$R_{\rm crit} \simeq 6.451\left(\frac{a^2}{4\pi G\rho_c}\right)^{\frac{1}{2}}. \tag{1.45}$$

Figure 1.3 shows a plot of $e^{-\varrho x}$ against $x/x_{\rm crit}$ (i.e. a plot of ρ/ρ_c against $r/R_{\rm crit}$) for a critical Bonnor-Ebert sphere. The central region is rather flat out to about one tenth of the critical radius. Towards the outer boundary of the sphere the density profile approaches a $1/r^2$ behaviour. The mass of the critical Bonnor Ebert sphere gives a precise theoretical value of the critical 'Jeans mass' for gravitational instability, and

may be written in the following ways:

$$M_{\rm crit} = 2.43\frac{a^2 R}{G}, \tag{1.46}$$

$$= 1.18\frac{a^4}{(G^3 P_{\rm ext})^{1/2}}, \tag{1.47}$$

where $P_{\rm ext} = \rho(R)a^2$ is the pressure at the outer boundary of the cloud.

1.6 References

Adams F. C., Shu F. H., 1985, 296, 655

Adams F. C., Shu F. H., 1986, 308, 836

Adams F. C., Lada C. J., Shu F. H., 1987, ApJ, 312, 788

Adams F. C., Lada C. J., Shu F. H., 1988, ApJ, 326, 865

Adelson L. M., Leung C. M., 1988, MNRAS, 235, 349

Albrecht M. A., Kegel W. H., 1987, A&A, 176 317

Alcalá J. M., Krautter J., Covino E., Neuhäuser R., Schmitt J. H. M. M., Wichmann R., 1997, A&A, 319, 184

André P., 1993, in Montmerle T., Lada C. J., Mirabel I. F., Tran Thanh Van J., eds, The Cold Universe, Editions Frontieres, Gif-sur-Yvette, France

André P., 1995, Ap&SS, 224, 29

André P., Montmerle T., 1994, ApJ, 420, 837 - AM

André P., Ward-Thompson D., Barsony M., 1993, ApJ, 406, 122 - AWB

André P., Ward-Thompson D., Motte F., 1996, ApJ, 314, 625

Arons J., Max C. E., 1975, ApJ, 196, L77

Avery L. W., Hayashi S. S., White G. J., 1990, ApJ, 357, 524

Bachiller R., Cernicharo J., Martin-Pintado J., Tafalla M., Lazareff B., 1990, A&A, 231, 174

Bally J., Lada C. J., 1983, ApJ, 265, 824

Basu S., Mouschovias T., 1994, ApJ, 265, 824

Beichman C. A., Myers P. C., Emerson J. P., Harris S., Mathieu R., Benson P. J., Jennings R. E., 1986, ApJ, 307, 337

Benson P. J., Myers P. C., 1989, ApJS, 71, 89

Bertout C., 1989, ARA&A, 27, 351

Bertout C., Basri G., Bouvier J., 1988, ApJ, 330, 350

Blake G. A., van Dishoeck E. F., Jansen D. J., Groesback T. D., Mundy L. G., 1994, ApJ, 428, 680

Bodenheimer P., Sweigart A., 1968, ApJ, 152, 515

Bonnor W. B., 1956, MNRAS, 116, 351

Bontemps S., André P., Ward-Thompson D., 1995, A&A, 297, 98

Bontemps S., André P., Terebey S., Cabrit S., 1996, A&A, 311, 858

Boss A. P., Myhill E. A., 1995, ApJ, 451, 218

Buckley H. D., Ward-Thompson D., 1996, MNRAS, 281, 294

Burkert A., Bate M. R., Bodenheimer P., 1997, MNRAS, 289, 497

Cabrit S., Goldsmith P. F., Snell R. L., 1988, ApJ, 334, 196

Cabrit S., Edwards S., Strom S. E., Strom K. M., 1990, ApJ, 354, 687

Calvet N., Hartmann L., Kenyon S. J., Whitney B. A., 1994, ApJ, 434, 330

Castor J. I., 1970, MNRAS, 149, 111

Chandler C. J., Sargent A. I., 1993, ApJ, 414, L29

Chen H., Myers P. C., Ladd E. F., Wood D. O. S., 1995, ApJ, 445, 377

Choi M., Evans N. J, II, Gregersen E. M., Wang Y., 1995, ApJ, 448, 742

Ciolek G. E., Mouschovias T. C., 1995, 454, 194

D'Antona F., Mazzitelli I., 1994, ApJS, 90, 467

Dent W. R. F., Matthews H. E., Walther D. M., 1995, MNRAS, 277, 193

Dickel H. R., Auer L. H., 1994, ApJ, 437, 222

de Jong T., Dalgarno A., Chu S.-I., 1975, ApJ, 199, 69

Dickman R. L., 1985, in Black D. C., Matthews M. S., eds, Protostars & Planets II. University of Arizona, Tuscon, p.150

Ebert R., 1955, ZAp, 37, 217

Falgarone E., Phillips T. G., Walker C. K., 1991, ApJ, 378, 186

Field G. B., 1978, in Gehrels T., ed., Protostars and Planets, University of Arizona Press, Tucson, p.243

Fleck R. C., 1980, ApJ, 242, 1019

Fleck R. C., 1981, ApJ, 246, 151L

Foster P. N., Chevalier R. A., 1993, ApJ, 416, 303

Frerking M. A., Langer W. D., Wilson R. W., 1987, ApJ, 313, 320

Fuller G. A., Myers P. C., 1992, ApJ, 384, 523

Galli D., Shu F. H., 1993, ApJ, 417, 220

Gaustad J. E., 1963, ApJ, 138, 1050

Greene T. P., Wilking B. A., André P., Young E. T., Lada C. J., 1994, ApJ, 434, 614

Goldreich P., Kwan J., 1974, ApJ, 189, 441

Goodman A. A., Benson P. J., Fuller G. A., Myers P. C., 1993, ApJ, 406, 528

Gregersen E. M., Evans N. J., II, Zhou S., Choi M., 1997, ApJ, 484, 256

Gueth F., Guilloteau S., Dutrey A., Bachiller R., 1997, A&A, in press

Hayashi C., 1966, ARA&A, 4, 171

Hayashi M., Ohashi N., Miyami S. M., 1993, ApJ 418, 71

Henriksen R., André P., Bontemps S., 1997, A&A, 323 549

Herbig G. H., Bell K. R., 1988, Lick Obs. Bull. 1111

Ho P. T. P., Young L. M., 1996, ApJ, 472, 742

Hogerheijde M. R., van Dishoeck E. F., Blake G. A., van Langevelde H. J., 1997, ApJ, in press

Hummer D. G., Rybicki G. B., 1968, ApJ, 153, L107

Hunter C., 1977, ApJ, 218, 834

Hurt R. L., Barsony M., Wootten A., 1996, ApJ, 456, 686

Juvela M., 1997, A&A, 322, 943

Keene J., Davidson J. A., Harper D. A., Hildebrand R. H., Jaffe D. T., Loewenstein R. F., Low F. J., Pernic R., 1983, ApJ, 274, L43

Kegel W. H., Piehler G., Albrecht M. A., 1993, A&A, 270, 407

Kenyon S. J., Hartmann L. W., 1987, ApJ, 323, 714

Kenyon S. J., Hartmann L. W., 1995, ApJS, 101, 117 - KH

Kenyon S. J., Calvet N., Hartmann L., 1993, ApJ, 414, 676

Kenyon S. J., Whitney B. A., Gomez M., Hartmann L., 1993b, ApJ, 414, 773

Kenyon S. J., Hartmann L. W., Strom K. M., Strom S. E., 1990, AJ, 99, 869

Keto E. R., 1990, ApJ, 355, 190

Keto E. R., Ho P. T. P., Haschick A. D., 1987, ApJ, 318, 712

Krügel E., Chini R., 1994, A&A, 287, 947

Kwan J., 1978, ApJ, 223, 147

Lada C. J., 1987 in Peimbert M., Jugaku J., eds, IAU Symposium 115, Star Forming Regions, Dordrecht, Reidel, p.1

Lada C. J., 1985, ARA&A, 23, 267

Lada C. J., Wilking B. A., 1984, ApJ, 287, 610

Ladd E. F., Hodapp K.-W., 1997, ApJ, 474, 749L

Ladd E. F., Adams F. C., Casey S., Davidson J. A., Fuller G. A., Harper D. A., Myers P. C., Padman R., 1991, ApJ, 366, 203

Landau L. D., Lifshitz E. M., 1959, Fluid Mechanics. Pergamon, Oxford

Larson R. B., 1969, MNRAS, 145, 271

Larson R. B., 1972, MNRAS, 157, 121

Lay O. P., Carlstrom J. E., Hills R. E., Phillips T. G., 1994, ApJ, 434, L75

Lehtinen K., 1997, A&A, 1997, 317, L5

Leung C. M., 1978, ApJ, 225, 427

Leung C. M., Brown R. L., 1977, ApJ, 214, L73

Leung C. M., Liszt H. S., 1976, ApJ, 208, 732

Li Z.-Y., Shu F. H., 1996, ApJ, 472, 211

Li Z.-Y., Shu F. H., 1997, ApJ, 475, 237

Liljeström T., Olofsson G., 1997, ApJ, 478, 381

Lizano S., Shu F. H., 1989, ApJ, 342, 834

Loren R. B., 1976, ApJ, 209, 466

Lucas R., 1974, A&A, 36, 465

Lucas R., 1976, A&A, 46, 473

Lucy L. B., 1971, ApJ, 163, 95

Lynden-Bell D., Pringle J. E., 1974, MNRAS, 168, 603

Mardones D., Myers P. C., Tafalla M., Wilner D. J., Bachiller R., Garay G., 1997, ApJ, in press

McCaughrean M. J, O'Dell C. R., 1996, AJ, 111, 1977

McCrea W. H., 1957, MNRAS, 117, 562

McKee C. F., 1989, ApJ, 345, 782

Menten K. M., Serabyn E., Güsten R., Wilson T. L., 1987, A&A, 177, L57

Mestel L., Spitzer L., Jr, 1956, MNRAS, 116, 505

Miyawaki R., Hayashi M., Hasegawa T., 1986, ApJ, 305, 353

Moriarty-Schieven G. H., Wannier P. G., Mangum J. G., Tamura M., Olmsted V. K., 1995, ApJ, 455, 190

Mouschovias T. Ch., 1991, in Lada C. J., Kyafalis N. D., eds, The Physics of Star Formation and Early Stellar Evolution, Kluwer, Dordrecht, 1991

Mouschovias T. Ch., 1994, in Clemens D. P., Barvainis R., eds, Clouds, Cores and Low Mass Stars, ASP Conference Series Vol 65, ASP, San Francisco, p. 134

Mouschovias T. Ch., Spitzer L., Jr, 1976, ApJ, 210, 326

Myers P. C., 1980, ApJ, 1980, 242, 1013

Myers P. C., Benson P. J., 1983, ApJ, 266, 309

Myers P. C., Linke R. A., Benson P. J., 1983, ApJ, 264, 517

Myers P. C., Ladd E. F., 1993, ApJ, 413, L47

Myers P. C., Bachiller R., Caselli P., Fuller G. A., Mardones D., Tafalla M., Wilner D. J., 1995, ApJ, 449, L65

Myers P. C., Mardones D., Tafalla M., Williams J. P., Wilner D. J., 1996, 465, L133

Myers P. C., Fuller G. A., Mathieu R. D., Beichman C. A., Benson P. J., Schild R. E., Emerson J. P., 1987, ApJ, 319, 340

Myhill E. A., Kaula W. M., 1992, ApJ, 386, 578

Narayanan G., Walker C. K., Buckley H. D., 1997, ApJ, submitted

Neufield D. A., Hollenbach D. J., 1996, ApJ, 471, L45

Norman C. A., Silk J., 1980, ApJ, 238, 158

Ohashi N., Hayashi M., Ho P. T. P., Momose M., Hirano N., 1996, ApJ, 466, 957

Ohashi N., Hayashi M., Ho P. T. P., Momose M., 1997, ApJ, 475, 211

Palla F., Stahler S. W., 1990, ApJ, 360, L47

Park Y.-S., Hong S. S., 1995, A&A, 300, 890

Park Y.-S., Hong S. S., Minh Y. C., 1996, A&A, 312, 981

Piehler G., Kegel W. H., 1995, A&A, 297, 841

Pudritz R. E. Wilson C. D., Carlstrom J. E., Lay O. P., Hills R. E., Ward-Thompson D. W., 1996, ApJ, 470, L123

Rawlings J. M. C., Hartquist T. W., Menten K. M., Williams D. A., 1992, MNRAS, 255, 471

Rudolph A., Welch W. J., Palmer P., Dubrulle B., 1990, ApJ, 363, 528

Safier P. N., McKee C. F., Stahler S. W., 1997, ApJ, 485, 660

Saito M., Kawabe R., Kitamura Y., Sunada K., 1996, ApJ, 473, 464

Sandell G., Knee L. B. G., Aspin C., Robson I. E., Russell A. P. G., 1994, A&A, 285, L1

Saraceno P., André P., Ceccarelli C., Griffin M., Molinari S., 1996, A&A, 309, 827

Scoville N. Z., Solomon P. M., 1974, ApJ, 187, L67

Serabyn E., Güsten R., Schultz A., 1993, ApJ, 413, 571

Shu F. H., 1977, ApJ, 214, 488

Shu F. H., Adams F. C., Lizano S., 1987, ARA&A, 25, 23

Shu F. H., Najita J., Galli D., Ostriker E., Lizano S., 1993, in Levy E. H., Lunine J. I., eds, Protostars and Planets III. University of Arizona Press, Tucson, p. 3

Silk J., 1995, ApJ, 438, L41

Simon M., Ghez A. M., Leinhert C. H., Cassar L., Chen W. P., Howell R. R., Jameson R. F., Matthews K., 1995, ApJ, 443, 625

Snell R. L., Loren R. B., 1977, ApJ, 211, 122 (SL)

Stahler S. W., 1988, ApJ, 332, 804

Stahler S. W., Shu F. H., Taam R. E., 1980, ApJ, 241, 637

Tamura M., Ohashi N., Hirano N., Itoh Y., Moriarty-Schieven G. H., 1996, AJ, 112, 2077

Terebey S., Chandler C. J., André P., 1993, ApJ, 414, 759

Terebey S., Shu F. H., Cassen P., 1984, ApJ, 286, 529

Tomisaka K., Ikeuchi S., Nakamura T., 1988, ApJ, 335, 239

Tscharnuter W. M., 1989, in Low Mass Star Formation & Pre-Main Sequence Objects, Knudsen, p. 75

van Langevelde H. J., van Dishoeck E. F., Blake G. A., 1994, ApJ, 425, L45

Velusamy T., Kuiper T. B. H., Langer W. D., 1995, ApJ, 451, L75

Walker R. N. F., Masheder M. R. W., 1997, MNRAS, 285, 862

Walker C. K., Carlstrom J. E., Bieging J. H., 1993, ApJ, 402, 655

Walker C. K., Naraynan G., Boss A. P., 1994, ApJ, 431, 767

Walker C. K., Lada C. J., Young E. T., Margulis M., 1988, ApJ, 332, 335

Walker C. K., Lada C. J., Young E. T., Maloney P. R., Wilking B. A., 1986, ApJ, 309, L47

Walter F. M., Brown A., Mathieu R. D., Myers P. C., Vrba F. J., 1988, AJ, 96, 297

Wang Y., Evans N. J., II, Zhou S., Clemens D. P., 1995, ApJ, 454, 217

Ward-Thompson D., 1996, ApSS, 239, 151

Ward-Thompson D., Buckley H. D., Greaves J. S., Holland W. S., André P., 1996, MNRAS, 281, L53

Ward-Thompson D., Scott P. F., Hills R. E., André P., 1994, MNRAS, 268, 276

Welch W. J., Dreher J. W., Jackson J. M., Terebey S., Vogel S. N., 1987, Science, 238, 1550

White R. E., 1977, ApJ, 211, 744

Whitworth A. P., Bhattal A. S., Francis N., Watkins S. J., 1996, MNRAS, 283, 1061

Wichmann R., Krautter J., Schmitt J. H. M. M., Neuhäuser R., Alcalá J. M., Zinnecker H., Wagner R. M., Mundt R., Sterzik M. F., 1996, A&A, 312, 439

Wolf-Chase G. A., Gregersen E., 1997, ApJ, 479, L67

Yang J., Ohashi N., Yan J., Liu C., Kaifu N., Kimura H., 1997, ApJ, 475, 683

Yorke H. W., 1986, ARA&A, 24, 49

Yun J. L., Clemens D. P., 1990, ApJ, 365, L73

Zhou S., 1995, ApJ, 442, 685

Zhou S., Evans N. J., II, Wang Y., 1996, ApJ, 466, 296

Zhou S., Evans N. J., II, Kompe C., Walmsley C. M., 1993, ApJ, 404, 232

Zhou S., Evans N. J., II, Wang Y., Peng R., Lo K. Y., 1994, ApJ, 433, 131

Zhou S., Evans N. J., II, Butner H. M., Kutner M. L., Leung C. M., Mundy L. G., 1990, ApJ, 363, 168

Zhou S., 1992, ApJ, 394, 204

Zuckerman B., Evans N. J., II, 1974, ApJ, 192, L149

Zuckerman B., Palmer P., 1974, ARA&A, 12, 279

Chapter 2

Radiative Transfer in Submillimetre Spectral lines

In this chapter we discuss the physical concepts underlying the radiative transfer of submillimetre rotational molecular line transitions. A full description is given of the STENHOLM Λ-iteration radiative transfer code (Matthews 1986) used in the modelling in Chapter 4 of this thesis. New modifications which have been made to the code are discussed, and tests of the performance of the code are presented.

2.1 Fundamental Concepts

2.1.1 Photons and the radiation field

Whilst writing this section, frequent reference was made to the textbooks of Emerson (1996), Pomraning (1973), Cannon (1983) and Mihalas (1978).

The radiation field is carried by photons, which are point massless particles associated with a frequency ν such that the energy and momentum of the photon are $h\nu$ and $h\nu/c$ respectively, where h is Plank's constant and c is the speed of light. Between collisions with matter, a photon is assumed to travel in a straight line with speed c and

with no change in frequency.

To specify the location of a photon in phase space, three position variables and three momentum variables are required. In the quantum mechanical treatment of photons there is a limit to the accuracy with which a photon can be located in phase space. In the following discussion, however, it is assumed that, for the system under consideration, the photons can be treated as classical particles with regard to their dynamics. Wave phenomena such as diffraction, interference, refraction and polarisation are neglected.

It is convenient to use the direction of travel $\hat{\mathbf{\Omega}}$ (a unit vector defined by two angular variables) and the frequency ν, to specify the photon momentum. The photon distribution function, f, (e.g. Pomraning 1973) is defined such that

$$dN = f(\mathbf{r}, \nu, \hat{\mathbf{\Omega}}, t)\, dV\, d\nu\, d\Omega \tag{2.1}$$

where dN is the number of photons in a volume element dV at position $\mathbf{r}$, in a frequency interval $d\nu$ about ν, and travelling in a solid angle $d\Omega$ about the direction $\hat{\mathbf{\Omega}}$. In spherical polar co-ordinates $d\Omega = \sin\theta\, d\theta\, d\phi = d\mu\, d\phi$, where $\mu \equiv -\cos\theta$.

The radiation **energy density**, u_ν, is the volume energy density of the radiation field, per unit frequency:

$$u_\nu(\mathbf{r}, \nu, t) = \int_{4\pi} h\nu f(\mathbf{r}, \nu, \hat{\mathbf{\Omega}}, t)\, d\Omega. \tag{2.2}$$

The **intensity**, I_ν, is defined such that

$$dE = I_\nu(\mathbf{r}, \nu, \hat{\mathbf{\Omega}}, t)\, dS\, d\nu\, d\Omega\, dt, \tag{2.3}$$

where dE is the radiant energy in the frequency range $d\nu$ about ν, travelling in a solid angle $d\Omega$ about the direction $\hat{\mathbf{\Omega}}$, which crosses an area dS perpendicular to $\hat{\mathbf{\Omega}}$, at position $\mathbf{r}$, between times t and $t + dt$. The intensity and distribution functions are related by

$$I_\nu(\mathbf{r}, \nu, \hat{\mathbf{\Omega}}, t) \equiv ch\nu f(\mathbf{r}, \nu, \hat{\mathbf{\Omega}}, t). \tag{2.4}$$

The **mean intensity** J_ν, defined by,

$$J_\nu(\mathbf{r},\nu,t) = \frac{1}{4\pi}\int_{4\pi} I_\nu(\mathbf{r},\nu,\hat{\mathbf{\Omega}},t)\,d\Omega \tag{2.5}$$

is the average of the intensity over all angles. Substituting equation 2.4 into the above expression, gives

$$J_\nu = \frac{c}{4\pi}\int_{4\pi} h\nu f\,d\Omega = \frac{c}{4\pi}u_\nu. \tag{2.6}$$

The **flux density**, F_ν, is defined by,

$$F_\nu(\mathbf{r},\nu,\hat{\mathbf{n}},t) = \int_{4\pi} I_\nu(\mathbf{r},\nu,\hat{\mathbf{\Omega}},t)\,\hat{\mathbf{\Omega}}\cdot\hat{\mathbf{n}}\,d\Omega \equiv \int_{4\pi} I_\nu\cos\theta\,d\Omega, \tag{2.7}$$

and is the net radiant energy flowing across a surface with normal $\hat{\mathbf{n}}$, per second, per unit area, per unit frequency range, after integrating the intensity over all directions. In the last expression, θ is the angle between the normal to the surface and the beam direction, $\hat{\mathbf{\Omega}}$.

The integral of the flux density over all frequencies is the **flux**, F;

$$F = \int_0^\infty F_\nu\,d\nu. \tag{2.8}$$

2.1.2 The equation of transfer

By analogy with the continuity equation for fluid flow:

$$\partial\rho/\partial t + \nabla\cdot(\rho\mathbf{v}) = \left.\frac{\partial\rho}{\partial t}\right|_{\text{sources}} + \left.\frac{\partial\rho}{\partial t}\right|_{\text{sinks}}, \tag{2.9}$$

(where ρ is the fluid density, and the source and negative sink terms allow for the possibility of creation or destruction of the fluid *in-situ*), one may write a continuity equation for the phase space density of photons (e.g. Pomraning 1973);

$$\frac{\partial f}{\partial t} + \frac{\partial(f\dot{x})}{\partial x} + \frac{\partial(f\dot{y})}{\partial y} + \frac{\partial(f\dot{z})}{\partial z} + \frac{\partial(f\dot{\nu})}{\partial \nu} + \frac{\partial(f\dot{\mu})}{\partial \mu} + \frac{\partial(f\dot{\phi})}{\partial \phi} = \left.\frac{\partial f}{\partial t}\right|_{\text{sources}} + \left.\frac{\partial f}{\partial t}\right|_{\text{sinks}} \tag{2.10}$$

The source and sink terms include the emission and absorption of photons by matter, as well as photon scattering, which may be pictured as the simultaneous destruction of one photon and creation of another photon with different frequency and/or direction.

The left hand side of equation 2.10 may be simplified by noting that $\dot{\mu}, \dot{\phi}$ and $\dot{\nu}$ are all zero, since the photons are assumed to propagate in a straight line and without change of frequency between interactions with matter. Also, since photons always travel at speed c, $\mathbf{v} = (\dot{x}, \dot{y}, \dot{z}) = c\hat{\mathbf{\Omega}}$. Equation 2.10 therefore reduces to

$$\left(\frac{\partial}{\partial t} + c\hat{\mathbf{\Omega}} \cdot \nabla\right) f(\mathbf{r}, \nu, \hat{\mathbf{\Omega}}, t) \equiv \frac{Df(\mathbf{r}, \nu, \hat{\mathbf{\Omega}}, t)}{Dt} = \left.\frac{\partial f}{\partial t}\right|_{\text{sources}} + \left.\frac{\partial f}{dt}\right|_{\text{sinks}}. \quad (2.11)$$

where D/Dt is the time derivative moving with the photons in the beam.

In the absence of interaction with matter (i.e. RHS = 0), we find,

$$\frac{DI_\nu(\mathbf{r}, \nu, \hat{\mathbf{\Omega}}, t)}{Dt} \equiv ch\nu \frac{Df(\mathbf{r}, \nu, \hat{\mathbf{\Omega}}, t)}{Dt} = 0. \quad (2.12)$$

The intensity of the beam of light therefore remains constant as the beam travels through empty space, i.e.

$$I_\nu(\mathbf{r}, \nu, \hat{\mathbf{\Omega}}, t) = I_\nu(\mathbf{r} + s\hat{\mathbf{\Omega}}, \nu, \hat{\mathbf{\Omega}}, t + s/c), \quad (2.13)$$

where s is distance along the direction of the beam.

Now attention is turned to the form of the source and sink terms in equation 2.11. As a photon travels a small distance through the medium, there will be some probability that it is absorbed or scattered, which will in general depend on the frequency of the photon, its position in the medium, and possibly also on time. For sufficiently small distances, the probability of absorption will be proportional to the distance (and hence the time) of travel. We define the **opacity**, $\kappa(\mathbf{r}, \nu, t)$, as the probability per unit distance travelled that a photon of frequency ν at position $\mathbf{r}$ and time t, be absorbed or scattered. In a stationary unmagnetised gas there is no preferential direction in the medium, and the opacity will not depend on the direction of travel of the photon (if the gas is moving this is only strictly true in the rest frame of the gas, since the velocity vector introduces a preferential direction). The probability per unit *time* for removal of a photon from the beam is therefore $c\kappa(\mathbf{r}, \nu, t)$, and we have

$$\left.\frac{\partial f(\mathbf{r}, \nu, \hat{\mathbf{\Omega}}, t)}{dt}\right|_{\text{sinks}} = -c\kappa(\mathbf{r}, \nu, t) f(\mathbf{r}, \nu, \hat{\mathbf{\Omega}}, t). \quad (2.14)$$

κ may also be thought of as a *cross-section per unit volume* for absorption and scattering.

The source term may be written in terms of the **emissivity**, $\varepsilon(\mathbf{r}, \nu, \hat{\mathbf{\Omega}}, t)$, which is the radiation *energy* emitted or scattered at $\mathbf{r}$ into the solid angle $d\Omega$ about $\hat{\mathbf{\Omega}}$, per unit volume, per unit frequency, per unit time, i.e.

$$\varepsilon(\mathbf{r}, \nu, \hat{\mathbf{\Omega}}, t) \equiv h\nu \left.\frac{\partial f}{dt}\right|_{\text{sources}} \tag{2.15}$$

Unlike the opacity, the emissivity cannot in general be assumed to be isotropic in the rest frame of the gas, because of the anisotropic contribution of photon scattering to the emissivity. The scattering probability of photons travelling through the gas is in general dependent on the angle of scatter. Furthermore, each scattering event is accompanied by a Doppler frequency shift, which is correlated with the angle of scatter. Anisotropic radiation fields therefore lead to anisotropic emissivities. In certain circumstances however, this anisotropy, which adds considerable complexity to the radiative transfer problem, may be neglected. This is discussed in some detail below, in connection with the 'complete redistribution approximation'.

Equation 2.11 may therefore be written as

$$\left(\frac{\partial}{\partial t} + c\hat{\mathbf{\Omega}} \cdot \nabla\right) f(\mathbf{r}, \nu, \hat{\mathbf{\Omega}}, t) = \frac{\varepsilon(\mathbf{r}, \nu, \hat{\mathbf{\Omega}}, t)}{h\nu} - cf(\mathbf{r}, \nu, \hat{\mathbf{\Omega}}, t)\kappa(\mathbf{r}, \nu, t). \tag{2.16}$$

Substituting $I = ch\nu f$ finally gives,

$$\frac{1}{c}\frac{\partial I_\nu}{\partial t} + \hat{\mathbf{\Omega}} \cdot \nabla I_\nu \equiv \frac{1}{c}\frac{\partial I_\nu}{\partial t} + \frac{\partial I_\nu}{\partial s} = \varepsilon - \kappa I_\nu, \tag{2.17}$$

where s denotes distance along the beam in its direction of travel. This is the fundamental equation of radiative transfer theory, and is commonly referred to as the **equation of transfer**. In order for it to be of practical use, however, explicit expressions relating ε and κ to the known properties of the medium must be found.

We now assume, as is usually the case, that the time for light to cross the system is much shorter than the timescales over which the system and boundary conditions

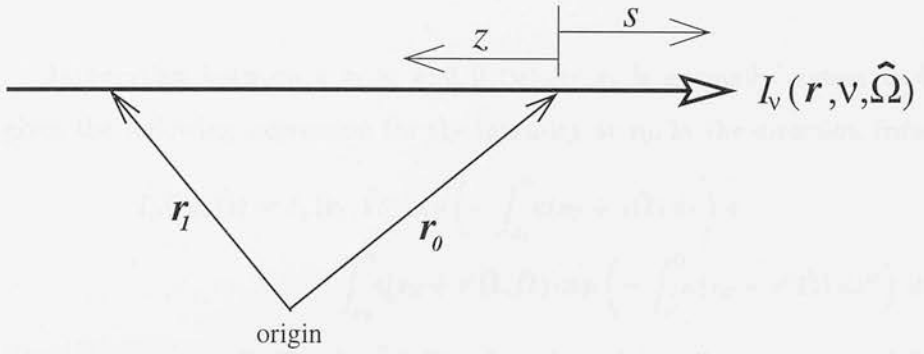

Figure 2.1: Diagram illustrating the geometry used in the integral of the equation of transfer.

change significantly. In this case the time-dependence of the problem may be ignored, and the time derivative in equation 2.17 may be dropped:

$$\frac{dI_\nu(\mathbf{r},\nu,\hat{\Omega})}{ds} = \varepsilon(\mathbf{r},\nu,\hat{\Omega}) - \kappa(\mathbf{r},\nu)I_\nu(\mathbf{r},\nu,\hat{\Omega}). \tag{2.18}$$

We define the relation between $\mathbf{r}$ and s by

$$\mathbf{r} = \mathbf{r}_0 + s\hat{\Omega}, \tag{2.19}$$

where $\mathbf{r}_0$ is a point along the beam chosen to define $s = 0$. s increases with distance in the beam direction, and is negative for points along the beam which are 'upstream' from $\mathbf{r}_0$ (e.g. point $\mathbf{r}_1$ in Figure 2.1).

Integral form of the transfer equation

Equation (2.18) may be integrated by first multiplying both sides by the integrating factor

$$\exp\left(\int_0^s \kappa(\mathbf{r}_0 + s'\hat{\Omega},\nu)\,ds'\right). \tag{2.20}$$

After collecting the terms in I_ν, the resulting expression may be written as

$$\frac{d}{ds}\left[I_\nu(\mathbf{r},\hat{\mathbf{\Omega}})\exp\left(\int_0^s \kappa(\mathbf{r}_0+s'\hat{\mathbf{\Omega}})\,ds'\right)\right] = \varepsilon(\mathbf{r},\hat{\mathbf{\Omega}})\exp\left(\int_0^s \kappa(\mathbf{r}_0+s'\hat{\mathbf{\Omega}})\,ds'\right), \quad (2.21)$$

where the explicit dependence of the quantities on ν has been suppressed for clarity.

Integrating between $s = s_1$ and 0 (where s_1 is normally chosen to be negative), gives the following expression for the intensity at $\mathbf{r}_0$, in the direction from $\mathbf{r}_1$:

$$I_\nu(\mathbf{r}_0,\hat{\mathbf{\Omega}}) = I_\nu(\mathbf{r}_1,\hat{\mathbf{\Omega}})\exp\left(-\int_{s_1}^0 \kappa(\mathbf{r}_0+s\hat{\mathbf{\Omega}})\,ds\right) + \int_{s_1}^0 \varepsilon(\mathbf{r}_0+s'\hat{\mathbf{\Omega}},\hat{\mathbf{\Omega}})\exp\left(-\int_{s'}^0 \kappa(\mathbf{r}_0+s''\hat{\mathbf{\Omega}})\,ds''\right)ds', \quad (2.22)$$

where $\mathbf{r}_1 = \mathbf{r}_0 + s_1\Omega$. If s_1 is negative then the point $\mathbf{r}_1$ lies upstream of the beam from $\mathbf{r}_0$.

Equation 2.22 may be written in a more transparent form. First define $z = -s$ for the absolute distance from $\mathbf{r}_0$ to a point upstream (Figure 2.1). The **optical depth**, $\tau_\nu(\mathbf{r}_0, z, \nu, \hat{\mathbf{\Omega}})$, may then be defined as

$$\tau_\nu(\mathbf{r}_0,z,\nu,\hat{\mathbf{\Omega}}) = \int_0^z \kappa(\mathbf{r}_0 - z'\hat{\mathbf{\Omega}},\nu)\,dz', \quad (2.23)$$

$$\equiv \int_s^0 \kappa(\mathbf{r}_0+s'\hat{\mathbf{\Omega}},\nu)\,ds'. \quad (2.24)$$

τ_ν increases with distance backwards along the beam, and we have $d\tau_\nu = \kappa dz = -\kappa ds$. Equation 2.22 becomes (restoring the explicit ν dependences)

$$I_\nu(\mathbf{r}_0,\nu,\hat{\mathbf{\Omega}}) = I_\nu(\mathbf{r}_1,\nu,\hat{\mathbf{\Omega}})e^{-\tau_\nu(\mathbf{r}_0,z_1,\nu,\hat{\mathbf{\Omega}})} + \int_0^{z_1} \varepsilon(\mathbf{r}_0+z'\hat{\mathbf{\Omega}},\nu,\hat{\mathbf{\Omega}})e^{-\tau_\nu(\mathbf{r}_0,z',\nu,\hat{\mathbf{\Omega}})}\,dz', \quad (2.25)$$

where $z_1 = -s_1$ and $\mathbf{r}_1 = \mathbf{r}_0 - z_1\hat{\mathbf{\Omega}}$.

The interpretation of this equation may be illustrated by considering the one dimensional problem of a beam of light passing perpendicularly through a plane slab of gas. Let $\mathbf{r}_1$ and $\mathbf{r}_0$ be the entry and exit points of the beam respectively. $I_\nu(\mathbf{r}_1,\nu,\hat{\mathbf{\Omega}})$ is the intensity of the beam at the frequency ν, as it enters the slab at $\mathbf{r}_1$. Removal of photons from the beam by absorption and scattering reduces its intensity

to $I_\nu(\mathbf{r}_1, \nu, \hat{\mathbf{\Omega}})e^{-\tau_\nu(\mathbf{r}_0, z_1, \nu, \hat{\mathbf{\Omega}})}$ by the time it reaches $\mathbf{r}_0$. The first term on the right hand side of (2.25) is therefore the contribution to the intensity at $\mathbf{r}_0$ from the incident beam at $\mathbf{r}_1$, after it has been attenuated by the optical depth of the slab. The second term on the right hand side of (2.25) gives the contribution from the slab *emission* to the intensity at $\mathbf{r}_0$. The integrand $\varepsilon(\mathbf{r}_0 + z'\hat{\mathbf{\Omega}}, \nu, \hat{\mathbf{\Omega}})e^{-\tau_\nu(\mathbf{r}_0, z', \nu, \hat{\mathbf{\Omega}})}\, dz'$ is the the product of the intensity $\varepsilon(\mathbf{r}_0 + z'\hat{\mathbf{\Omega}}, \nu, \hat{\mathbf{\Omega}})dz'$ emitted by the layer of slab between z' and $z' + dz'$, and the attenuation factor $e^{-\tau_\nu(\mathbf{r}_0, z', \nu, \hat{\mathbf{\Omega}})}$ due to absorption from the intervening part of the slab. The integral sums the contributions from all slab layers between $\mathbf{r}_0$ and $\mathbf{r}_1$.

If the dependence of ε and κ on position and frequency are known a-priori, then equation 2.25 may be evaluated for any combination of position, frequency and direction, once the boundary conditions on the radiation field are specified (i.e. any fixed sources of radiation, whether internal or external to the system). The emissivity and opacity are in general dependent on the radiation field itself, however, and since the radiation field is not known in advance, equation 2.25 cannot be evaluated directly.

An alternative form of the equation of transfer is found by substituting $d\tau_\nu = -\kappa ds$ in equation 2.18:

$$\frac{dI_\nu(\tau_\nu)}{d\tau_\nu} = I_\nu(\tau_\nu) - S_\nu(\tau_\nu). \tag{2.26}$$

where $S_\nu = \varepsilon/\kappa$ is known as the **source function**, and I_ν and S_ν are written as functions of optical depth rather than of position. In carrying out real calculations of complex radiative transfer problems, equation 2.26 is in general less useful than equation 2.18, since κ, ε, and S_ν, are most naturally expressed as functions of position in the medium, rather than of the optical depth, which generally depends in a complex way on the position of the 'observer', and the frequency under consideration.

The integral of equation 2.26 is found analagously to (2.22), with the result,

$$I_\nu(0) = I_\nu(\tau_\nu)e^{-\tau_\nu} + \int_0^{\tau_\nu} S_\nu(\tau'_\nu)e^{-\tau'_\nu}\, d\tau'_\nu, \tag{2.27}$$

If S_ν is independent of τ_ν over the range of the integral, which may be a good approx-

imation when conditions in the gas are close to local thermodynamic equilibrium (see below), equation 2.27 becomes

$$I_\nu(0) = I_\nu(\tau_\nu)e^{-\tau_\nu} + S_\nu\left(1-e^{-\tau_\nu}\right). \tag{2.28}$$

If the medium is also very optically thick, i.e. $\tau_\nu \gg 1$, the above expression simplifies to

$$I_\nu(0) \simeq S_\nu, \tag{2.29}$$

i.e. the intensity approximates to the source function.

2.1.3 The density of states

The picture of a radiation field composed of 'classical particles' is a good approximation as long as the characteristic length scale of the problem under consideration is much larger than the wavelength of the radiation. When the characteristic length scale of the problem is comparable with, or smaller than the wavelength, the wave nature of the radiation becomes important, and the behaviour of the photons must be described by quantum mechanics. When there is more than one length scale of interest, both pictures may be useful. For example, the classical picture may describe well the flow of photons on a macroscopic scale through an absorbing gas, whereas the actual absorption of a photon by a gas molecule is a microscopic process and requires a quantum mechanical treatment. It will therefore be useful to understand the relationship between the classical and quantum mechanical pictures.

In the quantum mechanical treatment of the radiation field, a photon can exist in one of a number of photon states. Each photon state may be represented by a complex function of space and time, called the state wavefunction. Given any set of boundary conditions, (e.g. the size and shape of a enclosure inside which the radiation field is confined), it is possible to choose a complete set of state wavefunctions, or *basis set*. Any radiation field satisfying the boundary conditions may be characterised by the number of photons occupying each photon state. Although there is a degree of arbitrariness in

the choice of basis set, it is always possible to make the choice such that the photon wavefunctions are mutually orthogonal, and each one corresponds to a definite photon energy.

It will be useful to find an expression for the number of photon states per unit volume and frequency range. It turns out that the result is largely independent of the boundary conditions or the basis set chosen, and for convenience it is assumed that the radiation field is enclosed inside a cubical cavity of side L, and the basis set is the set of standing waves of the form $Ae^{i\omega t}\cos k_x x \cos k_y y \cos k_z z$, where $\omega = ck$; $k^2 = \sum_{i=x,y,z} k_i^2$, and A is a normalization factor. The boundary condition is that the wavefunctions must vanish at the walls of the cavity, restricting the allowed values of $k_{i=x,y,z}$ to integral multiples of π/L, so that when plotted in k space, the allowed values form a cubical lattice with a nearest neighbour separation of π/L. Each photon state therefore occupys a cube of k-space 'volume' $(\pi/L)^3 = \pi^3/V$, where V is the real space volume of the cavity. Since replacing k_i by -k_i in the wavefunction leaves it unchanged, only the octant of k space where the $k_{i=x,y,z}$ are positive need be included when counting *distinct* states.

The above discussion has ignored the polarisation of the photon; for each standing wave there are *two* independent polarisation states. It follows that the number of distinct photon states between k and $k + dk$ (i.e. in a k-space volume $4\pi k^2 dk/8$), is given by

$$N(k, k+dk) = \frac{1}{8} \cdot \frac{4\pi k^2 dk}{\pi^3/V} \cdot 2 = \frac{V k^2 dk}{\pi^2}. \tag{2.30}$$

Substituting $k = 2\pi\nu/c$ produces the equivalent expression,

$$N(\nu, \nu+d\nu) = \frac{V 8\pi\nu^2 d\nu}{c^3} = V g_\nu d\nu, \tag{2.31}$$

where $g_\nu = 8\pi\nu^2/c^3$ is the number of photon states per unit volume and frequency, and is called the **density of states**.

The relation between the description of the radiation field in terms of the occupation numbers of photon states on the one hand and the photon distribution function,

$f(\mathbf{r}, \nu, \hat{\mathbf{\Omega}})$, on the other, is given by the expression, (cf. equation 2.1)

$$dN = f(\mathbf{r}, \nu, \hat{\mathbf{\Omega}})\, dV\, d\nu\, d\Omega = g_\nu dV\, d\nu\, \frac{d\Omega}{4\pi} \bar{n}_{\rm ph}(\mathbf{r}, \nu, \hat{\mathbf{\Omega}}), \tag{2.32}$$

where dN is the number of photons in the phase space volume $dV\, d\nu\, d\Omega$; $g_\nu dV\, d\nu d\Omega/4\pi$ is the number of distinct photon states 'occupying' this region of phase space and $\bar{n}_{\rm ph}(\mathbf{r}, \nu, \hat{\mathbf{\Omega}})$ is the average occupation number of these photon states.

Equation 2.32 leads to the following relation between f and $\bar{n}_{\rm ph}$:

$$\begin{aligned} f(\mathbf{r}, \nu, \hat{\mathbf{\Omega}}) &= \frac{g_\nu}{4\pi} \bar{n}_{\rm ph}(\mathbf{r}, \nu, \hat{\mathbf{\Omega}}), \\ &= \frac{2\nu^2}{c^3} \bar{n}_{\rm ph}(\mathbf{r}, \nu, \hat{\mathbf{\Omega}}). \end{aligned} \tag{2.33}$$

2.1.4 Thermodynamic Equilibrium

If the energy in a closed system is exchanged between all its different forms and between all regions over a sufficiently long time, then the system will eventually approach a state of **complete thermodynamic equilibrium (CTE)**, where there is no further net transport or transformation of energy. Although complete thermodynamic equilibrium is approximated to in only a few astrophysical situations, such as in stellar interiors, it is a useful concept because it provides an exact solution to the statistical equations describing interactions between the radiation field and matter. Moreover, the equilibrium relations for the radiation field, and the velocity and internal energy distributions of the system particles, may be found using statistical mechanics, and are independent of the detailed microphysics which is needed to calculate these quantities in non-equilibrium situations. These relations are all characterised by just a single parameter, the temperature T.

The equilibrium radiation field is known as the **blackbody radiation field**, and is a function of temperature and frequency only. It is described by the **Planck function**,

$$I_\nu = B_\nu(\nu, T) = \frac{c}{4\pi} \cdot h\nu \cdot g_\nu \cdot \bar{n}_{\rm ph}(\nu) \tag{2.34}$$

$$= \frac{2h\nu^3}{c^2}\frac{1}{(e^{\frac{h\nu}{kT}}-1)}. \tag{2.35}$$

In the first expression above, the Planck function has been written as the product of four terms: $c/4\pi$, the conversion factor between radiation energy density and mean intensity (cf equation 2.6); $h\nu$, the photon energy; $g_\nu = 8\pi\nu^2/c^3$, the density of states and $\bar{n}_{\rm ph}(\nu) = (e^{\frac{h\nu}{kT}}-1)^{-1}$, the mean occupation number of a photon state of frequency ν (e.g. Mandl 1971).

Using equations 2.7 and 2.8, the flux on the surface of a body placed in a blackbody radiation field is given by,

$$\begin{aligned} F &= \int_{2\pi}\int_0^\infty B_\nu(\nu,T)\cos\theta\, d\nu\, d\Omega \\ &= \frac{2\pi h}{c^2}\left(\frac{kT}{h}\right)^4 \int_0^\infty \frac{x^3}{e^x-1}\,dx = \sigma T^4. \end{aligned} \tag{2.36}$$

where the solid angle integral is only over 2π steradians since we are excluding the radiation emitted by the surface. The constant σ is called Stefan's constant and has the value,

$$\sigma = 5.67\times10^{-8}\mathrm{W\,m^{-2}K^{-4}}. \tag{2.37}$$

If the body in equilibrium with the radiation field is a **blackbody**, i.e a body which absorbs radiation perfectly at all wavelengths, then the radiation incident on and absorbed by the blackbody must exactly balance the radiation *emitted* by it. Therefore equation 2.36 also describes the radiation emitted at the surface of a blackbody at temperature T.

If the system under consideration is a gas containing a very large number of identical molecules, then the distribution of the molecules over their discrete internal energy levels is described, in thermodynamic equilibrium, by the Boltzmann equation:

$$\frac{n(E_i)}{n_{\rm tot}} = \frac{g(E_i)\,e^{-\frac{E_i}{kT}}}{\sum_{i'} g(E_{i'})\,e^{-\frac{E_{i'}}{kT}}}, \tag{2.38}$$

where $g(E_i)$ is the degeneracy of the energy level E_i, $n(E_i)$ is the number density of molecules occupying the energy level E_i, and $n_{\rm tot}$ is the total number density of

molecules. The sum in the denominator is over all internal energy levels. We have assumed that the temperature is low enough that dissociation and ionisation processes can be ignored. If the gas contains more than one type of molecule, then each molecular population separately satisfies equation 2.38. For any two levels, i and j, we have

$$\frac{n(E_i)}{n(E_j)} = \frac{g(E_i)}{g(E_j)} \exp[-(E_i - E_j)/kT]. \tag{2.39}$$

The velocity distribution of particles in CTE, is described, in the ideal classical limit (e.g. Mandl 1971), by the Maxwell velocity distribution:

$$n(\mathrm{v})d\mathrm{v} \;=\; 4\pi \left(\frac{m}{2\pi kT}\right)^{\frac{3}{2}} \exp\left(-m\mathrm{v}^2/2kT\right) \mathrm{v}^2 \, d\mathrm{v}, \tag{2.40}$$

where $n(\mathrm{v})d\mathrm{v}$ is the number density of particles with a velocity magnitude in the range $d\mathrm{v}$ about the velocity v, n_{tot} is the total number density, and m is the mass of a gas particle. Again, if more than one species of particle is present in the gas, then each population satisfies equation 2.40 separately. The corresponding distribution for a single component of the velocity, v_z say, is

$$n(\mathrm{v}_z)d\mathrm{v}_z = n_{\mathrm{tot}} \left(\frac{m}{2\pi kT}\right)^{\frac{1}{2}} \exp\left(-m\mathrm{v}_z^2/2kT\right) \, d\mathrm{v}_z. \tag{2.41}$$

In real astrophysical systems which depart from CTE, equations 2.35, 2.38 and 2.40 cannot be simultaneously satisfied with a unique constant temperature, T. If these equations are nevertheless rigidly applied, then the temperature parameters in equations 2.35, 2.38 and 2.40 will in general depend on the frequency, the choice of energy levels, and the velocity respectively. These 'temperatures' may sometimes still be useful and have physical meaning.

The brightness temperature T_b corresponding to an intensity I_ν is defined by $B_\nu(T_b) = I_\nu$. Inverting this equation gives

$$T_b = \frac{h\nu}{k} \left[\ln\left(1 + \frac{2h\nu^3}{c^2 I_\nu}\right)\right]^{-1}. \tag{2.42}$$

If $h\nu \ll kT$ (i.e. in the Rayleigh-Jeans limit) then

$$T_b \simeq \frac{c^2 I_\nu}{2k\nu^2}. \tag{2.43}$$

In submillimetre and radio astronomy the radiation temperature, $T_{\rm rad}$, is often used, which is defined using equation 2.43 with an equals sign, irrespective of whether the Rayleigh-Jeans approximation is a valid one.

Similarly, the number densities of molecules occupying any pair of energy levels, may be used to define an excitation temperature, $T_{\rm ex}$ through equation 2.39. If n_i and n_j are the number densities of molecules occupying energy levels E_i and E_j respectively, then

$$T_{\rm ex} = \frac{E_j - E_i}{k} \left[\ln \left(\frac{g(E_j)}{g(E_i)} \frac{n_i}{n_j} \right) \right]^{-1} . \tag{2.44}$$

The value of $T_{\rm ex}$ will in general depend on the pair of levels used to define it. Note that when the conditions depart markedly from equilibrium, $T_{\rm ex}$ may have a negative value for certain pairs of levels, which can lead to masing behaviour.

The Maxwell velocity distribution is set up by elastic collisions between gas molecules. In interstellar gas clouds, the velocity distribution of the particles is always close to Maxwellian, since the mean free time between elastic collisions is much shorter than the timescale for other processes (such as inelastic collisions) which change the velocity of the particles (Spitzer 1978). The temperature characterising the velocity distribution through equation 2.40 is known as the kinetic temperature, $T_{\rm kin}$, and we assume it is independent of velocity, although it may be a function of position. There is a tendency for inelastic collisions to drive the internal energy level populations towards the corresponding CTE distribution, i.e. $T_{\rm ex} \rightarrow T_{\rm kin}$. However the radiation field also acts on the level populations through radiative transitions, and the true level populations are determined by the competition between these two processes. This is discussed in more detail in the next section.

The term **Local Thermodynamic Equilibrium**, or **LTE**, is used to describe a less stringent equilibrium condition than CTE. In LTE, as with CTE,the velocity distribution of the gas particles and the internal energy level populations at a given po-

sition are described by the Maxwell velocity distribution and the Boltzmann equation respectively, with $T_{\rm ex} = T_{\rm kin}$ (this temperature being in general a function of position). The radiation field, however, is determined by the equations of radiative transfer with appropriate boundary conditions, and is not in general described by the Planck function.

2.2 Spectral line radiation

The energies of the quantum states for microscopic bound systems, such as atoms and molecules, do not form a continuum, but to a first approximation take on discrete values. Transitions may occur between states of different internal energy and angular momentum, the difference being supplied (or removed) by the absorption (or emission) of a photon. The strength of the emission or absorption accompanying such transitions is very strongly peaked about a photon frequency (as measured in the molecule's rest frame) $\nu_0 = \Delta E/h$, where ΔE is the energy gap between the two states. Alternatively, the transition may occur without the emission or absorption of a photon, if the energy and angular momentum change of the transition is transferred to or from another body through a collision.

If an ensemble of identical systems of this kind is allowed to reach a steady state equilibrium, the balance between transitions into and transitions out of any given state will determine the fraction of systems occupying that state. Once the number of systems in each state is known, the emission and absorption properties of the ensemble are completely determined. The radiative and collisional transition probabilities between states are therefore fundamental quantities in spectral line radiative transfer.

2.2.1 Radiative transitions

We consider three transition processes involving radiation: spontaneous emission, stimulated emission and radiative excitation.

Consider two energy levels of a molecule, the upper level lying at an energy $E = h\nu_0$ above the lower level. If the molecule initially occupies the upper energy level, it may spontaneously move into the lower energy level and emit a photon with a frequency very close to ν_0. This process is called spontaneous emission, and occurs irrespective of whether any external stimulus is being applied. The directions of the spontaneously emitted photons are randomly distributed in most cases, since any intrinsic directionality to the emission on a molecular scale will be smoothed out when averaged over a randomly orientated ensemble of molecules. The symbol A_{ul}, referred to as the Einstein A coefficient, is used to denote the total spontaneous emission probability per unit time between the upper and lower energy levels. Since the emission is isotropic, the probability per unit time for spontaneous emission into the solid angle $d\Omega$ may be written as $\mathrm{A}_{ul} d\Omega/4\pi$.

If a molecule occupying the upper level is irradiated with a beam of photons containing frequencies close to ν_0, then the probability per unit time that a further photon is emitted into the beam direction by the molecule (with an accompanying downward transition), is increased by an amount proportional to the intensity of the beam. This process is called stimulated emission, or radiative de-excitation. Since the frequency dependence of the stimulated emission probability is very strongly peaked about ν_0, usually only the intensity of the beam at ν_0 itself (in the molecule rest frame) needs to be considered. The range of photon frequencies about ν_0 for which there is an appreciable transition probability is approximately given by $\Delta\nu \sim \mathrm{A}_{ul}/2\pi$ (Emerson 1996). In the applications considered in this thesis, this broadening is completely negligible when compared with the broadening caused by the Doppler effect. The probability per unit time that a photon is emitted through stimulated emission into the solid angle $d\Omega$ about the direction of an incident beam of intensity $I_\nu(\nu_0, \hat{\mathbf{\Omega}})$, may be written as $\mathrm{B}_{ul} I_\nu(\nu_0, \hat{\mathbf{\Omega}}) d\Omega/4\pi$, where B_{ul} is called the Einstein B coefficient for stimulated emission.

If a molecule occupying the lower energy level is irradiated by a similar beam of radiation, it may absorb a photon from the beam and move into the upper energy level. The probability per unit time for such an event to occur is again proportional to the intensity of the incident beam. This process encompasses the time reverse of the two emission processes described above, and is termed absorption, or radiative excitation. The probability per unit time that a photon is absorbed through radiative excitation from a solid angle $d\Omega$ in the direction of the incident beam of intensity $I_\nu(\nu_0, \hat{\Omega})$ is written as $\mathrm{B}_{lu} I_\nu(\nu_0, \hat{\Omega}) d\Omega/4\pi$, where B_{lu} is called the Einstein B coefficient for absorption.

The two emission processes described above may be combined to give an expression for the probability per unit time for emission of a photon into the solid angle $d\Omega$. If R_{ul} is the total downward radiative transition probability per unit time for a molecule in the upper energy level, we have

$$\frac{dR_{ul}}{d\Omega} d\Omega = \mathrm{A}_{ul} \frac{d\Omega}{4\pi} + \mathrm{B}_{ul} I_\nu(\nu_0, \hat{\Omega}) \frac{d\Omega}{4\pi} \tag{2.45}$$

$$\frac{dR_{ul}}{d\Omega} = \frac{\mathrm{A}_{ul}}{4\pi} + \frac{\mathrm{B}_{ul}}{4\pi} I_\nu(\nu_0, \hat{\Omega}). \tag{2.46}$$

Similarly, writing R_{lu} as the total upward radiative transition per unit time for a molecule in the lower energy level to a photon from any direction, then

$$\frac{dR_{lu}}{d\Omega} = \frac{\mathrm{B}_{lu}}{4\pi} I_\nu(\nu_0, \hat{\Omega}). \tag{2.47}$$

Integrating equations 2.46 and 2.47 over solid angle gives the following expressions for the total transition probabilities, R_{ul} and R_{lu}:

$$R_{ul} = \mathrm{A}_{ul} + \mathrm{B}_{ul} J_{\nu_0}, \tag{2.48}$$

$$R_{lu} = \mathrm{B}_{lu} J_{\nu_0}. \tag{2.49}$$

The thermodynamic equilibrium relations may be used to find the ratios between the different Einstein coefficients. In thermodynamic equilibrium the radiation field is given by the Planck function (2.35), and in a large ensemble of molecules, the number

occupying each energy level satisfies the Boltzmann equation (2.39), with a unique value of the temperature T. Since the level populations must remain constant, the total number of transitions per second from the upper to the lower level must balance the transition rate for the reverse process. Writing n_u and n_l as the number density of molecules per unit volume in the upper and lower levels respectively, we have

$$n_u R_{ul} = n_l R_{lu}, \tag{2.50}$$

$$\frac{n_u}{n_l} = \frac{R_{lu}}{R_{ul}} = \frac{\mathrm{B}_{lu} J_{\nu_0}}{\mathrm{A}_{ul} + \mathrm{B}_{ul} J_{\nu_0}} \tag{2.51}$$

$$= \frac{g_u}{g_l} e^{-\frac{\Delta E}{kT}}, \tag{2.52}$$

where in the final expression the Boltzmann relation has been used. Rearranging for J_{ν_0}, and substituting $\Delta E = h\nu_0$ gives

$$J_{\nu_0} = \frac{\mathrm{A}_{ul}/\mathrm{B}_{ul}}{g_l \mathrm{B}_{lu}/g_u \mathrm{B}_{ul}\, e^{\frac{h\nu_0}{kT}} - 1}. \tag{2.53}$$

Statistical mechanics, however, predicts that the mean radiation intensity in thermodynamic equilibrium is given by the Planck function:

$$J_{\nu_0} \equiv \frac{2h\nu_0^3}{c^2} \frac{1}{(e^{\frac{h\nu_0}{kT}} - 1)}. \tag{2.54}$$

If these independent equations for J_{ν_0} are to be mutually consistent, the following relations between the Einstein coefficients (which must be independent of T) are required:

$$\mathrm{A}_{ul} = \frac{2h\nu_0^3}{c^2} \mathrm{B}_{ul}, \tag{2.55}$$

$$g_u \mathrm{B}_{ul} = g_l \mathrm{B}_{lu}, \tag{2.56}$$

where g_u and g_l are the degeneracies of the upper and lower states respectively.

2.2.2 The complete redistribution approximation

The preceding discussion is relevant to a molecule or ensemble of molecules at rest in the 'observers' frame. If the molecules are moving, then the frequencies at which they are seen to emit and absorb photons will differ from the transition frequency ν_0, as a result of the Doppler shift associated with the change of reference frame. In a

gas where particle velocities are spread over a continuous distribution, the frequency distribution over which emission and absorption in a given spectral line transition takes place will be broadened. The broadened frequency dependence of the absorption may be represented by the **line profile function**, $\phi(\mathbf{r}, \nu)$, which peaks at ν_0 in the velocity frame in which the bulk of the gas is at rest, and is normalised according to

$$\int_0^\infty \phi(\mathbf{r}, \nu)\, d\nu = 1. \tag{2.57}$$

In this context $\phi(\mathbf{r}, \nu)d\nu$ is the fraction of molecules close to $\mathbf{r}$ capable of absorbing radiation in the frequency range $d\nu$ about the frequency ν. For radiation of frequency ν in the observers frame to be Doppler-shifted to the frequency ν_0 in the frame of the molecule, the molecule must have a velocity along the beam direction of v$= c(1-\nu_0/\nu)$. The frequency range $d\nu$ therefore corresponds to the velocity range dv $= cd\nu/\nu_0$.

Let $R_{lu}^{\nu,\Omega} d\nu d\Omega$ be the probability per unit time per molecule (averaged over an ensemble of molecules with a distribution of velocities) for an upward transition with the absorption of a photon with a frequency *in the observers frame* in the range $d\nu$ about ν, travelling in a direction in the solid angle $d\Omega$ about $\hat{\mathbf{\Omega}}$, where $R_{lu}^{\nu,\Omega} \equiv d^2 R_{lu}/d\nu d\Omega$. If the frequency dependence of the absorption is described by the line profile function $\phi(\mathbf{r}, \nu)d\nu$, then equation 2.47 is replaced by

$$R_{lu}^{\nu,\Omega}(\mathbf{r}, \nu, \hat{\mathbf{\Omega}}) = \frac{\mathrm{B}_{lu}}{4\pi} I_\nu(\mathbf{r}, \nu, \hat{\mathbf{\Omega}})\phi(\mathbf{r}, \nu). \tag{2.58}$$

The total upward transition probability, R_{lu}, is found by integrating this equation over frequency and solid angle, which gives

$$R_{lu} = \mathrm{B}_{lu}\bar{J}_\nu, \tag{2.59}$$

where $\bar{J}_\nu$ is the frequency average of the mean intensity over the line absorption line profile function:

$$\bar{J}_\nu = \int_0^\infty J_\nu \phi(\nu)\, d\nu, \tag{2.60}$$

$$= \frac{1}{4\pi}\int_{4\pi}\int_0^\infty I_\nu \phi(\nu)\, d\nu\, d\Omega. \tag{2.61}$$

The effect of the molecular motions on the profile of *emission* is considerably more complicated, and is in general described by a function $\psi(\mathbf{r}, \nu, \hat{\mathbf{\Omega}})$ of direction as well as position and frequency, normalised such that

$$\frac{1}{4\pi} \int_{4\pi} \int_0^\infty \psi(\mathbf{r}, \nu, \hat{\mathbf{\Omega}}) \, d\nu \, d\Omega = 1. \tag{2.62}$$

By analogy with equation 2.58, the expression for the downward transition probability per unit time, per unit solid angle, per unit frequency, $R_{ul}^{\nu,\Omega}$, is

$$R_{ul}^{\nu,\Omega}(\mathbf{r}, \nu, \hat{\mathbf{\Omega}}) = \frac{\mathrm{B}_{ul}}{4\pi} I_\nu(\mathbf{r}, \nu, \hat{\mathbf{\Omega}}) \psi(\mathbf{r}, \nu, \hat{\mathbf{\Omega}}). \tag{2.63}$$

For an arbitrary radiation field, the function $\psi(\mathbf{r}, \nu, \hat{\mathbf{\Omega}})$ has the general form

$$\psi(\mathbf{r}, \nu, \hat{\mathbf{\Omega}}) \;=\; \alpha\phi(\mathbf{r}, \nu) + \frac{\beta}{4\pi \bar{J}_\nu(\mathbf{r})} \int_{4\pi} \int_0^\infty \chi(\mathbf{r}, \nu, \hat{\mathbf{\Omega}}, \nu', \hat{\mathbf{\Omega}}') \, I_\nu(\mathbf{r}, \nu', \hat{\mathbf{\Omega}}') \, d\nu' \, d\Omega' \tag{2.64}$$

where α and β are weighting factors (with $\alpha + \beta = 1$) for the terms on the right which respectively correspond to pure emission (i.e. emission following collisional excitation) and photon scattering. The function $\chi(\mathbf{r}, \nu, \hat{\mathbf{\Omega}}, \nu', \hat{\mathbf{\Omega}}')$ depends on the velocity distribution and systematic motion of the molecules in the gas relative to the frame of reference. The reason for the more complicated behaviour of the 'scattering' term may be illustrated by the following example:

Consider a gas which is irradiated by a beam travelling parallel to the x-axis, containing photons with a frequency ν that is slightly greater than the rest frequency ν_0 of one of the molecular transitions of the gas molecules. Only the molecules with $\mathrm{v}_x \simeq c(1 - \nu/\nu_0)$ can be radiatively excited by the beam, since only in the rest frames of these molecules do the beam photons have a frequency approaching ν_0. The molecules selected by the beam in this way are an unrepresentative sample of the overall velocity distribution. If the excited molecules are able to decay radiatively before undergoing velocity altering collisions, then the distribution of emitted photons in the observers frame will reflect this unusual velocity distribution. The frequency distribution of the emitted photons will be skewed to the blue in the forward direction (relative to the beam), and skewed to the red in the backward direction.

If the incident radiation field at the frequency $\nu \neq \nu_0$ is isotropic, the distribution of the scattered photons will also be isotropic. The frequency distribution, however, will still in general be different from the absorption line profile, $\phi(\nu)$, due to the absence of the contribution of molecules with speeds $v<|c(1-\nu/\nu_0)|$ to the photon scattering at this frequency.

The complicated nature of the emission line profile function adds considerable complexity to the general radiative transfer problem, if treated exactly. The situation is not as serious as it first appears, however, for the following reasons:

- If the scattering angle is close to 90° (i.e. $\hat{\Omega} \cdot \hat{\Omega}' \simeq 0$ in equation 2.64), then for these pairs of directions $\chi(\mathbf{r}, \nu, \hat{\Omega}, \nu', \hat{\Omega}') \simeq \phi(\mathbf{r}, \nu)\phi(\mathbf{r}, \nu')$, since the velocity distributions of the molecules along perpendicular directions are independent. It then follows from equation2.64 that $\psi(\mathbf{r}, \nu, \hat{\Omega}) \simeq \phi(\mathbf{r}, \nu)$.

- $\chi(\mathbf{r}, \nu, \hat{\Omega}, \nu', \hat{\Omega}') \simeq \phi(\mathbf{r}, \nu)\phi(\mathbf{r}, \nu')$ when ν' is close to the peak frequency of the absorption line profile, becoming an equality when $\nu' = \nu_{\rm peak}$ (Hummer 1971). If the radiation field at $\mathbf{r}$ is mainly confined to frequencies in the core of the absorption profile then $\psi(\mathbf{r}, \nu, \hat{\Omega}) \simeq \phi(\mathbf{r}, \nu)$.

- If the average time between elastic collisions is less than the radiative decay time $t_{\rm rad} \sim 1/A_{ul}$, then the velocities of the excited molecules will have time to become randomised by collisions before they decay, so that $\chi(\mathbf{r}, \nu, \hat{\Omega}, \nu', \hat{\Omega}') \simeq \phi(\mathbf{r}, \nu)\phi(\mathbf{r}, \nu')$, for all angles and frequencies, and $\psi(\mathbf{r}, \nu, \hat{\Omega}) \simeq \phi(\mathbf{r}, \nu)$.

- Molecules which are excited into the upper level of the transition through inelastic collisions should have the same velocity distribution as the ordinary gas molecules (Spitzer, 1978), in which case the frequency dependence of the emission from these molecules will be described by $\phi(\mathbf{r}, \nu)$. This is the origin of the first term on the right hand side of (2.64). When collisions dominate, $\alpha \gg \beta$, and again $\psi(\mathbf{r}, \nu, \hat{\Omega}) \simeq \phi(\mathbf{r}, \nu)$.

In the radiative transfer modelling carried out in this thesis, we follow the usual

practice of assuming that $\psi(\mathbf{r}, \nu, \hat{\mathbf{\Omega}}) = \phi(\mathbf{r}, \nu)$ holds exactly at all positions. This assumption, known as the **complete redistribution approximation**, is made primarily for expediency of numerical calculation, but is largely justified by the considerations mentioned above.

When the complete redistribution approximation is made, equation (2.65) becomes

$$R_{ul}^{\nu,\Omega}(\nu, \hat{\mathbf{\Omega}}) = \frac{1}{4\pi}[\mathrm{A}_{ul} + \mathrm{B}_{ul} I_\nu(\nu, \hat{\mathbf{\Omega}})]\phi(\nu). \tag{2.65}$$

Integrating over solid angle and frequency, we find for the total downward transition probability per unit time, R_{ul}, (cf. equation 2.59)

$$R_{ul} = \mathrm{A}_{ul} + \mathrm{B}_{ul}\bar{J}_\nu, \tag{2.66}$$

where $\bar{J}_\nu$ is as given in equation 2.61.

2.2.3 The relationship between microscopic and macroscopic quantities

An outline is now given of the relationship between the Einstein coefficients, the emissivity ε and the volume absorption cross-section, κ. Consider a beam of light which at the point $\mathbf{r}$ has an intensity $I_\nu(\mathbf{r}, \nu, \hat{\mathbf{\Omega}})$ over a spread of solid angle $d\Omega$ about the direction $\hat{\mathbf{\Omega}}$ and over the frequency interval $d\nu$ about ν. As they travel through the medium, photons may be removed from the beam by radiative excitation of a molecular transition, and photons may be added to the beam by spontaneous emission in the transition (where photons are emitted over random directions), or by stimulated emission (where all the emitted photons travel in the beam direction). Stimulated emission may therefore be treated as a kind of negative absorption, since a photon produced by stimulated emission 'replaces' one lost by absorption.

We introduce again the photon distribution function, f (see equation 2.1), where $f(\mathbf{r}, \nu, \hat{\mathbf{\Omega}})d\nu\, d\Omega$ is the number of photons per unit volume in the beam at $\mathbf{r}$ and $I_\nu =$

$ch\nu f$ (cf. 2.4). The net number of photons per unit time per unit volume added to the beam as it travels through the medium, by emission and absorption in the line, may be related to the net rate of transfer of molecules, per unit volume, from the upper level to the lower level of the transition in the following way:

$$\frac{Df(\mathbf{r},\nu,\hat{\mathbf{\Omega}})}{Dt}\,d\nu\,d\Omega = n_u(\mathbf{r})R_{ul}^{\nu,\Omega}(\mathbf{r},\nu,\hat{\mathbf{\Omega}})\,d\nu\,d\Omega - n_l(\mathbf{r})R_{lu}^{\nu,\Omega}(\mathbf{r},\nu,\hat{\mathbf{\Omega}})\,d\nu\,d\Omega. \tag{2.67}$$

Substituting for $R_{ul}^{\nu,\Omega}$ and $R_{lu}^{\nu,\Omega}$ using equations 2.58 and 2.65,

$$\frac{Df(\mathbf{r},\nu,\hat{\mathbf{\Omega}})}{Dt} = \frac{\mathrm{A}_{ul}}{4\pi}n_u(\mathbf{r})\phi(\mathbf{r},\nu) + \frac{1}{4\pi}[\mathrm{B}_{ul}n_u(\mathbf{r}) - \mathrm{B}_{lu}n_l(\mathbf{r})]\,I_\nu(\mathbf{r},\nu,\hat{\mathbf{\Omega}})\phi(\mathbf{r},\nu)\,d\nu. \tag{2.68}$$

Here $n_u(\mathbf{r})$ and $n_l(\mathbf{r})$ denote the number densities of molecules occupying the upper and lower levels of the molecular transition, respectively, as a function of position. Replacing f with $I_\nu/h\nu c$ in (2.68),

$$\frac{1}{c}\frac{DI_\nu(\mathbf{r},\nu,\hat{\mathbf{\Omega}})}{Dt} \equiv \frac{dI_\nu}{ds} = \frac{h\nu}{4\pi}\mathrm{A}_{ul}n_u(\mathbf{r})\phi(\mathbf{r},\nu) + \frac{h\nu}{4\pi}[\mathrm{B}_{ul}n_u(\mathbf{r}) - \mathrm{B}_{lu}n_l(\mathbf{r})]\,I_\nu\phi(\mathbf{r},\nu). \tag{2.69}$$

On comparing this equation with equation 2.17, the expressions for ε and κ are found to be:

$$\varepsilon(\mathbf{r},\nu) = \frac{h\nu}{4\pi}A_{ul}n_u(\mathbf{r})\phi(\mathbf{r},\nu), \tag{2.70}$$

$$\kappa(\mathbf{r},\nu) = \frac{h\nu}{4\pi}[\mathrm{B}_{lu}n_l(\mathbf{r}) - \mathrm{B}_{ul}n_u(\mathbf{r})]\phi(\mathbf{r},\nu). \tag{2.71}$$

Using the relations in equations 2.55 and 2.56, the source function $S_\nu = \varepsilon/\kappa$ may be expressed as

$$S_\nu(\mathbf{r}) = \frac{2h\nu_0^3}{c^2}\cdot\frac{1}{g_u n_l(\mathbf{r})/g_l n_u(\mathbf{r}) - 1}. \tag{2.72}$$

Where ν_0 is defined such that $h\nu_0$ is equal to the energy gap between the levels. Note that (2.72) is independent of the frequency ν.

The excitation temperature T_{ex} (equation 2.44) satisfies the relation:

$$\frac{n_u(\mathbf{r})}{n_l(\mathbf{r})} = \frac{g_u}{g_l}\exp[-h\nu_0/kT_{\mathrm{ex}}(\mathbf{r})], \tag{2.73}$$

Equation 2.72 may be written as

$$S_\nu(\mathbf{r}) = \frac{2h\nu_0^3}{c^2} \cdot \frac{1}{\exp[h\nu_0/kT_{\rm ex}(\mathbf{r})] - 1}, \tag{2.74}$$

$$= B_\nu[\nu_0, T_{\rm ex}(\mathbf{r})]. \tag{2.75}$$

In the notation of equation 2.23, the optical depth differential, $d\tau_\nu$, is given explicitly by

$$d\tau_\nu(\mathbf{r_0}, z, \nu, \hat{\mathbf{\Omega}}) = \frac{h\nu}{4\pi}[\mathrm{B}_{lu} n_l(\mathbf{r}') - \mathrm{B}_{ul} n_u(\mathbf{r}')]\, \phi(\mathbf{r}', \nu)\, dz, \tag{2.76}$$

where $\mathbf{r}' = \mathbf{r_0} - z\hat{\mathbf{\Omega}}$, is a point on the beam a distance z from $\mathbf{r_0}$ in the negative beam direction.

2.2.4 The line profile function

We now examine the explicit form of the line profile function $\phi(\nu)$ (ignoring the dependence on $\mathbf{r}$), when the shape is dominated by the broadening of absorption and emission frequencies caused by the thermal and turbulent motions of the gas particles and the Doppler effect. The contribution of the natural line width to the overall profile may be neglected provided $\mathrm{A}_{ul} \ll \nu_0\sigma_{\rm tot}/c$, where ν_0 is the line frequency, c is the speed of light, and $\sigma_{\rm tot}$, which is defined below, is a measure of the spread of particle velocities due to thermal and turbulent random motions. In the actual problems we shall consider in this thesis, $\sigma_{\rm tot} >\sim 100\, m\, s^{-1}$, and $\nu_0 \sim 3 \times 10^{11}$Hz, so the constraint above corresponds to $\mathrm{A}_{ul} \ll 10^5$. The molecular transitions that will be studied all have $\mathrm{A}_{ul} < 10^{-2}$, so this condition is more than amply satisfied.

In the following the microturbulent approximation is used, which assumes that the characteristic turbulent length scale is much smaller than both the photon mean free path, and the scale over which the physical properties of the cloud change significantly. The nature of the turbulent gas motions in protostellar envelopes is not yet properly understood (e.g. Vazquez-Semadeni, Canto & Lizano, 1996), and a more sophisticated treatment of turbulence may eventually be required. As discussed in the introduction

to this thesis, relaxing the microturbulent approximation leads to comparatively less self-absorbed line profiles (e.g. Dickman 1995; Park & Hong 1995; Juvela 1997). Lack of detailed knowledge about the true turbulent velocity field in protostellar envelopes, and the requirements of numerical expediency lead us to retain the microturbulent approximation, however.

Only the line of sight velocity component is relevant in determining the effect of Doppler shifts on the line profile. The one dimensional Maxwell velocity distribution (2.41) leads to the following expression for $\psi_{\mathrm{v_{th}}}$, the normalised thermal velocity distribution:

$$\psi_{\mathrm{v_{th}}}(\mathrm{v}_z) = \frac{n(\mathrm{v}_z)}{n_{\mathrm{tot}}} = \left(\frac{m}{2\pi kT}\right)^{\frac{1}{2}} \exp\left(-m\mathrm{v}_z^2/2kT\right), \tag{2.77}$$

where v_z is the molecular line of sight velocity, and $\psi_{\mathrm{v_{th}}}$ is normalised such that

$$\int_{-\infty}^{\infty} \psi_{\mathrm{v_{th}}}(\mathrm{v}_z)\, d\mathrm{v}_z = 1. \tag{2.78}$$

Defining $\sigma_{\mathrm{v_{th}}}$ as the thermal rms velocity dispersion, we have

$$\sigma_{\mathrm{v_{th}}} = \sqrt{kT/m}, \tag{2.79}$$

$$\psi_{\mathrm{v_{th}}}(\mathrm{v}_z) = \frac{1}{\sigma_{\mathrm{v_{th}}}\sqrt{2\pi}} \exp\left(-\frac{\mathrm{v}_z^2}{2\sigma_{\mathrm{v_{th}}}^2}\right). \tag{2.80}$$

For convenience, and in the absence of evidence to the contrary, we assume that the normalised turbulent velocity distribution, $\psi_{\mathrm{v_{tb}}}$, has a similar functional form:

$$\psi_{\mathrm{v_{tb}}}(\mathrm{v}_z) = \frac{1}{\sigma_{\mathrm{v_{tb}}}\sqrt{2\pi}} \exp\left(-\frac{\mathrm{v}_z^2}{2\sigma_{\mathrm{v_{tb}}}^2}\right), \tag{2.81}$$

where $\sigma_{\mathrm{v_{tb}}}$ is the turbulent rms velocity dispersion. The relationship between the full width at half maximum velocity and σ in these profiles is given by

$$\Delta\mathrm{v}_{r,\mathrm{FWHM}} = \sigma\sqrt{8\ln 2} \simeq 2.35\sigma. \tag{2.82}$$

If $\psi_{\mathrm{v_{tot}}}$ is defined as the velocity profile produced by convolving $\psi_{\mathrm{v_{th}}}$ and $\psi_{\mathrm{v_{tb}}}$, then

$$\psi_{\mathrm{v_{tot}}}(\mathrm{v}_z) = \frac{1}{\sigma_{\mathrm{v_{tot}}}\sqrt{2\pi}} \exp\left(-\frac{\mathrm{v}_z^2}{2\sigma_{\mathrm{v_{tot}}}^2}\right), \tag{2.83}$$

where

$$\sigma_{\mathrm{v_{tot}}}^2 = \sigma_{\mathrm{v_{th}}}^2 + \sigma_{\mathrm{v_{tb}}}^2. \tag{2.84}$$

The frequency line profile function $\phi(\nu)$ resulting from the velocity distribution, $\psi_{\mathrm{v_{tot}}}(\mathrm{v}_z)$, may be written as

$$\phi(\nu) \;=\; \psi_{\mathrm{v_{tot}}}(\mathrm{v}_z)\left|\frac{d\mathrm{v}_z}{d\nu}\right|. \tag{2.85}$$

$\phi(\nu)$ is normalised such that

$$\int_0^\infty \phi(\nu)\,d\nu = 1. \tag{2.86}$$

If a molecule is moving with a line of sight velocity $\mathrm{v}_r \ll c$, the frequency at which it emits or absorbs in a line is Doppler shifted in the observers frame by an amount

$$\Delta\nu \equiv \nu - \nu_0 = -(\mathrm{v}_z/c)\nu_0, \tag{2.87}$$

and therefore $d\nu/d\mathrm{v}_z = -\nu_0/c$. Substituting these expressions into equation 2.85 gives

$$\phi(\nu) = \frac{1}{\sigma_\nu\sqrt{2\pi}}\exp\left(-\frac{(\nu-\nu_0)^2}{2\sigma_\nu^2}\right), \tag{2.88}$$

where $\sigma_\nu = (\nu_0/c)\sigma_{\mathrm{v_{tot}}}$ is the *frequency* dispersion. A profile of this form is called a **Doppler profile.**

It is sometimes more convenient to express ϕ as a function of v_z rather than ν. Defining $\phi_{\mathrm{v}_z}(\mathrm{v}_z) \equiv \phi(\nu)$, we have

$$\phi_{\mathrm{v}_z}(\mathrm{v}_z) = \frac{c}{\sigma_{\mathrm{v_{tot}}}\nu_0\sqrt{2\pi}}\exp\left(-\frac{\mathrm{v}_z^2}{2\sigma_{\mathrm{v_{tot}}}^2}\right). \tag{2.89}$$

The effect of systematic motions on the line profile function

So far, the discussion has ignored possible systematic motions of the gas relative to the chosen frame of reference. We now ask the question: 'What is the line profile function of gas at a point $\mathbf{r}_1$, moving with velocity $\mathbf{v}(\mathbf{r}_1)$, from the point of view of an 'observer' at $\mathbf{r}_0$, moving with the velocity $\mathbf{v}(\mathbf{r}_0)$?'

Adopting a similar convention as was used in the discussion of the optical depth (equation 2.23), we write $\mathbf{r}_1 = \mathbf{r}_0 - z\hat{\mathbf{\Omega}}$, where $\hat{\mathbf{\Omega}}$ is the unit vector in the direction

from $\mathbf{r}_1$ to $\mathbf{r}_0$, and z is the distance between the two points. The speed at which the clump at $\mathbf{r}_1$ moves *away* along the line of sight from the 'observer' at $\mathbf{r}_0$, is given by

$$\mathrm{v}_z^{\mathrm{rec}}(\mathbf{r}_0, z, \hat{\mathbf{\Omega}}) = -\hat{\mathbf{\Omega}} \cdot \mathbf{v}(\mathbf{r}_1) + \hat{\mathbf{\Omega}} \cdot \mathbf{v}(\mathbf{r}_0). \tag{2.90}$$

The line profile function, ϕ_{v_z} of the the gas at $\mathbf{r}_1$, as seen by the 'observer' at $\mathbf{r}_0$, is centred on $\mathrm{v}_z^{\mathrm{rec}}$, and may therefore be written as

$$\phi_{\mathrm{v}_z}(\mathbf{r}_0, z, \mathrm{v}_z, \hat{\mathbf{\Omega}}) = \frac{c}{\sigma_{\mathrm{v_{tot}}}(\mathbf{r}_1)\nu_0\sqrt{2\pi}} \exp\left(-\frac{[\mathrm{v}_z - \mathrm{v}_z^{\mathrm{rec}}(\mathbf{r}_0, z, \hat{\mathbf{\Omega}})]^2}{2\sigma_{\mathrm{v_{tot}}}(\mathbf{r}_1)^2}\right), \tag{2.91}$$

where $\mathbf{r}_1 = \mathbf{r}_0 - z\hat{\mathbf{\Omega}}$. The shape of the line profile function therefore depends on the microscopic motions of the gas molecules, and the position of its peak depends on the systematic motion of the gas relative to the 'observer'.

2.2.5 Semi-classical quantum mechanical derivation of the Einstein coefficients

A complete derivation of the absolute values of Einstein A and B coefficients requires a quantum mechanical treatment of both the molecule and radiation field (e.g. Berestetskii, Lifshitz & Pitaevskii 1982). However, the correct expression for stimulated emission and absorption (i.e. the Einstein B coefficients) may be derived using a semi-classical treatment, where the radiation field is treated classically. An outline of this derivation is given below, following the treatment in Atkins & Friedman (1997).

It is assumed that the molecule has a permanent electric dipole moment, and that the contributions of the other electric and magnetic multipole moments to the interaction energy may be neglected. The energy of interaction between the molecular electric dipole moment $\mathbf{d} = e\mathbf{r}$ and the electric field component of a plane electromagnetic wave, $\mathbf{E} = \mathbf{E}_0 \cos\omega t$, is given by $V' = -\mathbf{d}\cdot\mathbf{E}_0 \cos\omega t$. As before we use the device of confining the radiation field to a cubical cavity with volume V.

The expression for the transition probability per unit time between initial and final molecular states, $|i\rangle$ and $|f\rangle$ (which here denote only the spatial parts of the state

wavefunctions), is given by time dependent perturbation theory (e.g. Schiff, 1968) as

$$\dot{P} = \frac{\pi}{2\hbar} \overline{|\langle f|\,\mathbf{d}\cdot\mathbf{E_0}\,|i\rangle|^2}\,\rho(\mathcal{E}), \tag{2.92}$$

where $\overline{|\langle f|\mathbf{d}\cdot\mathbf{E_0}|i\rangle|^2} = \frac{1}{3}\,|\langle f|d|i\rangle|^2 E_0^2$ is the average of the perturbation matrix element over all possible relative orientations of $\mathbf{d}$ and $\mathbf{E_0}$. $\rho(\mathcal{E})$ is the number of photon states in the cavity per unit photon energy, where $\mathcal{E} = h\nu$ is the energy of the photon emitted in the transition. The electromagnetic energy contained in each cavity mode is related to the electric field amplitude in that mode by $\mathcal{E} = \frac{1}{2}\varepsilon_0 E_0^2 V$. Substituting these expressions into 2.92 gives

$$\begin{aligned} \dot{P} &= \frac{\pi}{3\epsilon_0\hbar}|\langle f|\,\mathbf{d}\,|i\rangle|^2\,\frac{\mathcal{E}\rho(\mathcal{E})}{V}, \\ &= \frac{1}{6\epsilon_0\hbar^2}|\langle f|\,\mathbf{d}\,|i\rangle|^2 u_\nu. \end{aligned} \tag{2.93}$$

In the second expression above we have used $V u_\nu\, d\nu = \mathcal{E}\rho(\mathcal{E})\, d\mathcal{E}$, where u_ν is the radiation energy density per unit frequency (2.2), and $d\mathcal{E} = h\, d\nu$. Equation 2.93 may be compared with equation 2.66, to find an explicit expression for B_{ul}, the Einstein B coefficient for stimulated emission. Designating $|u\rangle$ and $|l\rangle$ as the upper and lower energy states of a downward molecular transition, and identifying $\dot{P}$ as the probability per unit time for stimulated emission, $\mathrm{B}_{ul}J_\nu$, we find, on substituting $u_\nu = 4\pi J_\nu/c$,

$$\begin{aligned} \mathrm{B}_{ul}J_\nu &= \frac{1}{6\epsilon_0\hbar^2}\,|\langle l|\,\mathbf{d}\,|u\rangle|^2\frac{4\pi J_\nu}{c} \\ \mathrm{B}_{ul} &= \frac{2\pi}{3\epsilon_0 c\hbar^2}\,|\langle l|\,\mathbf{d}\,|u\rangle|^2. \end{aligned} \tag{2.94}$$

As before, if the final level (in this case the lower level) of the transition is degenerate, the expression for B_{ul} must be summed over all the states in the final level. For each degenerate state in the initial level of a rotational transition, the sum over all the final level states is identical, since there is no preferred axis in space. Using the labels m_u and m_l to distinguish between the degenerate states in the upper and lower levels of the transition respectively, it is convenient to define a **line strength**, S_{ul}, by,

$$\mathrm{S}_{ul} = \sum_{m_u}\sum_{m_l} |\langle l\, m_l|\,\mathbf{d}\,|u\, m_u\rangle|^2, \tag{2.95}$$

Applying the relations given in equations 2.55 and 2.56, the explicit expressions for the Einstein coefficients are:

$$\mathrm{A}_{ul} = \frac{8\pi^2\nu_0^3}{3\epsilon_0 c^3\hbar}\cdot\frac{\mathrm{S}_{ul}}{g_u}, \tag{2.96}$$

$$B_{ul} = \frac{2\pi}{3\epsilon_0 c\hbar^2} \cdot \frac{S_{ul}}{g_u}, \tag{2.97}$$

$$B_{lu} = \frac{2\pi}{3\epsilon_0 c\hbar^2} \cdot \frac{S_{ul}}{g_l}, \tag{2.98}$$

where $h\nu_0$ is equal to the difference in energy between the levels.

Depending on the symmetry properties of the molecule, the dipole moment matrix elements in equation 2.95 may equal zero for particular pairs of levels, leading to selection rules forbidding radiative transitions between these levels (see section 2.2.8).

2.2.6 Collisional transitions

Transitions between the energy levels of a molecule may be brought about through inelastic collisions with other gas particles, as well as through radiative transitions. It is necessary to include collisional transitions rates in the determination of the equilibrium level populations of the molecule. In interstellar molecular clouds the hydrogen molecule is the predominant collision partner of all the gas molecules.

Collision rate coefficients

The following derivation of the collision rate coefficient formula is adapted from Flower (1990).

Consider a gas which, apart from trace quantities of a particular molecule of interest, is entirely composed of hydrogen molecules. Let n_{H_2} be the total number density of hydrogen molecules, and let $n_{X,i}$ be the number density of trace molecules occupying the internal energy level i. Also use $\mathrm{v_1}$ and $\mathrm{v_2}$ to distinguish between the velocity of a hydrogen molecule and a trace molecule respectively.

Now write $f_{H_2}(\mathbf{v}_1)d^3\mathrm{v}_1$ as the fraction of hydrogen molecules with velocities in the

velocity-space volume element $d^3\mathrm{v}_1$ about the velocity $\mathbf{v}_1$, where $d^3\mathrm{v}_1 = d\mathrm{v}_{1x}d\mathrm{v}_{1y}d\mathrm{v}_{1z}$. Similarly write $f_{X,i}(\mathrm{v}_2)d^3\mathrm{v}_2$ as the fraction of X molecules, in the level i, which have velocities in the velocity-space volume element $d^3\mathrm{v}_2$ about $\mathbf{v}_2$. In most cases of interest, $f_{X,i}$ will be independent of i (Spitzer 1978), and in the following we simply write f_X. Let $\sigma_{ij}(\mathrm{v})$ be the effective cross-section for an X-molecule in level i to undergo a transition into the level j, as the result of an inelastic collision with a hydrogen molecule with a relative speed $\mathrm{v}=|\mathbf{v_1}-\mathbf{v_2}|$. The determination of the function $\sigma_{ij}(\mathrm{v})$ requires an involved quantum mechanical scattering calculation. The procedure is outlined in Flower(1990).

The expression $[n_{X,i}f_X(\mathbf{v}_2)d^3\mathrm{v}_2]\,\mathrm{v}\sigma_{ij}(\mathrm{v})\,[n_{H_2}f_{H_2}(\mathbf{v}_1)d^3\mathrm{v}_1]$ gives the number of collisional transitions between levels i and j of X, per unit volume and time, due to collisions between X molecules in the i'th level, in the velocity space element $d^3\mathrm{v}_2$ about $\mathbf{v_2}$, and hydrogen molecules in the velocity space element $d^3\mathrm{v}_1$ about $\mathbf{v_1}$. The total number of collisional transitions of X between levels i and j, per unit volume, per unit time, is found by integrating over $d^3\mathrm{v}_1$ and $d^3\mathrm{v}_2$. Equating this with $n_{X,i}\mathrm{C}_{ij}$, where C_{ij} is the collisional transition rate per X-molecule occupying level i:

$$n_{X,i}\mathrm{C}_{ij} = \int_0^\infty n_{X,i}f_X(\mathrm{v}_2)\mathrm{v}\sigma_{ij}(\mathrm{v})n_{H_2}f_{H_2}(\mathrm{v}_1)\,d^3\mathrm{v}_1\,d^3\mathrm{v}_2, \tag{2.99}$$

$$\mathrm{C}_{ij} = n_{H_2}<\sigma\mathrm{v}>_{ij}, \tag{2.100}$$

$$<\sigma\mathrm{v}>_{ij} = \int_0^\infty \mathrm{v}\sigma_{ij}(\mathrm{v})f_{H_2}(\mathbf{v}_1)f_X(\mathbf{v}_2)\,d^3\mathrm{v}_1\,d^3\mathrm{v}_2. \tag{2.101}$$

$<\sigma\mathrm{v}>_{ij}$ is called the **rate coefficient** and is an average over the velocity distributions of both the incident and target particles. In most situations of interest, the velocity distributions $f_{H_2}(\mathbf{v}_1)$ and $f_X(\mathbf{v}_2)$ conform to the Maxwell velocity distribution (2.40), so that

$$\begin{aligned} f_{H_2}(\mathbf{v}_1) &\equiv f_{H_2}(\mathrm{v}_1) \\ &= \left(\frac{m_{H_2}}{2\pi kT}\right)^{\frac{3}{2}} \exp\left[-m_{H_2}(\mathrm{v}_{1x}^2+\mathrm{v}_{1y}^2+\mathrm{v}_{1z}^2)/2kT\right], \end{aligned} \tag{2.102}$$

and similarly for $f_X(\mathbf{v}_2)$. It is assumed that velocity distributions of both species are characterised by the same kinetic temperature, T. Substituting the explicit velocity distributions into equation 2.101 and eliminating v_{2x}, v_{2y} and v_{2z} in favour of the components of the relative velocity, v_x, v_y and v_z, using $\mathrm{v}=|\mathbf{v_1}-\mathbf{v_2}|$, the expression for

the rate coefficient becomes

$$<\sigma \mathrm{v}>_{ij} = \frac{(m_{H_2} m_X)^{\frac{3}{2}}}{(2\pi kT)^3} \int_0^\infty \mathrm{v}\sigma_{ij}(\mathrm{v}) \exp\left[-\frac{1}{2kT}\sum_{i=1}^{3} m_{H_2}\mathrm{v}_{1x_i}^2 + m_X(\mathrm{v}_{x_i} - \mathrm{v}_{1x_i})^2\right] d^3\mathrm{v}_1\, d^3\mathrm{v}, \tag{2.103}$$

where $d^3\mathrm{v} \equiv d\mathrm{v}_x d\mathrm{v}_y d\mathrm{v}_z$ and the x_i correspond to the three cartesian axes, x, y and z. The sum in the exponential may be written as

$$\sum_{i=1}^{3} m_{H_2}\mathrm{v}_{1x_i}^2 + m_X(\mathrm{v}_{x_i} - \mathrm{v}_{1x_i})^2 = \sum_{i=1}^{3}(m_{H_2}+m_X)\left(\mathrm{v}_{1x_i} - \frac{m_X \mathrm{v}_{x_i}}{m_{H_2}+m_X}\right)^2 + \frac{m_{H_2} m_X}{m_{H_2}+m_X}\mathrm{v}_{x_i}^2, \tag{2.104}$$

which when substituted into equation 2.103 allows the integrals over $\mathrm{v}_{1x}, \mathrm{v}_{1y}$ and v_{1z} to be carried out. Writing $\mu = m_{H_2} m_X/(m_{H_2} + m_X)$, where μ is called the **reduced mass** of the two colliding particles, the resulting expression is

$$\begin{aligned} <\sigma \mathrm{v}>_{ij} &= \left(\frac{\mu}{2\pi kT}\right)^{\frac{3}{2}} \int_0^\infty \mathrm{v}\sigma_{ij}(\mathrm{v}) \exp\left[-\frac{\mu}{2kT}(\mathrm{v}_x^2 + \mathrm{v}_y^2 + \mathrm{v}_z^2)\right] d^3\mathrm{v}, \\ &= 4\pi\left(\frac{\mu}{2\pi kT}\right)^{\frac{3}{2}} \int_0^\infty \mathrm{v}\sigma_{ij}(\mathrm{v}) \exp\left[-\frac{\mu \mathrm{v}^2}{2kT}\right] \mathrm{v}^2\, d\mathrm{v}, \end{aligned} \tag{2.105}$$

where we have used $d^3\mathrm{v} = 4\pi \mathrm{v}^2 d\mathrm{v}$, since the integrand has no angular dependence. Finally, substituting the dimensionless variable $x = \mu \mathrm{v}^2/2kT$,

$$<\sigma \mathrm{v}>_{ij} = \left(\frac{8kT}{\pi\mu}\right)^{\frac{1}{2}} \int_0^\infty x\, \sigma_{ij}[\mathrm{v}(x)]\, e^{-x}\, dx, \tag{2.106}$$

where $\mathrm{v}(x) = (2kTx/\mu)^{\frac{1}{2}}$. The factor in front of the integral is approximately equal to the r.m.s average of the relative velocity between the X molecules and hydrogen molecules, $\mathrm{v}_{\mathrm{rms}}$, and the integral is a weighted average of the collisional cross-section for the transition, giving maximum weight to the values of $\sigma_{ij}[v(x)]$ around $x \sim 1$, i.e. $\mathrm{v} \sim (2kT/\mu)^{\frac{1}{2}} \simeq \mathrm{v}_{\mathrm{rms}}$. Note that for an upward collisional transition, there must be sufficient kinetic energy in the centre of mass frame of the colliding particles for the energy gap of the transition to be traversed. This leads to the constraint $\sigma_{ij}(\mathrm{v}) = 0$ when $\frac{1}{2}\mu \mathrm{v}^2 < E_j - E_i$.

2.2.7 Statistical equilibrium including collisions

When collisionally induced transitions are included, the total probability per unit time for a molecule to undergo a transition from an upper to a lower level may be written

$$\dot{P}_{ul} = R_{ul} + \mathrm{C}_{ul} \equiv \mathrm{A}_{ul} + \mathrm{B}_{ul}\bar{J}_\nu + \mathrm{C}_{ul}. \tag{2.107}$$

Similarly, for the upward transition,

$$\dot{P}_{lu} = R_{lu} + \mathrm{C}_{lu} \equiv \mathrm{B}_{lu}\bar{J}_{\nu} + \mathrm{C}_{lu}. \tag{2.108}$$

In a multi-level molecule (i.e. a molecule with more than two levels), similar relations will apply for all pairs of levels. If in an ensemble of such molecules, the level populations have reached a steady state, then the *total* rate of transitions from a given level into all other levels will be balanced by the *total* rate of transitions in the opposite direction. When two levels of a multi-level system are considered in isolation, however, then the transition rate going from one level to the other is not in general balanced by the transition rate for the reverse process, that is to say $n_u\dot{P}_{ul} = n_l\dot{P}_{lu}$ does not apply in general, even in the steady state. One exception is the two-level molecule, where the relation just given necessarily holds in the steady state. For a multi-level molecule, this relation can only be assumed to hold for all pairs of levels if the system is in complete thermodynamic equilibrium, as a consequence of the principle of detailed balance. In this case we have

$$n_u(R_{ul} + \mathrm{C}_{ul}) = n_l(R_{lu} + \mathrm{C}_{lu}), \tag{2.109}$$

In CTE the radiation field is described by the Planck function, and the level population is described by the Boltzmann equation. Reversing the argument leading to equation 2.54, this implies that equation (2.51) holds, i.e.:

$$n_u R_{ul} = n_l R_{lu}. \tag{2.110}$$

The radiative terms in equation 2.109 therefore drop out, and we find

$$\begin{aligned} \frac{\mathrm{C}_{lu}}{\mathrm{C}_{ul}} &= \frac{<\sigma \mathrm{v}>_{lu}}{<\sigma \mathrm{v}>_{ul}}, \\ &= \frac{n_u}{n_l}, \\ &= \frac{g_u}{g_l} e^{-\frac{h\nu_0}{kT}}. \end{aligned} \tag{2.111}$$

Although this relation has been obtained by assuming complete thermodynamic equilibrium, the values of the rate coefficients are affected only by the velocity distribution of the gas particles. If the velocity distribution is Maxwellian with a kinetic temperature T_{kin}, then equation 2.111 holds with $T = T_{\mathrm{kin}}$, whether or not the other equilibrium relations are satisfied.

The two level molecule

We now discuss statistical equilibrium in an ensemble of two-level molecules. The behaviour of this system illustrates some of the concepts which are useful for understanding the behaviour of systems of multi-level atoms. The equation of statistical equilibrium for the two level molecule was given before as $n_u \dot{P}_{ul} = n_l \dot{P}_{lu}$, from which we obtain:

$$\frac{n_u}{n_l} = \frac{\mathrm{B}_{lu}\bar{J}_\nu + \mathrm{C}_{lu}}{\mathrm{A}_{ul} + \mathrm{B}_{ul}\bar{J}_\nu + \mathrm{C}_{ul}}. \tag{2.112}$$

This may be substituted into equation (2.72) for the source function, S_ν. Using the relations in equations 2.55, 2.56 and 2.111, we find, after some algebra (e.g. Emerson 1996):

$$S_\nu = \frac{\bar{J}_\nu + 2h\nu_0^3/c^2\,(\mathrm{C}_{ul}/\mathrm{A}_{ul})\exp(-h\nu_0/kT_{\mathrm{kin}})}{1 + (\mathrm{C}_{ul}/\mathrm{A}_{ul})[1 - \exp(-h\nu_0/kT_{\mathrm{kin}})]}. \tag{2.113}$$

On making the following substitution,

$$\epsilon = \frac{\mathrm{C}_{ul}}{\mathrm{A}_{ul}}[1 - \exp(-h\nu_0/kT_{\mathrm{kin}})], \tag{2.114}$$

equation 2.113 becomes

$$S_\nu \equiv B_\nu(\nu_0, T_{\mathrm{ex}}) = \frac{\bar{J}_\nu + \epsilon B_\nu(\nu_0, T_{\mathrm{kin}})}{1 + \epsilon}, . \tag{2.115}$$

ϵ is a measure of the relative importance of collisional over radiative transitions in determining the level populations. When $\epsilon \gg 1$ (i.e. collisions dominate), $S_\nu \rightarrow B_\nu(\nu_0, T_{\mathrm{kin}})$ and the excitation temperature approaches the kinetic temperature (i.e. the transition is **thermalised**). When $\epsilon \ll 1$, radiative transitions dominate, and the excitation temperature approaches the brightness temperature corresponding to the mean intensity, $\bar{J}_\nu$.

The transition between these two regimes occurs, to a first approximation, when $\mathrm{C}_{ul} = \mathrm{A}_{ul}$ (neglecting the exponential term in equation 2.114). This relation can be used to define the **critical density**, n_{crit}, for a two level atom;

$$n_{\mathrm{crit}} = \frac{\mathrm{A}_{ul}}{<\sigma \mathrm{v}>_{ul}}. \tag{2.116}$$

$n_{\rm crit}$ is an estimate of the threshold gas density above which the populations of the levels become thermalised due to collisions. It is important to realise that this is only an approximate condition, and the radiation field can still influence level populations even when the density is well above the critical density.

The critical density for thermalisation of a level i in a multi-level atom (see below) may be defined equivalently as

$$n_{{\rm crit},i} = \frac{\sum_{j<i} {\rm A}_{ij}}{\sum_j <\sigma {\rm v}>_{ij}}. \tag{2.117}$$

As a rule of thumb, when $n \gg n_{{\rm crit},i}$, the excitation temperature relating the populations of levels i and j, where $j < i$ (see equation 2.44) is equal to the kinetic temperature of the gas.

The multi-level molecule

Now consider statistical equilibrium when transitions between more than two energy levels are included. The total transition probability per unit time from level i to level j is given by

$$\dot{P}_{ij} = A_{ij} + B_{ij}\bar{J}_{\nu_{ij}} + {\rm C}_{ij}; \quad E_i > E_j, \tag{2.118}$$

$$\dot{P}_{ij} = B_{ij}\bar{J}_{\nu_{ij}} + {\rm C}_{ij}; \quad E_i < E_j, \tag{2.119}$$

where $h\nu_{ij} = |E_i - E_j|$, and

$${\rm A}_{ij} = \frac{2h\nu_{ij}^3}{c^2}\,{\rm B}_{ij}, \tag{2.120}$$

$$g_i\,{\rm B}_{ij} = g_j\,{\rm B}_{ji}, \tag{2.121}$$

$$g_i{\rm C}_{ij} = g_j{\rm C}_{ji}e^{-\frac{E_j-E_i}{kT}} \tag{2.122}$$

The rate of change in the population of the $i^{\rm th}$ energy level may be written as

$$\dot{N}_i = \sum_{j\neq i}(n_j\dot{P}_{ji} - n_i\dot{P}_{ij}). \tag{2.123}$$

In the steady state, the left hand side of (2.124) is zero for all i, and

$$\sum_{j\neq i}(n_j\dot{P}_{ji} - n_i\dot{P}_{ij}) = 0. \tag{2.124}$$

If we limit the total number of levels to $i_{\max}$, then only $i_{\max} - 1$ of these equations can be independent (this can easily be seen for the case of only two levels). The extra equation is provided by the conservation of the total number of molecules per unit volume, $n_{\rm tot}$, i.e.

$$\sum_i n_i = n_{\rm tot}. \tag{2.125}$$

Equations (2.124) and (2.125) may be expressed as a single matrix equation. Let the matrix M_{ij} be defined such that

$$M_{ii}(i < i_{\max}) = -\sum_{j \neq i} \dot{P}_{ij}, \tag{2.126}$$

$$M_{ij}(i < i_{\max}; j \neq i) = \dot{P}_{ji}, \tag{2.127}$$

$$M_{ij}(i = i_{\max}) = 1, \tag{2.128}$$

and define the vector y_i such that $y_i = 0$ for $i < i_{\max}$ and $y_i = n_{\rm tot}$ for $i = i_{\max}$. Equations (2.124) and (2.125) are then equivalent to the matrix equation

$$y_i = \sum_j M_{ij} n_j. \tag{2.129}$$

$$\tag{2.130}$$

The matrix M_{ij} may be inverted using standard techniques, and the solution for the equilibrium level populations is

$$n_i = \sum_j M_{ij}^{-1} y_j. \tag{2.131}$$

2.2.8 Rotational transitions in linear molecules

The preceding theoretical treatment is now applied to a problem of real astrophysical interest. Clouds of molecular gas and dust form a significant component of the interstellar medium. The principal constituent of these clouds is the hydrogen molecule, although many other molecules are found to be present at trace levels. The radiation emitted by the molecules in these clouds as they undergo transitions between their internal energy levels provides an important means by which the physical state and behaviour of the cloud may be studied. The low kinetic temperature of the gas in these clouds (generally below $100K$) restricts the range of molecules and molecular energy

levels which can be involved in spectral line emission. At these temperatures, collisions between molecules are not energetic enough to excite molecular vibrations, and only the rotational energy levels of the molecules are generally accessible. In the case of molecular hydrogen, even the rotational levels are at too high an energy to be accessible from the ground state through collisions. As a result, the rotational energy levels of trace molecules such as CO, CS, HCO^+ and NH_3, among others, contribute most to the line emission from molecular clouds.

The first three molecules in the list given above are linear molecules, whereas ammonia, having one axis of three-fold rotational symmetry, is a symmetric top molecule. We now examine the possible rotational energies for such molecules. The theoretical prototype is the symmetric top– a rigid body which has one axis about which there is a threefold or greater rotational symmetry (the linear molecule may be considered simple special case of the symmetric top). Classically, the rotational energy of a system rigidly rotating with angular velocity ω and angular momentum $\mathbf{J}$ is given by $E_{\rm rot} = \frac{1}{2}\mathbf{J}\cdot\omega$. The vectors $\mathbf{J}$ and ω are related to each other through the moment of inertia tensor I_{ij}, such that

$$\mathrm{J}_i = \sum_{j=1}^{3} I_{ij}\omega_j, \tag{2.132}$$

$$I_{ij} = \sum_{k=1}^{n} m_k x_i(k) x_j(k), \tag{2.133}$$

where i and j are indexes of the three cartesian axes x, y, and z, n is the number of atoms in the molecule, and $x_i(k)$ is the perpendicular distance of the $k^{\rm th}$ atom from axis i. In general, ω and $\mathbf{J}$ are not parallel, and I_{ij} has off-axis components. It is always possible, however, to diagonalise I_{ij} by a rotation of the co-ordinate axes (e.g. Arfken 1985). For a symmetric rotor, this is done by choosing one axis (e.g. the z axis) to coincide with the symmetry axis. We fix the origin at the centre of mass, since any body rotating freely in space must rotate about its centre of mass. The moment of inertia components about the two axes perpendicular to the symmetry axis I_{xx} and I_{yy}, turn out to be equal to one another (Atkins & Friedman 1997). Writing $I_{||} = I_{zz}$ as the moment of inertia about the symmetry axis, and $I_\perp = I_{xx} = I_{yy}$, the expression for the energy becomes

$$
\begin{aligned}
E_{\rm rot} &= \frac{\mathrm{J}_x^2 + \mathrm{J}_y^2}{2I_\perp} + \frac{\mathrm{J}_z^2}{2I_{||}} \\
&= \frac{\mathbf{J}^2}{2I_\perp} + \left(\frac{1}{2I_{||}} - \frac{1}{2I_\perp}\right)\mathrm{J}_z^2, \qquad (2.134)
\end{aligned}
$$

Here $\mathbf{J}^2 = \mathrm{J}_x^2 + \mathrm{J}_y^2 + \mathrm{J}_z^2$, and J_z is the component of angular momentum about the symmetry axis. When this system is treated quantum mechanically, $\mathbf{J}^2$ is replaced by the quantum mechanical angular momentum operator $\hat{\mathrm{J}}^2$, with eigenvalues $\mathrm{J}(\mathrm{J}+1)\hbar^2$, (J is a positive integer or zero). J_z is replaced by $\hat{\mathrm{J}_z}$ and has eigenvalues $\mathrm{K}\hbar$, where K can take on all integral values between -J and +J. The quantum mechanical expression for the energy then becomes (Rohlfs & Wilson 1996),

$$
\begin{aligned}
E_{\rm rot}(\mathrm{J},\mathrm{K}) &= \frac{\hbar^2\mathrm{J}(\mathrm{J}+1)}{2I_\perp} + \left(\frac{1}{2I_{||}} - \frac{1}{2I_\perp}\right)\hbar^2\mathrm{K}^2 \\
&= hB\mathrm{J}(\mathrm{J}+1) + h(A-B)\mathrm{K}^2. \qquad (2.135)
\end{aligned}
$$

In the second expression above the rotational constants $A = \hbar/4\pi I_{||}$ and $B = \hbar/4\pi I_\perp$ have been introduced, and have the dimension of frequency.

In a linear rotor, all the atoms in the rotating system lie along a single straight line axis, which is therefore a rotational symmetry axis. The moment of inertia, $I_{||}$ about this axis is provided only by the extension in space of the atoms themselves, and is much smaller than $I_\perp$. Rotation about this axis would therefore require much higher energies than for a perpendicular axis, and would manifest itself as excited electronic or nuclear states of the individual atoms. Excluding this case from the discussion of molecular rotation, we can take $K = 0$ and $E_{rot}(\mathrm{J}) = hB\mathrm{J}(\mathrm{J}+1)$ for a rigid linear molecule. The degeneracy $g(\mathrm{J})$ of the rotational energy level $E(\mathrm{J})$ is 2J+1, since there are 2J+1 different eigenvalues of the $\hat{\mathrm{J}}_z$ operator (where the z axis is now the *laboratory* z axis) for each value of J; the eigenvalues are $\hbar M_\mathrm{J}$ where M_J runs from -J to +J.

When real molecules rotate, their bond lengths undergo stretching in response to the centrifugal force. This increases the moment of inertia of the molecule, and will decrease the rotational energy for a given angular momentum, compared with an absolutely rigid

rotator. To a first approximation, the expression for the rotational energy is modified by centrifugal stretching to

$$E_{\rm rot}({\rm J}) = hB{\rm J}({\rm J}+1) - hD{\rm J}^2({\rm J}+1)^2, \tag{2.136}$$

where D, the centrifugal stretching constant, depends on the stiffness of the molecular bonds. It is necessarily positive and typically of order 10^{-5} times the magnitude of B. The energy gap between adjacent J levels is given by

$$\Delta E({\rm J} \rightarrow {\rm J}-1) \equiv h\nu_{\rm J}, \tag{2.137}$$

$$\nu_{\rm J} = 2B{\rm J} - 4D{\rm J}^3. \tag{2.138}$$

In the absence of centrifugal stretching, the frequencies of spectral line transitions between adjacent rotational energy levels would be equally spaced with increasing J number of the upper level. The centrifugal stretching term causes the separation in transition frequencies to decrease with increasing J.

The Einstein A and B coefficients for dipole radiative transitions between the rotational states of a linear molecule are given by equations 2.96, 2.97 and 2.98, where S_{ul} is zero except for transitions between adjacent rotational levels, which leads to the selection rule for dipole radiative transitions, $\Delta{\rm J} = \pm 1$. This results from the orthogonality of the angular part of molecular wavefunctions with different J numbers. Writing ${\rm J}_u$ as the J number of the upper level of a transition between adjacent levels, we have $g_u = 2{\rm J}_u + 1$, $g_l = 2{\rm J}_u - 1$. The line strength for transitions between ${\rm J}_u$ and ${\rm J}_u - 1$ is found to be (e.g. Landau & Lifshitz, 1977),

$$S_{ul}({\rm J}_u) = {\rm J}_u d_p^2, \tag{2.139}$$

where d_p is the **permanent dipole moment** of the molecule, the value of which may be obtained experimentally. The Einstein coefficients for dipole radiative transitions between rotational levels J and J$-$1 of a linear molecule are:

$${\rm A}_{ul}({\rm J}) = \frac{8\pi^2 d_p^2}{3\varepsilon_0 c^3 \hbar} \cdot \frac{{\rm J}\nu_{\rm J}^3}{2{\rm J}+1}, \tag{2.140}$$

$$B_{ul}(J) = \frac{2\pi d_p^2}{3\epsilon_0 c\hbar^2} \cdot \frac{J}{2J+1}, \tag{2.141}$$

$$B_{lu}(J) = \frac{2\pi d_p^2}{3\epsilon_0 c\hbar^2} \cdot \frac{J}{2J-1}, \tag{2.142}$$

where ν_J is the transition frequency, given by (2.138). Since $\nu_J \propto J$, to a first approximation, equation 2.140 shows that A_{ul}, the spontaneous transition coefficient, increases roughly as J^3. The critical density, n_{crit} for thermalisation of the upper level, also increases in a similar manner, since by equation 2.117,

$$n_{crit}(J) = \frac{A_{ul}(J)}{\sum_{J'} <\sigma v>_{J,J'}}, \tag{2.143}$$

where $<\sigma v>_{J,J'}$ is the collision rate coefficient for transitions from level J to level J'.

2.3 Numerical Radiative Transfer

The general radiative transfer problem with which the modelling in this thesis is mainly concerned is the following: Consider a cloud of gas with a specified distribution of density, kinetic temperature and composition, which may have internal turbulent and systematic motions. Let any radiation sources not forming part of the cloud itself also be specified. What is the steady state distribution of the rotational energy level populations of a given molecular species in the cloud, and what is the predicted emergent intensity around the frequency of a spectral line transition between two of these levels? The complexity of the problem derives from the fact that well separated parts of the cloud may communicate with each other through the radiation exchanged between them. This means that the solution for a given part of the cloud cannot be found in isolation; the solution for the whole cloud must be arrived at simultaneously. One way in which this can be done is to use a numerical iteration technique, which is described below.

2.3.1 The Λ-iteration method

Of all the techniques for solving complex radiative transfer problems numerically, the Λ-iteration method is conceptually the simplest. The flowchart in Figure 2.2 gives an

outline of the basic procedure.

The method exploits the fact that the run of molecular level populations and the steady state radiation field in the cloud are mutually dependent: the level populations may be substituted into equations 2.70 and 2.71 to find the run of emissivity and opacity in the cloud. The integral form of the equation of transfer (2.25) is then used to find the radiation field in the rest frame at each point in the cloud. The radiation field in turn enters the rate equations (2.124), which may be solved to give the level populations.

The solution for the steady state radiation field in the cloud must produce a run of level populations which, when used to calculate the radiation field, reproduces the original radiation field. This is obviously a necessary condition for self consistency. It is also a sufficient condition, in that any radiation field which satisfies this condition will be a steady state solution. It is conceivable that there may be more than one formal solution for the steady state radiation field in some systems, although we know of no examples of this. The Λ-iteration method will inherently tend to converge on a steady state solution of the radiation field, and in the following it is assumed that any such solution is unique.

The Λ-iteration method begins by assuming an initial radiation field in a more or less arbitrary manner, from which a 'false' run of level populations may be calculated by *assuming* that the steady state rate equations (2.124) hold. The level populations so obtained will generally lead to a different radiation field from that used to calculate the level populations in the first place. On repeating this procedure, however, each time using the new radiation field to calculate a new run of level populations, there is a strong tendency for the radiation field and level populations to converge. After a sufficiently large number of iterations, the fractional difference in the radiation field (or level populations) over the previous iteration will become negligible, and in subsequent iterations no significant further change will take place. Cannon (1983) discusses the convergence properties of Λ-iteration, and describes the method as a kind of simulation

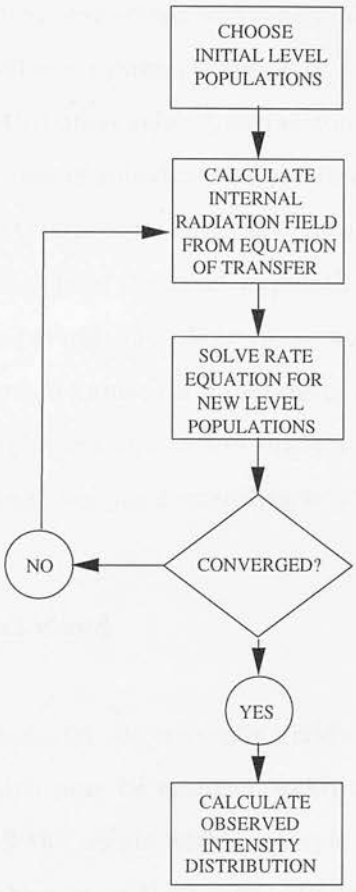

Figure 2.2: Flowchart showing the steps in the Λ-iteration method.

of photon diffusion, each iteration being equated to a successive photon scattering in the cloud. The value of the maximum optical depth in the cloud, to the nearest integer, therefore places a lower limit on the number of iterations required for proper convergence of the model, since in each iteration the photons progress a distance equivalent to an optical depth of approximately unity.

2.3.2 The STENHOLM Λ-iteration code

The modelling in this thesis was carried out using a modified version of the STENHOLM Λ-iteration code developed by Stenholm and expanded by Matthews, Little and Gibb at the University of Kent (Stenholm 1977; Matthews 1986; Heaton et al. 1993). The code uses the method described above to solve the spectral line radiative transfer problem for

the rotational transitions of linear molecules in a spherically symmetric model cloud. Radial profiles of systematic velocity, temperature, density, tracer molecule abundance and micro-turbulent velocity dispersion may be specified. The model cloud is discretised using a number of spherical shells, and the level populations in each shell are determined in the iteration process from the calculated mean radiation intensity in the comoving shell frame. Once the level populations have converged, a calculation is made of a simulated spectral line observation on the cloud. This part of the code carries out straightforward numerical integrations of the equation of transfer along parallel lines of sight through the cloud to find the emergent intensities for a grid of impact parameters, which are then weighted according to a two-dimensional gaussian beam profile function.

The model cloud

Radiative transfer codes usually divide the model cloud into a number of discrete cells, each of which may be assumed uniform in their physical properties throughout their volume. All the points within a single cell should have a similar geometrical relationship with the rest of the model, otherwise the radiation field would not in general be uniform throughout the cell, and we could not treat different points in the cell as being equivalent. Hence a spherically symmetric model can be divided into concentric spherical shells, but if the model has ellipsoidal symmetry, ellipsoidal shells do not suffice since the radiation fields at the pole and the equator of an ellipsoidal shell would not in general be identical. The STENHOLM code assumes spherical symmetry, and divides the model cloud into a number of concentric spherical shells. The parameter i is used to number the shells in order of radius, where $i = 1$ for the innermost shell.

Frequency and solid angle are also divided up into discrete bins. The frequency bins sample the line profile functions of the different rotational transitions of the molecule. It is convenient, however, to work in terms of velocity rather than frequency when making calculations involving the line profile function. If the frequency bins used to discretise the line profile function are centred on the frequencies $\nu(j)$, where bins are numbered consecutively from $j = 1$ to $j = j_{\max}$, then the velocity $\mathrm{v}_z(j)$ may also be

used to describe the frequency bins, where

$$\mathrm{v}_z(j) = c\frac{\nu_0 - \nu(j)}{\nu_0}. \tag{2.144}$$

ν_0 is the line centre frequency of the molecular transition in the molecule rest-frame. The emission in the frequency bin $\nu(j)$ (i.e. in the *velocity* bin $\mathrm{v}_z(j)$), arises from molecules with line of sight velocities (relative to the point under consideration) close to $\mathrm{v}_z(j)$. In a spherically symmetric model, there is azimuthal symmetry about any radial axis, and we use the parameter $\mu(k)$ to specify direction in direction dependent quantities, where k runs from 1 to k_{max}, and $\mu = \cos\theta$, θ being the angle between the specified direction and the outward radial axis (Figure 2.3).

The values of physical quantities such as density, temperature, composition, micro-turbulent velocity width and systematic velocity are specified on the outer boundary of each shell (n.b. the innermost 'shell' is actually a sphere). A uniform external radiation field may be specified, for example the 2.7K microwave background radiation. We write $I_\nu^{\mathrm{ext}}(\mathrm{J})$ for the intensity of the external radiation field at the frequency ν_{J} of the rotational transition J$\rightarrow$ J-1, and this intensity is assumed uniform over the line profile of the transition and over direction. Here and in the following equations, the appearance of J in the argument of a quantity specifies either the rotational level J or the transition J$\rightarrow$J-1, depending on the context.

The Λ-iteration numerical procedure

In order to begin the iteration process, either an initial set of level populations or an initial radiation field within the cloud must be chosen. For convenience we choose to specify the radiation field, or rather, the values of $\bar{J}_\nu$ (equation 2.61) for each molecular transition and in each shell, since these are needed to solve the rate equations (2.124) for the level populations. The final solution arrived at should be independent of the choice of initial radiation field, and this may be used as a test that the code is behaving properly. The speed of convergence may depend on this choice, however. One possible

choice is to set $\bar{J}_\nu$ equal to the microwave background radiation field, i.e.

$$\bar{J}_\nu(i,\mathrm{J}) = B_\nu[\nu_\mathrm{J}, 2.7K], \tag{2.145}$$

where B_ν is the Plank function (2.35) and ν_J is given by (2.138). The rotational quantum number J should not be confused with the average mean intensity $\bar{J}_\nu$. Another possible choice is to set $\bar{J}_\nu$ equal to the Planck function for the local kinetic temperature:

$$\bar{J}_\nu(i,\mathrm{J}) = B_\nu[\nu_\mathrm{J}, T(i)], \tag{2.146}$$

where $T(i)$ is the kinetic temperature on the outer boundary of shell i. This is the most expedient choice when the density and optical depth towards the centre of the cloud is very large, since for densities above the critical density (2.117), the excitation temperature will approach the kinetic temperature, and when the optical depth is very large the radiation field tends to approach the Planck function for the excitation temperature (equations 2.29 and 2.115).

The level populations are found by solving the rate equations using the method described previously (see equations 2.118-2.131). In the context of the present problem, the rate equations may be written as

$$\sum_{\mathrm{J}\neq\mathrm{J}'} [n(i,\mathrm{J})\dot{P}_{\mathrm{J},\mathrm{J}'}(i) - n(i,\mathrm{J}')\dot{P}_{\mathrm{J}',\mathrm{J}}(i)] = 0, \tag{2.147}$$

where the sum is over the rotational quantum numbers J, with J′ fixed, and this equation holds for each value of J′. The $\dot{P}_{\mathrm{J},\mathrm{J}'}$ are the total transition probabilities per unit time per molecule from level J to level J′ in shell i, and may be written as

$$\dot{P}_{\mathrm{J},\mathrm{J}}(i) = 0, \tag{2.148}$$

$$\dot{P}_{\mathrm{J},\mathrm{J}-1}(i) = \mathrm{A}_{ul}(\mathrm{J}) + \mathrm{B}_{ul}(\mathrm{J})\bar{J}_\nu(i,\mathrm{J}) + \mathrm{C}_{\mathrm{J},\mathrm{J}-1}(i), \tag{2.149}$$

$$\dot{P}_{\mathrm{J}-1,\mathrm{J}}(i) = \mathrm{B}_{lu}(\mathrm{J})\bar{J}_\nu(i,\mathrm{J}) + \mathrm{C}_{\mathrm{J}-1,\mathrm{J}}(i), \tag{2.150}$$

$$\dot{P}_{\mathrm{J},\mathrm{J}'}(i) = C_{\mathrm{J},\mathrm{J}'}(i); \qquad |\mathrm{J}-\mathrm{J}'| \geq 2. \tag{2.151}$$

The explicit expressions for the Einstein A and B coefficients are given in equations 2.140, 2.141 and 2.142. The collision rate term, $\mathrm{C}_{\mathrm{J},\mathrm{J}'}(i)$ may be written as

$$\mathrm{C}_{\mathrm{J},\mathrm{J}'} = n_{\mathrm{H}_2}(i)<\sigma\mathrm{v}>_{\mathrm{J},\mathrm{J}'}[T(i)]f_{\mathrm{He}} \tag{2.152}$$

where $n_{H_2}(i)$ and $T(i)$ are respectively the molecular hydrogen number density and kinetic temperature at the boundary of shell i. $<\sigma v>_{J,J'}[T(i)]$ is the the rate coefficient for the transition J→J′ due to collisions with hydrogen molecules with a Maxwellian distribution of velocities for the kinetic temperature $T(i)$. $f_{He} \simeq 1.03$ is a factor slightly larger than unity, which corrects for the contribution of Helium collisions to the collisional transition rate. The collision rates are usually only known for a limited number of the lowest rotational levels of the molecule. This is only a problem if the kinetic temperature is high enough to significantly populate the levels above the highest rotational level for which the collision rates are known. The observations and modelling in this thesis concentrate on the transitions of the CS and HCO^+ molecules. We used the H_2-CS rate coefficients for the first 21 rotational levels of CS and for kinetic temperatures between 5K and 300K (Green & Chapman 1978; Turner et al. 1992). HCO^+ collision rates for the first 11 levels, between 5 and 250K were collated from various sources (Monteiro 1985; Turner et al. 1992; L. Little 1995, private communication; E. Gregerson, 1997, private communication). The rate coefficients are listed for a number of different temperatures spanning the ranges just mentioned. The rates for temperatures lying between two of these temperatures are calculated by linear interpolation.

Conservation of the total number of tracer molecules provides an additional constraint which allows the rate equations to be solved for the level populations:

$$\sum_{J} n(i, J) = X(i) n_{H_2}(i) \tag{2.153}$$

where $X(i)$ is the fractional abundance of the tracer molecule relative to hydrogen molecules at the boundary of shell i.

Once the level populations have been calculated for each shell, the radiation field resulting from them may be found. The following expression (cf. 2.25) is used to calculate the intensity in the shell i_0, from the direction $\mu(k)$, in the rotational transition J→J−1, in the velocity bin $v_z(j)$:

$$I_\nu(i_0, j, k, J) = I_\nu^{ext}(J) e^{-\tau_\nu(i_0, m_{max}, j, k, J)}$$

$$+ \sum_{m=1}^{m_{\max}} \langle \varepsilon(i_0, m, j, k, \mathrm{J}) e^{-\tau_\nu(i_0,m,j,k,\mathrm{J})} \rangle_m [z(m) - z(m-1)]. \qquad (2.154)$$

In the expression above and in the following, triangular brackets means that the average value of the quantity in the brackets over consecutive values of the parameter in the subscript should be taken, for example $\langle X(m) \rangle_m \equiv \frac{1}{2}[X(m) + X(m-1)]$.

The explicit expressions for the optical depth, τ_ν, and emissivity, ε, as used in equation 2.154 are given below. The first term on the right hand side is the contribution of the external radiation field to the intensity. The second term calculates the contribution of the emission from the gas along the beam path. The beam path is divided into segments which extend between adjacent intersections of the path with the shell boundaries. Only the segments along the beam path upstream of the beam direction from i_0 are included in the sum. If the step in optical depth or systematic velocity across a segment is too large then the segment is divided further into subsegments, and values of the physical parameters intermediate between the values at the shell intersections are assigned to the subshell boundaries. This is discussed further in the section below on modifications to the code. The number of subsegments is chosen such that the optical depth across an individual subsegment is no greater than around 0.2, and the systematic velocity step across the subsegment is no greater than around 0.2 times the velocity dispersion of the shell. This is necessary for the accurate numerical integration of the equation of transfer. In the following, it is assumed for simplicity of notation that the shells are numerous enough that no subdivision of beam path segments is required.

The index m labels the shell intersections in increasing numerical order backwards along the beam from from $m = 0$ at the 'root' position on shell i_0, to $m = m_{\max}$ at the position where the beam first intersects the outer boundary of the model (Figure 2.3). The distance of the m'th intersection from the root position is denoted by $z(m)$. The symbol i_m is used to keep track of the shell boundary which is crossed at the m'th intersection (i_0 denotes the root shell by definition, and $i_{m_{\max}}$ is the outer shell of the model).

The term $\varepsilon(i_0, m, j, k, \mathrm{J})$ in equation 2.154 is the emissivity of the gas at the m'th shell intersection of the line of sight in the direction $\mu(k)$, in the velocity bin $\mathrm{v}_z(j)$ in the transition J→J−1, *as seen from the position and velocity frame of the gas at the root position on shell* i_0. The explicit expression for ε is (cf. 2.70)

$$\varepsilon(i_0, m, j, k, \mathrm{J}) = \frac{h\nu_\mathrm{J}}{4\pi} \mathrm{A}_{ul}(\mathrm{J}) n(i_m, \mathrm{J}) \phi(i_0, m, j, k, \mathrm{J}), \tag{2.155}$$

where $n(i, \mathrm{J})$ represents the number density of molecules in the rotational level J, at the outer boundary of shell i. The expression for $\phi(i_0, m, j, k, \mathrm{J})$, the line profile function, is adapted from equation 2.91:

$$\phi(i_0, m, j, k, \mathrm{J}) = \frac{c}{\sigma_{\mathrm{tot}}(i_m)\nu_\mathrm{J}\sqrt{2\pi}} \exp\left(-\frac{[\mathrm{v}_z(j) - \mathrm{v}_z^{\mathrm{rec}}(i_0, m, k)]^2}{2\sigma_{\mathrm{tot}}(i_m)^2}\right), \tag{2.156}$$

$\sigma_{\mathrm{tot}}(i_m)$ is the total velocity dispersion in shell i_m, after combining the thermal and turbulent velocity distributions:

$$\sigma_{\mathrm{tot}}(i_m)^2 = \sigma_{\mathrm{th}}(i_m)^2 + \sigma_{\mathrm{tb}}(i_m)^2. \tag{2.157}$$

The recession velocity $\mathrm{v}_z^{\mathrm{rec}}$ of the gas at the m'th intersection relative to the gas at the root position, is given by

$$\mathrm{v}_z^{\mathrm{rec}}(i_0, m, k) = \mu(k, m)v(i_m) - \mu(k, 0)v(i_0), \tag{2.158}$$

where $\mu(k, m)$ is the cosine of the angle between the line of sight k from the root position on shell i_0, and the outward radial direction at the m'th shell intersection of that line of sight (Figure 2.4). $\mu(k, 0)$, referred to previously as simply $\mu(k)$, is the cosine of the angle between the line of sight and the outward radial direction at the root position, and $\mathrm{v}(i)$ is the outward radial velocity on shell i (cf 2.90).

Similarly $\tau_\nu(i_0, m, j, k, \mathrm{J})$ is the optical depth at the frequency corresponding to $\mathrm{v}_z(j)$, of the gas at the m'th shell boundary intersection along the line of sight in the direction $\mu(k)$, as viewed from a reference position on shell i_0, in a velocity frame comoving with the shell at the reference position. Adapting equation 2.23, we find

$$\tau_\nu(i_0, m, j, k, \mathrm{J}) = \sum_{m'=1}^{m} \langle \kappa(i_0, m', j, k, \mathrm{J}) \rangle_m \Delta z(m'), \tag{2.159}$$

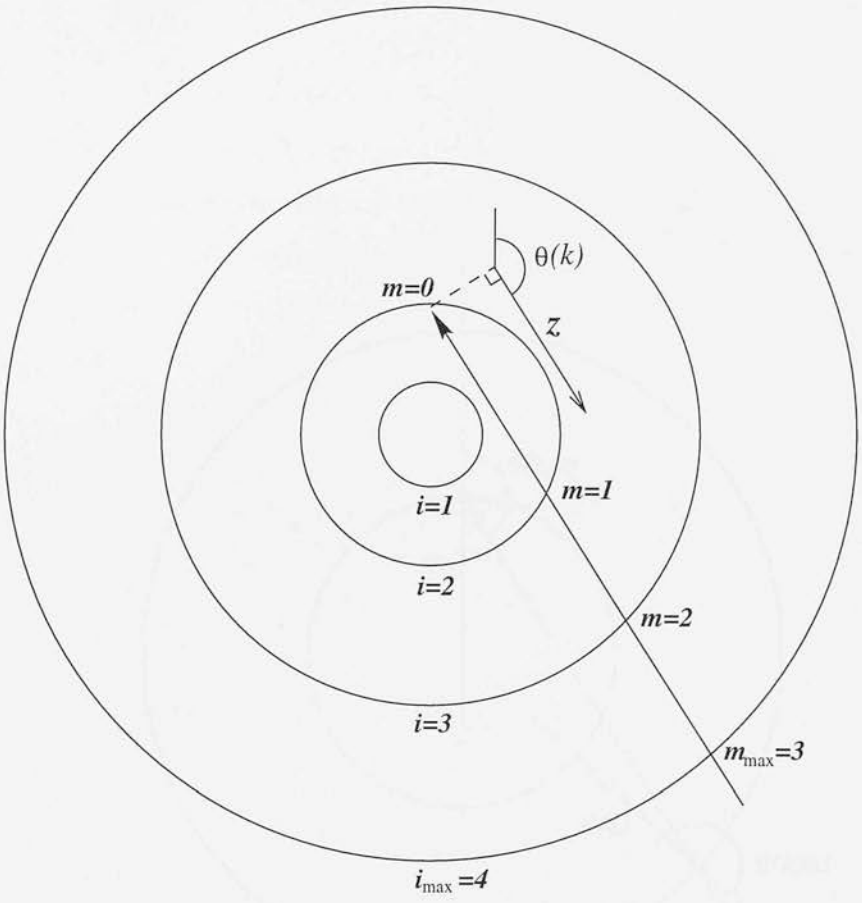

Figure 2.3: Diagram illustrating the notation scheme in equation 2.154. The beam path is shown by the long arrow, which terminates at the point at which the intensity is to be calculated (which we call the *root*). The points of intersection of the beam and shell boundaries are labelled by m, where $m = 0$ at the root position and increases by one each time a shell boundary is encountered moving backwards along the beam path from the root. The shell numbers i increase outwards from the centre, and the i_m have the following dependence on m: $i_0 = 2; i_1 = 2; i_2 = 3$, and $i_3 = i_{\max} = 4$. z measures the distance back along the beam path from the root position. The direction parameter μ and the angle θ (which is the angle between the outward radial direction at the root and the negative beam direction) are related by $\mu(k) = \cos\theta(k)$.

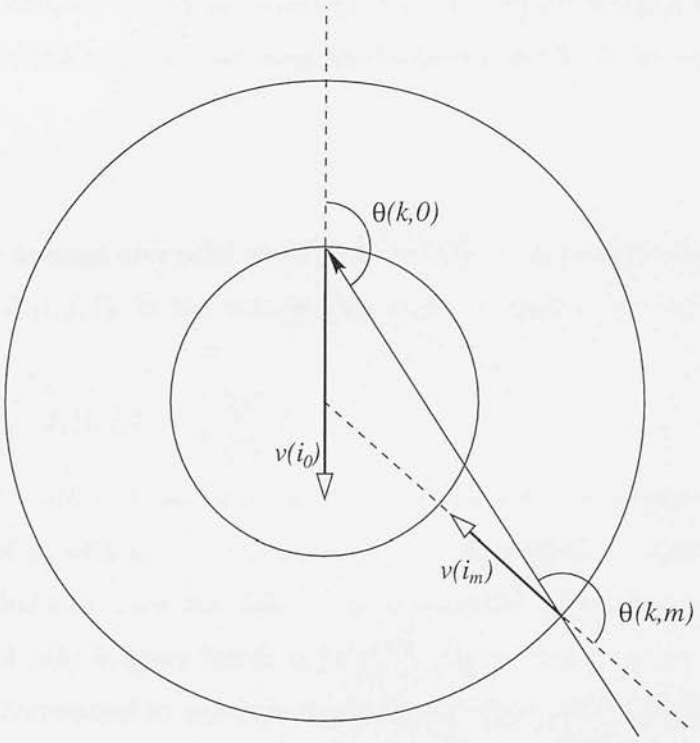

Figure 2.4: Geometry used in the calculation of v_z^{rec}, the line of sight relative velocity component (equation 2.158), where $\mu(k,0) = \cos[\theta(k,0)]$ and $\mu(k,m) = \cos[\theta(k,m)]$. Systematic velocities in the outward radial direction are positive by convention, and the velocities $v(i_0)$ and $v(i_m)$ in the diagram have negative magnitude.

where $\Delta z(m') = z(m') - z(m'-1)$, and from equation 2.71,

$$\kappa(i_0, m', j, k, \mathrm{J}) = \frac{h\nu_\mathrm{J}}{4\pi}[\mathrm{B}_{lu}(\mathrm{J})n(i, \mathrm{J}-1) - \mathrm{B}_{ul}(\mathrm{J})n(i, \mathrm{J})]\,\phi(i_0, m', j, k, \mathrm{J}). \qquad (2.160)$$

As mentioned above, the radiation field enters the rate equations (2.123) through the line-profile-averaged mean intensities $\bar{J}_\nu$ at each transition frequency (2.61). The value of $\bar{J}_\nu$ for a particular transition J and shell i, may be found using a discretised version of equation 2.61, by evaluating equation 2.154 for a grid of beam directions, $\mu(k)$, and a grid of velocities, $\mathrm{v}_z(j)$, sampling the frequency profile of the transition in the shell i.

Carrying out the average over solid angle first, we find the following expression for the mean intensity $J_\nu(i, j, \mathrm{J})$, in the velocity bin $\mathrm{v}_z(j)$, in shell i, for the transition J→J−1 (cf 2.6):

$$J_\nu(i, j, \mathrm{J}) = \frac{1}{2}\sum_{k=2}^{k_\mathrm{max}} \langle I_\nu(i, j, k, \mathrm{J})\rangle_k \,\Delta\mu(k), \qquad (2.161)$$

where $\Delta\mu(k) = \mu(k) - \mu(k-1)$, and it is assumed that the $\mu(k)$ are arranged in order of increasing value of μ, with $\mu_1 = -1$ and $\mu_{k_\mathrm{max}} = 1$. Since there is azimuthal symmetry about the radial axis, then the solid angle $\Delta\Omega$ covered by the beam directions between $\mu(k-1)$ and $\mu(k)$ is given by$\Delta\Omega = 2\pi\int_{\mu(k-1)}^{\mu(k)} d\mu = 2\pi[\mu(k) - \mu(k-1)]$, and equal intervals of μ correspond to equal intervals of solid angle. At least five different direction angles from the radial axis are normally used to sample the solid angle.

$\bar{J}_\nu$, the average of J_ν over the line profile function, is evaluated as follows (cf. 2.60):

$$\bar{J}_\nu(i, \mathrm{J}) = \sum_{j=2}^{j_\mathrm{max}} \langle J_\nu(i, j, \mathrm{J})\phi_0(i, j, \mathrm{J})\rangle_j \frac{\nu_\mathrm{J}}{c}\,\Delta\mathrm{v}_z(j), \qquad (2.162)$$

where $\Delta\mathrm{v}_z(j) = \mathrm{v}_z(j) - \mathrm{v}_z(j-1)$. $\phi_0(i, j, \mathrm{J})$ represents the intrinsic, rest-frame line profile function for the transition J in shell i (equivalent to setting $m = \mathrm{v}_z^\mathrm{rec} = 0$ in equation 2.156), and we have used the relation

$$\nu(j-1) - \nu(j) \equiv \Delta\nu(j) = \frac{\nu_\mathrm{J}}{c}\Delta\mathrm{v}_z(j), \qquad (2.163)$$

which follows from equation 2.144. In equation (2.162) it is assumed that the $v_z(j)$ are in increasing order of magnitude. The $v_z(j)$ should span the velocity profile at least $3\sigma_{\rm tot}(i)$ into the wings, to provide adequate sampling of the line profile function.

At the start of the numerical procedure, an initial set of $\bar{J}_\nu(i,{\rm J})$ were assumed. Using these, we have progressed to the point where a new set of $\bar{J}_\nu(i,{\rm J})$ are calculated. The whole process may then be repeated, until the model has converged to the point where no further change will take place in the subsequent iterations.

Testing for convergence

It is important to find a reliable test for the convergence of the model. One possible condition is that the maximum fractional change $\eta(i,j)_N$, of the level population $n(i,{\rm J})$ between iterations $N-1$ and N, is less than some specified value α, for all i and J, i.e.

$$\eta(i,{\rm J})_N = \frac{n(i,{\rm J})_N - n(i,{\rm J})_{N-1}}{n(i,{\rm J})_N} < \alpha, \tag{2.164}$$

for all i and J, where the subscripts specify the iteration numbers. In many cases, the value of $\eta(i,{\rm J})$ is a good estimate of the absolute fractional error in the corresponding level population, in which case convergence is ensured by setting a suitably low value of α (a value of 0.02 or less is usually found to be sufficient). When the rate of convergence is particularly slow, however, this test may give a misleading result, since the fractional change between two successive iterations may then significantly underestimate the total change produced over a large number of subsequent iterations. In terms of η, this argument may be expressed as follows: if $\eta(i,{\rm J})_N$ decreases only very slowly with N, then $\eta(i,{\rm J})_N$ will be a poor estimate of the total fractional change in the level population $n(i,{\rm J})$ between the N'th iteration and the fully converged model. The *rate* of decrease of η should somehow be taken into account.

Dickel & Auer (1994) use the following procedure to estimate the *total* fractional

error $\eta_{\rm tot}(i,{\rm J})_N$ of the level population $n(i,{\rm J})$ after the N'th iteration:

$$\eta_{\rm tot}(i,{\rm J})_N \simeq \left| \frac{\eta(i,{\rm J})_N}{[\eta(i,{\rm J})_N/\eta(i,{\rm J})_{N-1}] - 1} \right|. \qquad (2.165)$$

The convergence criterion is then $\eta_{\rm tot}(i,{\rm J}) < \alpha$ for all i and J, for some specified α much less than 1. Note that if $\eta(i,{\rm J})_N \simeq \eta(i,{\rm J})_{N-1}$ then $\eta_{\rm tot}(i,{\rm J})_N$ is much larger than $\eta(i,{\rm J})_N$, i.e. the total error is much larger than the fractional change between successive iterations.

The rate of convergence is fastest when the optical depth of the cloud is small, or when the hydrogen number density is much greater than the critical thermalisation density. When the optical depth is small, radiation can travel across the whole cloud in one iteration, allowing the level populations in different parts of the cloud to adjust to each other quickly. When the density is close to or above the critical density for the principal thermally accessible transitions of the molecule, the level populations are determined mainly by molecular collisions, and are insensitive to changes in the radiation field.

For optically thick regions where the density is below the critical density, the convergence rate is generally much slower. The low density results in low collision rates, and the level populations therefore depend more sensitively on the radiation field. The high optical depth, however, means that the radiation field will take many iterations to adjust to the conditions in distant parts of the cloud.

Figure 2.5 shows plots of the rate of convergence of the CS level populations for four similar model clouds. The models differ only in their hydrogen densities and CS abundances. In model (a) the hydrogen density is a factor of 100 greater than in model (b), such that model (a) has a density about equal to the critical density of the lower rotational transitions of CS, and model (b) has a density well below the critical density. The absolute CS number density is the same for both models, however, and is large enough to give both clouds an optical depth of at least 15 at the frequencies of the lower rotational transitions. The convergence rate of model (b) is significantly slower than

model (a), since the level populations in model (b) are sensitive to the radiation field, which takes many iterations to relax to the conditions in different parts of the cloud, as a result of the high optical depth. In model (b) the level populations are close to thermal, and are less sensitive to the radiation field. Models (c) and (d) use the same parameters as models (a) and (b) respectively, except that the CS abundances have been reduced by a factor of ten, whilst keeping the hydrogen number densities constant. The resulting reduction in the optical depth of the cloud significantly increases the rate of convergence in both models, since the relaxation time of the radiation field is decreased. In summary, the plots in Figure 2.5 (a), (b), (c) and (d) illustrate the relative convergence rate in the regimes of, respectively, high optical depth and high density; high optical depth and low density; low optical depth and high density; and low optical depth and low density.

Simulation of a telescope spectral line observation

Once the model has converged, a simulated observation on the model with a gaussian telescope beam is performed. Before describing this section of the code, a brief outline is given of the way in which submillimetre spectral line observations are carried out and calibrated. This is discussed in more detail in chapter 3.

The intensity scale in submillimetre spectral line observations is usually calibrated by presenting the line receivers with two extended uniform radiation sources of known intensities, and using the two measured signals to define a linear scale relating the signal measured when pointing at an astronomical source to the average intensity of the source over the telescope beam profile. The actual beam profiles produced by real telescopes are inevitably inferior to the ideal diffraction-limited beam shape, as a result of imperfections in the telescope dish and receiver optics, and obstructions in the light path such as the secondary mirror and support arms. The actual antenna pattern will usually take the form of an extended low-power error beam surrounding a central core which is proportional to the diffraction limited beam (e.g. Richer et al. 1993). The

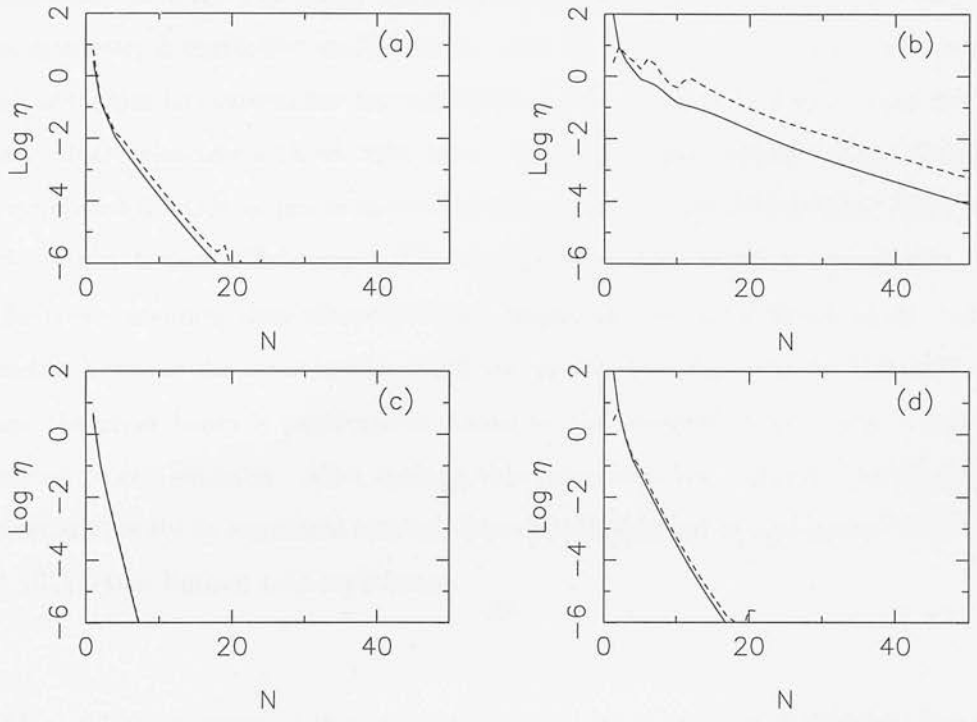

Figure 2.5: Plots showing the rate of convergence of the Λ-iteration method for three different model clouds, solving for the first 12 rotational levels of the CS molecule. The solid line plots the maximum value of $\eta(i,\mathrm{J})_N$ over i and J, where N is the iteration number. The dashed line plots the maximum value of the estimate of the *total* fractional error $\eta_{\mathrm{tot}}(i,\mathrm{J})_N$, at each N. In all three models the physical parameters are constant with radius, and are identical apart from the hydrogen number densities and tracer molecule abundances; the kinetic temperature of each model is 20K, the turbulent velocity width is $1\mathrm{km\,s^{-1}}$ (FWHM), the systematic velocity is zero, and the outer radius is 10,000 au. The initial radiation field in the cloud was set equal to the Planck function for a temperature of 10K. In (a), the hydrogen number density is $10^6\mathrm{cm^{-3}}$ and the CS relative abundance is 10^{-9} (relative to molecular hydrogen). In (b), the hydrogen density has been lowered to $10^4\mathrm{cm^{-3}}$, below the critical density, and the CS relative abundance has been raised by the same factor, to 10^{-7}. The absolute number density of CS is therefore the same in (a) and (b). In (c), the CS abundance has been lowered by a factor of 10, keeping the hydrogen number density the same.

extended beam pattern is extremely difficult to measure accurately, and will generally be non-axisymmetric and highly variable. If the observed source is reasonably compact, however, a corrective scaling factor may be applied to the observed spectrum which attempts to renormalise the spectrum to that which would have been obtained with a 'ideal' telescope with no error beam. The spectrum is usually simply divided by the estimated fraction of power in the diffraction-limited core of the beam (also known as the **main beam efficiency**). This clearly introduces some error, however, since it effectively assumes that the error beam makes no net contribution to the received intensity, however the error involved will not usually be more than around 10% or so, unless the error beam is particularly strong or the observed source is in a region of extended bright emission. After making this correction the observed spectra may be compared directly to simulated spectral line calculations which assume an 'ideal' gaussian, diffraction limited telescope beam.

Most telescope spectral line observations use either sky subtraction or frequency switching to eliminate atmospheric emission from the spectrum. Sky subtraction involves taking a spectrum of a piece of blank sky near to the source, and subtracting it from the spectrum taken on source. In frequency switching, two on-source spectra are shifted relative to each other along the frequency axis, and then subtracted from one another. This eliminates any spectral feature which is broader than the frequency shift. Both sky subtraction and frequency switching techniques inevitably subtract the full microwave background intensity from the on-source spectrum in the process. This is not necessarily balanced by the contribution of the microwave background to the on-source spectrum, because the background radiation will be attenuated by the frequency dependent optical depth of the source, which is largest in the region of any spectral lines. The net contribution of the microwave background to the final spectrum is therefore frequency dependent and will usually be either negative or zero. At submillimetre wavelengths, the correction involved is usually negligible, although it is included in the code.

The simulated telescope spectral line observation is carried out by calculating the emergent intensity from the model cloud (including the attenuated microwave back-

ground radiation from the far side of the cloud) for a number of parallel lines of sight (since the observer is assumed to be distant), which sample different regions of the gaussian, diffraction-limited telescope beam. After subtraction of the microwave background intensity, the intensities are multiplied by a weighting factor given by the beam profile function. The STENHOLM code uses a uniformly spaced grid of line of sight impact parameters to sample the gaussian beam profile. If the grid were not uniformly spaced, an additional weighting factor proportional to the solid angle sampled by each line of sight would need to be applied.

We use the co-ordinates (x, y) to specify position in the plane of the sky at the distance of the cloud, where the centre of the spherical model cloud is located at (0,0). Let (x_0, y_0), be the point on this plane at which the telescope beam is pointed, and let the positions of the lines of sight used to sample the telescope beam be at (x_l, y_l), where l is an index for the different lines of sight. Writing $\overline{I_\nu^{\rm obs}}(j, {\rm J})$ for the average intensity from the cloud over the beam profile function, at the velocity ${\rm v}_z(j)$ in the observers velocity frame, and in the spectral line transition ${\rm J} \rightarrow {\rm J}-1$, we have

$$\overline{I_\nu^{\rm obs}}(j, {\rm J}) = \frac{\sum_l w(l)\,[I_\nu(i_{\rm max}, j', k_l, {\rm J}) - B_\nu(\nu_{\rm J}, 2.7K)]}{\sum_l w(l)}, \qquad (2.166)$$

$$w(l) = \exp\left[-\frac{(x_l - x_0)^2 + (y_l - y_0)^2}{D^2_{\rm FWHM}/4\ln 2}\right], \qquad (2.167)$$

where $w(l)$ is the weighting factor applied to line of sight l and $D_{\rm FWHM}$ is the projected size of the FWHM beamwidth at the distance of the cloud. $I_\nu(i_{\rm max}, j', k_l, {\rm J})$ is the intensity emerging from the cloud along the l'th line of sight, in the frame of motion of the gas at the point where the line of sight first enters the model (i.e. *not* in the frame of the observer). The reason for calculating the intensity in this velocity frame is that equation 2.154 may then be used directly to integrate the equation of transfer along the line of sight through the cloud. The intensity in the velocity bin ${\rm v}_z(j')$ in this frame may then be assigned to the velocity bin ${\rm v}_z(j)$ in the observers frame, where

$${\rm v}_z(j) = {\rm v}_z(j') + v(i_{\rm max})\mu(k_l, 0). \qquad (2.168)$$

${\rm v}(i_{\rm max})$ is the outward radial velocity of the outer shell of the model, and $\mu(k_l, 0)$ is the cosine of the angle between the l'th line of sight and the outward radial direction

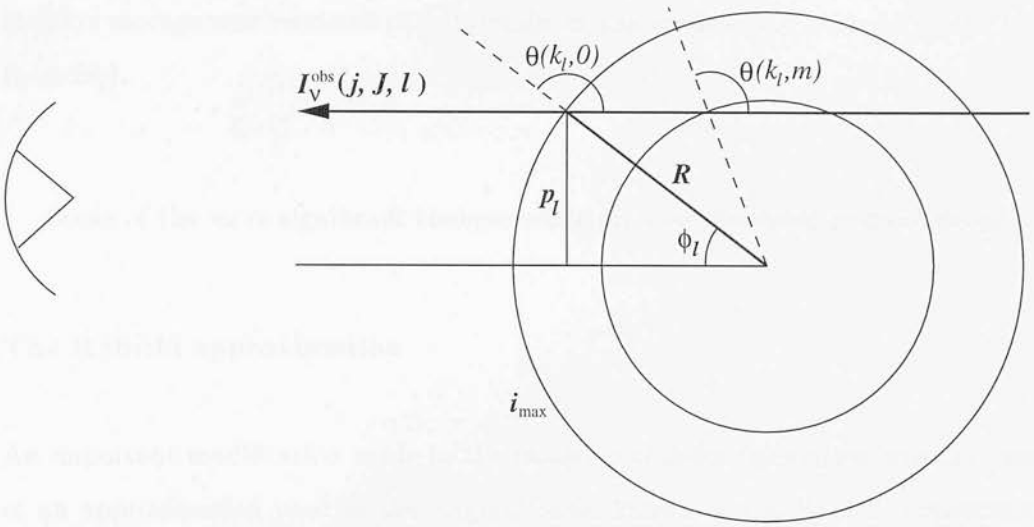

Figure 2.6: Geometry for the telescope observation calculation, showing the first and m'th intersections of the line of sight l with the shells in the model cloud.

at the point where the line of sight enters the model. Referring to Figure 2.6, we find that $\mu(k_l, 0) = \cos\theta(k_l, 0) = -\cos\phi_l = -\sqrt{1 - p_l^2/R^2}$, where $p_l^2 = x_l^2 + y_l^2$.

Once equation 2.166 has been evaluated, the beam averaged intensity $\overline{I_\nu^{\rm obs}}$ is converted to the main beam radiation temperature scale $T_{\rm mb}$, using the relation

$$T_{\rm mb}(j, \mathrm{J}) = \frac{c^2}{2k\nu_{\rm J}^2}\overline{I_\nu^{\rm obs}}(j, \mathrm{J}). \tag{2.169}$$

The plot of $T_{\rm mb}(j, \mathrm{J})$ against $\mathrm{v}_z(j)$ may then be directly compared with an actual observed spectrum to which the main beam correction has been applied (see above).

2.3.3 New additions to the code

We have made several improvements to the code since it was made available in September 1995. These have included changes to the internal structure of the code (e.g. modularising frequently used operations, such as integration of the equation of transfer along a beam; improving the shell subdivision algorithm; incorporating rotation into the line profile calculation) and improvements to the input and output interfaces (e.g. presentation of results using PGPLOT; a fully interactive user interface; the ability to examine a range of different cross-sections through the simulated data-cubes; help

facility; storage and retrieval of full details of the models and their solutions to and from file).

Some of the more significant changes made are now discussed in more detail.

The Rybicki approximation

An important modification made to the radiative transfer calculation was the removal of an approximation used in the original code, known as the Rybicki approximation (Rybicki 1972; Stenholm 1977; Rybicki 1984) which may be summarised as follows: suppose that at some point in the cloud the following relation is satisfied for all directions, $\hat{\Omega}$:

$$\tau_\nu(\mathbf{r}_0, z_b, \nu, \hat{\Omega}) > \gamma, \tag{2.170}$$

where z_b is the distance to the boundary of the model and γ is some prescribed constant. The intensity in all directions at that point is defined in the Rybicki approximation to be equal to the local source function, i.e.

$$I_\nu(\mathbf{r}_0, \nu) = S_\nu(\mathbf{r}_0, \nu). \tag{2.171}$$

Equation 2.171 is only applied for the particular values of ν for which 2.170 is valid. For increasing values of γ, the volume of the cloud to which the approximation applies becomes smaller, and disappears altogether when γ increases beyond the maximum optical depth of the cloud. The motivation behind the Rybicki approximation is that, as demonstrated above, regions of particularly high optical depth in the model cloud can slow down convergence of the Λ-iteration method significantly, and it would be useful if the level populations of these regions could be assigned independently of the radiative transfer calculation. Equation 2.29 shows that in a region of high optical depth where the source function is approximately uniform over a distance of one or two optical depths, then the radiation field is expected to approximate to the local source function, as assumed by the Rybiki approximation. Unfortunately, for the problems we will later consider, which involve strong spatial gradients in velocity, temperature

and density, the source function cannot be assumed to be uniform over distances corresponding to a few optical depths, and the Rybicki approximation cannot be used. We therefore do not use the Rybicki approximation in the modelling of this thesis.

Solid body rotation

In this context 'solid body' means that the angular velocity of all points in the cloud about some fixed axis is a constant; systematic radial motions in the rotating frame are still allowed. The radiative transfer effects of solid body rotation were fully accounted for by changes to the section of the code which calculates the emergent line profile from the cloud, after the Λ-iteration solution has been found. No change needs to be made to the Λ-iteration code itself, since the solution for the level populations in the cloud does not change when solid body rotation is introduced, as is now explained.

The radiation field in a frame comoving with the gas at a given point in the model can only be affected by a superimposed velocity field if the latter introduces changes in the relative *line of sight* velocities of other parts of the cloud (ignoring relativistic effects of order v^2/c^2 or less). This follows from equation 2.156. Solid body rotation, however, does not introduce changes in relative line of sight velocities from one part of the cloud to another. For example, consider a non-rotating cloud which has systematic radial velocities $\mathrm{v_r}(\mathbf{r_1})$ and $\mathrm{v_r}(\mathbf{r_2})$ at the positions $\mathbf{r_1}$ and $\mathbf{r_2}$ respectively. Writing $r_{12} = \mid \mathbf{r_2} - \mathbf{r_1} \mid$ for the distance separating the two points, the component of relative velocity, $\mathrm{v_{los}}$, along the line of sight between $\mathbf{r_1}$ and $\mathbf{r_2}$ is given by

$$\mathrm{v_{los}} = (\mathbf{r_2} - \mathbf{r_1}) \cdot [\mathrm{v_r}(\mathbf{r_2}) - \mathrm{v_r}(\mathbf{r_1})]/r_{12}. \tag{2.172}$$

Now assume the cloud is made to rotate in solid-body fashion with angular velocity $\mathbf{\Omega}$. Let the new systematic velocities at positions $\mathbf{r_1}$ and $\mathbf{r_2}$ be $\mathbf{v}(\mathbf{r_1})$ and $\mathbf{v}(\mathbf{r_2})$, where

$$\mathbf{v}(\mathbf{r_1}) = \mathrm{v_r}(\mathbf{r_1}) + \mathbf{\Omega} \times \mathbf{r_1}, \tag{2.173}$$

$$\mathbf{v}(\mathbf{r_2}) = \mathrm{v_r}(\mathbf{r_2}) + \mathbf{\Omega} \times \mathbf{r_2}. \tag{2.174}$$

The expression for v_{los} then becomes

$$v_{los} = (\mathbf{r_2}-\mathbf{r_1}) \cdot [\mathbf{v}(\mathbf{r_2})-\mathbf{v}(\mathbf{r_1})]/r_{12} \quad (2.175)$$

$$= (\mathbf{r_2}-\mathbf{r_1}) \cdot [v_r(\mathbf{r_2})-v_r(\mathbf{r_1})]/r_{12} + (\mathbf{r_2}-\mathbf{r_1}) \cdot [\mathbf{\Omega} \times (\mathbf{r_2}-\mathbf{r_1})]/r_{12} \quad (2.176)$$

$$= (\mathbf{r_2}-\mathbf{r_1}) \cdot [v_r(\mathbf{r_2})-v_r(\mathbf{r_1})]/r_{12}. \quad (2.177)$$

The final expression above is identical with equation 2.172, which means that the solid body rotation makes no difference to the relative line of sight velocities between any two points in the cloud. This further implies that the radiation field in the comoving frame at each point in the cloud is not affected by solid body rotation. Note that this result only applies to the radiation emitted by the cloud itself. Radiation entering the model from outside will be Doppler shifted in the gas frame by the rotation, but the effect of this will usually be completely negligible, especially if the external radiation has a very broad frequency dependence (e.g. the microwave background radiation). Also it is important to emphasize that if the rotation is not solid body, and the angular velocity varies with position in the cloud, then the result above no longer holds. A significant modification of the structure of the code would be required to treat this problem exactly, since the assumption of spherical symmetry could no longer be used.

Since the level populations at a given point in the cloud are determined by the radiation field at that point and the local physical conditions of the gas, it follows from the discussion above that solid body rotation does not affect the solution for the distribution of rotational level populations in the cloud. Solid body rotation does make a difference, however, to the prediction for the observed line profile, since the rotation does introduce changes in the line of sight velocities of different parts of the cloud *relative to an observer outside the cloud.* If $\hat{\mathbf{z}}$ is the unit vector parallel to the line of sight from the observer to the cloud, and $v_z(\mathbf{r})$ is the line of sight velocity (relative to the observer) of the gas at the position vector $\mathbf{r}$ (relative to the centre of the cloud), then

$$v_z(\mathbf{r}) = \hat{\mathbf{z}} \cdot v_r(\mathbf{r}) + \hat{\mathbf{z}} \cdot (\mathbf{\Omega} \times \mathbf{r}), \quad (2.178)$$

$$= v_{r,z}(\mathbf{r}) + y\Omega_x - x\Omega_y, , \quad (2.179)$$

where $v_{r,z}(\mathbf{r})$ is the component along the line of sight of the radial component of the gas velocity at $\mathbf{r}$, and x and y are, as before, spatial co-ordinates in the plane perpendicular to the line of sight at the distance of the cloud. Ω_x and Ω_y are the components of the angular velocity vector in this plane. Since the rotational terms on the right hand side of (2.179) depend on x and y but not z, the contribution of the rotation to the line of sight velocity relative to the observer is constant along any given line of sight through the cloud. The component of angular velocity parallel to the line of sight, Ω_z, does not appear in (2.179) and has no effect on the emergent spectrum from the cloud.

The effect of rotation on the predicted spectral line calculation may therefore be accommodated by rewriting equation 2.168 as

$$v_z(j) = v_z(j') + v(i_{\max})\mu(k_l, 0) + y_l\Omega_x - x_l\Omega_y, \tag{2.180}$$

i.e. we simply need to make a change to the velocity shift which is applied to bring the emergent intensities along each line of sight into the observers velocity frame. Apart from this velocity shift, the integral of the equation of transfer along each line of sight is not affected by the rotation.

Improvements to the equation of transfer integral calculation

In the original code, all the relative line of sight distances and velocities between the different shells required for the radiative transfer calculation were calculated and stored in arrays, in advance of carrying out the calculation. In the new treatment given to the equation of transfer integral calculation, the beam integral routine has been placed in an external subroutine called by the main program every time integration of the equation of transfer along a line of sight is required. This eliminated the repetition of large blocks of almost identical code which appeared in the original program, improving the structure of the code. The geometrical calculations are now performed as they are needed, eliminating the need for large arrays to store all the geometrical information in advance.

An improvement to the accuracy of the beam integration routine was made by

changing the way the values of physical parameters are assigned to the subshell boundaries when the beam path between two shell intersections is subdivided. Instead of interpolating along beam path between the values at the two shell intersections, as was done in the original code, the code now uses the radial co-ordinate *relative to the centre of the cloud*, to assign the values at each subshell boundary (interpolating along the *radial* direction where necessary). This gives a much more realistic treatment to beam paths which pass just outside a shell boundary at their point of closest approach to the cloud centre, as is illustrated in Figure 2.7. Consider the line of sight ABC on the diagram shown, which intersects shell 2 at A and C, and passes close to point D on shell 1, but does not intersect it. Now suppose that the code has subdivided beam segment AC, and one of the subshell boundaries lies at B. In the previous treatment, the emissivity and opacity, and line of sight velocity assigned to point B would be the mean of their values at points A and C. The shell 1 parameters would therefore have no bearing on the parameters assigned to point B, despite the fact that shell 1 was the closest shell to point B. In the new treatment, the parameters at B would be assigned by linear interpolation along DBE (i.e. along the *radial* direction) which weights the parameters at B strongly towards their values on shell 1. The new treatment therefore gives a more realistic estimate of the values of physical parameters in-between shell intersections, which should decrease the number of shells required to represent the model cloud properly.

2.3.4 Tests of the model

LTE comparison

Analytical solutions of the equation of transfer are in general unobtainable for all but the simplest of problems. However, in the limit that the level populations are completely thermalised by collisions (i.e. in LTE), the spectral line calculations from the numerical model may be compared directly with analytical predictions.

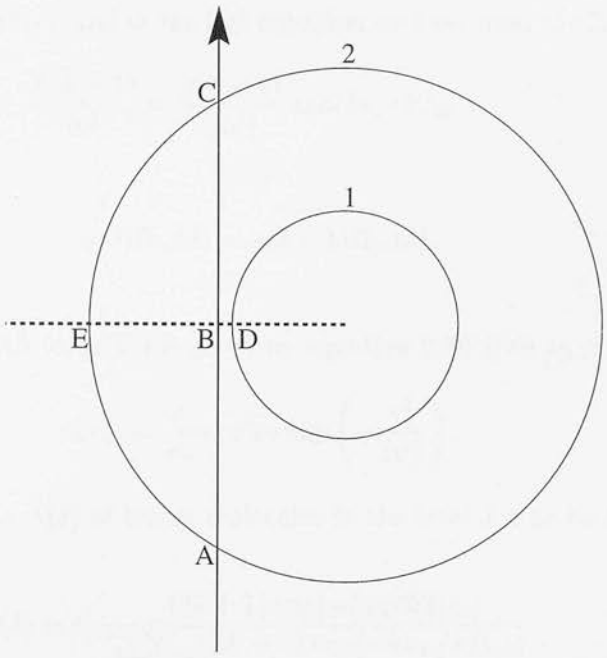

Figure 2.7: Diagram to illustrate the improved scheme for assigning parameters to the subshell boundaries. See text for details.

In LTE, the excitation temperature for each transition approaches the kinetic temperature of the gas, and from (2.75), the source function for the transition J$\rightarrow$ J-1 becomes $S_\nu(\mathbf{r}) = B_\nu[\nu_{\rm J}, T_{\rm kin}(\mathbf{r})]$. If $T_{\rm kin}$ is constant over the cloud, then the solution to the equation of transfer is given by equation 2.28, i.e.

$$I_\nu(\mathrm{v}_z, \mathrm{J}) = I_\nu^{\rm ext}(\mathrm{J}) e^{-\tau_\nu(\mathrm{v}_z)} + B_\nu(\nu_{\rm J}, T_{\rm kin}) \left(1 - e^{-\tau_\nu(\mathrm{v}_z)}\right), \tag{2.181}$$

where $\tau_\nu(\mathrm{v}_z)$ is the optical depth of the cloud at the frequency corresponding to the velocity bin v_z. For simplicity, we consider the intensity emerging from a uniform density isothermal cloud layer of thickness L, with no systematic motions, and with a constant velocity dispersion ($\sigma_{\rm v}$) and total tracer molecule number density ($n_{\rm tot}$). The optical depth through the cloud layer may be written as (cf. equation 2.76)

$$\begin{aligned}
\tau_\nu(\mathrm{v}_z) &= \kappa(\nu) L, & (2.182)\\
&= \frac{h\nu_{\rm J} L}{4\pi} [\mathrm{B}_{lu}(\mathrm{J}) n(\mathrm{J}-1) - \mathrm{B}_{ul}(\mathrm{J}) n(\mathrm{J})] \phi(\mathrm{v}_z), & (2.183)\\
&= \frac{h\nu_{\rm J} L}{4\pi} \mathrm{B}_{ul} n(\mathrm{J}) [\exp(h\nu_{\rm J}/kT_{\rm kin}) - 1] \phi(\mathrm{v}_z), & (2.184)
\end{aligned}$$

where $n(\mathrm{J})$ and $n(\mathrm{J}-1)$ are the number densities of tracer molecules in the upper and

lower level of the transition, and in the last equation we have used the fact that in LTE,

$$\frac{n(\mathrm{J}-1)}{n(\mathrm{J})} = \frac{g(\mathrm{J}-1)}{g(\mathrm{J})} \exp(h\nu_{\mathrm{J}}/kT_{\mathrm{kin}}), \tag{2.185}$$

and also

$$g(\mathrm{J})\mathrm{B}_{ul}(\mathrm{J}) = g(\mathrm{J}-1)\mathrm{B}_{lu}(\mathrm{J}). \tag{2.186}$$

The explicit equation for $\phi(\mathrm{v}_z)$ is given by equation 2.89 with $\nu_0 = \nu_{\mathrm{J}}$:

$$\phi(\mathrm{v}_z) = \frac{c}{\sigma_{\mathrm{v}}}\nu_{\mathrm{J}}\sqrt{2\pi}\exp\left(-\frac{\mathrm{v}_z^2}{2\sigma_{\mathrm{v}}^2}\right), \tag{2.187}$$

and the number density $n(\mathrm{J})$ of tracer molecules in the level J may be evaluated using equation 2.38:

$$n(\mathrm{J}) = n_{\mathrm{tot}}\frac{(2\mathrm{J}+1)\exp(-h\nu_{\mathrm{J}}/kT_{\mathrm{kin}})}{\sum_{\mathrm{J}'=0}^{\infty}(2\mathrm{J}'+1)\exp(-h\nu_{\mathrm{J}'}/kT_{\mathrm{kin}})}. \tag{2.188}$$

The sum in the denominator usually converges rapidly after about ten or so terms (depending on T_{kin}), and can be easily evaluated to the required accuracy.

Substituting these expressions into equation 2.28, with $I_\nu^{\mathrm{ext}}(\mathrm{J}) = B_\nu(\nu_{\mathrm{J}}, 2.73K)$, gives an expression for the predicted intensity as a function of v_z. To compare these predictions with the STENHOLM code, we used a static model cloud with a uniform kinetic temperature, hydrogen number density, velocity dispersion, and abundance. The hydrogen number density was set several orders of magnitude above the critical density to enforce LTE.

Figure 2.8 shows comparisons of the analytical and numerical predictions for the CS(J= 5 $\rightarrow$ 4) line, from LTE models with progressively increasing CS abundance, covering a wide range of cloud optical depths. The excellent agreement between the predicted spectra in all parts of the line, and across the large range of optical depths, is a good indication that the integration of the equation of transfer along the line of sight is being carried out correctly.

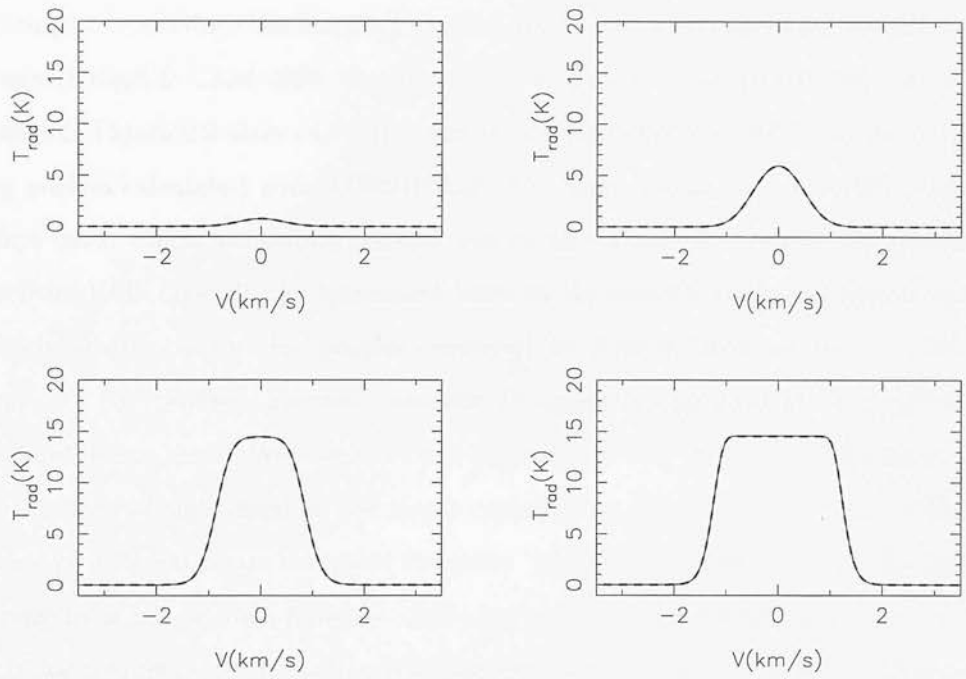

Figure 2.8: Comparison of analytical and numerical predictions of the CS(J= 5 → 4) spectra from four uniform LTE models with progressively increasing CS abundance. The solid and dashed lines show the numerical and analytical predictions respecitively. Each model has a radius of 10,000au, a uniform kinetic temperature of 20K, a uniform hydrogen number density of $10^{10}\mathrm{cm}^{-3}$, and a uniform FWHM velocity width of $1.0\mathrm{km\,s}^{-1}$. The uniform CS number density in the first model is $10^{-5}\mathrm{cm}^{-3}$, and increases by factors of 10 to $10^{-2}\mathrm{cm}^{-3}$ in the last model. The microwave background intensity has been subtracted from both sets of spectra.

Non-LTE comparison

The LTE comparison shown above, while instructive, does not test the ability of the code to carry out non-LTE radiative transfer calculations reliably. We have not found any exact analytical solutions for non-LTE radiative transfer problems in spherical geometry, to compare with the code in a similar manner as shown above. Instead, we attempt to reproduce the line profiles obtained in a previous non-LTE radiative transfer study (Krügel & Chini 1994, hereafter KC), which used a somewhat different numerical method. Figure 2.9 shows a comparison of profiles taken from KC with the corresponding profiles calculated with STENHOLM. The figure caption gives details of the model cloud used, which has strong velocity and density gradients towards the centre, and is far from LTE. Overall, the agreement between the two sets of line profiles is very good. The intensities of the line profiles predicted by STENHOLM are up to 10% weaker than the KC profiles, however, and the disagreement appears to be greatest for the smallest beam sizes. We checked that this was not the result of inadequate sampling of the lines of sight used in the beam convolution, by recalculating the profiles for a range of different beam sampling densities. The small disagreement in the line profile strengths is not serious, however, and may be caused by differences in the spatial, angular or frequency discretisation schemes used in the models, or small differences in the precise values of several of the parameters used. Particularly encouraging is the very good agreement in the *shapes* of the corresponding lines.

2.4 Summary

This chapter has given an overview the physics of non-LTE radiative transfer in submillimetre molecular lines, which underpins the modelling presented later in this thesis. The radiative transfer code which we will use has been described in some detail, including some improvements which we have made to the code. We have highlighted some of the approximations used in the code, such as microturbulence, complete redistribution, and spherical symmetry, which considerably reduce the computational effort required

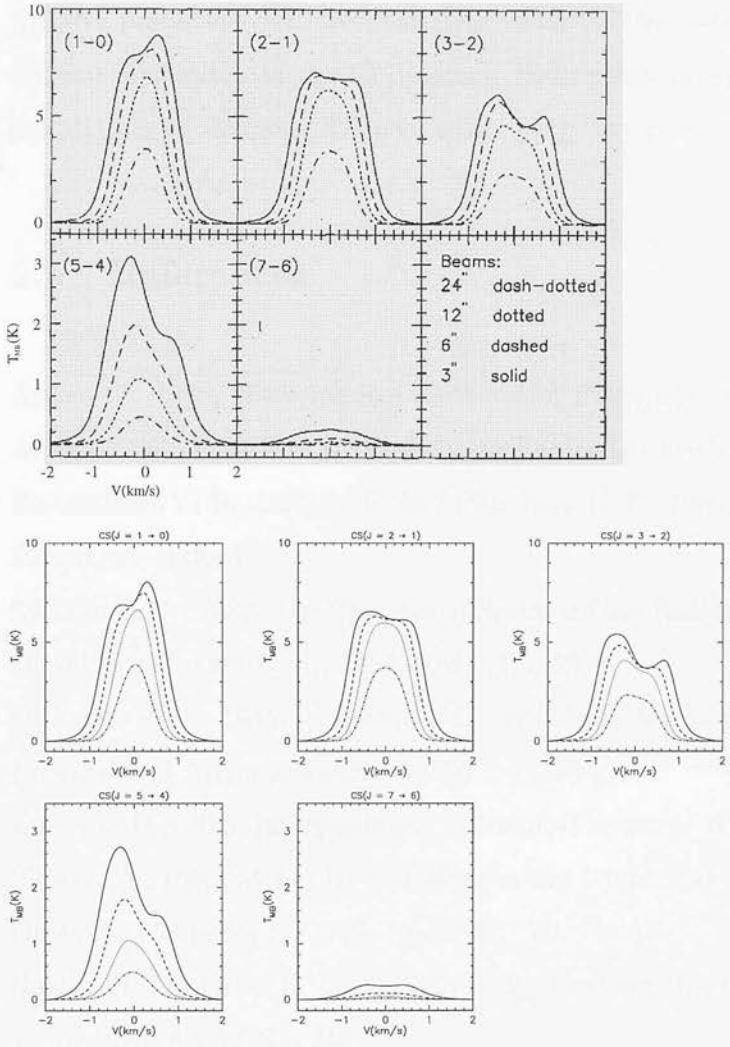

Figure 2.9: Comparison of the CS line profile calculations from Figure 11 of Krügel & Chini (1994) (top), with those produced by STENHOLM for the same model cloud. For each transition, line profiles are plotted for a number of different FWHM beam sizes, as indicated in the bottom right hand panel of the top diagram. The model cloud had an outer radius of 6684 AU and was assumed to lie at a distance of 450 pc. The adopted hydrogen number density and velocity profiles were of the form $n_{\mathrm{H_2}}(r) \propto r^{-3/2}$ and $\mathrm{v}(r) \propto r^{-1/2}$ respectively, with $n_{\mathrm{H_2}} = 1.1 \times 10^5$ and v=-0.237 $\mathrm{km\,s^{-1}}$ at the outer edge of the cloud. The kinetic temperature was set to 10K up to the half-way radius, then rising linearly to a value of 20K at the edge of the cloud. The microturbulent velocity width and the CS abundance were assumed to be constant throughout the cloud, with values of 0.5 $\mathrm{km\,s^{-1}}$ (FWHM) and $2{\times}10^{-9}$ respectively. Both calculations used the CS collision rates from Green & Chapman (1978).

to solve problems, but have uncertain validity. The code has been tested against analytical predictions in the LTE regime, and against previously published independent calculations in the non-LTE regime, showing very good agreement in both cases.

2.5 References

Arfken G., 1985, Mathematical Methods for Physicists. Academic Press, Boston

Atkins P. W., Friedman R. S., 1997, Molecular Quantum Mechanics. OUP, New York

Berestetskii V. B., Lifshitz E. M., Pitaevskii L. P., 1982, Quantum Electrodynamics. Pergamon, Oxford

Cannon C. J., 1985, The Transfer of Spectral Line Radiation. CUP, Cambridge

Dickel H. R., Auer L. H., 1994, ApJ, 437, 222

Dickman R. L., 1985, in Black D. C., Matthews M. S., eds, Protostars & Planets II. University of Arizona, Tuscon, p.150

Emerson D., 1996, Interpreting Astronomical Spectra. Wiley, Chichester

Flower, D., 1990, Molecular Collisions in the Interstellar Medium. CU Cambridge

Green S., Chapman S., 1978, ApJS, 37, 169

Heaton B. D., Little L. T., Yamashita T., Davies S. R., Cunningham C. T., Monteiro T. S., 1993, A&A, 278, 238

Hummer D. G., Rybicki G., 1971, ARA&A, 9, 237

Juvela M., 1997, A&A, 322, 943

Krügel E., Chini R., 1994, A&A, 287, 947

Landau L. D., Lifshitz E. M., 1977, Quantum Mechanics. Pergamon, Oxford

Mandl F., 1971, Statistical Physics, Chichester, John Wiley & Sons

Matthews N., 1986, PhD thesis, University of Kent

Mihalas D., 1978, Stellar Atmospheres, Freeman, San Fransisco

Monteiro T. S., 1985, MNRAS, 214, 419

Park Y.-S., Hong S. S., 1995, A&A, 300, 890

Pomraning G. C., 1973, The Equations of Radiation Hydrodynamics. Pergamon, Oxford

Richer J. S., Padman R., Ward-Thompson D., Hills R. E., Harris A. I., 1993, MNRAS,

262, 839

Rohlfs K., Wilson T. L., 1996, Tools of Radio Astronomy. Springer, Berlin

Rybicki G. B., 1972, Line Formation in Magnetic Fields. National Centre for Atmospheric Research, Boulder, Colorado

Rybicki G. B., 1984, in Kalkofen W., ed., Methods in Radiative Transfer. CUP, Cambridge

Schiff L. I., 1968, Quantum Mechanics, McGraw-Hill, New York

Spitzer L., Jr., 1978, Physical Processes in the Interstellar Medium. Wiley, New York

Stenholm L. G., 1977, A&A, 54, 577

Turner B. E., Chan K. W., Green S., Lubowich D. A., 1992

Vazquez-Semadeni E., Canto J., Lizano S., 1996, BAAS, 189, 1504

Chapter 3

Observations of Protostellar Envelopes

In this chapter, results are presented of a submillimetre spectral line study of the gas envelopes surrounding a number of candidate low mass protostars. After giving an overview of the instruments and observing methods used, the data are presented and discussed.

3.1 The James Clerk Maxwell Telescope

The temperature of most of the gas in dense star-forming cores lies in the range 10-100K, and it therefore radiates primarily at far-infrared, submillimetre and millimetre wavelengths. Telescopes designed to work in the submillimetre range ($\sim 350 - 2000\mu$m) have been in existence for some years now and are invaluable tools in the study of star formation. The data presented in this chapter were taken using the James Clerk Maxwell Submillimetre Telescope (JCMT), which is currently the largest telescope in the world which routinely operates over the full submillimetre wavelength range. The JCMT is a 15 metre alt-azimuth telescope, situated on Mauna Kea, a volcanic peak on the main island of Hawaii, at an altitude of 4092 metres and a latitude of $+19^\circ\,49'\,33''$.

Full details of the telescope and its operation are given in Matthews (1996). A brief overview is given below.

The telescope and its instruments are designed to operate in the submillimetre region of the electromagnetic spectrum, in the approximate frequency range 100-1000 GHz (i.e. in the wavelength range 300-3000 μm). The primary mirror is a parabolic dish 15 metres in diameter, with an r.m.s. surface accuracy of around 30μm. Incoming radiation is reflected off the primary and chopping secondary mirrors, onto the flat tertiary mirror situated in a receiver cabin behind the primary surface, at the Cassegrain focus. The tertiary mirror directs the radiation either to one of several spectral line receivers located in the receiver cabin, or to a continuum receiver located on one of the Nasmyth platforms of the telescope.

The r.m.s. pointing accuracy is typically around 2 arcseconds, and is checked frequently during the observations. The tracking accuracy is usually better than 1 arcsecond over a period of about one hour.

3.1.1 Atmospheric transmission in the submillimetre waveband

Figure 3.1 shows the atmospheric transmission across the operating frequency range of the JCMT, and how it varies with the water vapour content of the atmosphere. Frequency bands of reasonably good atmospheric transmission lie between strong absorption lines due to atmospheric oxygen and water vapour. The atmospheric transmission deteriorates at all frequencies when the water vapour content of the atmosphere increases, although some frequencies are affected more than others. The atmospheric 'window' below 300 GHz stays open (i.e. transmission $>\sim 0.3$) even when conditions are comparitively poor. The higher frequency windows are more sensitive to changes in atmospheric water vapour content, and the window centred around 650 GHz ($\sim 450\mu$m) is only usable in excellent observing conditions.

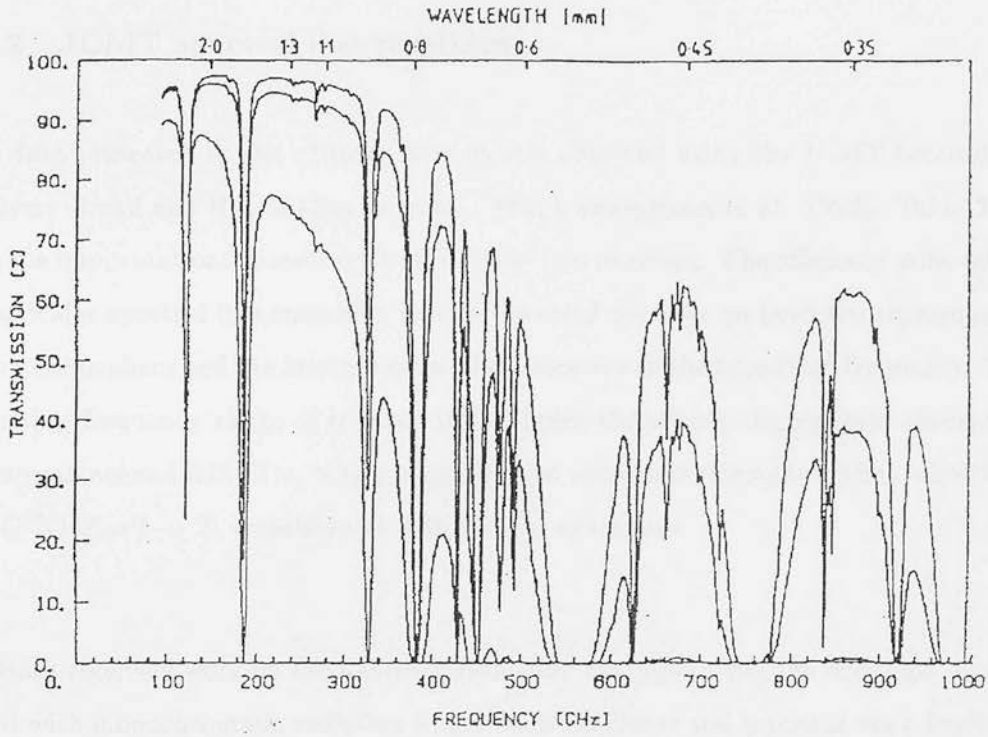

Figure 3.1: Plot of the calculated atmospheric transmission as a function of frequency in the submillimetre region, for three different values of the atmospheric precipitable water vapour content, corresponding to 'excellent' (0.5 mm), 'good' (1.0 mm), and 'poor' (5 mm) observing conditions on Mauna Kea (Duncan 1990). This plot was produced using the ATM atmospheric model (Cernicharo 1992) which does not include ozone lines.

The state of the atmosphere during the observing is monitored from the JCMT using a link to the Caltech Submillimetre Observatory radiometer, which measures the intensity of the 225 GHz sky emission at different elevations. The results are fitted to an atmospheric model, providing an automatic update of the zenith atmospheric optical depth at this frequency every few minutes. The behaviour of this optical depth over a period of few hours gives a good indication of the quality and stability of the observing conditions.

3.1.2 JCMT spectral line receivers

The data presented in this chapter were mostly obtained using the JCMT heterodyne receivers RxA2 and RxB3i (Davies et al. 1992; Cunningham et al. 1992). Table 3.1.2 lists the important parameters relating to these two receivers. The efficiency with which a particular spectral line transition can be observed depends on both the transmission of the atmosphere and the internal noise of the receiver at the transition frequency. The operating frequency range of receiver B3i includes the strong atmospheric absorption feature at around 325 GHz, which degrades the system performance when observing the $C^{18}O(J = 3 \rightarrow 2)$ transition at 329GHz, for example.

Both receivers work on the following principle: radiation from the telescope is combined with monochromatic radiation from a local oscillator and is passed via a feedhorn to a non-linear mixing element (i.e. an electronic component with an I-V curve which differs markedly from Ohm's law). The output voltage from the mixer includes the difference frequencies between the local oscillator frequency and the signal frequencies, as well as the signal and oscillator frequencies themselves, and multiples and combinations of these frequencies (e.g. Lesurf 1990). If the local oscillator frequency, $\nu_{\rm osc}$, is close to the signal frequency, $\nu_{\rm sig}$, then the difference frequency, $\nu_{\rm IF}$, also known as the **intermediate frequency** (IF), will be much smaller than either. The IF signal can be filtered, amplified, and processed further using conventional electronic techniques, which cannot be used on the direct signal.

The mixer stage acts as a frequency down-converter, retaining the spectral and phase information in the original signal. It is important to realise that the IF output at the frequency $\nu_{\rm IF}$ is a superposition of the contributions from the signal frequencies $\nu_{\rm sig} = \nu_{\rm osc} \pm \nu_{\rm IF}$. For a given range of IF frequency, the corresponding range of signal frequencies using this relation is called the *upper sideband* when the positive sign is taken, and the *lower side band* when the negative sign is taken. The signal and noise in both sidebands are therefore down-converted onto the same range of IF frequency, and the lower sideband is 'flipped' along the frequency axis in the process. This can in

Receiver Name	Frequency Range	Beam FWHM	Efficiencies			Atmos. Trans.
			η_a	η_{mb}	η_{fss}	
RxA2	205-280 GHz	24-18″	0.57	0.69	0.80	0.9
RxB3i	298-380 GHz	17-13″	0.49	0.58	0.70	0.7

Table 3.1: Parameters relating to the JCMT heterodyne receivers RxA2 and RxB3i. The efficiencies given were typical at the time of the observations, and the zenith atmospheric transmission is for 'average' conditions, away from any strong atmospheric absorption features within the band. η_a is the aperture efficiency, which is the ratio of the strength of signal actually received from a point source to the predicted strength for a 'perfect' telescope of the same diameter, with no surface errors, blockage or losses. The main beam efficiency, η_{mb}, is the fraction of power contained in the main diffraction beam of the telescope. η_{fss} is the forward spillover and scattering efficiency, defined as the fraction of power within a circular aperture of 0.5° diameter.

theory lead to ambiguities in the interpretation of a measurement. In practice, however, any ambiguity can normally be easily resolved. For example, changing the local oscillator frequency by a small amount causes features in the upper and lower side-bands to move in opposite directions along the IF frequency axis, which allows the sideband of any ambiguous feature to be identified. The terms **signal** and **image** sideband are normally used to distinguish between the sideband which encompasses the frequency range of observational interest, and the other sideband which usually contains no signal. The image sideband does contribute noise to the observation however, unless there is a facility to suppress the image sideband (this facility was not available at the time the observations were made).

Figure 3.2 shows the optical layout for RxA2, prior to the mixer stage. A similar scheme is used for RxB3i (Cunningham et al. 1992). The local oscillator arrangement consists of a Gunn oscillator, which produces microwave radiation in the frequency range $\sim 70 - 95$ GHz; this is followed by a Schottky diode frequency tripler, which up-converts the oscillator frequency to the range of operation of the receiver. The Gunn oscillator relies on the Gunn diode, which displays the phenomenon known as

the Gunn effect, found to occur in the bulk of certain homogeneous semiconductors (e.g. n-type gallium arsenide). If a steady electric field, stronger than about $300\,\mathrm{kV\,m^{-1}}$, is set up across a Gunn diode, the current through it is found to flow in regular pulses with a period proportional to the length of the sample (e.g. Seymour 1981). This is accompanied by strong microwave emission at the frequency of the pulses, typically in the Gigahertz range. Various techniques are available to control the frequency and frequency stability of the radiation produced by the device, such as phase-locked and frequency locked electronic feedback loops (e.g. Wilmhurst et al. 1990).

The mixing element is a lithographically produced superconductor-insulator-superconductor (SIS) sandwich. An outline of the physics of this device is given by Phillips (1988). Its main advantage is that it gives a highly non-linear response over a voltage range of around a millivolt, which is well matched to photon energies in the submillimetre region ($1\,\mathrm{mV} \simeq 240\,\mathrm{GHz}$).

The spectral analysis of the IF signal, following the mixer stage, is carried out by a digital autocorrelation spectrometer (the DAS). This method is based on a theorem in Fourier analysis, known as the Wiener-Khinchin Theorem, which states that the power spectrum of a function, $f(t)$, is equal to the Fourier transform of its autocorrelation function (e.g. Burke & Graham-Smith, 1997). The autocorrelation function, $R(t')$, of $f(t)$, is defined by

$$R(t') = \lim_{T\to\infty} \int_{-T}^{T} f(t) f(t+t')\, dt. \tag{3.1}$$

Writing $P(\nu)$ as the power spectrum of $f(t)$, the theorem is expressed mathematically by the following equation:

$$P(\nu) \equiv |F(\nu)|^2 = \frac{1}{2\pi} \int_{-\infty}^{\infty} R(t') e^{-2\pi i \nu t'}\, dt', \tag{3.2}$$

where

$$F(\nu) = \frac{1}{2\pi} \int_{-\infty}^{\infty} f(t) e^{-2\pi i \nu t}\, dt. \tag{3.3}$$

In the actual operation of the DAS, the function $f(t)$ (i.e. the IF signal) is replaced by a fairly coarse digital representation, by passing it through a 3-level (2-bit) analogue

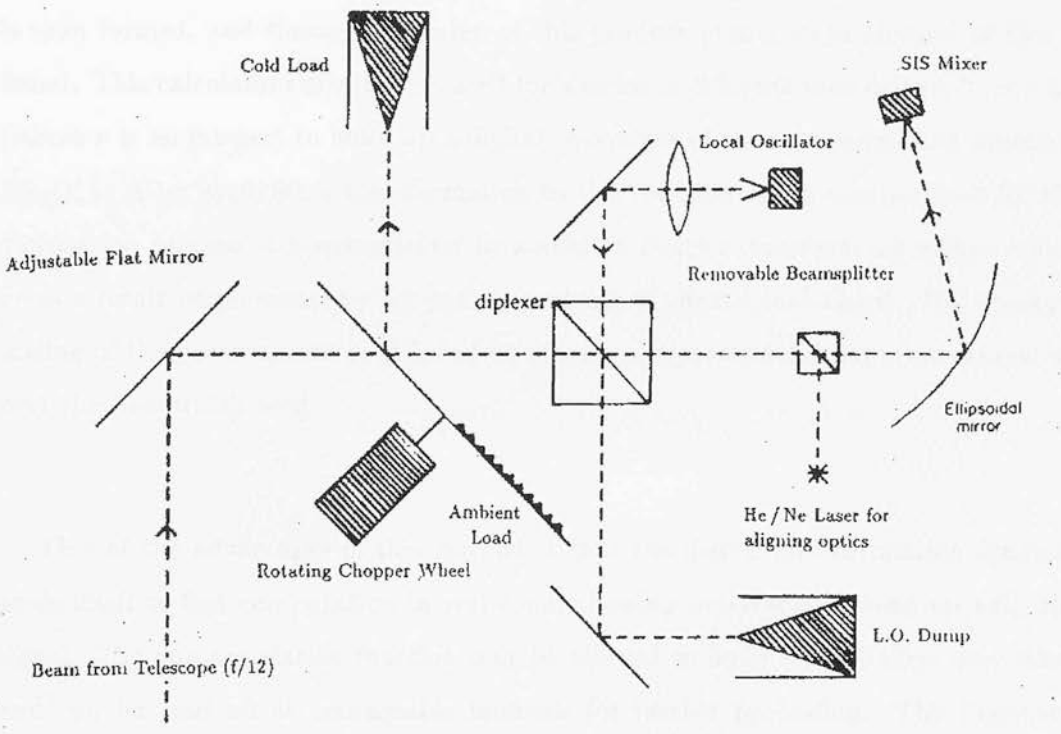

Figure 3.2: Schematic diagram of the optical layout for Receiver A2 (from Davies et al. 1992). The radiation from the telescope is directed past the chopper wheel to the diplexer (a piece of mylar film) which combines the local oscillator signal with the beam. The beam is then focussed onto the SIS mixer feedhorn by the ellipsoidal mirror. The chopper wheel allows ambient temperature and cold (100K) loads to be presented to the mixer, for calibration purposes.

to digital converter. This samples the amplitude of the signal at a sampling frequency which must be at least twice the desired band-width of the observation. The digitised signal retains only the information on whether the amplitude of the signal is positive or negative, and whether its magnitude is above or below some predefined threshold. The digital equivalent of the equation 3.1 is evaluated by introducing a delay, t' into a section of the digitised IF signal; the product of the delayed and undelayed signals is then formed, and the average value of this product over a large number of bits is found. This calculation may be repeated for a series of different time delays, $t'_n = n\Delta t'$ (where n is an integer) to build up a digital equivalent of the autocorrelation function, $R_{\rm dig}(t'_n)$. After applying a transformation to this function which compensates for the digitisation process, it is operated on by a discrete Fourier transform algorithm, which gives a result *proportional* to the power spectrum of the original signal. The absolute scaling of the power spectrum is found by making a separate total power measurement over the bandwidth used.

One of the advantages of this method is that the digital autocorrelation function lends itself to fast computation in real time, allowing processors to keep up with the signal. The autocorrelation function may be allowed to build up in buffers over time, and can be read off at manageable intervals for further processing. The frequency resolution of the spectrometer is approximately equal to the reciprocal of the longest delay introduced in the calculation of the autocorrelation function (i.e. $\delta\nu \simeq 1/(N\delta t)$). The best spectral resolution that the DAS can achieve is 95 kHz, although the actual resolution of the spectra can also depend on intrinsic broadening originating in the receiver system. In the case of RxA2, the intrinsic phase-instability of the Gunn local oscillator at the time of use limited the spectral resolution to about 400 kHz (equivalent to $\simeq 0.5 {\rm km\,s^{-1}}$ at 245 GHz – the frequency of the CS($J = 5 \rightarrow 4$) transition). This problem does not affect RxB3i, however, and for this instrument the spectral resolution is limited only by the DAS.

3.1.3 Calibration of submillimetre spectral line observations

The signal measured from an astronomical source is calibrated using the direct, two load method (e.g. Kutner & Ulich, 1981), whereby measurements are taken of the signal produced when a 'hot load' (ambient temperature), and a cold load (liquid nitrogen), are presented to the receiver. The output signal V of the receiver, when uniformly illuminated *in both sidebands* with radiation of intensity $I_\nu \equiv 2kT_{\rm rad}\nu^2/c^2$, is given by

$$V = g(T_{\rm rec} + T_{\rm rad}) \tag{3.4}$$

where $T_{\rm rec}$ is a property of the receiver and is fairly constant, and g is the double sideband gain, appropriate for when the input signal appears in both sidebands equally. Using the measurements of V for the hot and cold loads, $T_{\rm rec}$, and g may be easily derived. The gains appropriate to the signal and image sidebands taken individually, g_s and g_i (where $g = g_s + g_i$) are more difficult to find, although it is often the case that $g_s \simeq g_i \simeq g/2$.

The signal $V_{\rm sky}$ measured by the receiver when the telescope is pointing at 'blank' sky may be written as

$$V_{\rm sky} = gT_{\rm rec} + g(1-\eta_{\rm tel})J_{\rm amb} + \eta_{\rm tel}[g_s T_{\rm sky}({\rm sig}) + g_i T_{\rm sky}({\rm im})], \tag{3.5}$$

where $J_{\rm amb}$ is the radiation temperature of the emission from the immediate telescope surroundings, at the physical temperature $T_{\rm amb}$:

$$J_{\rm amb} \simeq \frac{h\nu/k}{\exp(h\nu/kT_{\rm amb}) - 1}, \tag{3.6}$$

and $\eta_{\rm tel}$ is the telescope efficiency. The latter quantity is the product of η_r, the radiation efficiency, which accounts for ohmic losses at the reflecting surfaces and in the membrane which protects the dish, and η_{rss}, the rear scattering and spillover efficiency, where $(1-\eta_{rss})$ is the fraction of beam power which is directed in the backward directon (i.e. towards the ground), terminating at the ambient temperature. $T_{\rm sky}({\rm sig})$ and $T_{\rm sky}({\rm im})$ are the sky radiation temperatures in the signal and image sidebands respectively, where

$$T_{\rm sky} = J_{\rm atm}(1-\eta_{\rm sky}). \tag{3.7}$$

$\eta_{\rm sky}$ is the transmission of the atmosphere at the relevant frequency, and $J_{\rm atm}$ is an 'effective radiation temperature' of the atmosphere, typically around 10K less than $J_{\rm amb}$.

Now suppose the telescope is pointed at an astronomical source, which has a radiation temperature (outside the atmosphere) at the peak of the antenna pattern, of $T_{\rm r}$. The signal $V_{\rm on}$ measured by the receiver when the telescope is pointing at an astronomical source may be written as

$$V_{\rm on} = V_{\rm sky} + g_s \eta_{\rm tel} \eta_{\rm sky} \eta_f T_{\rm r}, \tag{3.8}$$

$$= V_{\rm sky} + g_s T_A, \tag{3.9}$$

where η_f is the coupling of the source to the forward antenna pattern of the telescope (see below) and T_A is called the **antenna temperature** (Ulich & Haas, 1976):

$$T_A = \eta_{\rm tel} \eta_{\rm sky} \eta_f T_{\rm r}. \tag{3.10}$$

We now define T_A^* as the **corrected antenna temperature**, corrected for atmospheric attenuation, ohmic losses, and rear spillover and scattering:

$$T_A^* = \frac{T_A}{\eta_{tel} \eta_{\rm sky}}, \tag{3.11}$$

$$= \eta_f T_{\rm r}. \tag{3.12}$$

From equation 3.9 we have

$$T_A^* = \frac{V_{\rm on} - V_{\rm sky}}{g_s \eta_{\rm tel} \eta_{\rm sky}} = \frac{V_{\rm on} - V_{\rm sky}}{V_{\rm sky}} T_{\rm sys}, \tag{3.13}$$

where

$$T_{\rm sys} = \frac{V_{\rm sky}}{g_s \eta_{\rm tel} \eta_{\rm sky}}. \tag{3.14}$$

$T_{\rm sys}$ is called the **system temperature**, and is a measure of the noise in the observation, including contributions from the receiver and the atmosphere. The automatic online calibration at the telescope evaluates $T_{\rm sys}$ for each observation, and produces spectra on the T_A^* scale, using a reference 'blank sky' observation to carry out the analysis described above.

Spectral line temperature scales

T_A^* is an estimate of the radiation temperature that would be measured outside the atmosphere, with no telescopic losses, and for an antenna pattern which is truncated to zero in all directions in the rear hemisphere relative to the dish. Adapting the notation of Kutner & Ulich (1981), the observed value of T_A^* when the telescope is pointing in the direction $\hat{\mathbf{\Omega}}_0$, may be written as

$$T_A^*(\hat{\mathbf{\Omega}}_0) = T_\mathrm{r}\left[\frac{\int_{2\pi} P_0(\hat{\mathbf{\Omega}})B_n(\hat{\mathbf{\Omega}})\,d\Omega}{\int_{2\pi} P_0(\hat{\mathbf{\Omega}})\,d\Omega}\right], \tag{3.15}$$

where P_0 is the antenna power pattern, centred on $\hat{\mathbf{\Omega}}_0$, B_n is source brightness distribution, normalised to unity in the direction $\hat{\mathbf{\Omega}}_0$, T_r is the source radiation temperature in this direction, as before, and the quantity in square brackets is equal to η_f (see above). In both integrands, $\hat{\mathbf{\Omega}}$ is the unit vector in the direction of the solid angle element $d\Omega$. The integration range is over the hemisphere in the forward direction relative to the dish, however this is only strictly valid when the telescope is pointing at the zenith. The error involved in truncating the beam rearward of the dish, rather than towards the ground, is only likely to be significant for observations very close to the horizon, however (Kutner & Ulich 1981).

The value of T_A^* defined in this way, is related to $\bar{I}_\nu(\hat{\mathbf{\Omega}}_0)$, the average of the source radiation intensity over the truncated beam pattern, by the following relation:

$$\bar{I}_\nu(\hat{\mathbf{\Omega}}_0) = 2kT_A^*\nu_\mathrm{obs}^2/c^2, \tag{3.16}$$

$$= \frac{\int_{2\pi} P_0(\hat{\mathbf{\Omega}})I(\hat{\mathbf{\Omega}})\,d\Omega}{\int_{2\pi} P_0(\hat{\mathbf{\Omega}})\,d\Omega}, \tag{3.17}$$

where ν_obs is the frequency of the observation.

Since the antenna power pattern, $\mathrm{P}_0(\hat{\mathbf{\Omega}})$, is usually only known with any degree of certainty over a solid angle much less than 2π, equation 3.15 is not very convenient for modelling purposes. To address this problem, Kutner & Ulich (1981) proposed a different temperature scale, T_r^*, defined by

$$T_\mathrm{r}^* = T_\mathrm{r}\eta_\mathrm{c},, \tag{3.18}$$

$$\eta_c = \frac{\int_{\Omega_d} P_0(\hat{\Omega}) B_n(\hat{\Omega})\, d\Omega}{\int_{\Omega_d} P_0(\hat{\Omega})\, d\Omega}, \tag{3.19}$$

where η_c is the efficiency with which the beam pattern is coupled to the source, and the beam pattern is now truncated to zero outside the small solid angle Ω_d around the beam direction. In terms of T_A^*:

$$T_\mathrm{r}^* = T_A^*/\eta_{fss}, \tag{3.20}$$

$$\eta_\mathrm{fss} = \frac{\int_{\Omega_d} P_0(\hat{\Omega})\, d\Omega}{\int_{2\pi} P_0(\hat{\Omega})\, d\Omega}. \tag{3.21}$$

It is conventional to define Ω_d as the solid angle subtended by a 0.5° diameter disk, so that η_fss, the forward scattering and spillover efficiency, may be measured using the full moon. T_r^* is the convolution of the actual source radiation temperature distribution, $T_\mathrm{r} B_n(\hat{\Omega})$, with an antenna beam pattern which is truncated to zero outside the solid angle Ω_d centred on the peak of the beam pattern. Ω_d more than adequately accommodates the main diffraction and error beams at all operating frequencies at the JCMT (e.g. Richer et al. 1993). It eliminates the very extended, very low power beam component caused by small scale surface inaccuracies in the main dish and scattering past the secondary mirror and support arms.

If the characteristic angular diameter of the source is comparable with the FWHM diameter of the main diffraction limited component of the telescope beam, it may be useful to define yet another temperature scale — the main beam temperature, T_mb. This estimates the temperature that would be observed if the antenna pattern were the ideal diffraction limited gaussian profile, with no error beam:

$$T_\mathrm{mb} = T_A^*/\eta_\mathrm{mb}, \tag{3.22}$$

$$\eta_\mathrm{mb} = \frac{P_0(\hat{\Omega}_0) \int_0^\infty \exp[-(4\ln 2)\,\theta^2/\sigma_\mathrm{FWHM}^2]\, 2\pi\theta\, d\theta}{\int_{2\pi} P_0(\hat{\Omega})\, d\Omega}, \tag{3.23}$$

$$= \frac{2\pi\,(\sigma_\mathrm{FWHM}/2.35)^2 P_0(\hat{\Omega}_0)}{\int_{2\pi} P_0(\hat{\Omega})\, d\Omega}, \tag{3.24}$$

where σ_FWHM is the full-width-at-half-maximum diffraction limited beam size. σ_FWHM

given by

$$\sigma_{\rm FWHM} = 1.22\lambda_{\rm obs}/D_{\rm ap}, \tag{3.25}$$

where $\lambda_{\rm obs}$ is the wavelength of the observation, and $D_{\rm ap}$ is the diameter of the primary mirror.

Use of the main beam temperature scale requires the strongest a-priori assumption about the source brightness distribution (i.e. that it is compact) of all the temperatures defined so far. Emission from the source on a scale more extended than the main diffraction beam will make $T_{\rm mb}$ greater than the 'ideal' value, although if this emission is much weaker than the emission inside the main beam, then the error in $T_{\rm mb}$ will be small. Even if the source is of uniform brightness over a region of the size of Ω_d (i.e. a disk 0.5° in diameter), $T_{\rm mb}$ will only be over-estimated by the factor $\eta_{\rm fss}/\eta_{\rm mb}$ (i.e. $\sim 15-20\%$).

In summary, the corrected antenna temperature scale, T_A^*, naturally emerges from the on-line calibration at the telescope, and includes the full forward-directed antenna pattern. $T_{\rm r}^*$ is the most appropriate temperature scale for objects which are very extended in comparison to the beam size. In this case the beam is effectively truncated to zero outside a region the size of the full moon, but includes the main diffraction and error beams. The main beam temperature scale, $T_{\rm mb}$, may be useful if the emission from the object is reasonably strongly peaked on scales of a few times the beam size or less. In this case only the main diffraction limited beam is assumed to be significant. Since this component of the beam is well known, spectra calibrated on the main beam temperature scale may be readily compared with synthetic observations produced using numerical radiative transfer models.

3.1.4 Spectral line observing modes

A full discussion of observing techniques available for use with JCMT heterodyne receivers is given in Matthews (1996). Single point observations can be made using one of three modes: position switching, beam switching, and frequency switching. Mapping

of objects can be carried out either by making a number of pointed observations over a grid of positions (grid-mapping), or by using the raster-mapping technique. All of these modes were used at various times to obtain the data presented in this chapter, and a brief overview is now given.

In position-switched observations, the telescope observes alternately at the source position and a reference position, every 30 seconds or so. The telescope software uses the reference spectra to calibrate the result and eliminate atmospheric and instrumental effects. The reference position should ideally be as close to the source as possible, whilst avoiding emission in the reference beam. If the source lies in an extended region of emission, however (e.g. when observing CO emission in molecular clouds), position switches as large as one degree may be necessary, but not desirable.

For compact sources, beam switching may be appropriate. In the beam-switching mode, the secondary mirror is 'chopped' at a rate of around 1Hz between the source position and a nearby reference position, and the difference between the two measurements is taken. Every 20 seconds or so the telescope dish moves (or 'nods') so that the source lies in the other chopping beam - this helps to remove standing wave ripples from the final spectrum. Beam-switching is effective in minimising sky noise, but can only be used for reference positions separated by $<\sim$ 3 arcminutes from the observed source.

The problem of finding a reference position free of emission is avoided by using the frequency switching technique. Here the telescope spends the entire duration of the observation on-source, which means that frequency switching is more efficient than position or beam-switching. The observed frequency is alternated above and below the line frequency by a small amount every 20 seconds or so, and the difference between the resulting spectra is taken, producing a positive and negative image of the line profile, separated along the frequency axis. The frequency switch must be large enough that there is no overlap between the two line profile images, and is otherwise chosen to be as small as possible, whilst minimising the effect of standing waves in the receiver.

After the observation, the positive and negative images may be combined using data reduction software. A disadvantage of using frequency switching is that it tends to produce curved or sinusoidal baselines, which makes detection of broad, low-level features difficult or impossible.

Maps can be made in either grid-mapping or raster-mapping mode. Grid maps are simply an array of single point observations, using one of the switching modes described above. Grid maps are less efficient than raster maps, but allow greater flexibility in the shape of the map and the distribution of integration times in different parts of the map.

In raster-mapping mode, the telescope is scanned along lines of constant declination, whilst the signal is continuously integrated by the DAS. The average of the signal received whilst traversing each map cell is formed and stored. At the end of each scanning row, a position switched observation at a fixed pre-specified reference position is carried out. Raster-mapping is extremely efficient (up to $\sim 75\%$ of the observing time spent on source) for bright extended sources, and for mapping large areas.

3.2 Observations

The observations presented here were carried out entirely at the JCMT, using receivers RxB3i and RxA2, with the DAS backend. Details of the observing runs are given in Table 3.2. The February 1995 observations were carried out by Dr Wayne Holland and Dr Jane Greaves as part of their backup observing proposal, and the January 1997 observations were carried out in serviced mode by the JAC staff. The remaining two runs were carried out by us at the telescope.

No significant instrumental problems were encountered, except for the poor frequency resolution ($\sim$ 400kHz) of RxA2 mentioned previously. RxA2 was unavailable

during the March 1996 run as it had been moved from the telescope for repairs. Pointing and focus checks were performed roughly once per hour during each run. The focus was found to be very stable throughout, and the pointing accuracy was $\sim$ 2 arcsec. Observations of standard sources were taken once or twice per run for each transition observed. We estimate the absolute calibration is accurate to within $\sim$25%, although the relative calibration between different observations should be much better than this. Throughout the observations the DAS was configured with the optimum frequency resolution of 95kHz per channel, giving a usable bandwidth of 125MHz (equivalent to at least $\sim 100\,\mathrm{km\,s^{-1}}$ at the frequencies observed).

Most of the pointed observations were made using position switching. Frequency switching was used only for some of the HCO^+ and $H^{13}CO^+$ observations, and to check for emission-free reference positions during position switching. Beam-switching was used only occasionally, for sources which were known to have very compact emission. Comparison of identical observations using each of these observing modes gives excellent agreement in each case.

Mapping of extended sources was carried out in both grid mapping and raster mapping mode. In some of the maps, the noise is greater towards the edge of the map than at the centre, due to a reduced integration time per map point at these positions. In the individual raster maps, integration times of 4-6 seconds per cell were used, as recommended in the JCMT Users Guide (Matthews 1996). Longer integration times per point were obtained by repeating the raster.

Table 3.2 gives details of the various spectral line transitions observed. Data from the JCMT data archive were also used to supplement our observations where possible, as indicated in the table. The JCMT archive is operated by the Canadian Astronomy Data Centre.

Date (HST)	Shift (HST)	R.A. Range (h)	T_{sys}(K)		τ_{225}	Ref.
			CS(5-4)	HCO^+(4-3)		
1995, 9-10 Feb.	17:30-01:30	03-18	450 - 500	~ 1000	-	f95
1995, 26-28 July	01:30-09:30	18-05	500 - 600	700 - 1100	0.04-0.14	j95
1996, 17-22 March	01:30-09:30	16-19	-	500 - 800	0.03-0.10	m96
1997, 30 Jan	01:30-09:30	16-18	~ 400	-	-	j97

Table 3.2: Details of the JCMT observing runs. The system temperature ranges of RxA2 and RxB3i are given for the CS($J = 5 \rightarrow 4$) and HCO^+($J = 4 \rightarrow 3$) transition frequencies respectively, which are well removed from atmospheric absorption features.

Data reduction

Data reduction was carried out mostly using the **SPECX** package (Padman 1990). Baseline calibration was usually performed by subtracting a straight line fit through sections of baseline placed on either side of the spectral feature of interest, carefully chosen to avoid suppression of low level wing emission. Frequency switching tends to produce moderately curved and/or sinusoidal baselines. Curved baselines were removed by subtracting a second order polynomial fit to sections of baseline on either side of the observed spectral feature. This procedure was checked on several occasions by making observations of the same object in both frequency-switched and position-switched mode, giving very good agreement between the line profiles.

The spectra presented in this chapter are calibrated in terms of the main beam temperature scale (as described above), apart from the maps, where the corrected antenna temperature, T_A^*, is used. The efficiencies listed in Table 3.1.2 may be used to convert between the various temperature scales.

The integrated intensity and centroid velocity, position-velocity and channel maps presented below were also produced using the standard **SPECX** map-making facilities. To improve the appearance of the contouring in these maps, the observed grids were

Molecule	Transition	Frequency (GHz)	FWHM (″)	δv (km s^{-1})	$T_{\rm sys}$ (K)	Source
HCO^+	$J = 3 \rightarrow 2$	267.557625	18.3	~0.25	~ 500	archive
	$J = 4 \rightarrow 3$	356.734248	13.6	0.080	~ 800	j95/m96
$H^{13}CO^+$	$J = 3 \rightarrow 2$	260.25548	18.8	~0.25	~ 500	archive
	$J = 4 \rightarrow 3$	346.998540	14.1	0.082	~ 800	j95/m96
CS	$J = 5 \rightarrow 4$	244.935606	19.3	~ 0.25	~ 500	f95/j95/j97
	$J = 7 \rightarrow 6$	342.88294	14.2	0.083	~ 800	f95/j95/m96
CO	$J = 3 \rightarrow 2$	345.795979	14.1	0.082	~ 800	m96
$C^{18}O$	$J = 2 \rightarrow 1$	219.56032	22.1	~ 0.25	~ 500	archive
$C^{18}O$	$J = 3 \rightarrow 2$	329.33050	14.8	0.087	~ 1500	m96

Table 3.3: Table giving details of the submillimetre line transitions observed using the JCMT. The line frequencies were taken from the Lovas spectral line catalogue (Lovas 1992). The observing runs during which each transition was observed are indicated in the last column (cf. Table 3.2). Also indicated are transitions which were obtained from the JCMT data archive. The CO($J = 3 \rightarrow 2$) and CS($J = 7 \rightarrow 6$) transitions were observed simultaneously, by selecting a frontend frequency which placed one transition in each sideband.

first interpolated onto a grid with twice the spatial sampling rate.

Centroid velocity analysis

The centroid velocity over a given velocity interval is calculated using the following formula:

$$v_c = \frac{\sum_i v_i T^*_{A_i}}{\sum_i T^*_{A_i}}, \tag{3.26}$$

where v_i and $T^*_{A_i}$ are the velocity and antenna temperature of the i'th velocity channel, and the sum is over the $n_{\rm ch}$ velocity channels lying in the specified velocity interval.

An expression can be found for the error in the centroid velocity determination using the standard relations for the propogation of errors (Narayanan, Walker & Buckley, 1997). If we define $S_{vT} = \sum_i v_i T^*_{A_i}$ and $S_T = \sum_i T^*_{A_i}$, then the variance of the centroid velocity, $\sigma^2_{v_c}$, may be written as (e.g. Bevington & Robinson 1992),

$$\frac{\sigma^2_{v_c}}{v_c^2} = \frac{\sigma^2_{S_T}}{S_T^2} + \frac{\sigma^2_{S_{vT}}}{S_{vT}^2} - 2\frac{\sigma^2_{S_T,S_{vT}}}{S_T \cdot S_{vT}}, \tag{3.27}$$

where

$$\sigma^2_{S_T} = \lim_{N\to\infty} \frac{1}{N} \sum_{j=1}^{N} (S_T(j)^2 - \overline{S_T}^2), \tag{3.28}$$

$$= \lim_{N\to\infty} \frac{1}{N} \sum_{j=1}^{N} \left[\left(\sum_{i=1}^{n_{\rm ch}} T^*_{A_i}(j) \right)^2 - \left(\sum_{i=1}^{n_{\rm ch}} \overline{T}^*_{A_i} \right)^2 \right], \tag{3.29}$$

$$\sigma^2_{S_{vT}} = \lim_{N\to\infty} \frac{1}{N} \sum_{j=1}^{N} S_{vT}(j)^2 - \overline{S_{vT}}^2, \tag{3.30}$$

$$= \lim_{N\to\infty} \frac{1}{N} \sum_{j=1}^{N} \left[\left(\sum_{i=1}^{n_{\rm ch}} v_i T^*_{A_i}(j) \right)^2 - \left(\sum_{i=1}^{n_{\rm ch}} v_i \overline{T}^*_{A_i} \right)^2 \right], \tag{3.31}$$

$$\sigma^2_{S_T,S_{vT}} = \lim_{N\to\infty} \sum_{j=1}^{N} (S_T(j) - \overline{S_T})(S_{vT}(j) - \overline{S_{vT}}) \tag{3.32}$$

$$= \lim_{N\to\infty} \frac{1}{N} \sum_{j=1}^{N} \left[\left(\sum_{i=1}^{n_{\rm ch}} v_i (T^*_{A_i}(j) - \overline{T}^*_{A_i}) \right) \left(\sum_{i=1}^{n_{\rm ch}} T^*_{A_i}(j) - \overline{T}^*_{A_i} \right) \right]. \tag{3.33}$$

The index i is used to sum over the $n_{\rm ch}$ channels in the chosen velocity range, and j is used to sum over an arbitrarily large number of repetitions of the observation. Bars over quantities indicate their average over repeated observations. In the above equations, the fractional error in the velocity assigned to each channel is assumed to be negligible compared with the fractional error of the temperature measurement. Assuming further that there is no correlation between the noise in separate velocity channels, then the cross terms in the expansion of equations (3.29), (3.31), and (3.33) average to zero over a large number of observations, which leads to the following simplified equations:

$$\sigma^2_{S_T} = \sum_{i=1}^{n_{\rm ch}} \sigma^2_{T_A} = n_{\rm ch} \sigma^2_{T_A} \tag{3.34}$$

$$\sigma^2_{S_{vT}} = \sigma^2_{T_A} \sum_{i=1}^{n_{\rm ch}} v_i^2, \tag{3.35}$$

$$\sigma^2_{S_T,S_{vT}} = \lim_{N\to\infty} \frac{1}{N} \sum_{j=1}^{N} \left[\sum_{i=1}^{n_{\rm ch}} v_i (T^*_{A_i}(j) - \overline{T}^*_{A_i})^2 \right], \tag{3.36}$$

$$= \sum_{i=1}^{n_{\rm ch}} v_i \sigma_{T_A}^2 = \sigma_{T_A}^2 \sum_{i=1}^{n_{\rm ch}} v_i, \tag{3.37}$$

where σ_{T_A} is the rms noise in a single channed, assumed to be constant for all the channels in the velocity window under consideration.

The final explicit expression for $\sigma_{v_c}^2$ is obtained on substitution of these relations into equation 3.27:

$$\frac{\sigma_{v_c}^2}{v_c^2} = \frac{n_{\rm ch}\sigma_{T_A}^2}{(\sum_i T_{A_i}^*)^2} + \frac{\sigma_{T_A}^2 \sum_i v_i^2}{(\sum_i v_i T_{A_i}^*)^2} - \frac{2\sigma_{T_A}^2 \sum_i v_i}{(\sum_i T_{A_i}^*) \cdot (\sum_i v_i T_{A_i}^*)}. \tag{3.38}$$

This equation is used to derive the error bars for the centroid velocity measurements presented below

3.2.1 The source list

Details of the sources observed are given in Table 3.2.1. The source list was chosen on criteria of proximity, observability, and probable evolutionary status. Objects from the Perseus, Ophiuchus and Serpens star forming regions are included, as well as isolated regions of individual star formation. The list is comprised exclusively of Class 0 and Class I sources, which represent the youngest protostellar stages (see Chapter 1 for a discussion of these classes). IRAS 16293-2422 and L483 have previously been proposed as infall candidates. In the remainder of this section the observations of each of these objects are presented and discussed in turn.

3.2.2 NGC1333-IRAS 2

NGC 1333 is a reflection nebula associated with the L1450 dark cloud, which lies at a distance of about 220pc (Cernis 1990), in the Perseus molecular cloud complex (Sargent 1979). To the south of the reflection nebula lies a $\sim 450\,{\rm M}_\odot$ molecular core, with a central density and temperature of $10^4{\rm cm}^{-3}$ and ~ 18K respectively (Warin et al. 1995; Lada et al., 1974). This is a site of highly active low and intermediate mass star formation, evidenced by the large concentration of T-Tauri and Herbig Ae/Be stars

Source Name	R.A.(1950) h m s	Dec.(1950) ° ′ ″	Class	D (pc)	T_A^*(K) HCO$^+$ (4→3)	H^{13}CO$^+$ (4→3)	CS (5→4)	CS (7→6)
L1448-IRS3	03 22 31.8	+30 34 45	0/I	300	5.0 m	1.5	1.5	-
N1333-IRAS2	03 25 49.9	+31 04 16	0	220	4.5 m	1.8	1.5 m	1.7
VLA1623	16 23 24.9	-24 17 46	0	125	6.0	1.8	1.5	1.0
L1689S-IRS67	16 28 58.5	-24 50 21	I	125	2.5 m	0.5	1	0.3 m
IRAS16293-2422	16 29 21.1	-24 22 15	0	125	23 m	2.0	8.0	8.0 m
L483	18 14 50.6	-04 40 49	0/I	200	6.0	0.7	2	1.5
Serp. SMM1	18 27 17.3	+01 13 23	0	300	3.5	1.8	-	2.3
Serp. SMM4	18 27 24.7	+01 11 10	0	300	8.0 m	0.7	2.0	1.5 m
Serp. SMM3	18 27 27.3	+01 11 55	0	300	6.2	-	-	1.0
Serp. SMM2	18 27 28.0	+01 10 45	0	300	3.1	0.4	1.0	<0.4

Table 3.4: List of sources, showing the peak antenna temperatures measured in selected transitions. The label 'm' is used to indicate that the source was mapped in the corresponding transition.

(Lada, Alves & Lada 1996; Aspin, Sandell & Russell 1994), Herbig-Haro objects, (Bally, Devine & Reipurth 1996), and bipolar jets and outflows (Hodapp & Ladd 1995; Liseau, Sandell & Knee 1988) in and surrounding the core. Loren (1976) originally suggested that the star formation in NGC1333 is being triggered by the collision of two dense molecular clouds. More recently, Warin et al. (1996) have argued that the morphology of the region supports a sequential star formation scenario, where outflows produced by one generation of stars compresses the surrounding gas which triggers collapse and further star formation.

Jennings et al. (1987) listed nine compact IRAS sources associated with the NGC1333 cloud, five of which drive bipolar molecular outflows (Liseau, Sandell & Knee 1988). Of these, IRAS 2 and IRAS 4 have no associated on-source optical or near-infrared emission. A full submillimetre continuum survey of NGC 1333-IRAS 2 was carried out by Sandell et al. (1994) using the JCMT. A strong compact peak was found at all wavelengths, with low-level emission at 800μm extending northwest and southeast of the peak, in a 'flattened bar' morphology. Sandell et al. (1994) derived an envelope mass

of $\sim 0.8\,M_{\odot}$ for the compact submillimetre source. The total far infrared luminosity of IRAS2 was estimated at $17\,L_{\odot}$ by Jennings et al. (1987) (for a distance of 220pc) and an upper limit of $26\,L_{\odot}$ was found by Ward-Thompson et al. (1996). The latter authors quote the ratio of bolometric to submillimetre luminosity to be $L_{\rm BOL}/L_{\rm SUBMM} \leq 130$, within the Class 0 threshold of 200 (André, Ward-Thompson & Barsony 1993).

Two bipolar outflows have been associated with IRAS2, observed in CO ($J = 3 \rightarrow 2$) emission (Sandell et al. 1994; Sandell & Aspin 1993), several transitions of CS (Langer, Castets & Lefloch 1996; Sandell et al. 1994), and 2.12μm shock-excited molecular hydrogen emission (Hodapp & Ladd 1995). The outflows are oriented nearly perpendicular to each other on the plane of the sky, at position angles of $\sim 24°$ and $\sim 104°$. Figure 3.3 shows the high velocity CO($J = 3 \rightarrow 2$) map of Sandell & Aspin (1993), in which the north-south outflow is seen to be significantly more extended and less collimated than the jet-like east-west outflow. The north-south outflow also appears much brighter and more extended in $2.12\,\mu$m emission (Hodapp & Ladd 1995, Figure 1), and is probably much older. Part of the eastern outflow lobe appears in the HH7–11 $HCO^{+}(J = 4 \rightarrow 3)$ map of Dent et al. (1993), although they interpreted this as an adjacent molecular clump. Sandell et al. (1994) estimated dynamical timescales for the north-south and east-west outflows of $\sim 6 \times 10^{3}$ and $\sim 2.5 \times 10^{4}$ yr respectively.

The east-west outflow axis appears to coincide exactly with the IRAS2 continuum peak, and is symmetrical about this position, making its physical association with IRAS2 quite secure. The alignment of the north-south outflow with IRAS2 is poorer, which led Sandell et al. (1994) to suggest that this outflow is driven by a separate, more evolved source situated $\sim 10 - 15$ arcseconds to the west of IRAS2. Hodapp & Ladd (1995) claimed that the axis of the $2.12\,\mu$m emission associated with the north-south outflow passes within 3 arcseconds of IRAS2, although a different and possibly more plausible choice of axis has a minimum separation 8 arcseconds to the west. The small misalignment of the north-south outflow with the IRAS2 submillimetre continuum peak therefore appears to be real, although the nature of the driving source of this outflow is uncertain. Hodapp & Ladd did not detect any $2.12\,\mu$m emission from a more evolved,

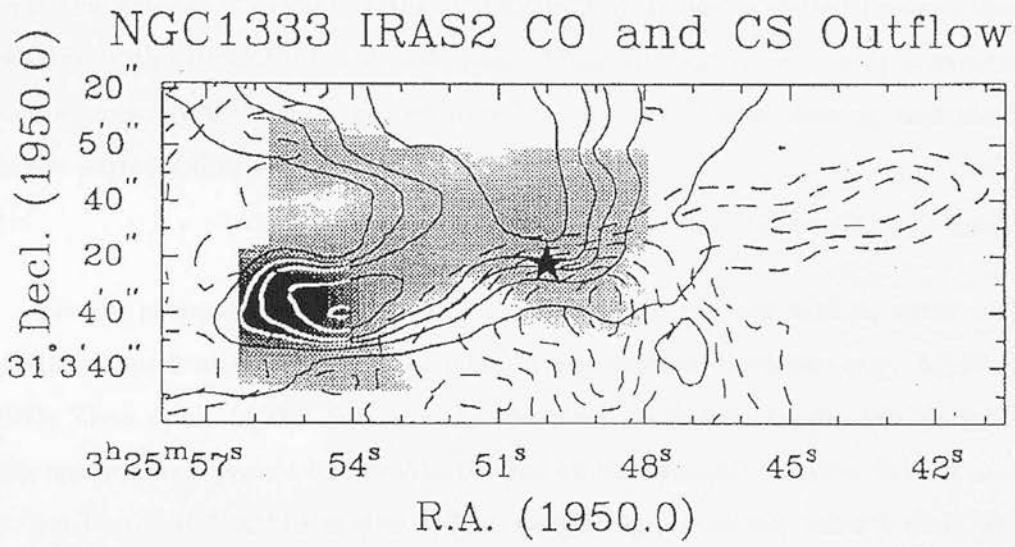

Figure 3.3: Map of the central part of the IRAS2 outflow, taken from Sandell & Aspin (1993). The solid and dashed contours show integrated red- and blue-shifted CO($J = 2 \rightarrow 1$) emission respectively. The greyscale is integrated red-shifted CS($J = 5 \rightarrow 4$) emission.

less deeply embedded companion to IRAS2, as speculated by Sandell et al. (1994). One possible explanation is that the companion is still deeply embedded, although less so than IRAS2 itself, and is responsible for the southeast-northwest elongation of the submillimetre continuum emission. In this case, the position of the north-south outflow driving source would lie $\sim 10 - 15$ arseconds to the *northwest* of the submillimetre continuum peak. Interferometer observations may be able to resolve this question.

New observations

JCMT spectra taken at the position of NGC1333-IRAS2 (hereafter IRAS2) are presented in Figure 3.4. Both the $HCO^+(J = 4 \rightarrow 3)$ and CS($J = 5 \rightarrow 4$) spectra show asymmetric double peaked line profiles, with the blue peak stronger. The absorption dip in the $HCO^+(J = 4 \rightarrow 3)$ line profile is particularly strong, and coincides in velocity with the peak of the isotopic line. Also visible in the main line HCO^+ and CS spectra are broad, low-level wings, which are probably tracing the outflowing gas associated

with this source. The peak of the $C^{18}O(J = 2 \rightarrow 1)$ line is shifted towards the blue relative to the $H^{13}CO^+(J = 4 \rightarrow 3)$ peak. Since $H^{13}CO^+(J = 4 \rightarrow 3)$ is expected to be the optically thinner of the two lines, we interpret this as showing that the $C^{18}O$ line is partially optically thick in this object.

Several properties of the spectra displayed, which we now outline, agree with the predicted qualitative signatures of infall in protostellar envelopes (e.g. Myers et al. 1995; Zhou et al. 1993). For optically thin lines, radiative transfer models predict a symmetric single peaked line profile, centred on the systemic velocity. Such a profile is shown by the $H^{13}CO^+(J = 4 \rightarrow 3)$ line, suggesting a systemic velocity of $7.7\,\mathrm{km\,s^{-1}}$. The asymmetric double-peaked line profiles skewed towards blue velocities seen in both the $HCO^+(J = 4 \rightarrow 3)$ and $CS(J = 5 \rightarrow 4)$ spectra are predicted by radiative transfer models of infalling envelopes for optically thick lines (see Chapters 1 and 4). The velocity of the self-absorption minimum may coincide with the systemic velocity, or be red-shifted with respect to it, depending on the optical depth of the line and the velocity and density structure of the envelope. The $C^{18}O(J = 2 \rightarrow 1)$ line profile, which is slightly asymmetric, and blue-shifted with respect to the systemic velocity, is also consistent with infall model predictions for a line with small but non-negligible optical depth. The only disagreements with the qualitative expectations of a pure infall model are the strong high velocity wings seen in several of the spectra (infall models do predict high velocity wings, but at a lower level than observed here), and the very small red-shift of the peak of the $CS(J = 7 \rightarrow 6)$ line profile, with respect to the inferred systemic velocity.

Recently, Mardones et al. (1997) obtained on-source spectra of IRAS 2 in $CS(J = 2 \rightarrow 1)$, $N_2H^+(JF_1F_2 = 101 \rightarrow 102)$ and H_2CO $J_{K_{-1}K_1} = (2_{12} \rightarrow 1_{11})$, using the IRAM 30-m telescope. The CS line is single-peaked and approximately symmetrical, peaking at the systemic velocity ($7.7\,\mathrm{km\,s^{-1}}$), and the N_2H^+ line has an infall type asymmetrical profile. Within the infall scenario, this would suggest that the CS line is more optically thin than the N_2H^+ line, contrary to expectations. The H_2CO line profile observed by Mardones et al. (1997) has a complicated, multiple-peaked struc-

ture, with a very broad red-shifted wing, suggesting that this line is sensitive to the outflow. The line core is symmetrical and skewed to the red, which contrasts with the blue-skewed profiles line profiles shown in Figure 3.4. The complete set of spectral line observations at the position of this object do not, therefore, paint a wholly consistent picture. On the whole, however, they are in reasonable agreement with the qualitative expections for an infalling envelope, although the case for infall is weakened by the fact that outflow emission is probably contributing significantly to the line cores in many of the observed transitions.

The spatial dependence of the observed line profiles may be able to shed light on this question. Grid maps of IRAS2 in $HCO^+(J = 4 \rightarrow 3)$ and $CS(J = 5 \rightarrow 4)$ emission are presented in Figures 3.5 and 3.6 respectively. In both maps the emission is centrally peaked, and the strength of the self-absorption feature decreases away from the peak. The off source spectra in the maps show an interesting variety of profiles. In the HCO^+ map there is a clear trend towards broader linewidths from south to north, which is also discernable in the CS map. The CS map spectra show broader and relatively stronger wing emission than the HCO^+ spectra, and may therefore be more sensitive to outflow gas. In a detailed submillimetre spectral line study of the NGC1333-IRAS4 protobinary source, Blake et al. (1995) came to a similar conclusion, finding that the CS abundance is considerably *enhanced* in the outflow, and HCO^+ appears to be less depleted than other neutral species in the dense protostellar envelope.

North of the map centre, a dramatic reversal of the line asymmetry in the HCO^+ map is seen, and the CS spectra show weaker blue-asymmetries. One possible explanation for this is that the emission from the northern (red-shifted) outflow lobe is enhancing the redshifted emission, perhaps due to an interaction with ambient gas at this position. The broader line widths at the northern map positions may also be connected with this, although this is rather speculative.

Centroid velocity maps calculated from the HCO^+ and CS grid maps are shown in

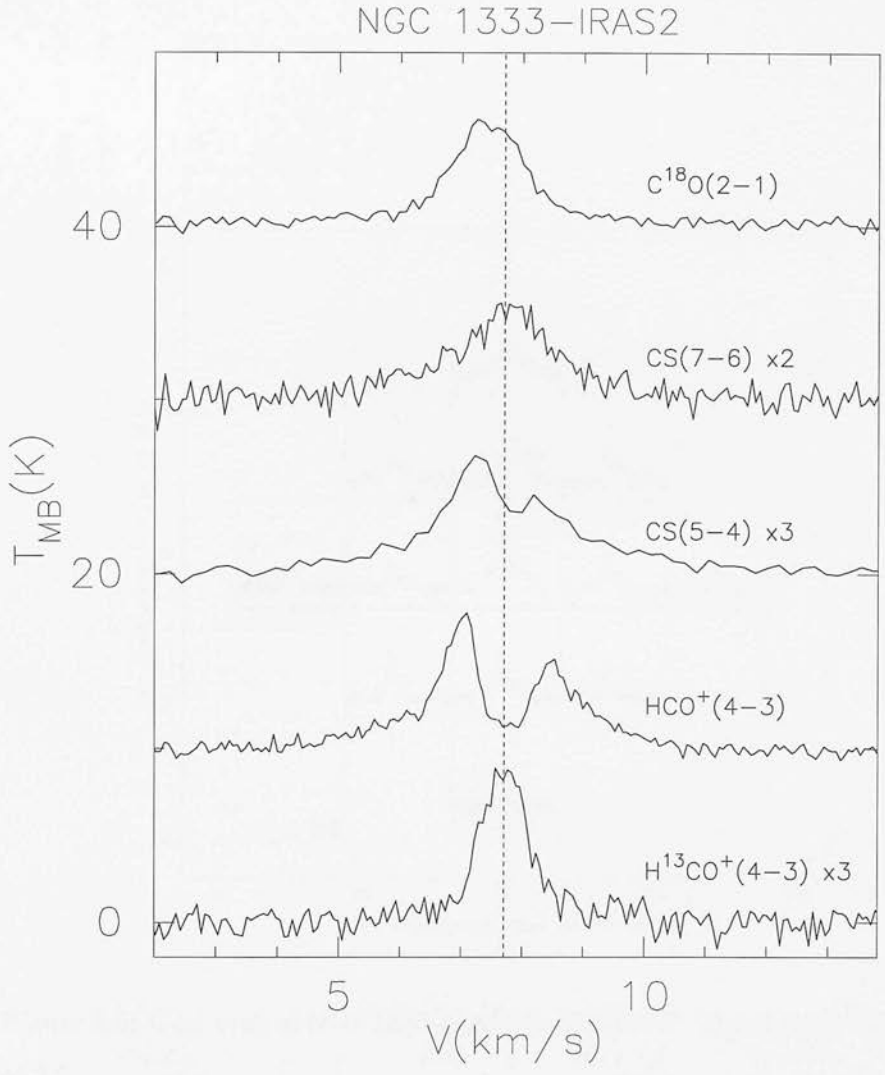

Figure 3.4: Spectra observed towards NGC1333-IRAS2 with the JCMT. The vertical dashed line is at a velocity of $7.7\,\mathrm{km\,s^{-1}}$.

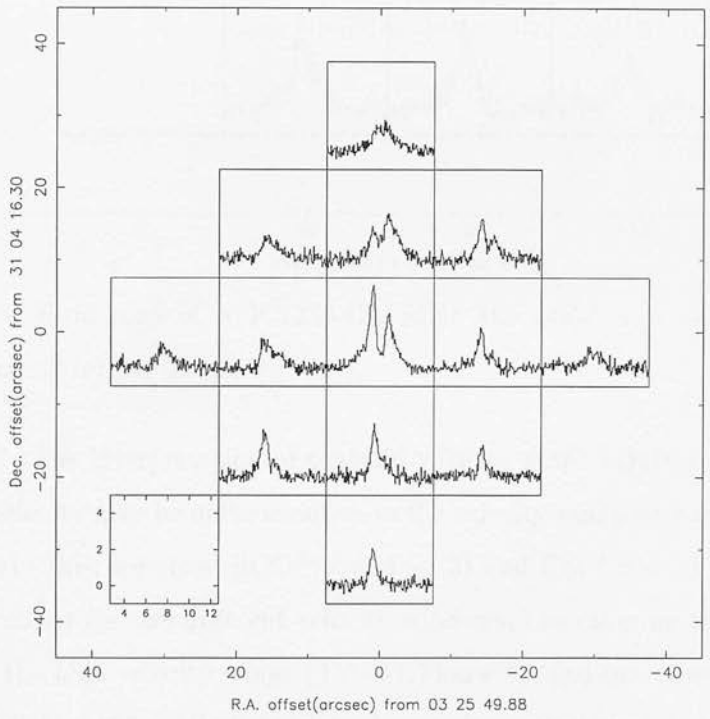

Figure 3.5: Grid map of NGC1333-IRAS2 in the $HCO^+(J = 4 \rightarrow 3)$ transition, in units of T_A^*.

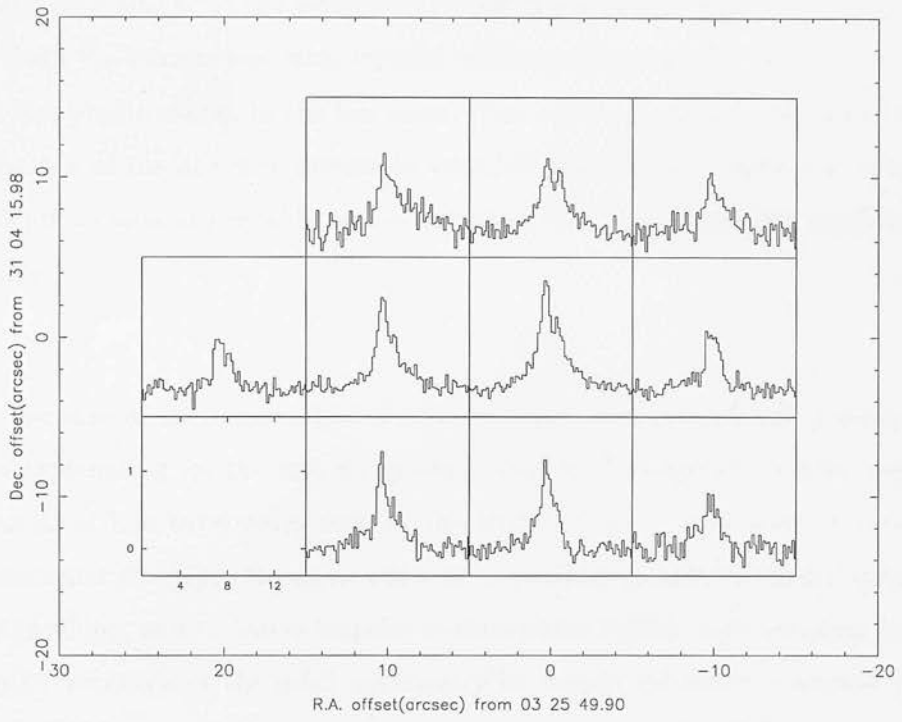

Figure 3.6: Grid map of NGC1333-IRAS2 in the CS($J = 5 \rightarrow 4$) transition. The spectra are calibrated on the T_A^* scale.

Figure 3.7. The interpretation of centroid velocity maps requires some care, since the centroid velocity may be quite sensitive to the velocity range over which it is calculated. To illustrate this, we show $HCO^+(J = 4 \rightarrow 3)$ and CS($J = 5 \rightarrow 4$) centroid velocity plots calculated for two different velocity windows, one covering the entire line profile, including the high velocity wings (3.7 - 11.7 km s^{-1}), and one covering mainly the line core (6.2 - 9.2 km s^{-1}). All of the plots show a clear velocity gradient along an axis with a position angle between 0° and 20°. The velocity gradient is in the same sense as the north-south bipolar outflow (cf. Figure 3.3), suggesting a possible physical connection with it. The east-west outflow may be responsible for the small east-west velocity gradient apparent in the centroid velocity plots calculated over the wider velocity window.

The wide velocity window centroid velocity plots clearly show a much stronger velocity gradient than the narrow velocity window plots, particularly in the CS($J = 5 \rightarrow 4$) maps. This is consistent with the idea that this gradient is caused by the north-south bipolar outflow, and also supports the suggestion that CS is a more sensitive outflow

tracer than HCO^+ . The agreement in the direction of the centroid velocity gradient for both the narrow and wide velocity windows suggests that the outflow even affects the line profile shapes in the line cores. This adds a serious complication to the interpretation of the line core profiles in terms of infall models, since it is then extremely difficult to separate reliably the contribution of the envelope and outflow to the line profile.

Because of the importance of this question, we now examine a possible alternative explanation for the velocity gradient seen in the centroid velocity maps, and the reversal of line asymmetry seen in the $HCO^+(J = 4 \rightarrow 3)$ map — rotation of the protostellar envelope. Rotation will tend to produce a centroid velocity gradient across the envelope, and radiative transfer models which include both rotation and gas infall predict reversals of the infall asymmetry at certain off-centre positions (Zhou 1995; also see Chapter 4), although the *degree* of reversal in the HCO^+ spectrum north of the map centre in Figure 3.5 is larger than typically predicted by such models. Since the line wings of our CS and HCO^+ observations *are* clearly affected by the outflow, we concentrate on centroid velocities calculated over the line core only.

Figure 3.8 shows linear fits to the combined $CS(J = 5 \rightarrow 4)$ and $HCO^+(J = 4 \rightarrow 3)$ centroid velocities calculated over the velocity window 6.7–8.7 $km\,s^{-1}$, along north-south and east-west axes through the source. The fit to the north-south centroid velocity gradient is $7.7(\pm0.9) \times 10^{-3}\,km\,s^{-1}arcsec^{-1}$. For a distance of 220pc, this is equivalent to $7.2\pm0.8\,km\,s^{-1}pc^{-1}$. The corresponding numbers for the east-west velocity gradient are $-8.0(\pm0.8)\times\ 10^{-5}\,km\,s^{-1}arcsec^{-1}$ and $7.5(\pm0.7) \times 10^{-2}\,km\,s^{-1}pc^{-1}$. The interpretation of centroid velocities is complicated by optical depth effects, since both the transitions are optically thick in the line centre. Furthermore, infall motions in the envelope will tend to skew the profiles of optically thick lines towards bluer velocities, in a spatially non-uniform manner. One indication of this is the fact that the centroid velocities along the east-west axis are blue-shifted by $\simeq 0.1\,km\,s^{-1}$, on average, with respect to the systemic velocity. The measured centroid velocity gradient for an optically thick line is therefore an unreliable measure of the actual velocity gradient in

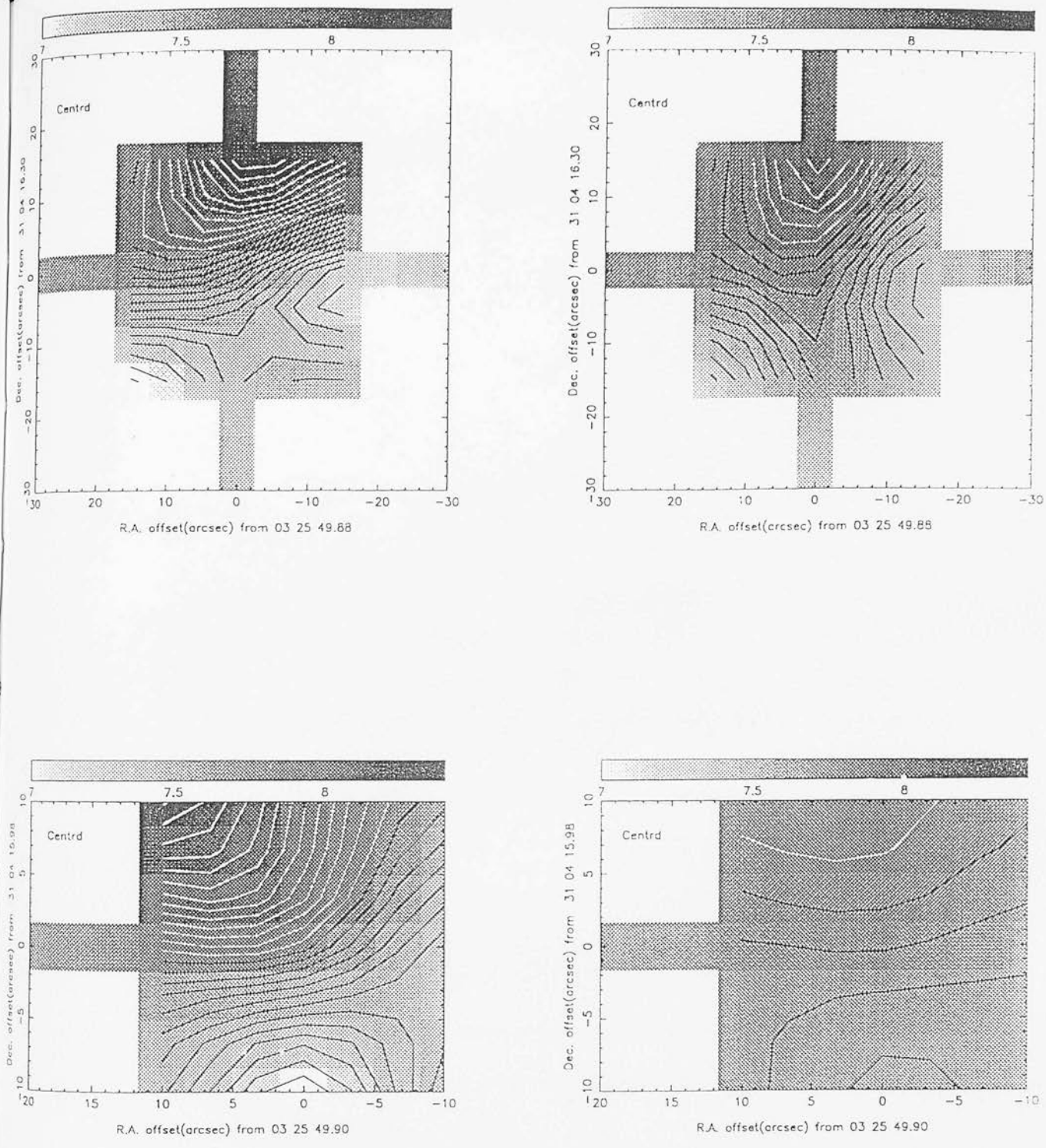

Figure 3.7: Comparison of centroid velocity maps calculated over the velocity range 3.7-11.7 $\mathrm{km\,s^{-1}}$(left) and 6.2-9.2 $\mathrm{km\,s^{-1}}$(right), respectively covering the whole line profiles and the line cores. The top and bottom panels show $HCO^+(J = 4 \rightarrow 3)$ and $CS(J = 5 \rightarrow 4)$ centroid velocity plots respectively. The greyscaling and contour spacing (0.05 $\mathrm{km\,s^{-1}}$) are identical over all of the maps. The first light contour in each case marks a centroid velocity of 7.7 $\mathrm{km\,s^{-1}}$.

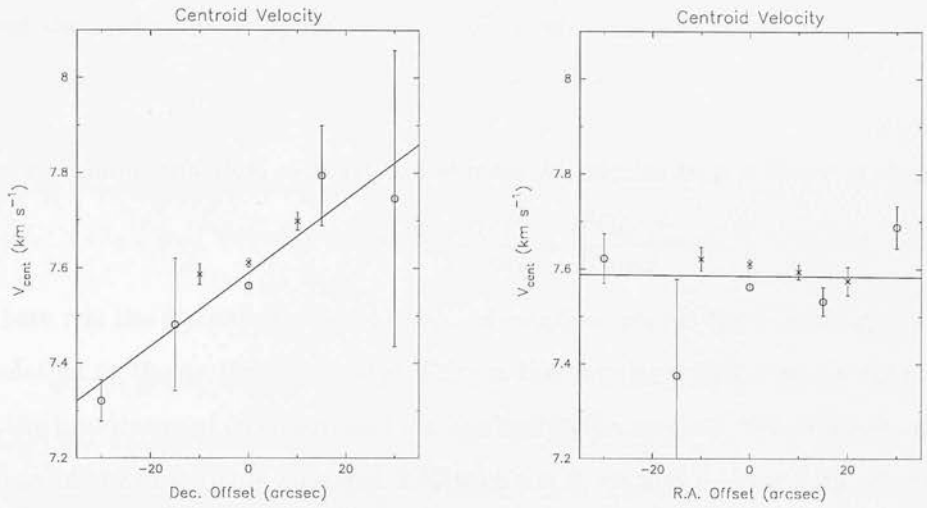

Figure 3.8: Plot showing weighted least-squares linear fits to the centroid velocities along north-south (left) and east-west (right) axes through the position of NGC1333-IRAS2 submillimetre continuum peak (at the map origin). The circles and crosses denote $HCO^+(J = 4 \rightarrow 3)$ and $CS(J = 5 \rightarrow 4)$ measurements respectively. The centroid velocity was calculated over the line core (6.7-8.7 km s^{-1}). The fit parameters are given in the text.

the object, and a proper treatment requires full radiative transfer modelling, or the use of optically thin lines to eliminate optical depth effects. For the purposes of the present discussion, however, we assume that our centroid velocity gradient measurements give a reasonable indication of the actual line-of-sight velocity gradient across the object due to rotation.

Using the assumption that the velocity gradient is due to rotation, a lower limit for the binding mass can be estimated by supposing the rotation is centrifugally balanced by gravity, and that the rotation axis lies in the plane of the sky. This gives a lower limit, because the actual rotation rate may be greater if the rotation axis is inclined out of the plane of the sky, and magnetic fields and pressure gradients may also contribute to the support of the envelope. Furthermore, if part of the envelope is infalling, as some of the observations suggest, then at some level the gravitational forces must dominate

over the centrifugal support.

Assuming spherical symmetry, the mass M interior to a radius r is then given by

$$M = \frac{rv(r)^2}{G\cos i} = \frac{r^3\Omega(r)^2}{G\cos i} \tag{3.39}$$

where r is the distance from the centre of rotation, $v(r)$ is the line of sight velocity at r (relative to the systemic velocity), $\Omega(r)$ is the angular velocity of the rotation at r, G is the gravitational constant, and i is the inclination angle of the rotation axis from the plane of the sky. Using equation 3.39 with $i = 0$, we find a lower limit of of $0.40\,M_\odot$for the enclosed mass inside a 30 arcsecond (6600AU) radius. Sandell et al. (1994) estimated a total dust and gas mass in the IRAS2 protostellar envelope of $0.79\,M_\odot$, and to this must be added the mass of the central protostar. This analysis therefore does not reject the hypothesis that the line-core centroid velocity gradient is tracing rotation about an east-west axis (when projected onto the plane of the sky). Assuming this to be correct, the most likely model is that the east-west bipolar outflow is driven by the Class 0 source, and the protostellar envelope is rotating about this outflow axis. The older north-south outflow is driven by a separate, more evolved (and as yet unobserved) object which may or may not be physically associated with the Class 0 source.

Although we have not been able to eliminate on physical grounds the possibility that the centroid velocity gradient in the line core is due to rotation, we consider it more likely that this velocity gradient is tracing the north-south outflow.

3.2.3 The Ophiuchus star-forming region

The nearby (~125 pc- de Geus, de Zeeuw & Lub 1989) Ophiuchus molecular cloud complex is one of the best known regions of low to intermediate mass star formation (Wilking 1992). The extensive $^{13}CO(J = 2 \rightarrow 1)$ map of the region made by Loren (1989) shows a symmetric morphology to the large scale molecular gas distribution, with the massive cores L1688 and L1689 each connected to lower density filaments extending towards the northeast. Certain morphological and spectroscopic features of

the cloud suggest that the star formation in the complex is being triggered by the passage of a shock front, driven by the adjoining Sco OB2 association (Vrba 1977; Loren & Wootten 1986; Loren 1989; Loren, Wootten & Wilking 1990). Lépine and Duvert (1994) proposed a different scenario, suggesting that the Ophiuchus complex was produced when a high velocity HI cloud collided with and passed through the galactic plane.

The L1688 cloud (also referred to as the ρ Oph cloud) is associated with a rich cluster of about 100 embedded young stellar objects (e.g. Greene & Young 1992; André & Montmerle 1994; Greene et al. 1994; Strom, Kepner & Strom 1995; Greene & Lada 1996). It contains a number of dense cores, believed to be current or probable future sites of star formation (Mezger et al. 1990; Loren, Wootten & Wilking 1990; AWB; Abergel et al. 1996). L1688 has been noted for its apparently high star formation efficiency (SFE $= M_{\rm stars}/[M_{\rm stars}+M_{\rm cloud}]$), suggesting a bound cluster is forming. This conclusion, however, depends on a disputed value of the molecular gas mass (Liseau et al. 1995). Estimates of the mass of the cloud range from $550\,{\rm M}_\odot$ (Wilking & Lada 1983) to $2500\,{\rm M}_\odot$ (Liseau et al. 1995).

3.2.4 VLA 1623

The warm ($T_{\rm kin} \sim$ 30-45 K) ρ Oph A core, situated towards the northwestern boundary of L1688, hosts the prototypical Class 0 source, VLA 1623, which powers an extremely collimated and energetic bipolar outflow lying close to the plane of the sky (André et al. 1990; AWB; Dent, Matthews & Walther 1995). VLA 1623 has an estimated envelope mass and luminosity of $0.6\,{\rm M}_\odot$ and 0.5–$2.5\,{\rm L}_\odot$ respectively (AWB), and a ratio $L_{\rm submm}/L_{\rm bol} \sim 0.1$. Despite showing a strong dust continuum peak, VLA 1623 is remarkable for the absence of peaked emission in virtually all observed molecular transitions (e.g. Wootten et al. 1994; Yu & Chernin 1997). This is often attributed to the depletion of molecules onto dust grains in the cold, dense envelope. There has recently been speculation that VLA 1623 is a multiple source driving two separate but closely aligned bipolar outflows (Dent et al. 1995; Yu & Chernin 1997), although the

evidence for this is not yet convincing.

The density structure of the VLA 1623 envelope has been investigated both by radiative transfer modelling of the dust continuum emission (AWB) and by modelling the extinction of the smooth near-infrared background by the protostellar envelope (Dent et al. 1995). Both these studies have found that Shu model density profiles cannot produce an adequate fit to the observations, and suggest that the actual density profile may be closer to a gaussian distribution.

Several features point to VLA 1623 being an unusually young Class 0 source: It has one of the largest values of $L_{\rm submm}/L_{\rm bol}$, usually taken to be a measure of youth, of all the Class 0 sources, and the dynamical timescale for the collimated outflow is only $\sim 5 \times 10^3\,{\rm yr}$ (André et al. 1990). The relatively low bolometric luminosity implies a small value for the central protostellar mass $<\sim 0.1\,{\rm M}_\odot$ (if the luminosity is derived from accretion at the expected rate), which in turn implies a collapse age of $\sim 10^4\,{\rm yr}$ (AWB). The strong molecular depletion in the envelope suggests that the the central protostar has not had sufficient time or luminosity to warm dust grains and sublimate ice mantles back into the gas phase. Finally, most collapse models predict that soon after the formation of the central protostar, the envelope density distribution should approach a power law distribution (e.g. Larson 1969; Foster & Chevalier 1993; Galli & Shu 1993). The fact that the density distribution in the VLA 1623 envelope appears to be approximately gaussian may therefore provide further support for a very young age.

New observations

Figure 3.9 shows the on source spectra observed towards VLA 1623. The $H^{13}CO^+(J = 4 \rightarrow 3)$ profile is symmetric, narrow, and is probably optically thin, so we use the peak of this line as the best indicator of the systemic velocity. All of the other lines in the figure show a strong blue wing, probably tracing the outflow, and secondary

peaks are apparent in the blue wing of the $HCO^+(J = 4 \rightarrow 3)$ and $CS(J = 5 \rightarrow 4)$ lines. Apart from the blueshift of the peak of the $C^{18}O(J = 3 \rightarrow 2)$ line relative to that of the $H^{13}CO^+(J = 4 \rightarrow 3)$ line, the set of line profiles do not show the signatures expected for infall. Since VLA 1623 is the 'prototypical' Class 0 source, this is somewhat surprising. The orientation of the outflow close to the plane of the sky would appear to be a favorable configuration for observing infall in the 'equatorial' plane, if present (although it may be argued that if the outflow lies in the plane of the sky, its emission will be projected onto lower velocities, possibly producing greater confusion with the emission from the protostellar envelope).

If the VLA 1623 envelope is actually infalling, then the lack of observed infall signatures may be partly explained by factors relating to the extreme youth of the source. During the earliest stages of collapse, the infall velocities are expected to be relatively small compared to the later stages, and may be difficult to detect spectroscopically. The observed line profiles are probably adversely affected by the strong depletion of tracer molecules in the envelope. Conversely, the gas entrained in the outflow and in the boundary layer between the outflow and the envelope is probably much warmer than the gas in the envelope, causing tracer molecules or their progenitors to be locally released from grain mantles into the gas phase. The excavation of an outflow cavity may also allow the central protostar to be more efficient at heating the envelope along the cavity walls. This could have the result that the molecular emission in the earliest stages of protostellar evolution preferentially traces gas which is being perturbed by the outflow. The depletion of molecules in the rest of the envelope would also have the effect of reducing the attenuation of the outflow emission as it passes through the envelope on the way to the observer. The absence of clear infall signatures observed towards this object does not necessarily rule out, therefore, the possibility that infall is taking place. We simply do not find any evidence in favour of it. This example highlights some of the inherent difficulties in using molecular line emission as a probe of protostellar envelope dynamics.

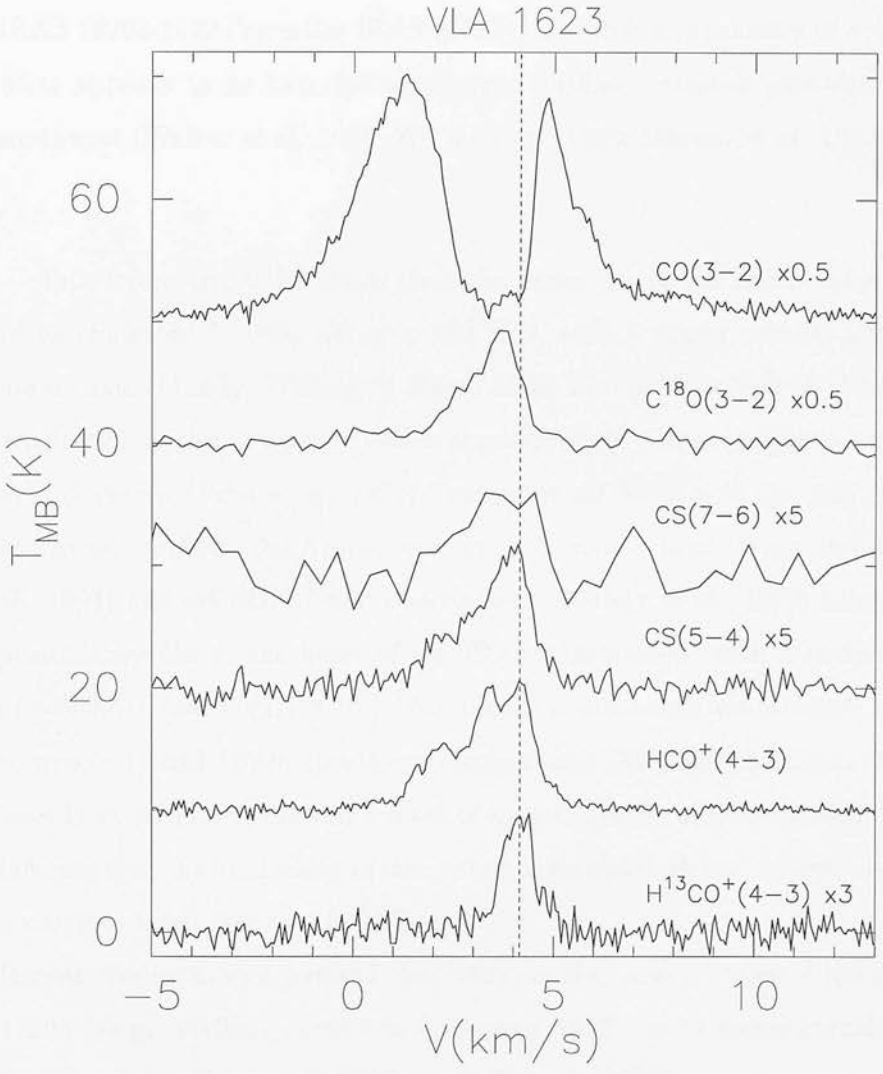

Figure 3.9: JCMT spectra observed towards VLA 1623. The vertical dashed line marks the inferred systemic velocity of $4.1\,\mathrm{km\,s^{-1}}$.

3.2.5 IRAS 16293 -2422

About one degree to the east of L1688 lies the L1689 cloud, which divides into northern and southern components, labelled L1689N and L1689S, in the $^{13}CO(J = 1 \rightarrow 0)$ map of Loren (1988). The 15 $M_{\odot}$ L1689N core hosts the well studied protobinary source, IRAS 16293-2422 (hereafter IRAS 16293). This has a luminosity of $\sim 30 L_{\odot}$ and drives what appears to be two distinct bipolar outflows oriented east-west and northeast-southwest (Walker et al. 1988; Walker et al. 1990; Mizuno et al. 1990).

Interferometric $C^{18}O$ maps show the dense gas in the inner region of IRAS 16293 to be elongated ($\sim$1800 AU $\times <$ 800 AU), with a strong velocity gradient along the major axis (Mundy, Wilking & Myers 1986; Mundy, Wootten & Wilking 1990). The orientation of the elongation axis is approximately perpendicular to both the magnetic field direction (Vrba et al. 1976; Tamura et al. 1993) and the axis of the northeast-southwest outflow. VLA observations at 2cm and 6cm (Wootten 1989; Estalella et al. 1991) and OVRO 2.7-mm observations (Mundy et al. 1992) have revealed that a protobinary lies at the heart of the IRAS 16293 cloud, with a separation on the sky of $\sim$650 AU (see Figure 3.10). The binary components are labelled 1629a (southeast component) and 1629b (northwest component) (Walker, Carlstrom & Bieging 1993). Mundy et al. (1992) derived a mass of approximately 0.5 $M_{\odot}$ for each component, and inferred that the luminosity of the system is provided almost entirely by accretion, with a required infall rate of $10^{-5}\,M_{\odot}yr^{-1}$.
Recent studies have suggested that 1629a is the focus of most of the activity in IRAS 16293. (e.g. Walker, Carlstrom & Bieging 1993). H_2O maser emission has been detected towards this object (Wilking & Claussen 1987).

IRAS 16293 was one of the first protostellar candidates claimed to show spectroscopic evidence for gas infall (Walker et al. 1986). This claim was disputed by Menten et al. (1987), who argued that rotation of the gas envelope and foreground absorption gave a more consistent explanation of the observed line profiles. More recently, Zhou (1995) re-examined the issue, and found good agreement with a model incorporating

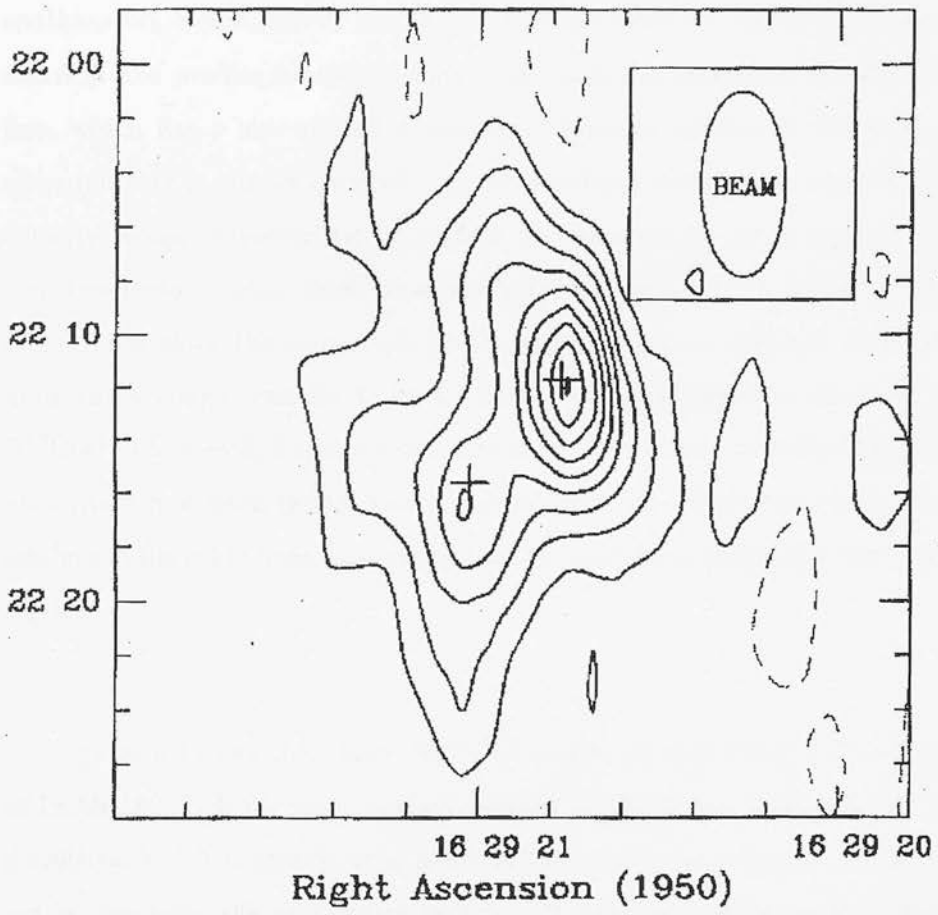

Figure 3.10: 3-mm continuum map of the IRAS 16293 protobinary, taken with the Hat Creek interferometer (from Walker, Carlstrom & Bieging 1993).

both infall and rotation.

New observations

Figure 3.11 shows the spectral line profiles observed towards the position of 1629a, the southeastern component of the IRAS 16293 protobinary. All of the lines show asymmetrical line profiles consistent with infall, with the exception of the CO($J = 3 \rightarrow 2$) line, which has a blue-shifted absorption minimum relative to the systemic velocity, although this is almost certainly due to unrelated foreground material. Broad high-velocity wings characteristic of outflow are apparent in all of the main-line spectra. The two isotopic lines show remarkably broad line cores ($\sim 3\,\mathrm{km\,s^{-1}}$FWHM). None of the lines show the symmetric profile expected for an optically thin line. We estimate the systemic velocity to be $4.1\,\mathrm{km\,s^{-1}}$, by assuming that the outer parts of the $H^{13}CO^{+}(J = 4 \rightarrow 3)$ line are symmetrical about systemic velocity. The velocity of the absorption minimum in this line is significantly red-shifted relative to the absorption minima of the other lines, suggesting that the absorbing material is well inside the infall region.

Figures 3.12 and 3.13 show $HCO^{+}(J = 4 \rightarrow 3)$ and CS($J = 7 \rightarrow 6$) raster maps of IRAS 16293. Both maps are well peaked at the origin, and show blue-asymmetric double-peaked line profiles over much of the central map region. To the south of the centre, however, the asymmetry becomes weaker, and can be seen to reverse at some positions towards the southern edge of the HCO^{+} map. This trend was also found in the CS($J = 3 \rightarrow 2$) map of Menten et al. (1987) and in the CS($J = 2 \rightarrow 1$) map of Walker, Carlstrom & Bieging (1993), and was attributed to rotation of the cloud. The integrated intensity greyscale map in Figure 3.14 reveals a low level 'halo' of HCO^{+} emission well over an arcminute across, surrounding the compact central emission peak. A secondary emission peak lies to the east of the main peak, extending beyond the eastern edge of the map, which we label 16293-E. The main peak itself is well resolved in the 13.6″ beam, (the FWHM level is approximately given by the first

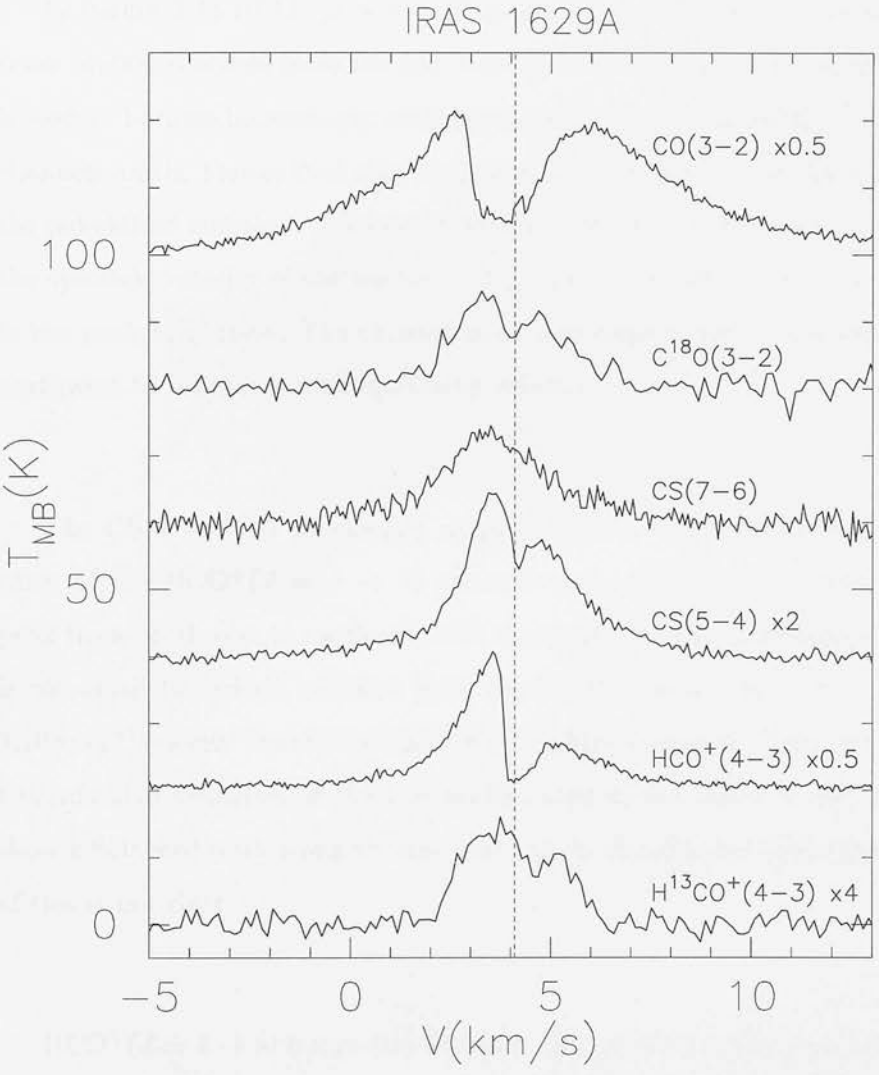

Figure 3.11: JCMT spectra observed towards IRAS 1629a. The vertical dashed line is at a velocity of 4.1 km s^{-1}.

light contour), and we estimate the deconvolved size of the HCO^+ peak to be $27'' \times 19''$, with the major axis oriented at a position angle of $\simeq 100°$. In the lower contours, an extension of bright emission towards the northwest can be seen.

In Figure 3.15 $HCO^+(J = 4 \rightarrow 3)$ channel maps are plotted. As the velocities become further removed from the rest velocity of the source ($\sim 4.1\,\mathrm{km\,s^{-1}}$), the emission is seen to become increasingly confined towards the central position. Furthermore, the channels on the blue-shifted side of the systemic velocity are consistently brighter than the red-shifted emission. Because of the self-absorption the channel which encompasses the systemic velocity of the source ($\sim 4.1\,\mathrm{km\,s^{-1}}$) actually represents a local *minimum* in the peak brightness. The channel maps also show a shift of the emission peak from northwest to southeast with increasing velocity.

The $CS(J = 7 \rightarrow 6)$ channel maps in Figure 3.16 reproduces many of the features of the $HCO^+(J = 4 \rightarrow 3)$ channel maps, including the shift in the emission peak from northwest to southeast with increasing velocity, although the area coverage is too small to include emission from the 16293-E peak. In both channel maps, the $3.10\,\mathrm{km\,s^{-1}}$velocity channel contains the brightest emission. This reflects the skewing towards blue velocities of the line profiles seen in the raster maps. Both transitions show a flattened peak along an east-west axis in this channel, although the significance of this is not clear.

$HCO^+(J = 4 \rightarrow 3)$ integrated intensity and centroid velocity maps, over the region of strongest emission, are compared in Figure 3.17. The centroid velocity map clearly shows a coherent velocity gradient across the bright HCO^+ peak, along an axis with a position angle of $+60°$. This velocity gradient has been noted in previous molecular line studies of IRAS 16293 (Menten et al. 1987; Walker, Carlstrom & Bieging 1993). In contrast to NGC1333-IRAS2, the centroid velocity gradient can be ascribed with reasonable confidence to rotation, first because of the remarkably parallel and coherent centroid velocity contours over a large part of the envelope, and secondly because there

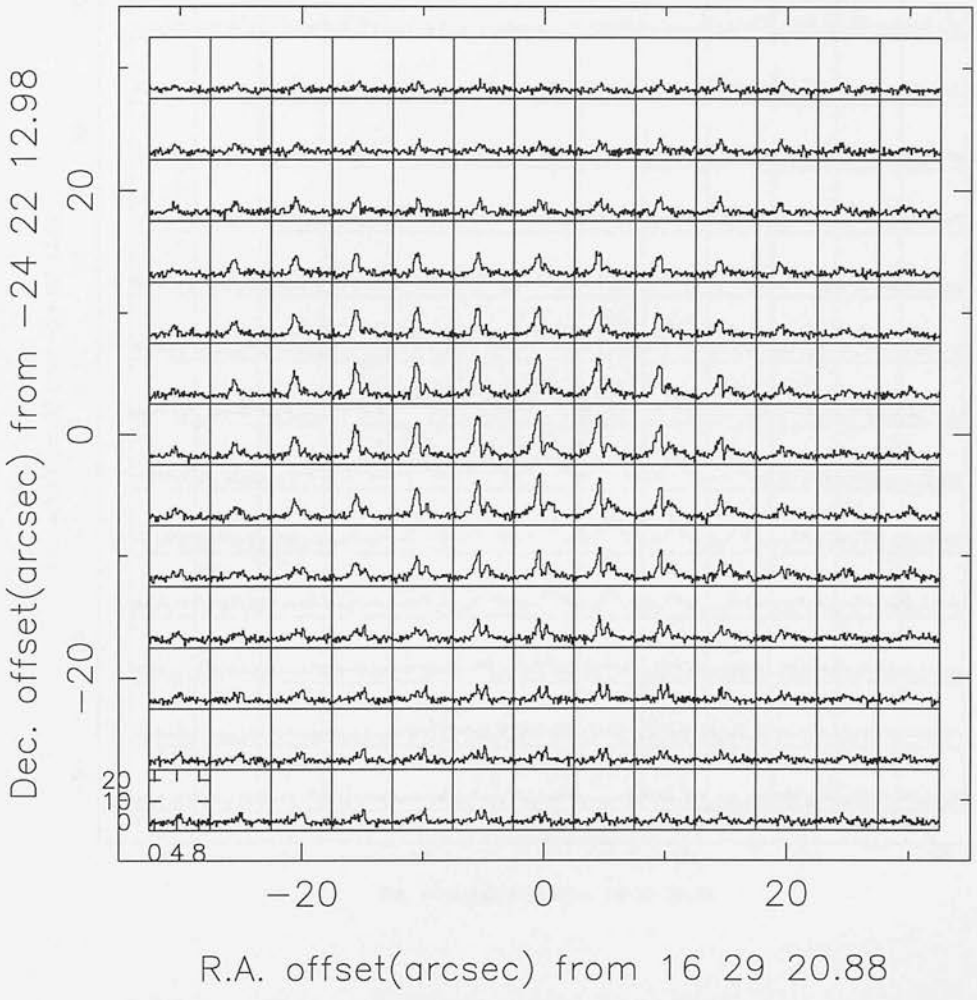

Figure 3.12: Central region of the $HCO^+(J = 4 \rightarrow 3)$ raster map of IRAS 16293.

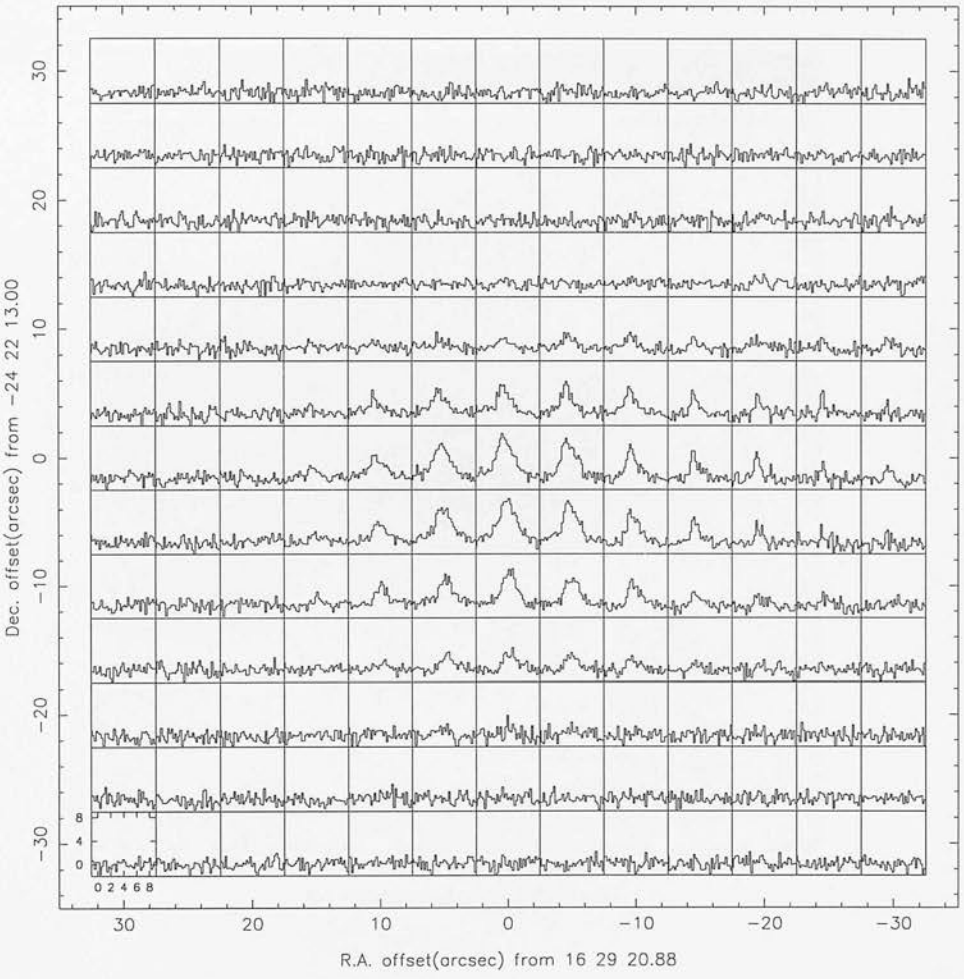

Figure 3.13: Raster map of IRAS 16293-2422 in the CS($J = 7 \rightarrow 6$) transition.

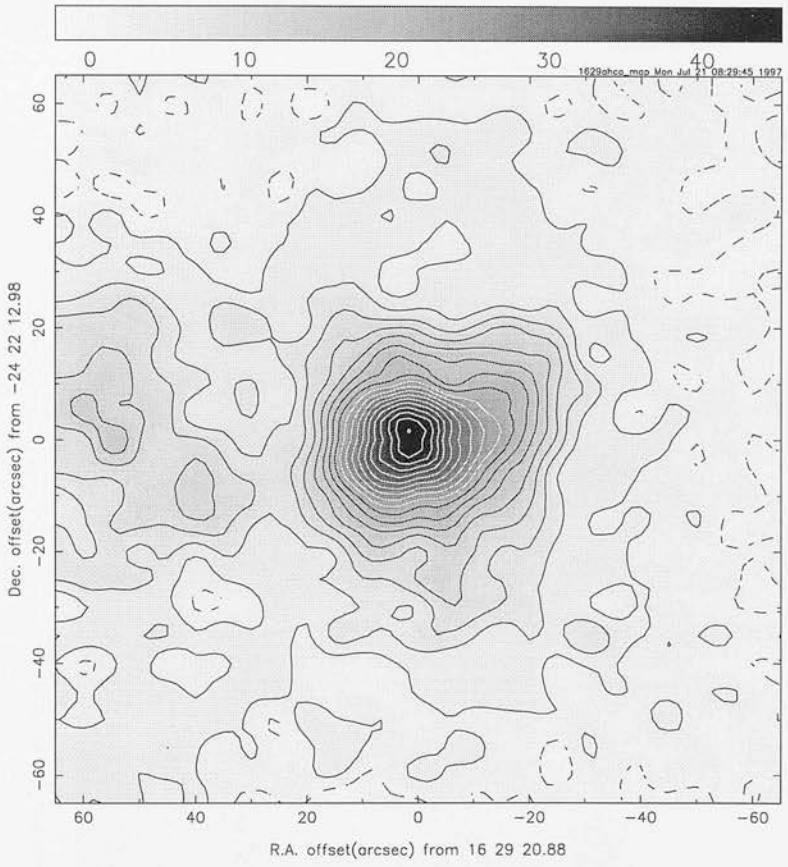

Figure 3.14: Greyscale map of IRAS 16293-2422 in integrated $HCO^+(J = 4 \rightarrow 3)$ emission, between 1.1 and 7.1 km s^{-1}. The contour step is 2.5K km s^{-1}starting at -2.5K km s^{-1}. The beam size is 13.6 arcseconds.

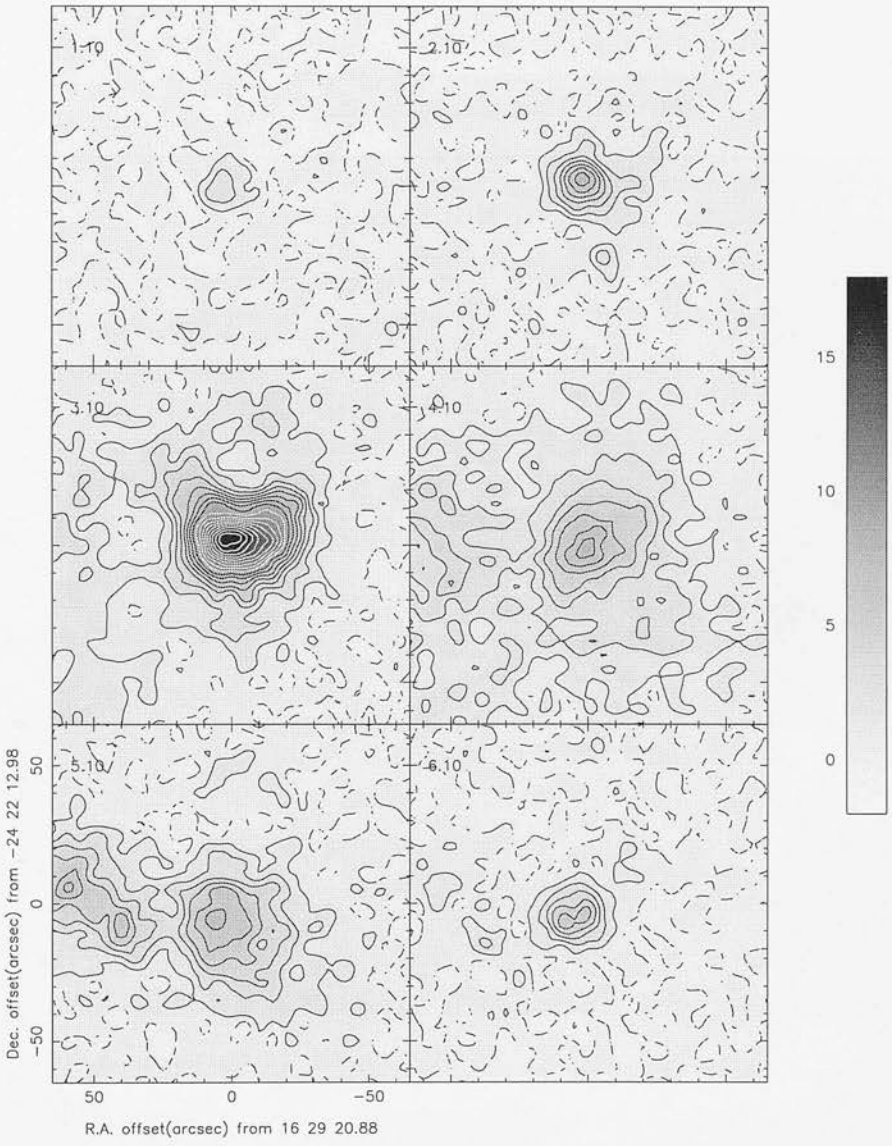

Figure 3.15: Channel maps of IRAS 16293-2422 in $HCO^+(J = 4 \rightarrow 3)$ emission. Contours increase in steps of 1.0K km s^{-1}from a base level of -1.0K km s^{-1}.

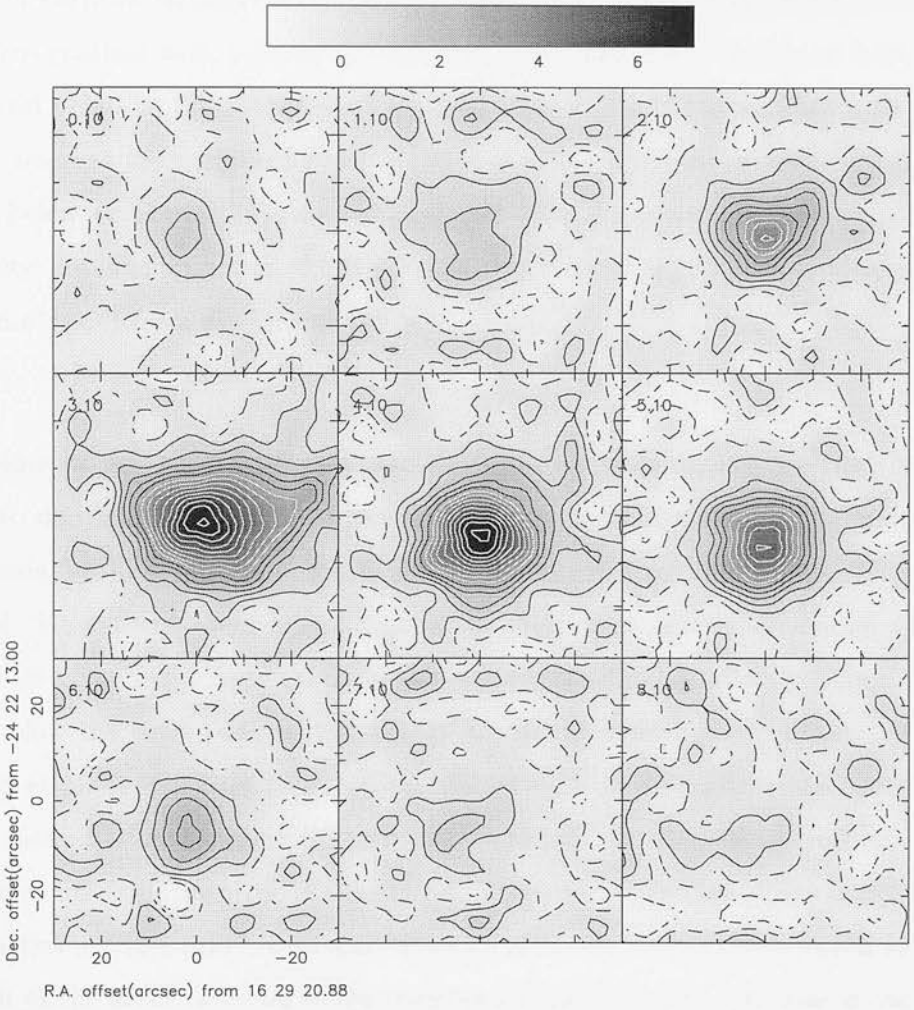

Figure 3.16: CS($J = 7 \rightarrow 6$) channel maps of IRAS 16293. Contours start at -0.5K km s^{-1}and increase in intervals of 0.5K km s^{-1}.

appears to be no confusion from the outflow (the velocity gradient of the CO outflow in this direction has an *opposite sign* to the gradient measured here – see Figure 3.20 below).

Plots of centroid velocity versus position along axes parallel and perpendicular to the velocity gradient axis, passing through the origin, are shown in Figure 3.18. We selected grid points in the observed maps displaced less than ~4 arcseconds from each axis, and assigned the measured centroid velocity to the point along the axis perpendicularly below or above the observed position. The measured gradient parallel to the velocity gradient axis was -0.040(±0.003) $\mathrm{km\,s^{-1}arcsec^{-1}}$. This is equivalent to 66(±5) $\mathrm{km\,s^{-1}pc^{-1}}$ for a distance of 125 pc.

As before we assume the velocity gradient is due to rotation, and use the inferred rotation to derive a lower limit for the mass of the central region, by assuming the rotation axis lies in the plane of the sky, and that the central region is centrifugally supported. We derive a lower limit for the mass enclosed between the position offsets -15 and +10 along the velocity gradient axis (see Figure 3.18) of $0.3\,\mathrm{M_\odot}$. This is comfortably below the corresponding estimate of $1.2\,\mathrm{M_\odot}$(for a distance of 125pc) derived by Mezger et al. (1992) from observations of dust continuum emission, and probably indicates that rotational support is not dominant at this scale, unless the rotation axis is highly inclined from the plane of the sky (cf. Walker, Carlstrom & Bieging, 1993). It is nevertheless possible that centrifugal flattening of the envelope is responsible for the elongation of the lower contours of the integrated $\mathrm{HCO^+}(J = 4 \rightarrow 3)$ map in the top panel of Figure 3.17, which are approximately aligned perpendicularly to the rotation axis inferred from the centroid velocity map.

The 16293-E peak coincides with the western limb of the $\sim 4\,\mathrm{M_\odot}$ ammonia core discovered by Mizuno et al. (1990), who found evidence that this core was interacting with the eastern blue-shifted outflow lobe from IRAS 16293. Examination of the channel maps, however, shows that 16293-E peaks in the $5.1\,\mathrm{km\,s^{-1}}$ velocity bin, i.e. it

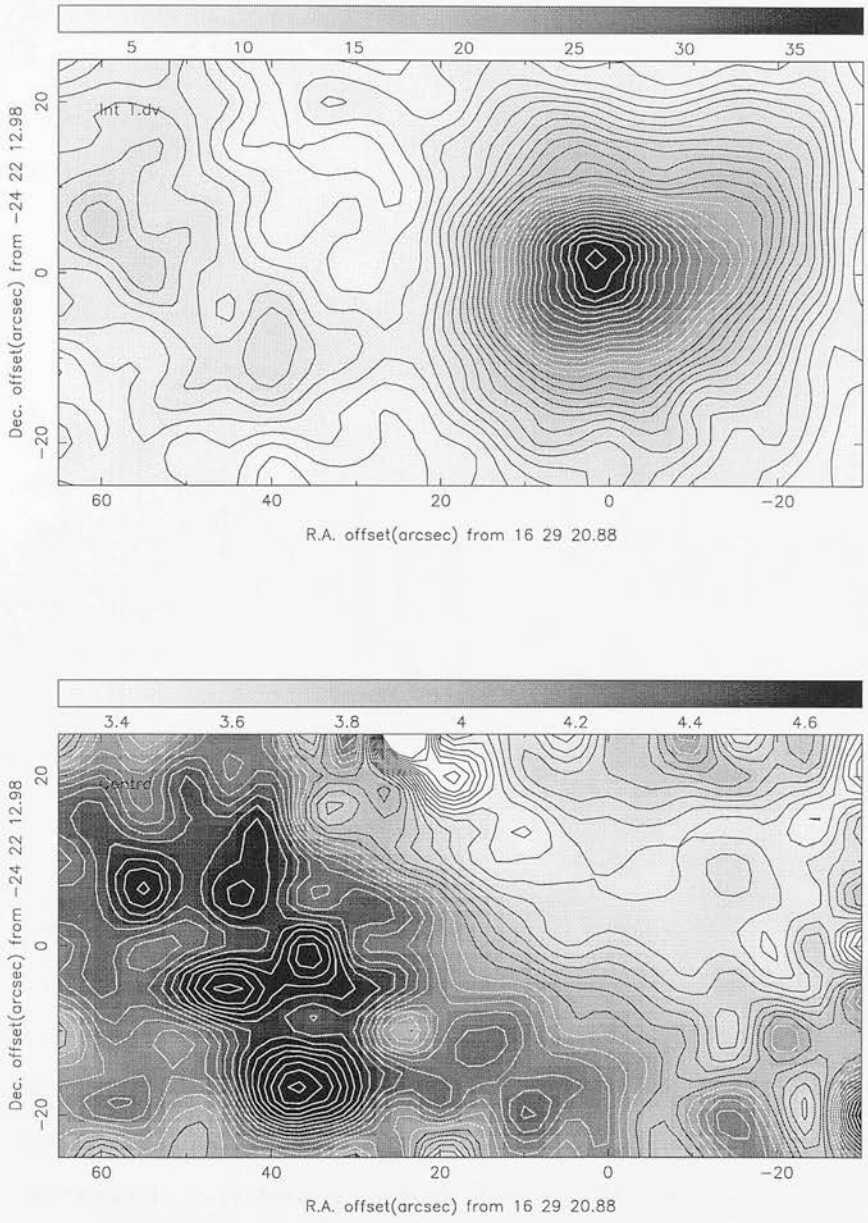

Figure 3.17: $HCO^+(J = 4 \rightarrow 3)$ Integrated intensity map (top) and centroid velocity map (bottom) of the IRAS 16293 and 16293-E, calculated over the velocity interval 2.1-6.1 $km\,s^{-1}$. The integrated intensity map has a peak contour of 37.5 $K\,km\,s^{-1}$ and a contour interval of 1.25 $K\,km\,s^{-1}$. The centroid velocity map has a contour spacing of 0.07 $km\,s^{-1}$. The first light contour, at 4.05 $km\,s^{-1}$, is approximately equal to the systemic velocity.

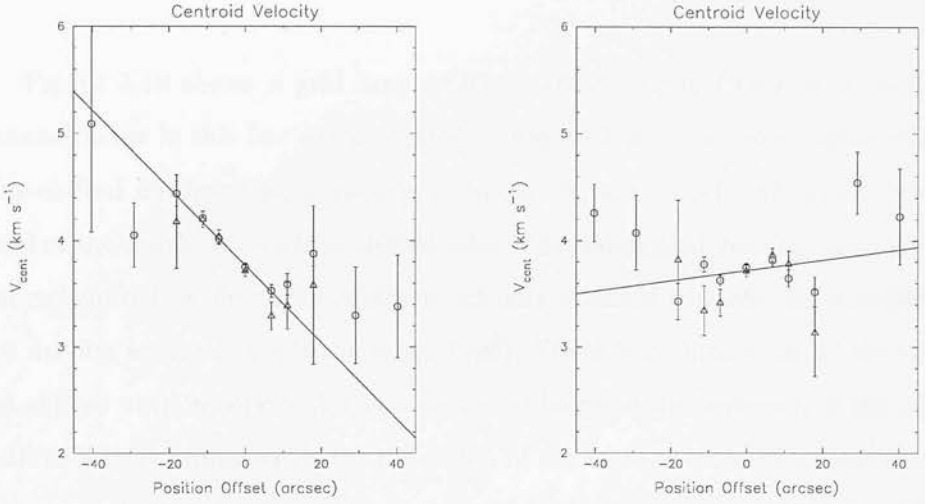

Figure 3.18: Weighted least-squares fits to the centroid velocity gradient along axes through the origin, parallel (left) and perpendicular (right) to the velocity gradient axis at a position angle of 60°. The circles and triangles indicate measurements from the $HCO^+(J = 4 \rightarrow 3)$ and $CS(J = 7 \rightarrow 6)$ raster maps respectively. In both plots, the origin coincides with the origin used in the maps, and increasing position offset corresponds to increasing position from the left hand edge of the maps. In the left hand plot, only points with a position offset between -25 and +15 arcseconds were used in the line fit.

is *red-shifted* with respect to the source rest velocity. This can also be seen from the centroid velocity map in Figure 3.17. If 16293-E is produced by the interaction of the eastern blue-shifted outflow lobe with the ammonia core, as the morphology suggests, then these observations may support the hypothesis of Mizuno et al. (1990), that the red-shifted north-eastern outflow lobe results from the deflection of the eastern blue-shifted outflow lobe after impacting with the ammonia core.

Figure 3.19 shows a grid map of IRAS 16293 in the CO($J = 3 \rightarrow 2$) line, and channel maps in this line are presented in Figure 3.20. The inner region of the eastern blue-shifted outflow lobe is clearly visible in the low velocity channels, as well as the head of the southwestern blue-shifted lobe. The red-shifted velocity bins show the western red-shifted outflow lobe, which is actually oriented towards the northwest, close to the driving source (e.g Walker et al. 1990). There is no indication of the northeastern red-shifted outflow lobe which is observed at larger scales however. If the northeastern outflow lobe is produced by the deflection of the eastern blue-shifted outflow lobe from the ammonia core to the east, as proposed by Mizuno et al. (1990) (see discussion of the HCO^+ data above), then this would explain the absence of the northeastern outflow lobe from our CO map. The origin of the southwestern blue-shifted outflow lobe, which *is* seen in the CO channel maps, is not explained by this model however.

The IRAS 16293 system is clearly very complex and is still not yet fully understood. We have argued, however, that the complex outflow motions do not dominate the $HCO^+(J = 4 \rightarrow 3)$ line profiles observed close to the central protobinary, and that the possible signatures of rotation and infall shown to be present in this data may be attributed with some confidence to the protostellar envelope itself.

3.2.6 L1689S-IRS67

The little studied $\sim$50 $M_\odot$ L1689S cloud, situated about half a degree to the south of IRAS 16293, contains an interesting variety of objects. The only IRAS source in

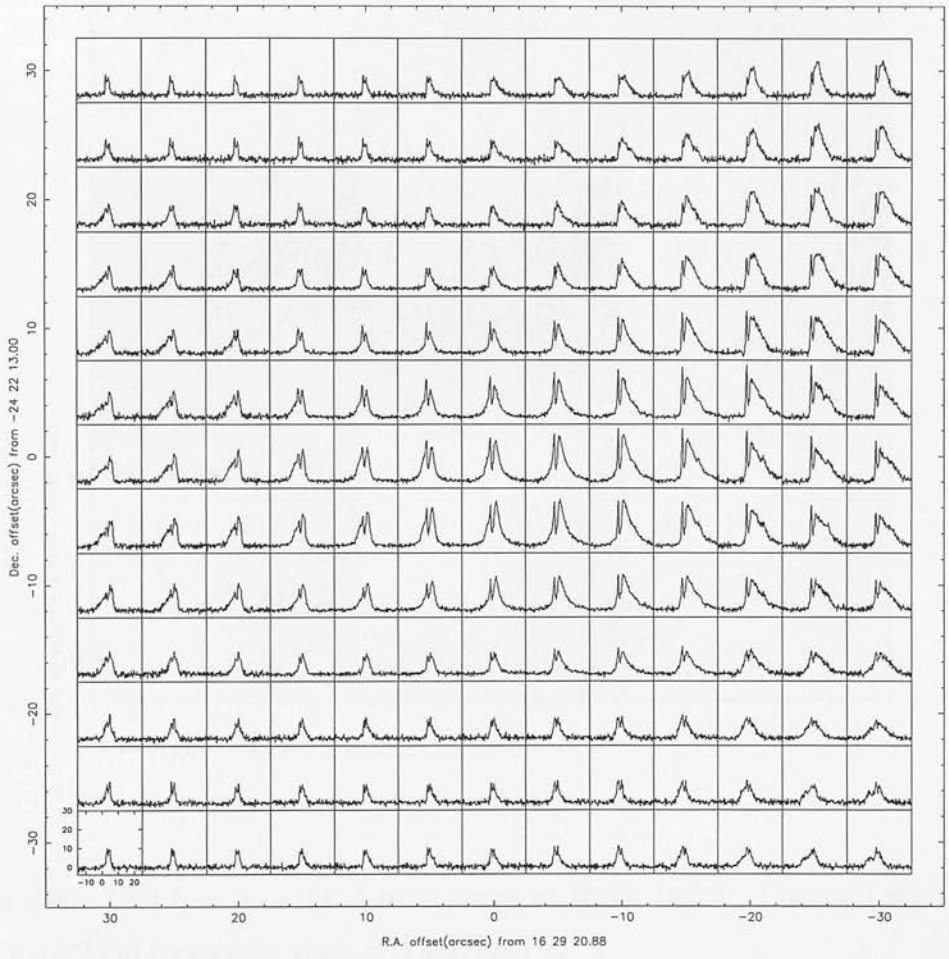

Figure 3.19: CO($J = 3 \rightarrow 2$) raster map of IRAS 16293.

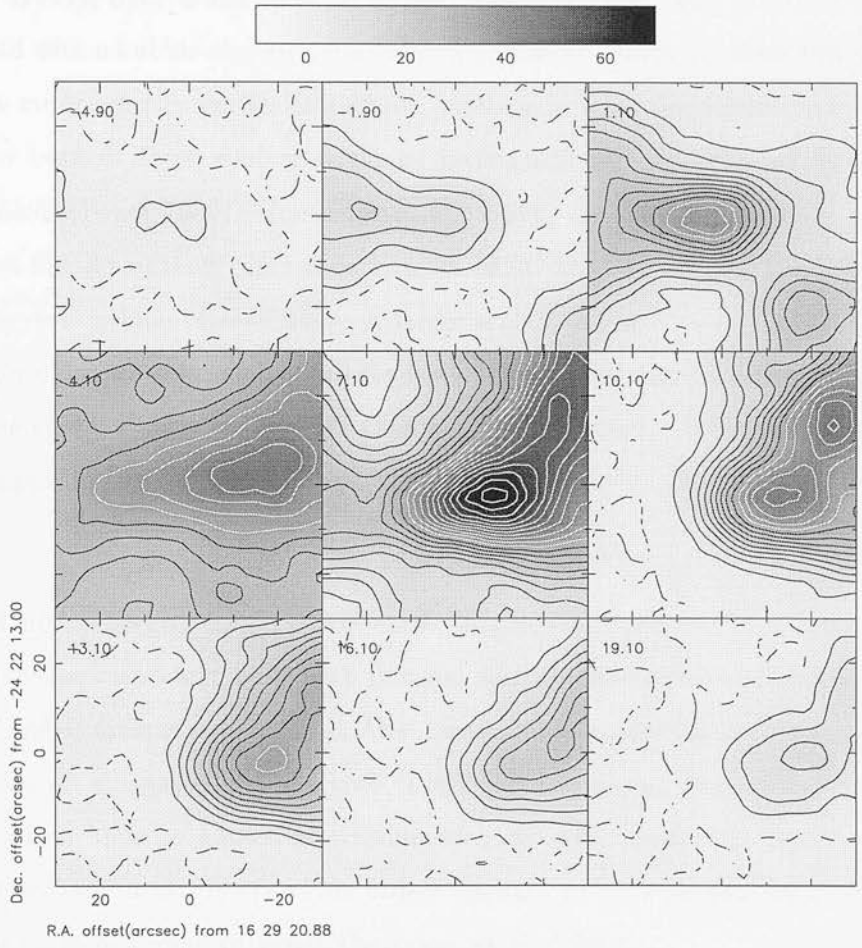

Figure 3.20: CO($J = 3 \rightarrow 2$) channel maps of IRAS 16293. Contours start at -6.66K km s^{-1}and increase in steps of 3.33K km s^{-1}.

the cloud, IRAS 16289-2450, is actually comprised of two Class I near-infrared sources, with a combined luminosity of $\sim 7 L_{\odot}$, separated by about 2 arcminutes in the east-west direction (Wilking 1992; Hodapp 1994; Greene et al. 1994). In the 2.12μm image of Hodapp (1994), the western infrared source (L1689S#1) appears to be double, and is associated with a bubble-shaped nebulosity. The eastern source (L1689S-IRS 67), shows a narrow monopolar extension at 2.12μm, pointing in a north-northwesterly direction. Either or both of these sources could be responsible for the CO outflow associated with L1689S (Fukui 1989). Bontemps et al. (1996) detected an apparent southeast-northwest bipolar outflow centred on L1689S-IRS67 in CO($J = 2 \rightarrow 1$) emission (with the northwestern lobe blue-shifted). A larger scale CO($J = 1 \rightarrow 0$) map of the region (A. Mizuno, private communication) reveals a complicated distribution of high velocity gas in the cloud, suggestive of more than one outflow source. In this map, the IRS67 outflow appears to be aligned along a north-south axis.

A 1.3 millimetre continuum IRAM map of the region (F. Motte, priv. comm.) shows compact peaks coincident with both infrared sources, tracing circumstellar envelopes with estimated masses of $\sim 0.1\,\mathrm{M}_{\odot}$. About one arcminute to the south of the infrared sources lies an elongated $\sim 1\,\mathrm{M}_{\odot}$ core (L1689#2) containing four or five subcondensations, which have no known association with compact infrared or radio continuum sources (Buckley et al. 1997). This object appears to have similar properties to the prestellar cores described in Ward-Thompson et al. (1994).

New observations

Figure 3.21 shows the on-source spectra observed towards L1689S-IRS67 (hereafter IRS67). A narrow absorption feature is visible in the $HCO^+(J = 4 \rightarrow 3)$ line profile, which gives the line a double-peaked, blue-skewed appearance, and a red 'knee' is apparent in the CS($J = 5 \rightarrow 4$) line profile. These two lines identify IRS67 as a possible infall candidate. The $H^{13}CO^+(J = 4 \rightarrow 3)$ line is very weak, and has a rather low signal to noise, although there is some suggestion that it has a double-peaked profile.

Within the noise, the $C^{18}O(J = 3 \rightarrow 2)$ and $CS(J = 7 \rightarrow 6)$ profiles appear to be symmetric about the systemic velocity. The $CO(J = 3 \rightarrow 2)$ profile is quite unusual, with a double-peaked asymmetric core, skewed to the red, and a very bright, blue wing, which unambiguously identifies this object as an outflow source.

Figure 3.22 shows a $HCO^+(J = 4 \rightarrow 3)$ grid map of IRS67. The strength of both emission and absorption are seen to peak close to the source position. At several positions the profiles show enhanced emission in the wings, particularly at the on-source position and along the eastern edge of the map. A northeast-southwest velocity gradient is apparent in the centroid velocity map shown in Figure 3.23. The direction of the velocity gradient is approximately perpendicular to the axis of the bipolar outflow detected towards IRS67 by Bontemps et al. (1996), which suggests the velocity gradient may be tracing rotation rather than outflow.

Linear fits to the centroid velocity, calculated between 2.0 and $6.0\,\mathrm{km\,s^{-1}}$, along axes parallel and perpendicular to the direction of maximum velocity gradient, are shown in Figure 3.24. The right hand panel in the figure shows variation of centroid velocity along the southeast-northwest axis through the source, perpendicular to the velocity gradient. Although the number of data points is small, there appears to be a minimum in the centroid velocity at the position of the source along this axis. This is consistent with model predictions for the variation of centroid velocity parallel to the rotation axis of a rotating and infalling protostellar envelope (e.g. Walker, Narayanan & Boss 1994). The fit to the gradient along the northeast-southwest axis (in the left hand panel of the figure) is $(5.1 \pm 0.4) \times 10^{-2}\,\mathrm{km\,s^{-1}\,arcsec^{-1}}$, which is equivalent to $88 \pm 7\ \mathrm{km\,s^{-1}\,pc^{-1}}$ for an assumed distance of 120 pc. If this is interpreted as being due to rotation, the lower limit on the mass contained within the central 20 arcseconds is $\sim 0.35\,M_\odot$. As stated above, the mass of the envelope alone estimated from dust continuum observations is $\sim 0.1\,M_\odot$, and to this must be added the unknown mass of the central protostar. The possibility that the centroid velocity gradient is due to rotation is therefore not ruled out on these grounds. Whether the outflow could be responsible for this velocity gradient still needs to be considered, however.

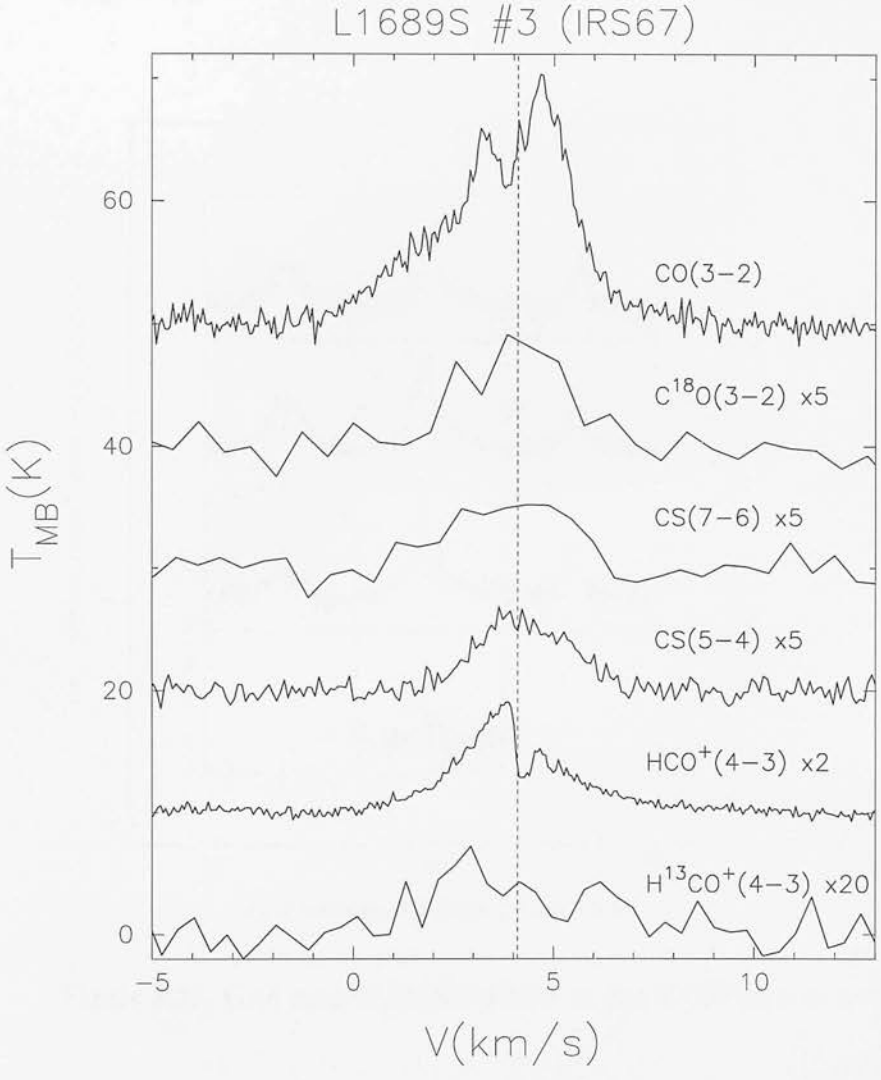

Figure 3.21: JCMT spectra of L1689S-IRS67

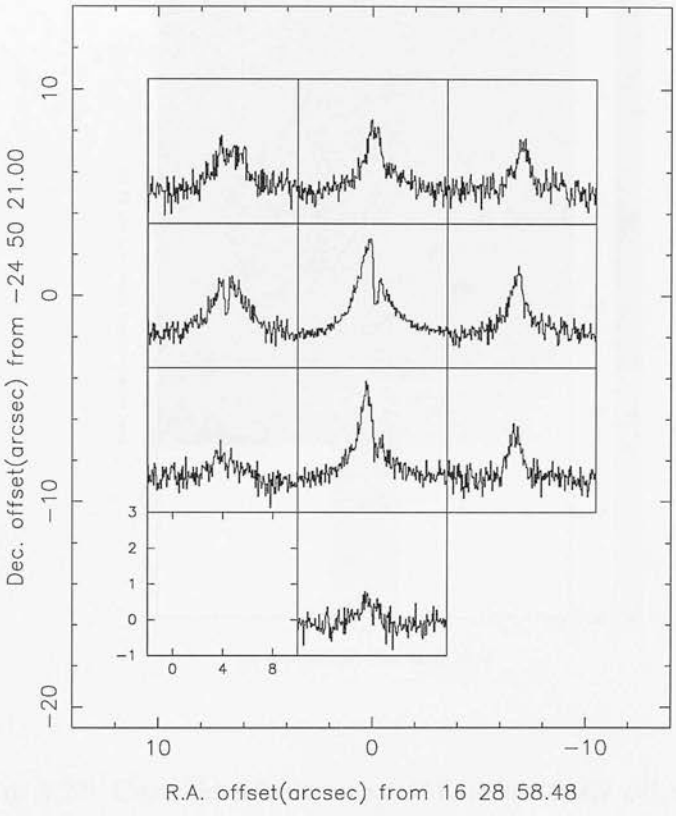

Figure 3.22: Grid map of L1689S-IRS67 in the $HCO^+(J = 4 \rightarrow 3)$ transition

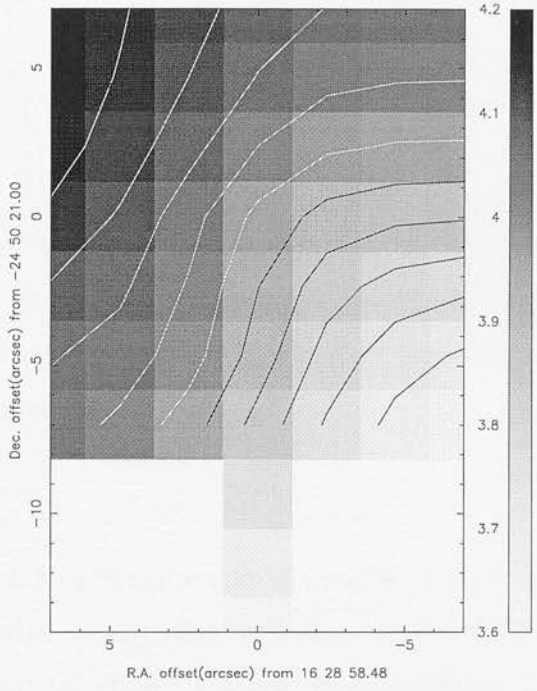

Figure 3.23: Centroid-velocity map of L1689S-IRS67 calculated from the $HCO^+(J = 4 \rightarrow 3)$ map shown in Figure 3.22, over the velocity range 3.1-5.1 $km\,s^{-1}$. The contour step is 0.05 $km\,s^{-1}$.

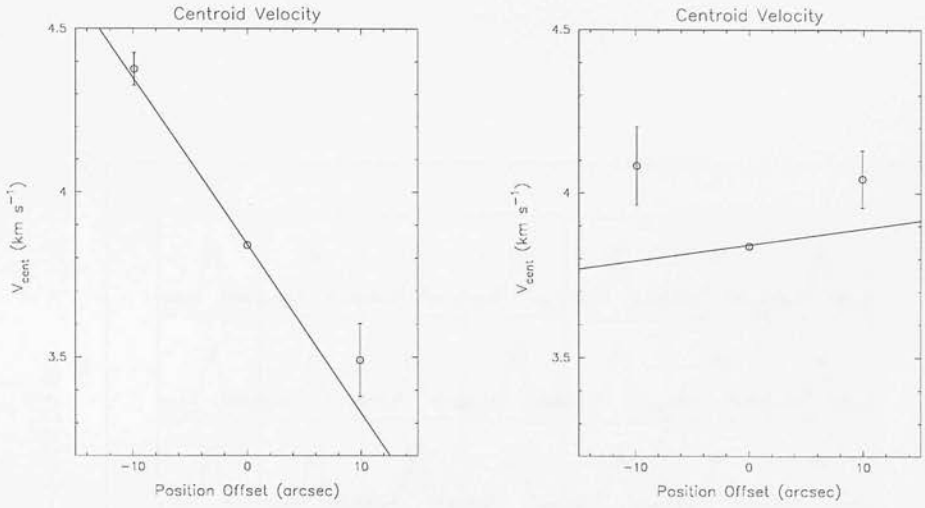

Figure 3.24: Weighted least-square fits to the centroid velocity gradients along northeast-southwest (left) and southeast-northwest (right) axes through L1689S-IRS67. The centroid velocity gradient is calculated over the velocity range 2.0–4.0 km s^{-1}. See the text for more details.

A CO($J = 3 \rightarrow 2$) raster map of the close vicinity of IRS67 is shown in Figure 3.25. The line profiles clearly show enhanced wing emission at many positions, especially at blue-shifted velocities. Channel maps produced from this map are presented in Figure 3.26. The red-shifted lobe extending south from IRS67 in the channel maps is consistent with previous observations of the outflow associated with this source (see above). There is little indication, however, of a northern or northwestern blue-shifted outflow lobe in the channel maps – rather, a blue-shifted outflow lobe is seen pointing towards the *west*. There are many examples of outflows which show very different morphologies on large and small scales (e.g. see the discussions of the IRAS 16293-2422 and Serpens SMM4 outflows in this chapter). One possible explanation for this is that outflows are intrinsically highly variable in direction. Another possibility is that the morphology of bipolar outflows is to a large extent determined by the way they interact with their surroundings. A map with identical sampling but greater area coverage would be helpful in addressing this question. In any case, it is reasonably

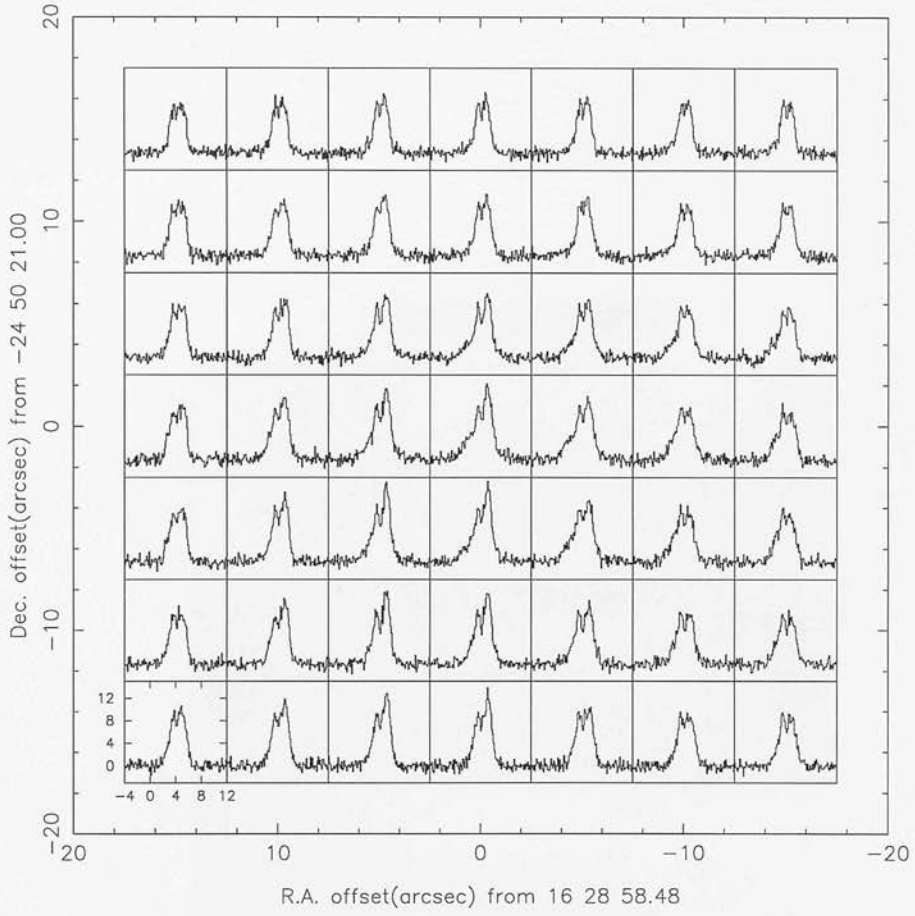

Figure 3.25: Grid map of L1689S-IRS67 in the CO($J = 3 \rightarrow 2$) transition.

certain that the velocity gradient measured in the $HCO^+(J = 4 \rightarrow 3)$ map cannot be attributed to the outflow, since there appears to be little correlation between the HCO^+ and CO velocities (e.g. the CO emission is red-shifted south of IRS67, whereas the HCO^+ emission is blue-shifted in the south.)

3.2.7 Serpens SMM1–4

The Serpens molecular cloud is a low to intermediate mass star-forming region which has been the subject of intensive observational study (e.g. Eiroa 1991; Eiroa & Casali 1992; White, Casali & Eiroa 1995, hereafter WCE). The distance to the region has

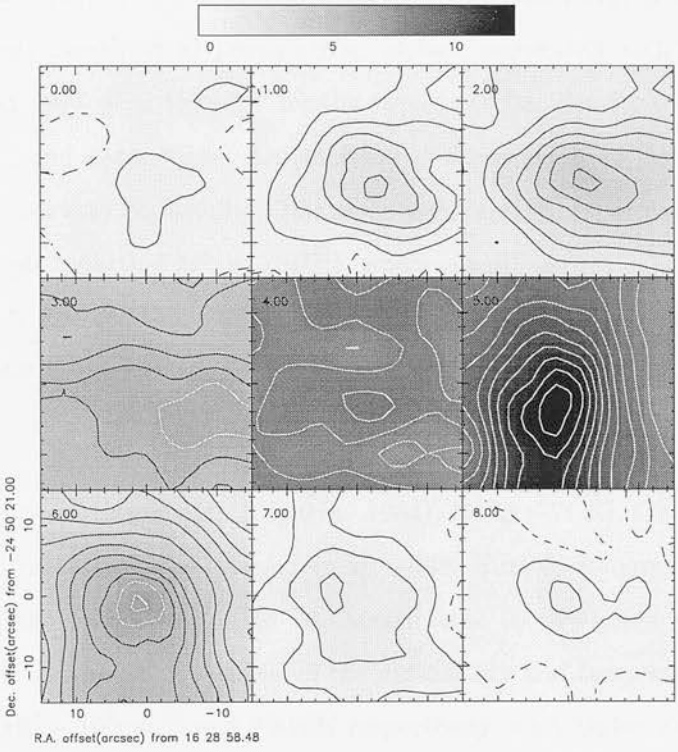

Figure 3.26: Channel map of L1689S-IRS67 in the CO($J = 3 \rightarrow 2$) transition.

been the source of some debate, with estimates ranging from 250 parsecs (Chavarria et al. 1988), to 750 parsecs (Zhang et al. 1988), based on spectroscopic parallaxes of stars believed to be physically related to the cloud. The most recent studies (de Lara et al. 1991; Straižys, Černis & Bartašiūtė, 1996) have identified misclassifications of the spectral types of some of the stars used in the previous distance determinations, and suggest an actual distance of 300 ± 30 parsecs.

Eiroa & Casali (1992) carried out a comprehensive near-infrared survey of the region and positively identified 51 young stellar objects associated with the cloud. They estimated a lower limit of $\simeq 450$ pc^{-3} for the average stellar density over a region $\simeq$0.5 parsecs diameter, and a star formation efficiency in the range 8–28 per cent, suggesting that a bound cluster may be forming. The peak of the star formation activity is centred close to the Serpens reflection nebula (SRN), which is a diffuse optical and near-infrared nebula (Gómez de Castro, Eiroa & Lenzen 1988; Eiroa & Casali 1992) powered by the luminous pre-main sequence star SVS 2 (Strom, Vrba & Strom 1976).

Maps in ammonia (Ungerechts & Gusten 1984), C^{17}O (WCE), CS (McMullin et al. 1994) and far-infrared emission (Zhang et al. 1988; Hurt & Barsony 1996) show the gas and dust in the central region to be concentrated in two cores, aligned approximately northwest-southeast. Estimates of the gas density and temperature in the cores lie in the range $10^4 - 10^5$cm^{-3} and 20-30K respectively, with higher temperatures and densities towards some of the embedded sources. The $\sim 70\,M_\odot$ northwestern core contains the well studied far-infrared source Serpens FIRS 1 (Harvey et al. 1984), which is associated with a highly collimated, high velocity (~ 300 km s^{-1}) radio continuum jet (Rodriguez et al. 1980, 1989; Curiel et al. 1993, 1996), and a linear near-infrared feature, approximately aligned with the northwestern lobe of the radio jet (Eiroa & Casali 1989). This source was labelled SMM1 by CED, and is the strongest of the submillimetre continuum sources in the cloud.

The more massive southeastern core overlaps the reflection nebula, and contains

a small cluster of compact submillimetre continuum sources (Casali, Eiroa & Duncan 1993, hereafter CED), two of which (SMM2 and SMM4) have no near-infrared counterparts. Barsony et al. (1996) used a maximum correlation algorithm to enhance the spatial resolution of the IRAS maps of this region, and derived upper limits for the far-infrared luminosities of the submillimetre sources. SMM1–4, and S68N (McMullin et al. 1994) were identified as Class 0 sources. Hurt, Barsony & Wootten (1996) have observed each of these sources in the high density molecular tracer H_2CO. In the $H_2CO(J_{K_{-1}K_1} = (3_{03} \rightarrow 2_{02})$ transition, four out of the five sources showed asymmetrical line profiles suggestive of infall. The remaining source, SMM1, showed a symmetrical double-peaked profile. Gregersen et al. (1997) included Serpens SMM1–4 in their HCO^+ survey of Class 0 sources, and found strong infall signatures towards SMM2 and SMM4.

The CO ($J = 2 \rightarrow 1$) outflow map in Figure 3.27, taken from WCE, shows possible bipolar outflow associations with SMM1 (southeast-northwest) and SMM4 (approximately north-south), and perhaps SMM2 (southeast-northwest). Establishing the presence or absence of outflows driven by the other Serpens objects is hindered by the considerable confusion from overlapping outflow lobes.

New observations

Figure 3.28 shows the $HCO^+(J = 4 \rightarrow 3)$ and $H^{13}CO^+(J = 4 \rightarrow 3)$ spectra observed towards the Serpens Class 0 sources SMM 1-4. Of the four sources, SMM2 and SMM4 show line profiles most suggestive of infall. SMM4 in particular shows the classic signature of a double-peaked self-absorbed main line profile skewed heavily towards the blue, with an absorption minimum redshifted relative to the peak of the optically thin isotopic line. The SMM1 main-line profile shows a deep absorption minimum, close to the peak velocity of the isotopic line, and a very mild blue asymmetry. Strong high velocity wings are also visible, which are probably tracing the energetic bipolar jet and outflow driven by this source. The $HCO^+(J = 4 \rightarrow 3)$ spectrum observed towards SMM3 does not show any sign of self-absorption, but a strong blue-shifted wing, prob-

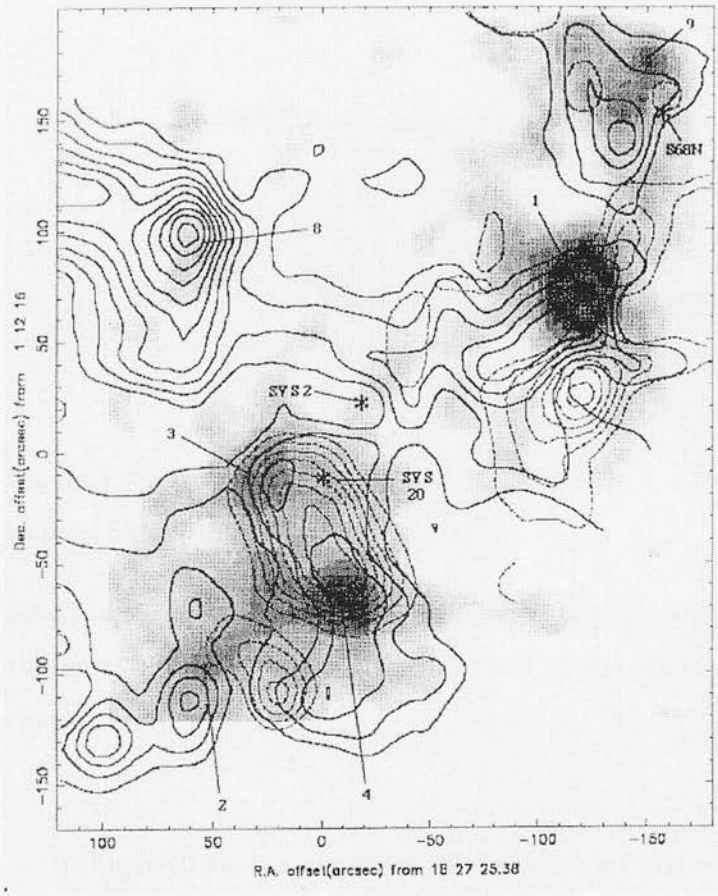

Figure 3.27: Map of the Serpens core in blue-shifted (dashed contours) and red-shifted (solid contours) high velocity CO($J = 2 \rightarrow 1$) emission, and 1100 μm continuum emission, taken from WCE. The numbers refer to the SMM source labels defined by CED and WCE.

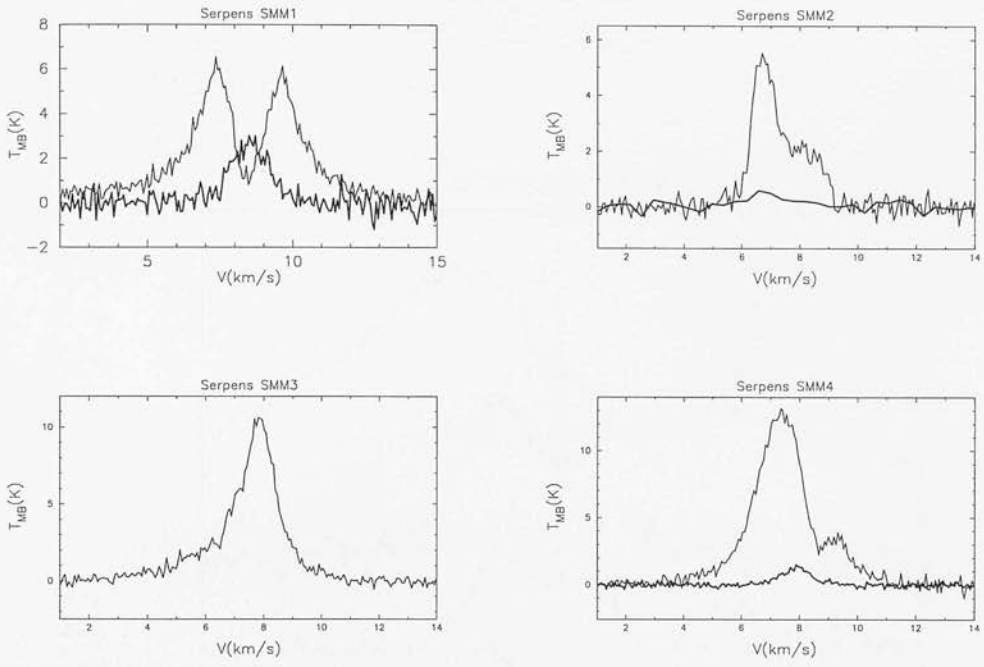

Figure 3.28: $HCO^+(J = 4 \rightarrow 3)$ and $H^{13}CO^+(J = 4 \rightarrow 3)$ (bold) spectra of the Serpens sources SMM1-4.

ably tracing an outflow, is clearly seen. In the following we concentrate primarily on the sources SMM2 and SMM4, as the best protostellar infall candidates in the Serpens cloud.

In Figure 3.29, the on-source spectra observed towards Serpens SMM2 are shown. Blue asymmetric line profiles are seen in most of the transitions shown, although $CS(J = 7 \rightarrow 6)$ emission was not detected above the $\sim$0.2K noise of the observation. There is a remarkable similarity between line profiles of the main line HCO^+ transitions and their isotopic counterparts, although the signal to noise ratio in the $H^{13}CO^+(J = 4 \rightarrow 3)$ line profile is too low to attach too much weight to this.

Figure 3.30 shows a grid map of Serpens SMM2 in the $HCO^+(J = 4 \rightarrow 3)$ transition. This map was obtained from the JCMT data archive, and the observing runs during which these data were taken are described in WCE. The $HCO^+(J = 4 \rightarrow 3)$ emission

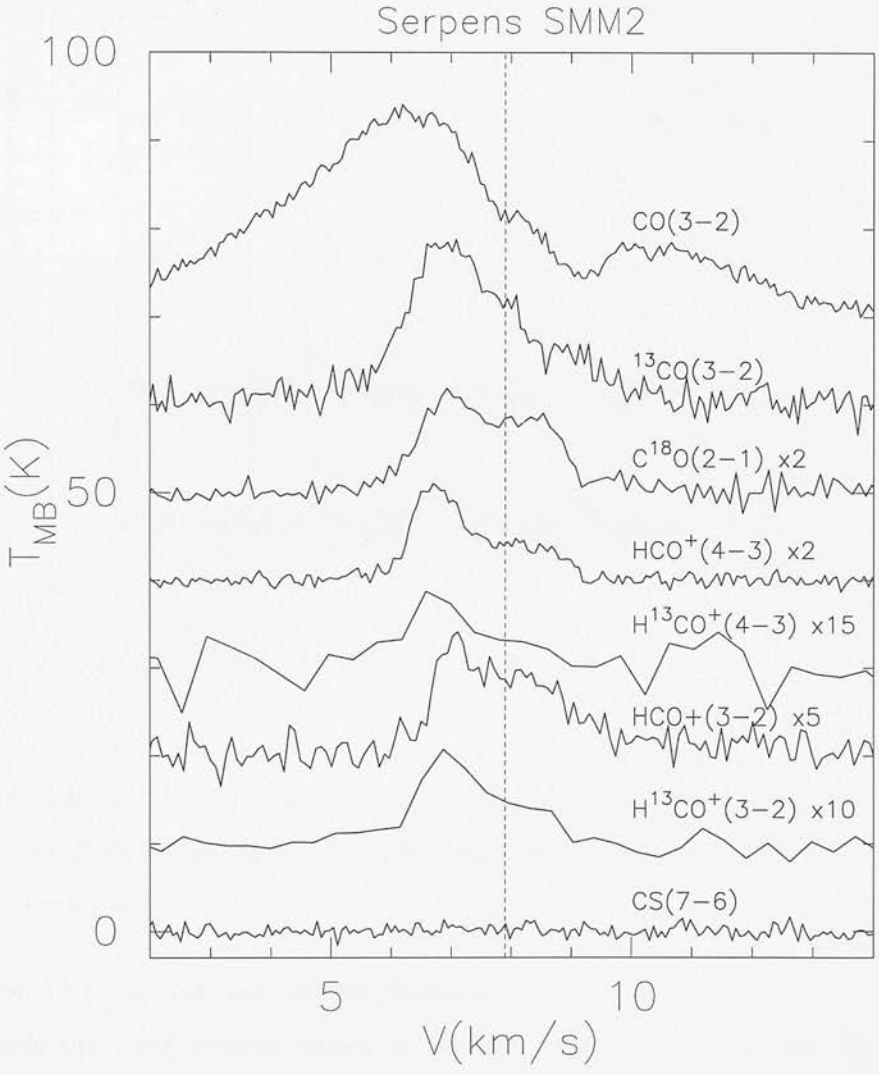

Figure 3.29: Spectra observed towards the position of the Serpens SMM2 continuum peak. The dashed line indicates a velocity of 7.9 km s^{-1}.

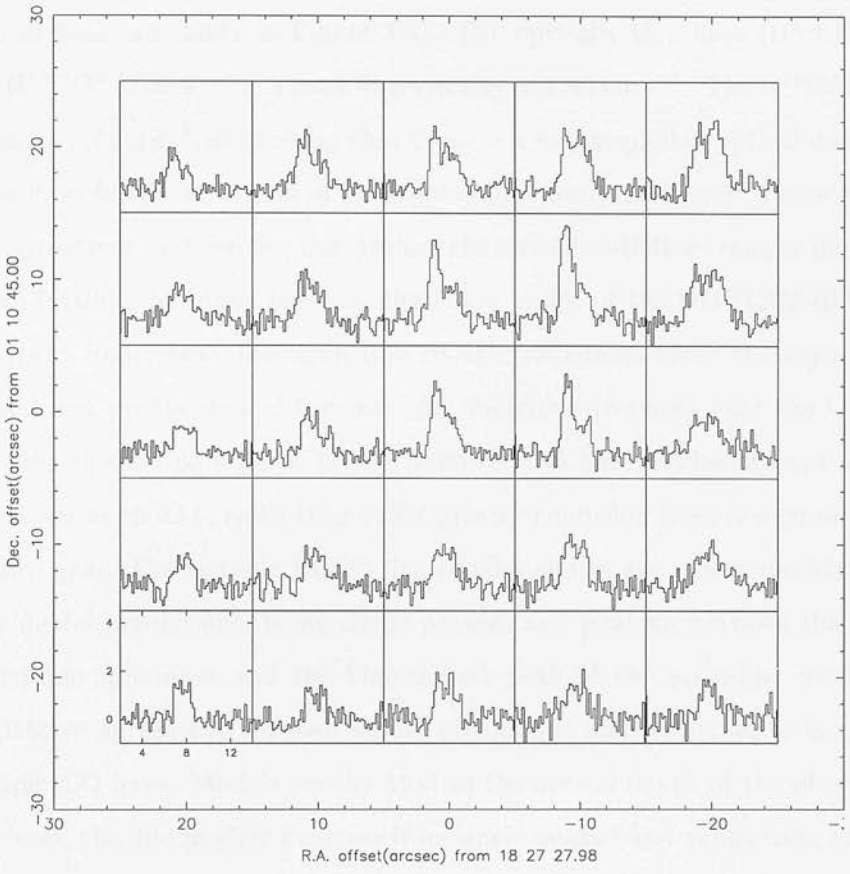

Figure 3.30: Grid map of Serpens SMM2 in the $HCO^+(J = 4 \rightarrow 3)$ transition (taken from the JCMT data archive). The origin is at the position of the submillimetre continuum peak.

is seen to peak northwest of the continuum peak. The bright line profiles observed towards the north-western corner of the map include a contribution from the outer envelope of SMM4 however, which lies at an offset of (-25,+50), and shows extended bright emission in $HCO^+(J = 4 \rightarrow 3)$ (see Figure 3.32). This may in part explain the similar velocity structure of the isotopic and main line profiles discussed above, if the emission arises from overlapping clumps with different velocities along the line of sight. There is no reliable way, however, to separate the overlapping contributions to the line profiles, and we therefore do not discuss this source any further.

The spectra observed towards the position of the Serpens SMM4 submillimetre con-

tinuum peak are shown in Figure 3.31. The optically thin lines ($H^{13}CO^+(J = 3 \rightarrow 2)$ and $H^{13}CO^+(J = 4 \rightarrow 3)$) peak at a velocity of $7.95\,km\,s^{-1}$. The $C^{18}O(J = 3 \rightarrow 2)$ line peaks at $7.7\,km\,s^{-1}$, suggesting that there is a non-negligible optical depth in this line, as we have found for several of the objects previously discussed. There is good qualitative agreement between the line profiles shown and radiative transfer model predictions for an infalling envelope (see the discussion above of the NGC1333-IRAS 2 on-source spectra). First, both the main line HCO^+ transitions show the asymmetric double-peaked line profile skewed towards blue velocities (we note that the $CO(J = 3 \rightarrow 2)$ line also shows this type of profile, however CO line profiles are not as robust infall indicators as HCO+, since they suffer greater confusion from foreground material and outflow gas). The isotopic HCO^+ line profiles shown are also in qualitative agreement with model predictions, being single-peaked, and peaking between the velocity of the absorption minimum and the blue-shifted peak of the main-line profile. A further qualitative agreement between model predictions and observations is shown by three isotopic CO lines. Models predict that as the optical depth of the observed transition increases, the line profiles progress from single peaked and symmetric, to single-peaked and skewed to the blue, to double-peaked with the blue peak brighter than the red (Myers 1995). This is just the progression observed in the CO line profiles as the isotopic abundance increases. The CS line profiles represent the intermediate optical depth stage, being single peaked and skewed to the blue. Taken as a whole, therefore, the set of line profiles shown in the figure are remarkably consistent with the qualitative expections for an infalling envelope.

Figure 3.32 shows a grid map of the SMM4 envelope in the $HCO^+(J = 4 \rightarrow 3)$ transition. The strongest emission is found at the origin and at the grid position immediately north of the origin. Blue-skewed line profiles are evident in most of the spectra shown, although double peaked line profiles are only found in the central and western map columns. Comparison of the spectra in the southeast and northwest corners of the map reveals a shift in the peak velocity of about $1\,km\,s^{-1}$towards the blue along the southeast-northwest direction (see Figure 3.33). A centroid velocity map calculated from this grid map is shown in Figure 3.34, from which a southeast-northwest

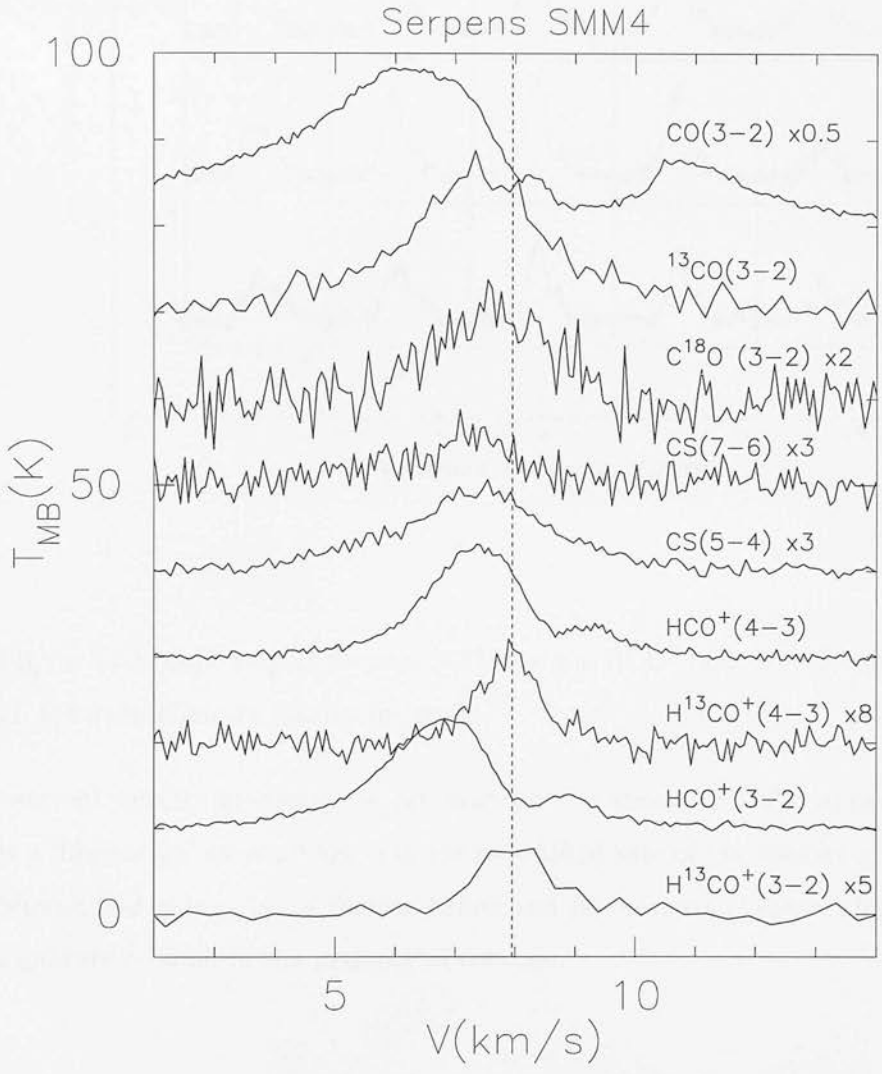

Figure 3.31: Spectra observed towards the Serpens SMM4 continuum peak. The dashed vertical line indicates a velocity of 7.95 km s^{-1}.

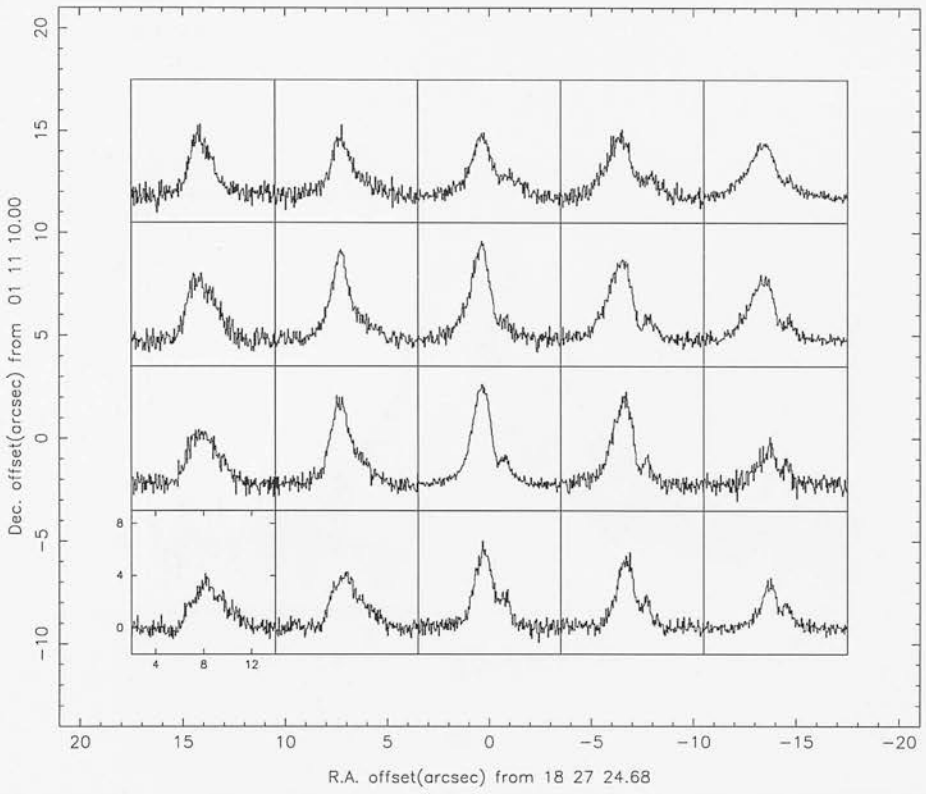

Figure 3.32: Grid map of Serpens SMM4 in the $HCO^+(J = 4 \rightarrow 3)$ transition, centred on the submillimetre continuum peak.

centroid velocity gradient of $\sim 30\,\mathrm{km\,s^{-1}pc^{-1}}$ is measured. Also apparent in this plot is a 'blue-bulge' encroaching onto the red-shifted side of the velocity gradient from the blue-shifted side. As we discuss below and in the next chapter, this is a predicted signature of infall in the presence of rotation.

A larger area $HCO^+(J = 4 \rightarrow 3)$ raster map of SMM4 is shown in Figure 3.35, which has been convolved with a 7 arcsecond FWHM gaussian beam to improve the signal to noise ratio. The high spatial sampling of the map allows a 40% improvement in the signal to noise ratio at the expense of only a 12% increase in the effective beam size, from 13.6 to 15.3 arcseconds FWHM.

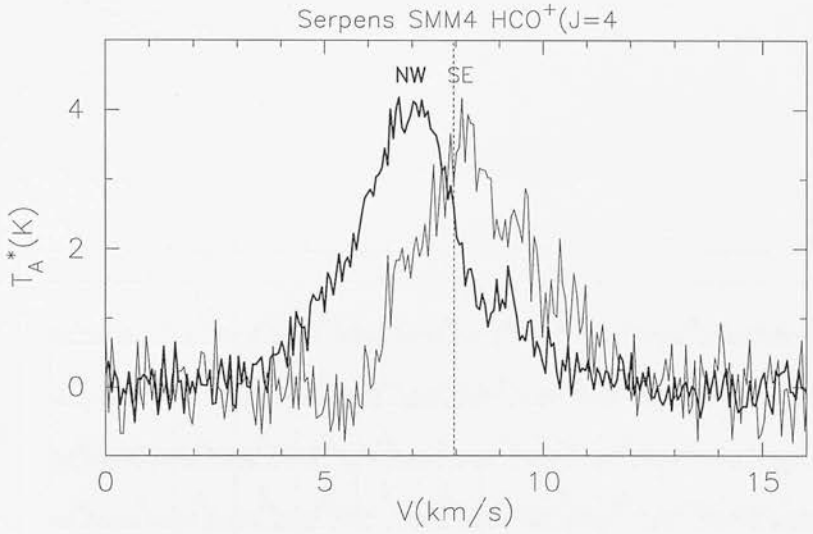

Figure 3.33: Comparison of spectra in the northeast (-14,+14) and northwest (+14,-7) corner of the $HCO^+(J = 4 \rightarrow 3)$ grid map shown in Figure 3.32

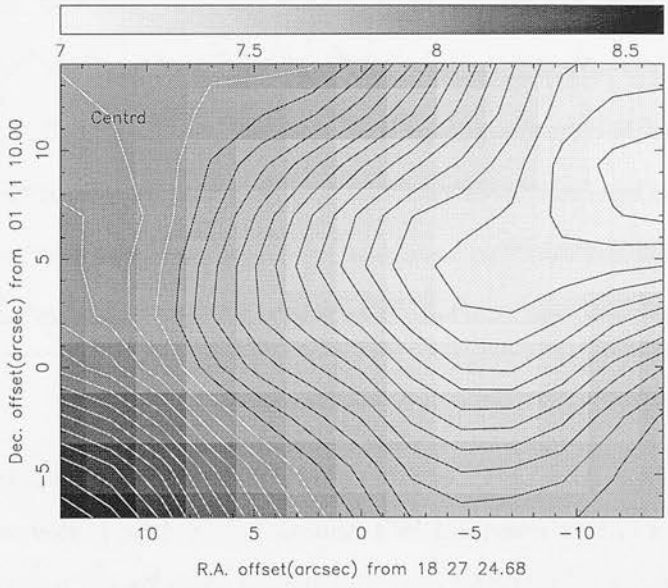

Figure 3.34: Centroid velocity map derived from the $HCO^+(J = 4 \rightarrow 3)$ grid map of Serpens SMM4 shown in Figure 3.32, over the velocity range 5.0-11.0 $\mathrm{km\,s^{-1}}$. The contour spacing is 0.05 $\mathrm{km\,s^{-1}}$.

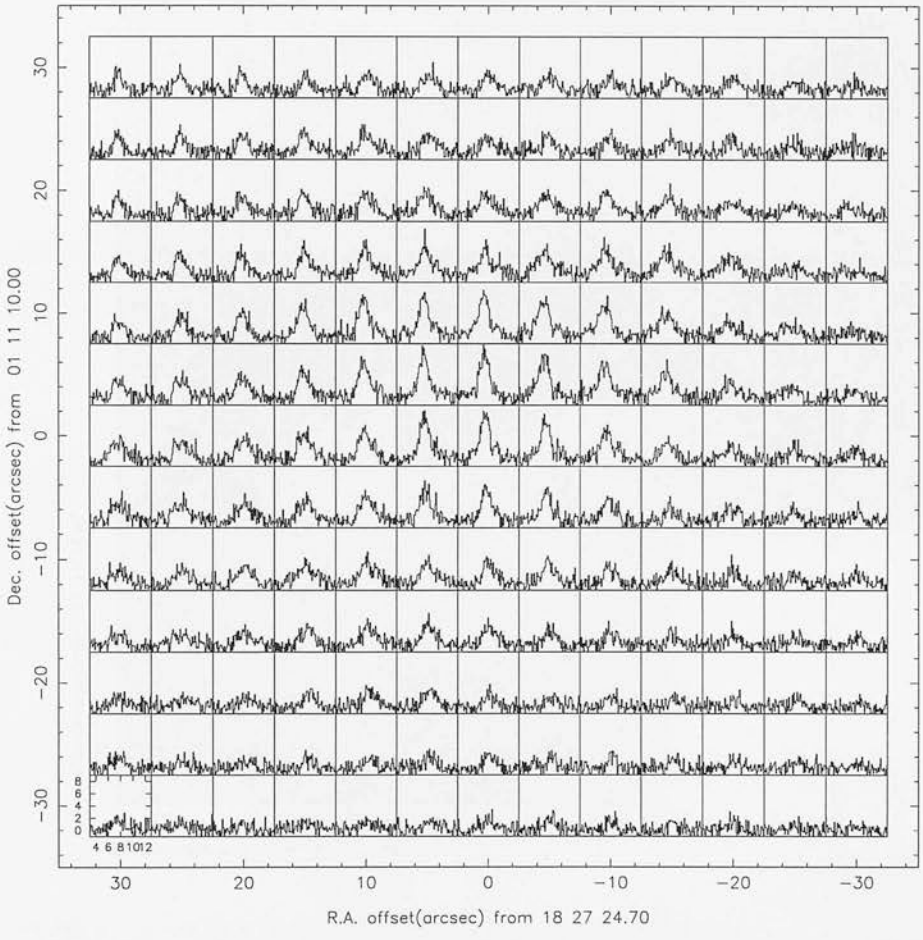

Figure 3.35: Raster map of Serpens SMM4 in the $HCO^+(J = 4 \rightarrow 3)$ transition. This map has been convolved with a 7-arcsecond FWHM beam to improve the signal to noise ratio, increasing the effective beamwidth from 13.6 to 15.3 arcseconds.

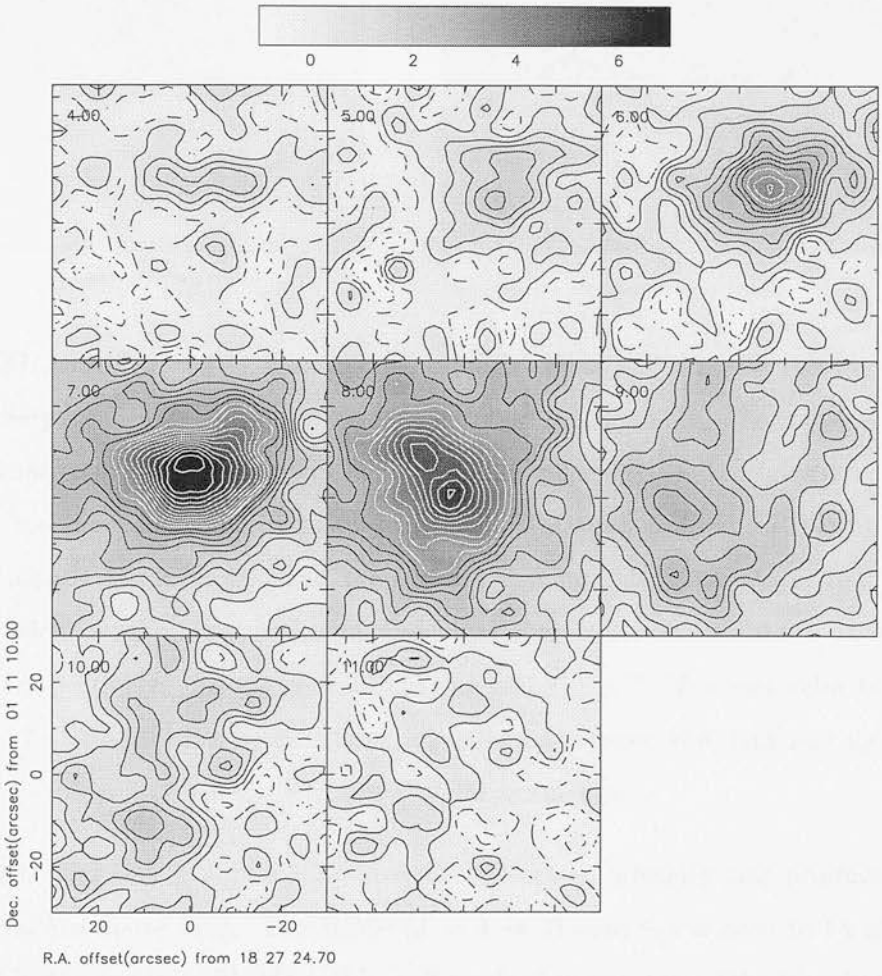

Figure 3.36: Channel map of Serpens SMM4 in the $HCO^+(J = 4 \rightarrow 3)$ transition, produced from the raster map in Figure 3.35

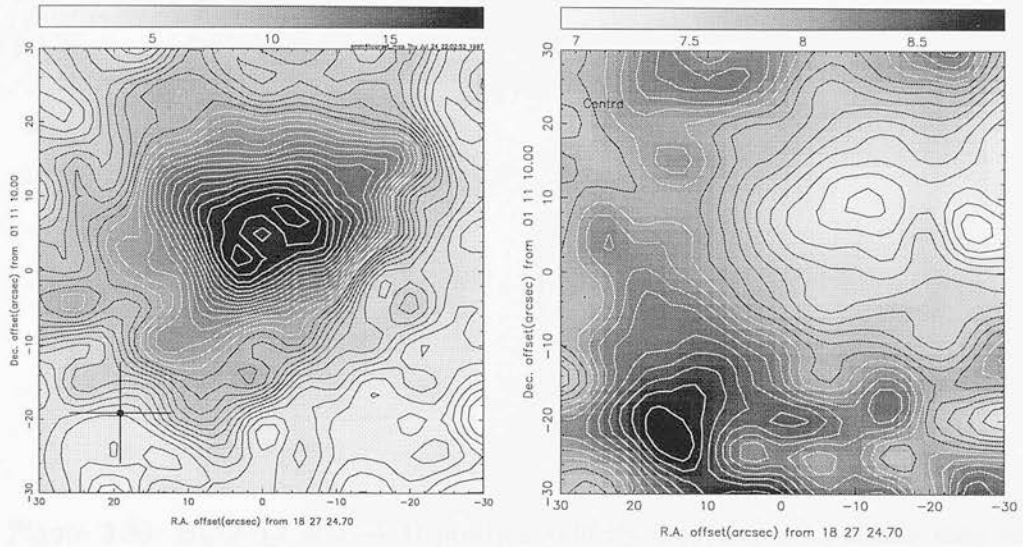

Figure 3.37: $HCO^+(J = 4 \rightarrow 3)$ integrated intensity (left) and centroid velocity (right) maps of Serpens SMM4, over the velocity interval 4-12 $km\,s^{-1}$. The maps are both derived from the raster map shown in Figure 3.35, although for the integrated intensity map the *unsmoothed* raster map was used. The peak contour of the integrated intensity map is 18.6K $km\,s^{-1}$, and the contour spacing is 0.6K $km\,s^{-1}$($\simeq 1\sigma$). In the centroid velocity map, the minimum and maximum contours levels are at 6.8 and 8.8 $km\,s^{-1}$respectively, and the contour spacing is 0.1 $km\,s^{-1}$. The rest velocity of the source ($\simeq$ 7.95 $km\,s^{-1}$) lies in the transition interval between the dark and light contours. The crosses indicate the effective FWHM beam sizes.

The left hand plot in Figure 3.37 shows the integrated intensity map produced from the *unsmoothed* raster map. The $HCO^+(J = 4 \rightarrow 3)$ emission is seen to be strongly enhanced in the region of SMM4 and is well resolved in our beam (the transition from dark to light contours in the figure marks the half-maximum level). The emission is approximately centred around the offset position (0,+5) on the map. Towards this point the integrated intensity flattens off into a plateau, and there is a shallow minimum at the central point itself, surrounded by horseshoe-shaped peak. The lower contours reveal an extension of the peak towards the northeast, and a flattened linear feature oriented along a southeast-northwest axis through the peak.

In the right hand panel of Figure 3.37, the centroid velocity map calculated from the

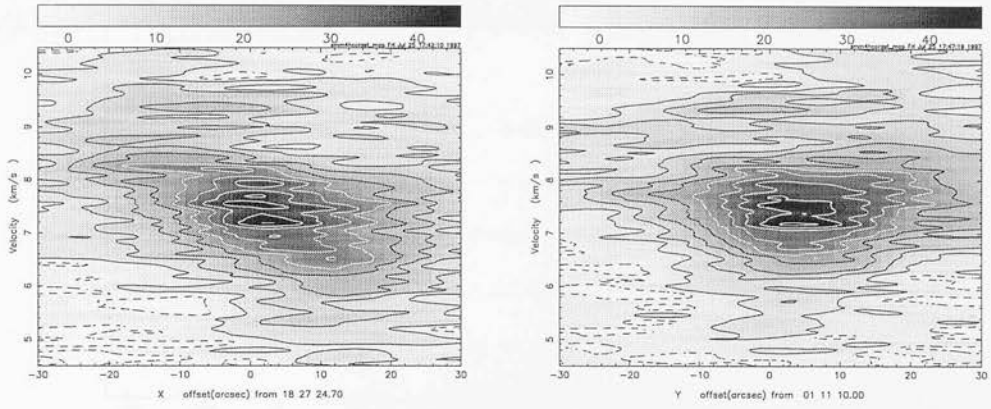

Figure 3.38: $HCO^+(J = 4 \rightarrow 3)$ position velocity diagrams for position cuts parallel (left) and perpendicular (right) to the elongated linear feature at a position angle of $\simeq -50°$ in the integrated intensity map. They were calculated from the raster map shown in Figure 3.35, after interpolation onto a rotated grid which placed the elongated feature parallel to the x-direction.

spatially convolved $HCO^+(J = 4 \rightarrow 3)$ raster in Figure 3.35 is shown. Centroid velocity maps suffer more from low signal to noise ratios than integrated intensity maps, and the small loss of spatial resolution associated with the convolution is not significant. The southeast-northwest velocity gradient already mentioned is again very apparent in the figure. Comparison of integrated intensity and centroid velocity maps show the region of brightest integrated $HCO^+(J = 4 \rightarrow 3)$ emission to coincide with the blue-shifted part of the velocity gradient, which makes the symmetric appearance of the plot about the line rest velocity all the more remarkable. The axis of the steepest velocity gradient (P.A.$\simeq -40°$) is close to (but not coincident with) the axis of the elongated feature in the integrated intensity map (P.A.$\simeq -50°$). A further illustration of the velocity gradient is given in Figure 3.38, which shows position-velocity diagrams along axes parallel and perpendicular to the flattened feature in the integrated intensity map. A clear velocity gradient is seen along the parallel axis, but not along the perpendicular axis.

Figure 3.39 shows the fits to the velocity gradient along axes parallel to and per-

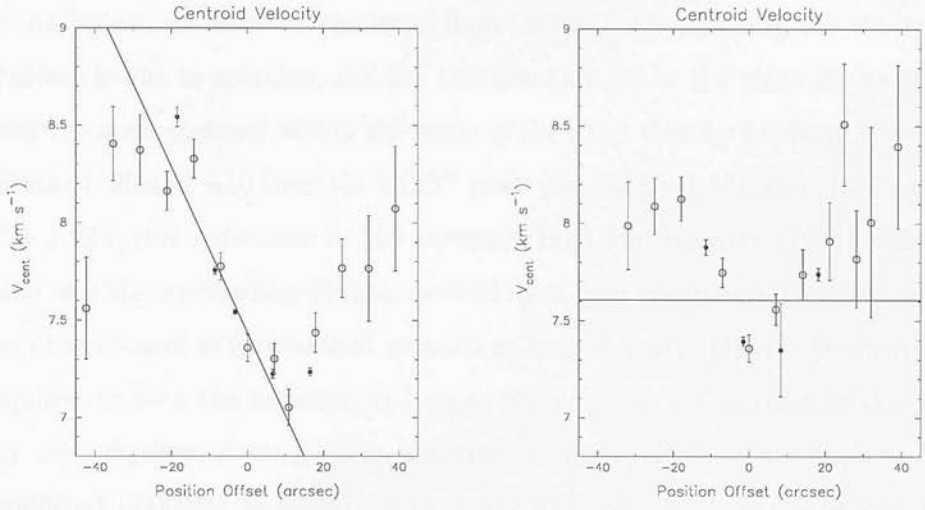

Figure 3.39: Weighted least-squares fits to the centroid velocity gradient along axes parallel (left) and perpendicular (right) to the elongated feature at a position angle of -50° in the $HCO^+(J = 4 \rightarrow 3)$ greyscale map (Figure 3.37). The open and filled circles represent measurements taken from the $HCO^+(J = 4 \rightarrow 3)$ raster map (Figure 3.35) and grid map (Figure 3.32) respectively. In both plots, the origin coincides with the peak of the $HCO^+(J = 4 \rightarrow 3)$ emission, and increasing position offset corresponds to increasing distance from the eastern edge of the maps. In the left hand plot, the line fit was calculated using only the points lying between the position offsets -30 and +12.

pendicular to the flattened feature, as in the position-velocity maps. The velocity gradient in the parallel direction is seen to be remarkably linear within a 15 arcsecond radius of the origin. The gradient of the straight line fit is $-4.1(\pm 0.15) \times 10^{-2}\,\mathrm{km\,s^{-1}arcsec^{-1}}$, which implies a velocity gradient of $28 \pm 1\,\mathrm{km\,s^{-1}pc^{-1}}$, for a distance of 300pc. The corresponding fit values for the perpendular velocity gradient are $-4.0(\pm 3.9) \times 10^{-5}\,\mathrm{km\,s^{-1}arcsec^{-1}}$, and $0.03 \pm 0.9\,\mathrm{km\,s^{-1}pc^{-1}}$, however the points in this plot are not well fitted by a straight line. The centroid velocities along this axis clearly shift towards bluer velocities at positions near to the central peak. This 'blue-bulge' signature, parallel to the rotation axis of a rotating, infalling protostellar envelope, was first predicted by the radiative transfer analysis of Walker, Narayanan & Boss (1994; see Chapter 4).

As before, we estimate the lower limit on the mass assuming the observed velocity gradient is due to rotation, and the rotation axis lies in the plane of the sky. We consider the mass enclosed within the limits of the steep velocity gradient between position offsets of -20 and +10 from the HCO^+ peak (see Figure 3.39), and obtain a lower limit of $\sim 1.9\,M_\odot$(for a distance of 300 parsecs). Hurt and Barsony (1996) estimated a gas mass of $3\,M_\odot$surrounding SMM4, derived from dust continuum emission, which, along with the mass of any embedded protostars, is sufficient to provide the centripetal force required to bind the rotation, as long as the rotation axis is close to the plane of the sky. Nevertheless, if our analysis is correct, centrifugal effects are likely to have a very significant influence on the equilibrium and dynamics of the envelope gas. It is tempting to speculate that the striking elongation seen in the integrated $HCO^+(J = 4 \rightarrow 3)$ map (see Figure 3.37), which is aligned approximately perpendicular to the inferred rotation axis, is caused by centrifugal flattening of the outer envelope (e.g Pudritz & Norman 1987). We note that a similar, although less striking, elongation was found in the only other source in our sample which unambiguously shows a strong rotational velocity gradient, IRAS 16293-2422.

It remains to be considered whether outflowing gas might be responsible for the observed velocity gradient in the $HCO^+(J = 4 \rightarrow 3)$ maps. Gregersen et al. (1997) detected a velocity gradient in the same sense and along the same axis in their $HCO^+(J = 3 \rightarrow 2)$ map of SMM4, but interpreted it in terms of *outflow* rather than rotation. SMM4 has previously been associated with a north-south bipolar outflow (WCE; Figure 3.27), however no well sampled CO maps have previously been published to our knowledge, which show the detailed structure of the outflow in the direct vicinity of SMM4. Figure 3.40 shows our $CO(J = 3 \rightarrow 2)$ raster map of SMM4. Channel maps derived from this map are presented in Figure 3.41.

The first thing to notice from the channel maps is that SMM4 lies in a very confused region of high velocity gas. In the velocity bins centred on -1 and $+2\,km\,s^{-1}$, a outflow lobe is seen to emerge eastwards from the vicinity of the SMM4 continuum peak, curving towards the northeast. A second region of high velocity blue-shifted emission

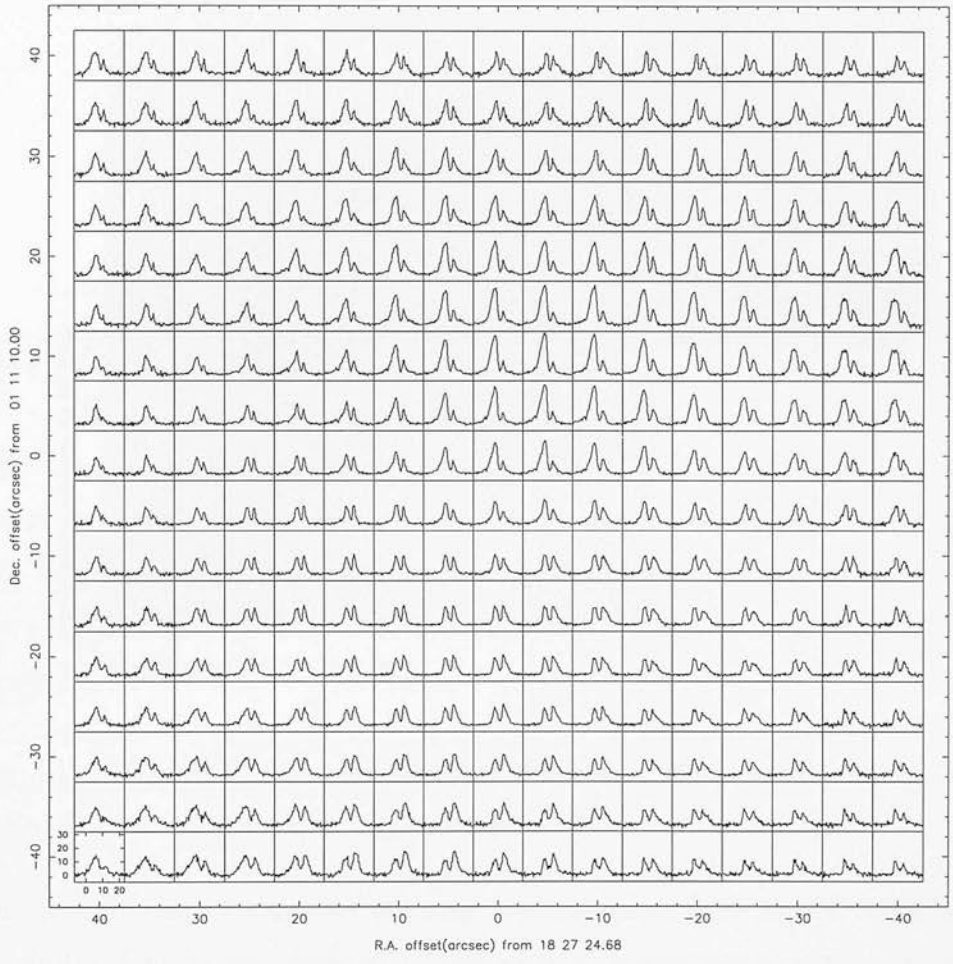

Figure 3.40: CO($J = 3 \rightarrow 2$) raster map of Serpens SMM4 and its close surroundings. The origin is at the position of the submillimetre continuum peak.

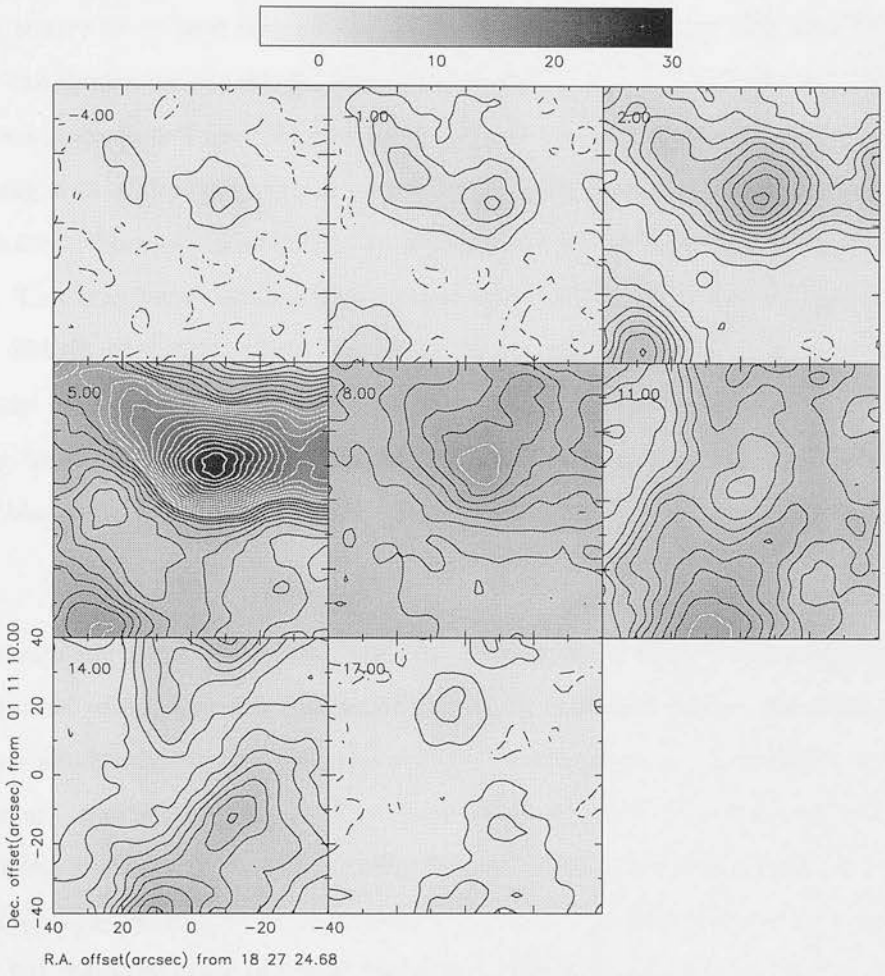

Figure 3.41: CO($J = 3 \rightarrow 2$) channel maps of Serpens SMM4 and its surroundings, produced from the raster map in Figure 3.40.

lies in the southeastern corner of the map, well separated from SMM4. Blue-shifted high velocity gas was also detected at this position in the CO($J = 2 \rightarrow 1$) outflow map of WCE, however it is unclear from where this high velocity gas originates. In the $+2\,\mathrm{km\,s^{-1}}$blue-shifted velocity bin a second 'lobe' is seen to the west of SMM4, and appears to be connected to it.

Turning attention now to the high velocity red-shifted emission, a striking lobe extending northwestwards from the southern edge of the map is seen in the $14\,\mathrm{km\,s^{-1}}$velocity bin, which is very suggestive of a collimated outflow lobe, and appears to originate from

a driving source at or just beyond the southern edge of the map. We have found no plausible candidates for the driving source in the literature however. We note, however, that the southern half of our CO map overlaps with the extremely compact SVS4 cluster of young stellar objects (Eiroa & Casali 1989). Also visible in the 14 km s^{-1} velocity bin is a narrow filament of emission extending southwards from the northern edge of the map. This may be an outflow lobe associated with the double Class I source SVS20 (labelled SMM6 by CED), which lies about 12 arcseconds beyond the northern edge of the map in the direction of the filament. In the highest redshifted velocity bin, a curving southern high velocity lobe is seen, similar to the curved lobe seen in the -1 km s^{-1} blue-shifted velocity bin.

The confusion from the overlap of different regions of high velocity gas apparent in the channel maps, and the limited extent of the mapped region, prevents the unambiguous association of these regions with particular sources. A probable exception is the eastern/northeastern blue-shifted lobe which emerges from the northern half of SMM4 in the northern half of the -1 km s^{-1} velocity bin. This is supported by the fact that a counterpart to this lobe is also seen in the $HCO^+(J = 4 \rightarrow 3)$ channel maps (see Figure 3.36). Identification of the expected red-shifted counterlobe is confused by the strong southeast-northwest redshifted lobe dominating the southern half of the map at redshifted velocities, which is probably not associated with SMM4. We tentatively suggest, however, that the shallow decline of the emission on the southwestern side of this red-shifted lobe is due to the overlap of the southwestern red-shifted counterpart to the SMM4 northeastern blue-shifted lobe. The origin of the other high velocity features, in particular the striking southeast-northwest redshifted outflow lobe, is left as an interesting area for future study.

The orientation of the bipolar outflow (approximately northeast-southwest) suggested above to be driven by SMM4, is approximately perpendicular to the direction of the velocity gradient inferred from the $HCO^+(J = 4 \rightarrow 3)$ data (e.g. Figure 3.37). This would appear to rule out this outflow being responsible for the observed velocity gradient in the northwest-southeast direction. We also largely discount the influence of

the strong redshifted outflow which is oriented approximately parallel to the velocity gradient, for the following reasons. First, there is actually very little overlap between this lobe, as seen in the CO channel maps, and the bright peak of $HCO^+(J = 4 \rightarrow 3)$ emission. Secondly, it is implausible that the interaction of a highly red-shifted outflow lobe with the SMM4 gas envelope could produce a coherent velocity gradient featuring strongly *blue-shifted* as well as red-shifted velocities. It is possible, however, that red-shifted emission contributed by this outflow is responsible for the slight disagreement between the axis of elongation in the $HCO^+(J = 4 \rightarrow 3)$ greyscale map and the velocity gradient axis (see Figure 3.37). In summary, we conclude that the velocity gradient measured in the SMM4 $HCO^+(J = 4 \rightarrow 3)$ map is not significantly affected by outflow gas, and is most likely due to rotation of the gas envelope.

3.2.8 L1448-IRS3

The L1448 dense globule lies at the western end of the Perseus dark cloud complex, at a distance of about 300pc (Cernicharo, Bachiller & Duvert 1985). Bachiller et al. (1990) mapped the globule in various transitions of CO, CS and NH_3, and derived a mass of $\sim 50 M_\odot$, a kinetic temperature of 12-14K, and a central density of $n_{H_2} \sim 5 \times 10^4 cm^{-3}$. The ammonia emission was found to be spatially separated into two distinct cores, which were later mapped in $HCO^+(3 \rightarrow 2)$ and $CS(5 \rightarrow 4)$ by Davis et al. (1994), using the JCMT.

The southern ammonia core peaks close to the Class 0 source L1448-C, which has an estimated luminosity of $9 \pm 3 L_\odot$ (Bachiller, André & Cabrit 1991). L1448-C (also referred to by the names L1448-mm and L1448-S) is the driving source of one of the most powerful and collimated bipolar outflows discovered to date (Bachiller et al. 1990), with $CO(2 \rightarrow 1)$ observations recording a terminal radial velocity of around $\pm 70 km\ s^{-1}$. An extended knotty jet is seen in $2.12 \mu m$ H_2 $v = 1 - 0$ S(1) emission (Terebey 1991; Bally et al. 1993; Davis et al. 1994), which mainly follows the northern lobe of the approximately north-south bipolar outflow. Using the VLA, Curiel et al. (1990)

detected 2-cm radio continuum emission coincident with the submillimetre continuum peak, which they attributed to shock ionisation produced by a fast neutral wind from the central star.

The northern core harbors the $11L_{\odot}$ Class 0 source IRS3 (Bachiller & Cernicharo 1986), (also referred to as L1448-N). It coincides in the plane of the sky with the northern, blue-shifted lobe of the L1448-C bipolar outflow (see Figure 3.42), but probably lies in the foreground, since the molecular hydrogen jet appears to be extincted at this position (Davis 1994). L1448-IRS3 is itself driving a weaker collimated bipolar outflow, aligned SE-NW, and was detected as a double source at 2-cm and 6-cm wavelengths by Curiel et al. (1990).

New observations

Figure 3.43 shows our on source observations towards L1448-IRS3. Although only three different transitions were observed, the line profiles are consistent with infall predictions and follow a similar pattern to the other good infall candidates in our sample. In particular, the $HCO^+(J = 4 \rightarrow 3)$ line shows a double-peaked, blue-asymmetric profile, and the isotopic line peaks in the absorption minimum of the main line.

The $HCO^+(J = 4 \rightarrow 3)$ grid map of L1448-IRS3 paints a somewhat more complicated picture. To the north and east of the source position, the line profiles are skewed strongly to the *red*. It is tempting to attribute this to the strong outflow in this object, although it is difficult to understand why the outflow should produce such a strong enhancement in the red-shifted $HCO^+(J = 4 \rightarrow 3)$ emission at the northern position, when the red-shifted outflow from this source extends in a southeasterly direction. We note that a very similar kind of reversal was seen in the $HCO^+(J = 4 \rightarrow 3)$ grid map of NGC1333-IRAS2 (see Figure 3.5), although in that case the position of the reversal coincided with a red-shifted outflow lobe. Part of the confusion may arise from the fact

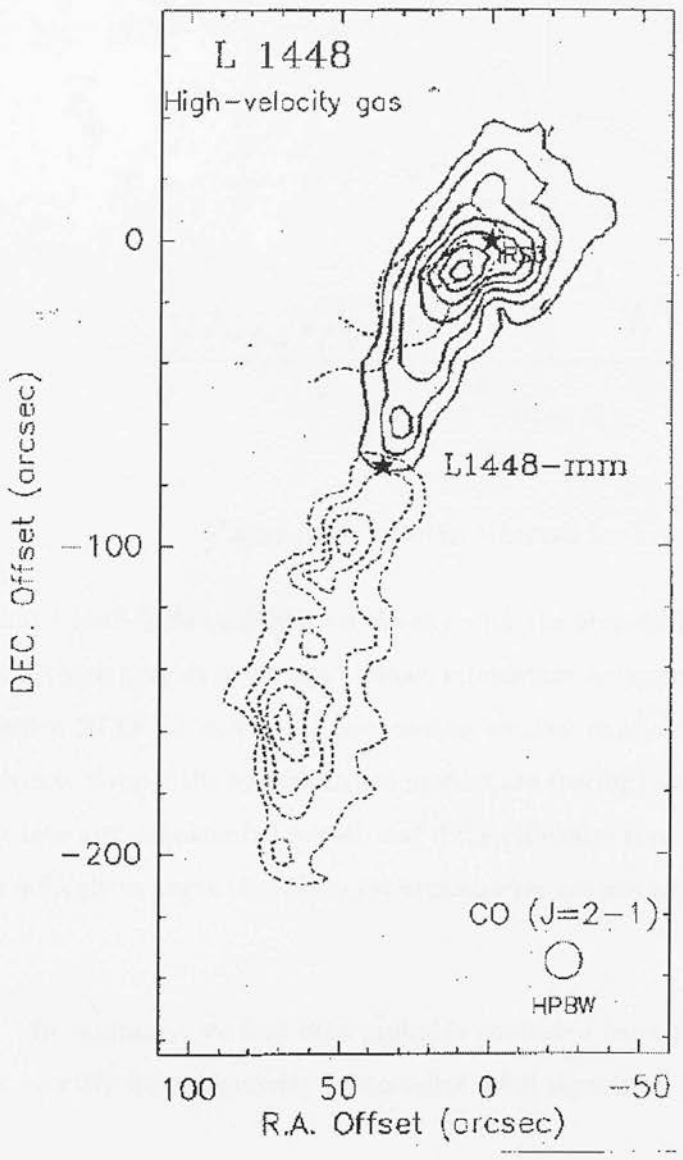

Figure 3.42: CO($J = 2 \rightarrow 1$) map of the L1448-C and L1448-N outflows (labelled in the figure as L1448-mm and IRS3 respectively), from Bachiller et al. (1991).

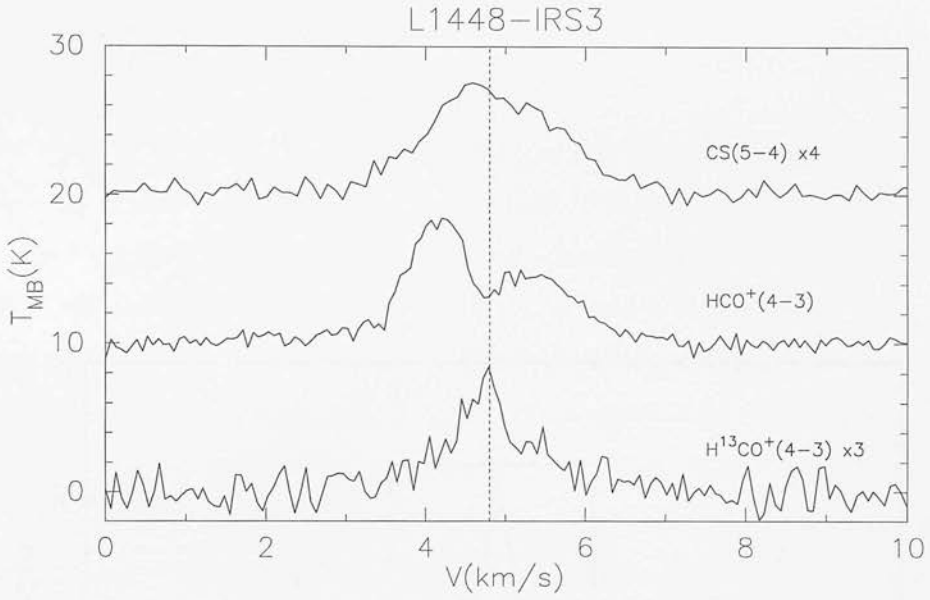

Figure 3.43: Spectra observed towards L1448-IRS3.

that L1448-IRS3 coincides on the sky with the blue-shifted outflow lobe from L1448-C, and there may even be some direct interaction between the two. In any case, the off-centre $HCO^+(J = 4 \rightarrow 3)$ line profiles weaken considerably the case for infall in this object. Even if the on-source line profiles are tracing infall, the off-centre profiles do not fit into any simple infall model, and if the off-centre profiles are caused by the outflow, it is difficult to argue that the on-source spectra are not also contaminated by the outflow.

In summary, we find that probable confusion from the outflow makes it impossible to identify unambiguously protostellar infall signatures in this object.

3.2.9 L483

L483 is a $\sim 21 M_\odot$ isolated core containing a deeply embedded young stellar object (IRAS 18148-0440), which drives a collimated east-west bipolar outflow (Fuller et al. 1995; Anglada, Sepúlveda & Gómez 1997). A distance of 200pc to the cloud was as-

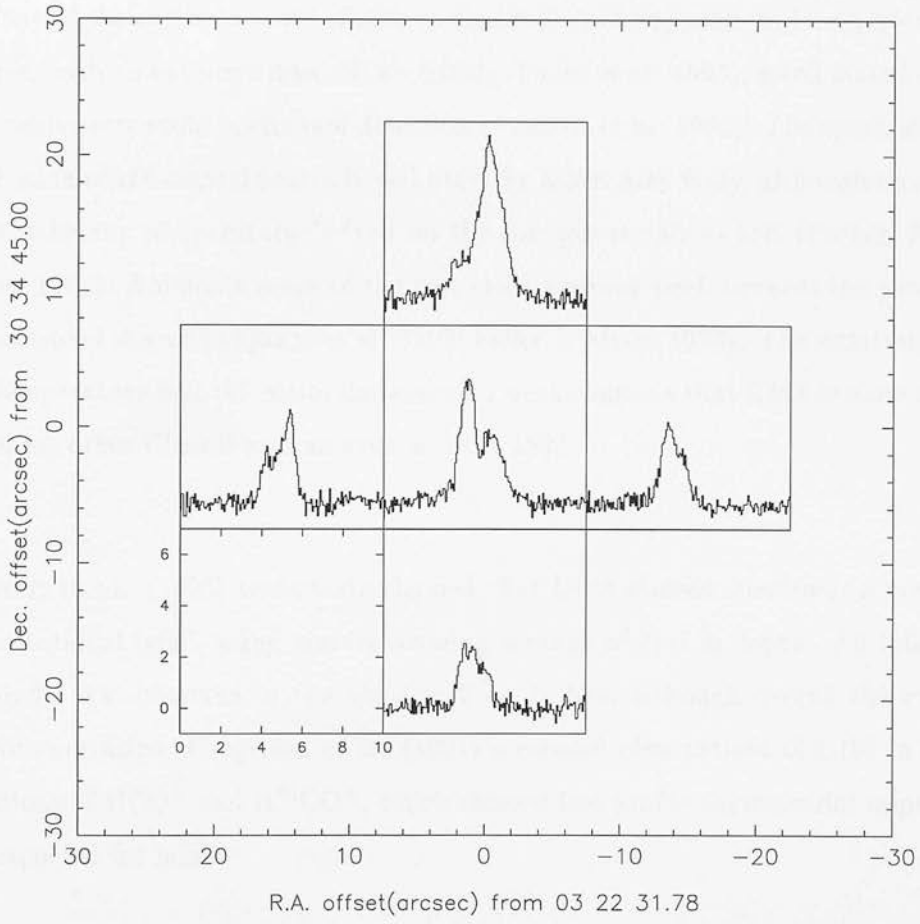

Figure 3.44: Grid map of L1448-IRS3 in the $HCO^+(J = 4 \rightarrow 3)$ transition.

sumed by Ladd et al. (1991), but no reliable distance estimate has been published to our knowledge.

The striking bipolar near-infrared reflection nebula associated with this source (see Figure 3.48) is produced by the scattering of light from the central protostar from the walls of cavities cleared by the outflow. The asymmetric near-infrared brightness distribution in the two lobes of the nebula can be understood if the outflow is inclined from the plane of the sky by $>\sim 40°$ (Fuller et al. 1995). L483 appears to be a typical Class 0 source, with an envelope mass of $>\sim 0.3\,M_{\odot}$(Fuller et al. 1995), a collimated outflow and a centimetre radio continuum detection (Anglada et al. 1997). The spectral energy distribution of the central source is well fitted by a 40K grey body, although on a larger scale the kinetic temperature derived for the core gas is only $\sim$ 12K (Parker, Padman & Scott 1991). Ammonia maps of the core show a strong peak towards the position of the embedded source (Anglada et al. 1997; Fuller & Myers 1993). The relatively warm dust temperature and the molecular emission peak suggests that L483 is more evolved than some other Class 0 sources such as VLA 1623.

Myers et al. (1995) tentatively claimed that L483 showed spectroscopic evidence of gravitational infall, using tracers covering a range of optical depth. An infall type line profile was observed in the CS($J = 2 \rightarrow 1$) line, although overall the evidence was not conclusive. Gregersen et al. (1997) presented observations of L483 in several transitions of HCO^+ and $H^{13}CO^+$, which showed line profile asymmetries opposite to that expected for infall.

New observations

Figure 3.45 shows the on-source spectra observed towards L483. The CS($J = 5 \rightarrow 4$) and HCO^+($J = 4 \rightarrow 3$) lines are clearly skewed towards red velocities, relative to the systemic velocity ($5.6\,km\,s^{-1}$), which was estimated from the centroid of the

$H^{13}CO^+(J = 4 \rightarrow 3)$ line. Apart from the $H^{13}CO^+(J = 4 \rightarrow 3)$ line, the line profiles do not show any of the characteristic signatures of infall, and are in fact more consistent with an *expanding* envelope model. One possible explanation is that we are looking at the L483 core through entrained gas in the blue-shifted outflow lobe, which has a sufficiently large inclination and opening angle to allow it to intersect with the line of sight to the central source.

Figure 3.46 shows a $HCO^+(J = 4 \rightarrow 3)$ grid map of L483. Red-skewed asymmetric line profiles are seen over most of the map. The red-shifted peak varies strongly in intensity with position, reaching a maximum at the position northwest of the origin. Figure 3.47 shows a wider area $HCO^+(J = 4 \rightarrow 3)$ raster map of L483. In Figure 3.48 a greyscale map of the integrated $HCO^+(J = 4 \rightarrow 3)$ intensity is compared with the 2.12μm map of Fuller et al. (1993). The first thing to notice is that the HCO^+ emission does not peak at the origin, which, in fact, coincides with a weak saddle point in the HCO^+ emission. The overall morphology of the HCO^+ emission appears to be well correlated with the western lobe of the bipolar infrared reflection nebula centred on the L483. Since this lobe of the reflection nebula is clearly associated with the blue-shifted bipolar outflow lobe (Fuller et al. 1995), this strongly suggests that the off-centre $HCO^+(J = 4 \rightarrow 3)$ emission is dominated by the outflow.

To investigate this further, we show in Figure 3.49 channel maps derived from the raster map in Figure 3.47. Surprisingly, the $HCO^+(J = 4 \rightarrow 3)$ emission to the west of the centre is not biased towards blue-shifted velocities, as would be expected if it mainly arises in the blue-shifted outflow lobe – in fact the strongest emission in this region is seen in the red-shifted $6.1\,\mathrm{km\,s^{-1}}$ velocity bin.

The line profile shapes and morphology shown by our spectral line observations of L483 do not fit into any simple source model. The observations are clearly not consistent with infall, and in contrast to VLA 1623, we cannot plausibly attribute this to strong depletion, since the gas in the L483 envelope is much warmer than in

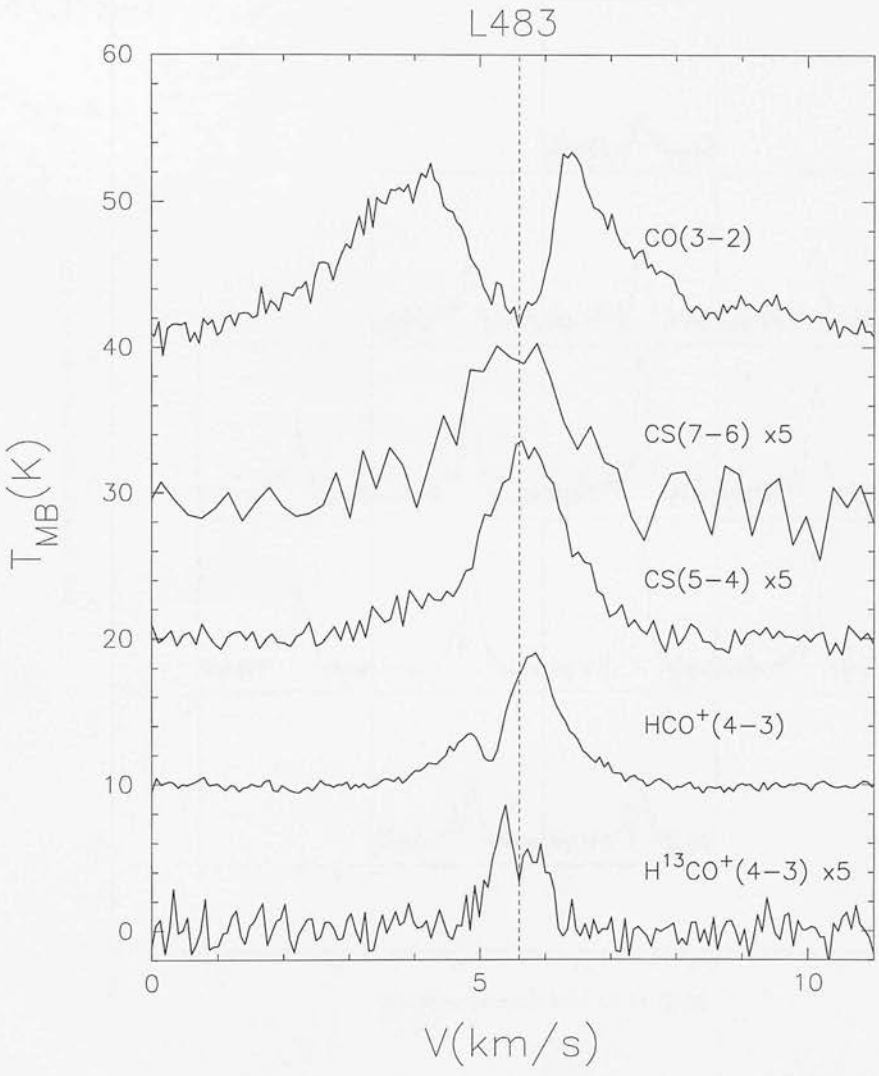

Figure 3.45: Spectra observed towards the peak of L483. The vertical dashed line is at a velocity of $5.6\,\mathrm{km\,s^{-1}}$.

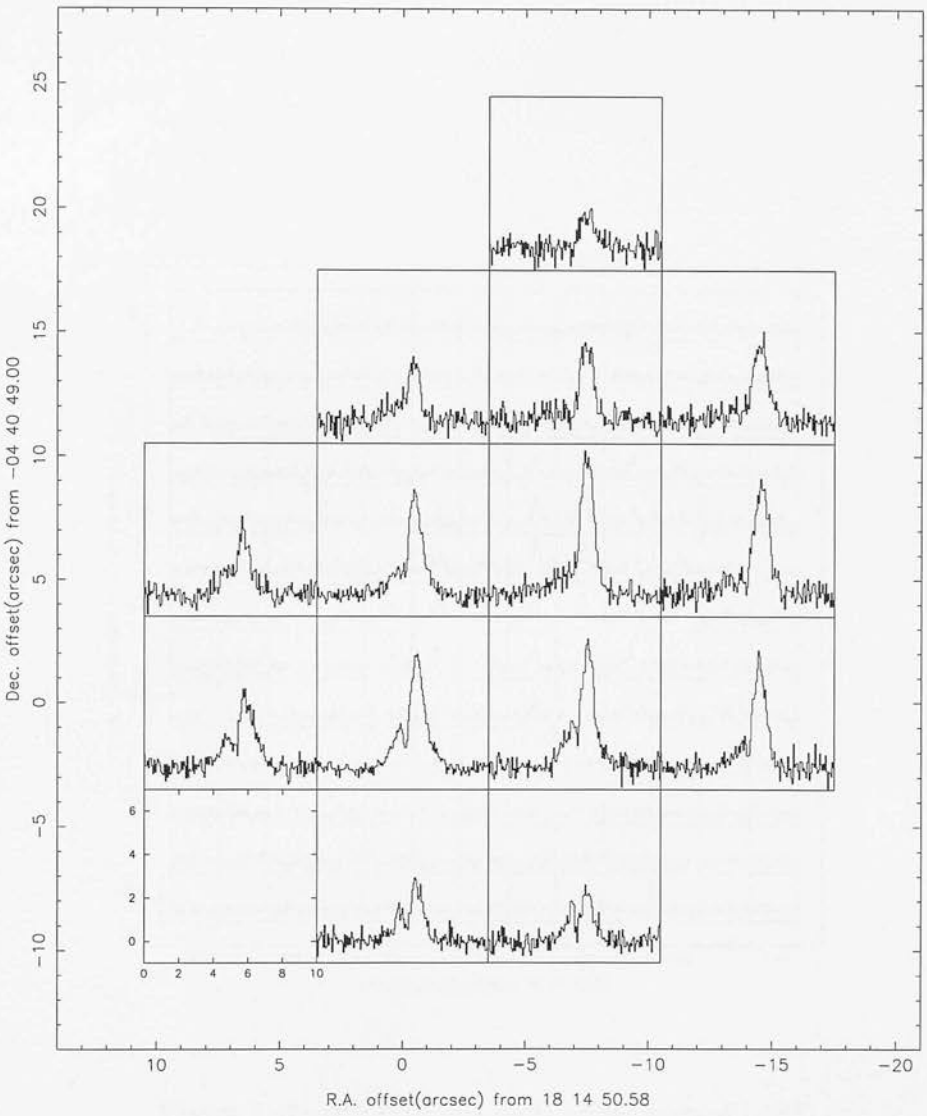

Figure 3.46: Grid map of L483 in the $HCO^+(J = 4 \rightarrow 3)$ transition.

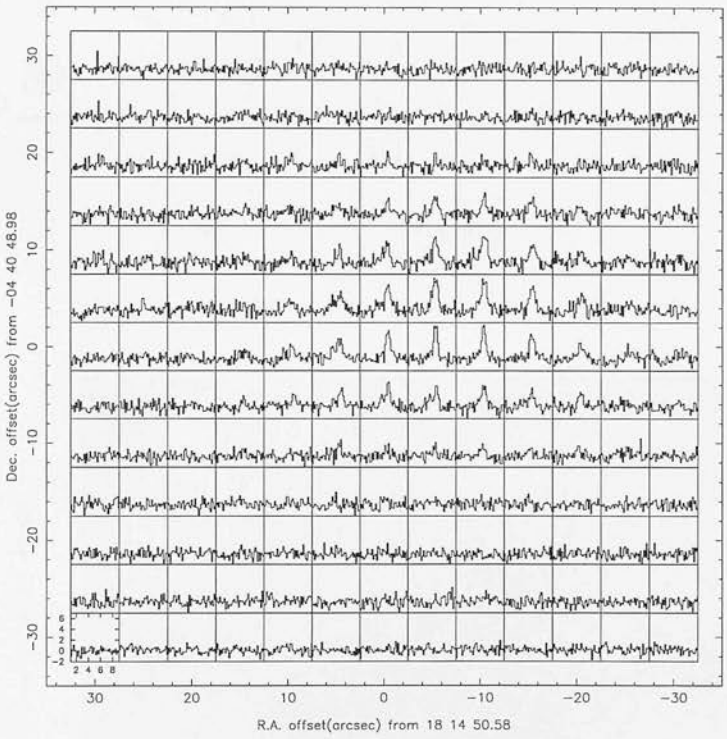

Figure 3.47: $HCO^+(J = 4 \rightarrow 3)$ raster map of L483.

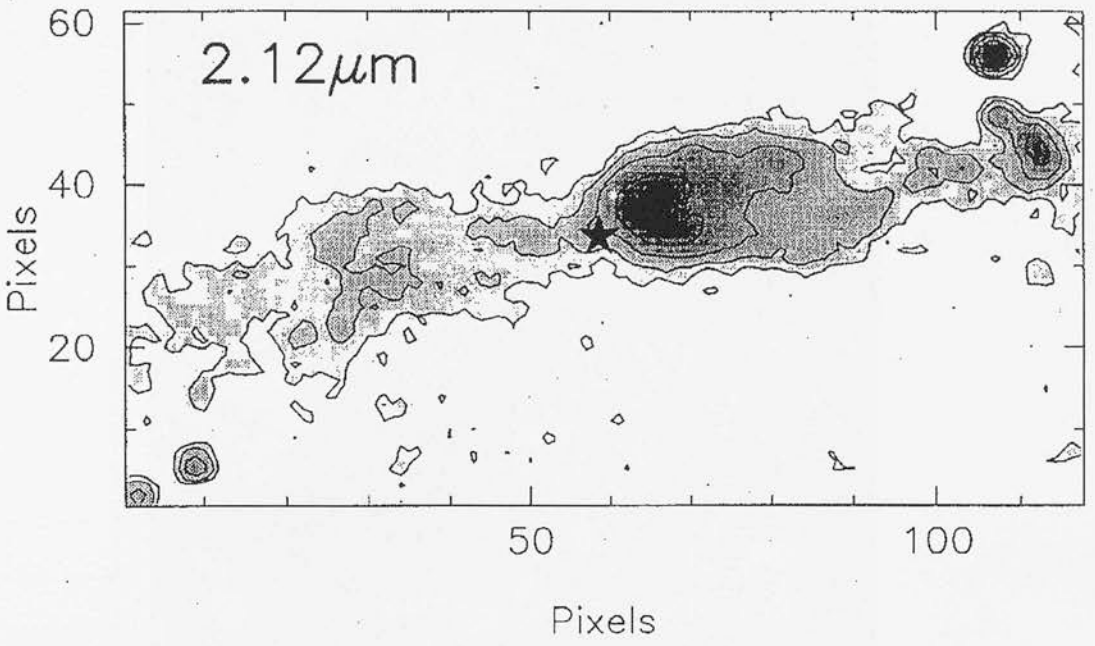

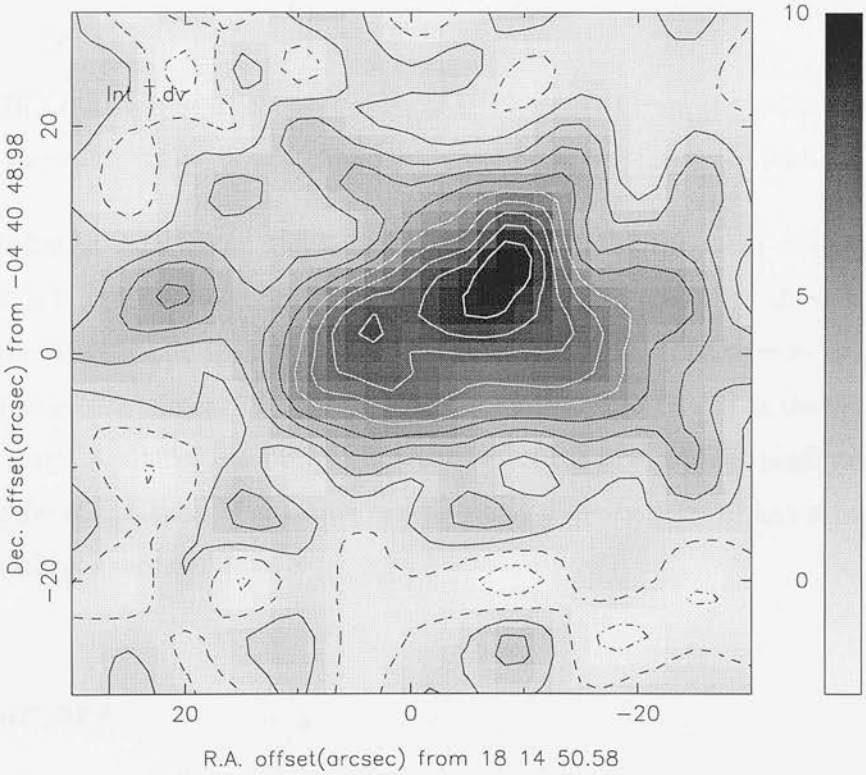

Figure 3.48: The top diagram shows the 2.12 μm map of the L483 infrared nebula, from Fuller et al. (1995). The pixel scale is 1 pixel$\equiv$1.09″. The position of the protostar is indicated by the 'star'. The bottom map shows the integrated $HCO^+(J = 4 \rightarrow 3)$ emission towards L483, between 3.0 and 9.0 $km\,s^{-1}$.The contour step is 1.0 K $km\,s^{-1}$, and the origin coincides with the position of the protostar.

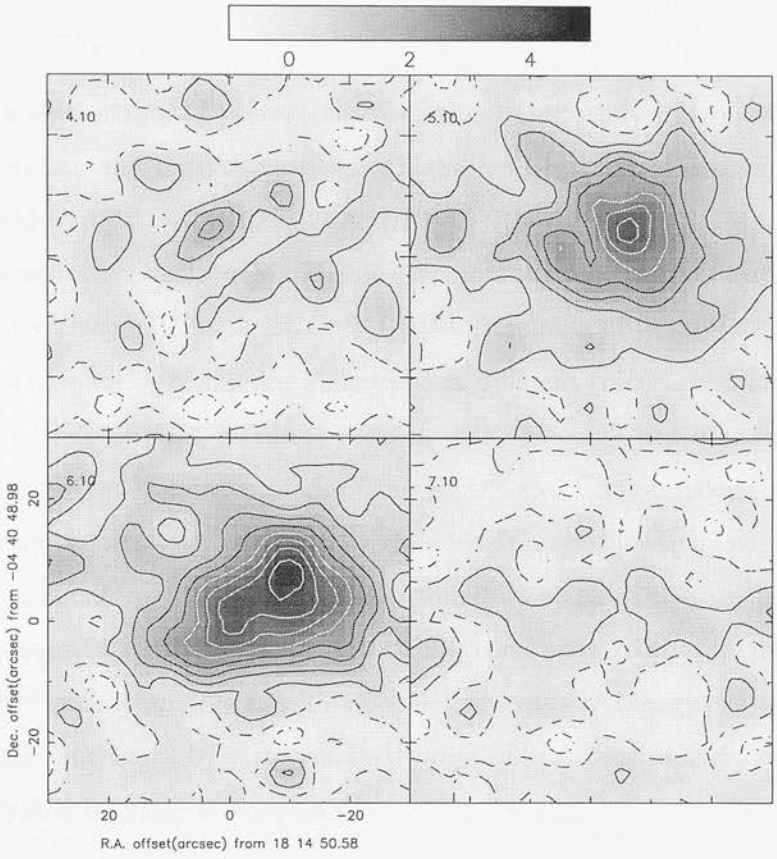

Figure 3.49: $HCO^+(J = 4 \rightarrow 3)$ channel maps of L483, derived from the raster map in Figure 3.47. The contours begin at -0.5K km s^{-1}, and increase in steps of 0.5K km s^{-1}.

VLA1623. Taken at face value, the line profiles suggest that the L483 envelope is expanding. It is interesting to contrast the line profiles in this map with those in the Serpens SMM4 $HCO^+(J = 4 \rightarrow 3)$ map shown in Figure 3.32. The profiles in each map appear remarkably similar to the reflections along the velocity axis of the profiles in the other map. A similar relation is found between the line profiles predicted by radiative transfer calculations of envelope models which differ only by a change in sign of the systematic gas motion.

3.3 Summary

In this chapter we have presented results from a submillimetre spectral line survey using the James Clerk Maxwell Telescope, of a sample of objects representing the

earliest known stages of protostellar evolution. Our study has revealed a mixture of infall, rotation and outflow motions. Of the ten objects included in our sample, five (NGC1333-IRAS2; IRAS 16293-2422; L1689S-IRS67; Serpens SMM2; Serpens SMM4) showed qualitative signatures of infall (i.e. blue-skewed line profiles) in the high critical density tracers, CS and HCO^+ . Of the remaining objects, four showed either no signature of infall or conflicting signatures in different tracers, and one (L483) showed red-skewed line profiles, in direct conflict with the infall expectation. We examined the evidence that the line profiles of the HCO^+ and CS transitions observed towards each of the objects were confused by emission from outflows, by comparing the morphology and centroid velocity gradients found in maps of these transitions with CO outflow maps, wherever possible. A strong conclusion of this study is that the CS and HCO^+ submillimetre transitions, which are usually thought of as good tracers of protostellar envelopes by virtue of their large critical densities, are often significantly contaminated by outflow emission.

We identify two objects from the five infall candidates in our sample, Serpens SMM4 and IRAS 16293-2422, for which we find little or no evidence of contamination by outflows in the HCO^+ and CS data. These objects appear to have many similarities. Both show strong evidence for rotation ($\Omega \sin i \simeq 28$ and 66 $\mathrm{km\,s^{-1}\,pc^{-1}}$ for SMM4 and IRAS 16293 respectively), and appear to be elongated perpendicular to the rotation axis in maps of integrated $HCO^+(J = 4 \rightarrow 3)$ emission. This may provide evidence that centrifugal support is significant in parts of the envelope. Both these objects are also associated with complicated outflows. We identify NGC1333-IRAS2 as a third strong infall candidate, although in this object the HCO^+ and CS spectra show evidence of contributions from the outflow.

3.4 References

Abergel A., et al., 1996, A&A, 315, L329

André P., Montmerle T., 1994, ApJ, 420, 837

André P., Ward-Thompson D., Barsony M., 1993, ApJ, 406, 122 - AWB

André P., Ward-Thompson D., Motte F., 1996, A&A, 314, 625

André P., Martín-Pintado J., Despois D., Montmerle T., 1990, A&A, 236, 180

Anglada G., Sepúlveda I., Gómez J. F., 1997, A&AS, 121, 255

Anglada G., Rodriguez L. F., Torelles J. M., Estalella R., Ho P. T. P., Cantó J., López R., Verdes-Montenegro L., 1989, ApJ, 341, 208

Aspin C., Sandell G., Russell A. P. G., 1994, A&A, 106, 165

Bachiller R., Cernicharo J., 1986, A&A, 168, 262

Bachiller R., André P., Cabrit S., 1991, A&A, 241, L43

Bachiller R., Cernicharo J., Martin-Pintado J., Tafalla M., Lazareff B., 1990, 231, 174

Bally J., Devine D., Reipurth B., 1996, ApJ, 473, L49

Bally J., Lada E. A., Lane A. P., 1993, ApJ, 418, 322

Bevington P. R., Robinson D. K., 1992, Data Reduction and Error Analysis for the Physical Sciences, McGraw-Hill, New York

Blake G. A., Sandell G., van Dishoeck E. F., Groesbeck T. D., Mundy L. G., Aspin C., 1995, ApJ, 441, 689

Bontemps S., André P., Terebey S., Cabrit S., 1996, A&A, 311, 858

Burke B. F., Graham-Smith F., 1997, An Introduction to Radio Astronomy, Cambridge, CUP

Buckley H. D., Ward-Thompson D., André P., Motte F., Bontemps S., Wootten A., 1998, in prep.

Casali M. M., Eiroa C., Duncan W. D., 1993, A&A, 275, 195 (CED)

Cernicharo J., Bachiller R., Duvert G., 1985, A&A, 149, 273

Cernicharo J., 1992, ATM: A program to compute theoretical atmospheric opacity for frequencies lower than 1000 GHz, IRAM Internal Report, 15 April

Cernis K., 1990, Ap&SS, 166, 315

Chavarria K. C., de Lara E., Finkenzeller U., Mendoza E. E., Ocegueda J., 1988, A&A, 197, 151

Cunningham C. T., Hayward R. H., Wade J. D., Davies S. R., Matheson D. N., 1992, Int. J. Infrared Millimetre Waves, 13, 1827

Curiel S., Raymond J. C., Rodriguez L. F., Canto J., Moran J. M., 1990, ApJ, 365, L85

Curiel S., Rodriguez L. F., Moran J. M., Canto J., 1993, ApJ, 415, 191

Curiel S., Rodriguez L. F., Gomez J. F., Torrelles J. M., Ho P. T. P., Eiroa C., 1996, ApJ, 456, 677

Davies S. R., Cunningham C. T., Little L. T., Matheson D. N., 1992, Int. J. Infrared Millimetre Waves, 13, 647

Davis C. J., Dent W. R. F., Matthews H. E., Aspin C., Lightfoot J. F., 1994, MNRAS, 266, 933

de Geus E., de Zeeuw P. T., Lub J., 1989, A&A, 216, 44

de Lara E., Chavarria K. C., Lopez-Molina G., 1991, A&A, 243, 139

Dent W. R. F., Matthews H. E., Walther D. M., 1995, MNRAS, 277, 193

Dent W. R. F., Cunningham C., Hayward R., Davies S. R., Wade D., Avery L. W., Mayer C. J., Masuda N. T., 1993, MNRAS, 262, L13

Duncan W. D., Robson E. I., Ade P. A. R., Griffin M. J., Sandell G., 1990, MNRAS, 243, 126

Eiroa C., 1991, in Reipurth B., ed., Low Mass Star Formation in Southern Molecular Clouds, ESO Scientific Report No. 11, p.197

Eiroa C., Casali M. M., 1989, A&A, 223, L17

Eiroa C., Casali M. M., 1992, A&A, 262, 468

Estalella R., Anglada G., Rodríguez L. F., Garay G., 1991, ApJ, 371, 626

Foster P. N., Chevalier R. A., 1993, ApJ, 416, 303

Fukui Y., 1989, in Reipurth B., ed., Low Mass Star Formation and Pre-Main Sequence Objects, Garching, ESO, p.95

Fuller G. A., Lada E. A., Masson C. R., Myers P. C., 1995, ApJ, 453, 754

Galli D., Shu F. H., 1993, ApJ, 417, 220

Gómez de Castro A. I., Eiroa C., Lenzen R., 1988, A&A, 201, 299

Greene T. P., Lada C. J., 1996, ApJ, 112, 2184

Greene T. P., Young E. T., 1992, ApJ, 395, 516

Greene T. P., Wilking B. A., André P., Young E. T., Lada C. J., 1994, ApJ, 434, 614

Gregersen E. M., Evans N. J., II, Zhou S., Choi M., 1997, ApJ, 484, 256

Harvey P. M., Wilking B. A., Joy M., 1984, ApJ, 278, 156

Hodapp K.-W., 1994, ApJS, 94, 615

Hodapp K.-W., Ladd E. F., 1995, ApJ, 453, 715

Hurt R. L., Barsony M., 1996, ApJ, 460, L45

Hurt R. L., Barsony M., Wootten A., 1996, ApJ, 456, 686

Jennings R. E., Cameron D. H. M., Cudlip W., Hirst C. J., 1987, MNRAS, 226, 461

Kutner M. L., Ulich B. L., 1981, ApJ, 250, 341

Kutner M. L., Mundy L., Howard R. J., 1984, ApJ, 283, 890

Lada C. J., 1991, in Lada C. J., Kylafis N. D., eds., The Physics of Star Formation and Early Stellar Evolution, Kluwer, Dordrecht, p.329

Lada C. J., Alves J., Lada E. A., 1996, AJ, 111, 1964

Langer W. D., Castets A., Lefloch B., 1996, ApJ, 471, L111

Larson R. B., 1969, MNRAS, 145, 271

Lépine J. R. D., Duvert G., 1994, A&A, 286, 60

Lesurf J. C. G., 1990, Millimetre-wave Optics, Devices & Systems, Bristol, IOP

Liseau R., Sandell G., Knee L. B. G., 1988, A&A, 192, 153

Lizeau R., Lorenzetti D., Molinari S., Nisini B., Saraceno P., Spinoglio L., 1995, A&A, 300, 493

Little L. T., Davies S. R., Cunningham C. T., 1992, Int. J. Infrared Millimetre Waves, 13, 659

Loren R. B., 1976, ApJ, 209, 466

Loren R. B., 1989, ApJ, 338, 902

Loren R. B., Wootten A., 1986, ApJ, 306,142

Loren R. B., Wootten A., Wilking B. A., 1990, ApJ, 365, 269

Lovas F. J., 1992, J. Phys. Chem. Ref., 21, 181

Mardones D., Myers P. C., Tafalla M., Wilner D. J., Bachiller R., Garay G., 1997, ApJ, in press

Matthews H., 1996, JCMT Guide for Prospective Users

McMullin J. P., Mundy L. G., Wilking B. A., Hezel T., Blake G. A., 1994, ApJ, 424 222

Menten K. M., Serabyn E., Güsten R., Wilson T. L., 1987, A&A, 177, L57

Mezger P. G., Sievers A. W., Zylka R., Haslam C. G. T., Kreysa E., Lemke R., 1992, A&A, 265, 743

Mizuno A., Fukui Y., Iwata T., Nozawa S., Takano T., 1990, ApJ, 356, 184

Momose M., Ohashi N., Kawabe R., Hayashi M., Nakano T., 1996, ApJ, 407, 1001

Mundy L. G., Wilking B. A., Myers S. T., 1986, ApJ, 311, L75

Mundy L. G., Wootten A., Wilking B. A., 1990, ApJ, 352, 159

Mundy L. G., Wootten A., Wilking B. A., Blake G. A., Sargent A. I., 1992, ApJ, 385, 306

Myers P. C., Bachiller R., Caselli P., Fuller G. A., Mardones D., Tafalla M., Wilner D. J., 1995, ApJ, 449, L65

Narayanan G., Walker C. K., Buckley H. D., 1997, ApJ, in prep.

Parker N. D., Padman R., Scott P. F., 1991, 252, 442

Padman R., 1990, Specx Users Manual. MRAO, University of Cambridge

Phillips T. G., 1988, in Wolstencroft R. D., Burton W. B., eds, Millimetre and Submillimetre Astronomy. Dordrecht, Kluwer, p.17

Pudritz R. E., Wilson C. D., Carlstrom J. E., Lay O. P., Hills R. E., Ward-Thompson D., 1996, ApJ, 470, L123

Terebey S., 1991, in Palla F., Persei P., Zinnecker H., eds, Young Stars and Early Stellar Evolution, Mem.Soc.Astron.Ital., 62(4), 823

Richer J. S., Padman R., Ward-Thompson D., Hills R. E., Harris A. I., 1993, MNRAS, 262, 839

Sandell G., Knee L. B. G., Aspin C., Robson I. E., Russell A. P. G., 1994, A&A, 285, L1

Sargent A. I., 1979, ApJ, 223, 884

Seymour J, 1981, Electronic Devices and Components, Pitman, London, p.378

Straižys V., Černis K., Bartašiūtė S., 1996, Baltic Astronomy, 5, 125

Strom K. M., Kepner J., Strom S. E., 1995, ApJ, 438, 813

Strom S. E., Vrba F. J., Strom K. M., 1976, AJ, 81, 638

Tamura M., Hayashi S. S., Yamashita T., Duncan W. D., Hough J. H., 1993, ApJ, 404, L21

Ulich B. L., Haas R. W., 1976, ApJS, 30, 247

Van Dishoeck E. F., Blake G. A., Jansen D. J., Groesbeck T. D., 1995, ApJ, 447, 760

Vrba F. J., 1977, AJ, 92, 198

Vrba F. J., Strom S. E., Strom K. M., 1976, AJ, 81, 958

Walker C. K., Carlstrom J. E., Bieging J. H., 1993, ApJ, 402, 655

Walker C. K., Lada C. J., Young E. T., Margulis M., 1988, ApJ, 332, 335

Walker C. K., Carlstrom J. E., Bieging J. H., Lada C. J., Young E. T., 1990, ApJ, 364, 173

Walker C. K., Lada C. J., Young E. T., Maloney P. R., Wilking B. A., 1986, ApJ, 309, L47

Walker C. K., Naraynan G., Boss A. P., 1994, ApJ, 431, 767

Ward-Thompson D., Scott P. F., Hills R. E., André P., 1994, MNRAS, 268, 276

Ward-Thompson D., Buckley H. D., Greaves J. S., Holland W. S., André P., 1996, MNRAS, 281, L53

Warin S., Castets A., Langer W. D., Wilson R. W., Pagani L., 1996 A&A, 306, 935

White G., Casali M. M., Eiroa C., 1995, A&A, 298, 594 (WCE)

Wilking B. A., 1992, in Reipurth B., ed., Low Mass Star Formation in Southern Molecular Clouds, ESO Scientific Report 11, Garching, ESO, p.159

Wilking B. A., Lada C. J., 1983, ApJ, 274, 698

Wilking B. A., Claussen M. J., 1987, ApJ, 320, L133

Wilking B. A., Lada C. J., Young E. T., 1989, ApJ, 340, 823

Wootten A., 1989, ApJ, 337, 858

Wootten A., 1994, in Clemens D. P., Barvainis R., eds, Clouds, Cores and Low Mass Stars, ASP Conference Series, Vol 65, p. 294

Yu T., Chernin L. M., 1997, ApJ, 479, L63

Zhang C. Y., Laurejs R. J., Clark F. O., Wesselius P. R., 1988, A&A, 196,236

Zhou S., 1995, ApJ, 442, 685

Zhou S., Evans N. J., Kompe C., Walmsley C. M., 1993, ApJ, 404, 232

Chapter 4

Modelling Protostellar Infall

In this chapter, we discuss the general approach to the modelling of infall line profiles using spherically symmetric radiative transfer models, dealing with each physical parameter in turn. Using the STENHOLM radiative transfer code described in Chapter 2, we investigate the qualitative dependence of the predicted line profiles on a number of different model parameters. Model fits to the HCO^+ and CS observations of NGC1333-IRAS2 and Serpens SMM4 are presented and discussed.

4.1 Approach to the modelling

The approach to the data modelling is necessarily a compromise between the desire to represent realistically the object being modelled, and the practical need to limit the parameter space and running time of the numerical simulations. Ideally, the model should include two or three dimensional source geometries, with clumpiness and macroscopic turbulence, and a self-consistent treatment of the dynamics, heating and cooling, chemistry, and ionisation balance (and hence magnetic support) in the protostellar envelope. This lies beyond the aims of this thesis, however.

The observations are modelled using the spherically symmetric microturbulent Λ-

iteration radiative transfer code described in Chapter 2. Such a model is better matched to the level of sophistication of the observations than the 'ideal' model mentioned above. Even with the considerable simplification of spherical symmetry, however, the choice of parameters is formidable. Radial profiles of density, kinetic temperature, molecule abundance, systematic velocity, and microturbulent velocity width must be specified. Additional parameters include the choice of inner and outer boundaries of the model, the incident radiation fields at the inner and outer boundaries, and the distance to the object. Strictly speaking, the number of parameters required to constrain each radial profile fully is equal to the number of discrete radial shells used to represent the model cloud. Some a-priori assumptions must be made about the *forms* taken by these profiles, so that they may be described by specifying only a few parameters. For example, some of the profiles may be assumed to have a power law dependence on radius, which requires only the power law exponent and a normalisation factor to be specified. Wherever possible, theoretical considerations are used to guide the choice of parameters used to describe the radial profiles. In the following sections we discuss each physical parameter profile in turn.

4.1.1 The systematic velocity profile

Following the onset of fully dynamical collapse, the radial velocity profile should tend towards a freefall $r^{-1/2}$ profile (e.g. Larson 1969; Shu 1977; Hunter 1977; Zhou 1992; Foster & Chevalier 1993). The pure free-fall velocity profile may be written as:

$$v_r(r) = -\left(\frac{2GM}{r}\right)^{\frac{1}{2}}, \tag{4.1}$$

$$\simeq -1.3 \left(\frac{M}{\mathrm{M}_\odot}\right)^{\frac{1}{2}} \cdot \left(\frac{r}{1000\,\mathrm{AU}}\right)^{-\frac{1}{2}} \mathrm{km\,s^{-1}}. \tag{4.2}$$

Hunter (1977) argued that the infall velocity profiles in non-rotating clouds which collapse from different initial conditions should approximately converge, even when the mass accretion rates are very different, as long as the comparison is made at times when the central protostellar masses are equal. This gives some justification for our use of the Shu model velocity profiles to *parameterise* the infall velocity field in the radiative transfer modelling. This allows the velocity field to be described in terms of only two

quantities: the infall radius, $r_{\rm inf}$ and the effective sound speed $a_{\rm eff}$, We stress again that these are merely used as parameters characterising the velocity field, and their actual physical significance is model dependent.

We have found the following empirical fit to the exact velocity profile predicted by the standard Shu model (Shu 1977; see Chapter 1), inside the infall radius at $r_{\rm inf} = a_{\rm eff}t$:

$$\frac{v_r(r)}{a_{\rm eff}} \simeq -\sqrt{2}\left(\frac{r}{r_{\rm inf}}\right)^{-\frac{1}{2}} + \sqrt{2}\left(\frac{r}{r_{\rm inf}}\right)^{0.15}. \tag{4.3}$$

If the collapsing cloud has some initial rotation, then centrifugal effects are expected to become important at small radii, and the radial velocity profile should turn over close to the centre as well. According to the Terebey, Shu & Cassen (1984) model, if the collapsing cloud has an initial angular velocity Ω, then the inner radius, r_d, at which centrifugal forces begin to dominate depends on the mass already accreted, $M_{\rm acc}$, and the radius, R, enclosing this mass in the initial singular isothermal sphere, through the following relation:

$$r_d = \frac{\Omega^2 R^4}{G M_{\rm acc}}, \tag{4.4}$$

$$\simeq 17\left(\frac{\Omega}{\rm km\,s^{-1}\,pc^{-1}}\right)^2 \cdot \left(\frac{R}{5000\,\rm AU}\right)^4 \cdot \left(\frac{M_{\rm acc}}{\rm M_\odot}\right)^{-1} \rm AU. \tag{4.5}$$

$$\tag{4.6}$$

4.1.2 The microturbulent velocity profile

As discussed in Chapter 2, the radiative transfer code used to model the data in this thesis makes use of the microturbulent approximation, which assumes that random 'turbulent' motions can be treated in the same way as thermal molecular motions, i.e. they are incorporated into the local line profile function. Comparisons between radiative transfer codes which model macroscopic and microscopic turbulence suggest that the main effect of relaxing the microturbulent approximation is to reduce the strength of self-absorption features (Park & Hong 1995).

Although observations appear to indicate random motions of some kind must be present in protostellar envelopes, very little theoretical work has been done on the role of turbulence and turbulent support in protostellar collapse. Lizano & Shu (1989) derived a 'turbulent equation of state' using the well known 'Larson's Laws' (Larson 1981), which relate the observed velocity dispersion (σ), size (R), and average density ($\bar{\rho}$) in molecular clouds and cores:

$$\sigma \propto R^{\frac{1}{2}}, \tag{4.7}$$

$$\bar{\rho} \propto R^{-1}. \tag{4.8}$$

These correlations apply to ensembles of clouds and also to observations of individual clouds in different molecular tracers, and are believed to characterise the turbulent motions in molecular clouds (e.g. Myers 1983). Together they imply

$$\sigma \propto \bar{\rho}^{-\frac{1}{2}}. \tag{4.9}$$

Zhou (1992) assumed that this relation describes the spatial variation of turbulent velocity with density in an individual protostellar envelope, in radiative transfer calculations of infall line profiles from self-similar collapse models.

Lizano & Shu (1989) defined the 'turbulent pressure', $P_{\rm tb}$, by the relation

$$\sigma^2 = dP_{\rm tb}/d\rho, \tag{4.10}$$

which when combined with equation 4.9 leads to

$$P_{\rm tb} = A \log \rho. \tag{4.11}$$

This was suggested to characterise the mechanical support provided by the turbulence. When added to the thermal pressure $P_{\rm th}$, it leads to the following 'equation of state':

$$P = \rho a^2 + A \log \rho, \tag{4.12}$$

where a is the isothermal sound speed and A is a variable parameter. This is known as a 'logotropic' equation of state.

McLaughlin & Pudritz (1996) derived a similar but different equation of state by using the relation $\sigma^2 = P_{\rm tot}/\rho$ in place of equation 4.10 (where $P_{\rm tot}$ is the combined turbulent and thermal pressure), and incorporating deviations from the standard line-width size relation (4.7) observed towards high mass cores (Caselli & Myers 1995), with the result:

$$\frac{P_{\rm tot}}{P_c} = 1 + A \ln(\frac{\rho}{\rho_c}), \tag{4.13}$$

where P_c and ρ_c are the central density and pressure in a cloud.

Vásquez-Semadeni, Cantó & Lizano (1997) have recently argued that equations of state derived from Larson's Laws may be inappropriate to *dynamically* collapsing clouds, because Larson's Laws were determined from observations of clouds which were in *equilibrium* configurations, i.e. "instead of representing a number of different states for the same cloud, they represent the same state for different clouds". They carried out numerical hydrodynamic and magnetohydrodynamic simulations to test the behaviour of the turbulence during the collapse, and found that, in contrast to equation 4.9, the turbulent velocity dispersion actually *increases* with density during the collapse. For purely hydrodynamic and weakly magnetic collapse models the relation between the turbulent velocity dispersion and the density approached a power law of the form $\sigma \propto \rho^{1/2}$ (i.e. $P_{\rm tb} \propto \rho^2$). In the case of strongly magnetically inhibited collapse, the power law index changed to $\sigma \propto \rho^{1/4}$ ($P_{\rm tb} \propto \rho^{3/2}$), consistent with the predicted behaviour for the slow compression of Alfvén waves (McKee & Zweibel 1995). The increase in turbulent velocity dispersion during the collapse was likened to the heating of a gas (i.e. increasing thermal velocity dispersion) under adiabatic compression.

As the preceding discussion has illustrated, the behaviour of the turbulence in infalling protostellar envelopes is theoretically rather uncertain. Turbulence nevertheless plays a very important part in the formation of line profiles, and is unfortunately one of the principal sources of uncertainty in the radiative transfer modelling. In the models in this Chapter, we will usually assume that the turbulent velocity is spatially uniform.

4.1.3 The density profile

In a region where the infall velocity has a free-fall profile (Equation 4.2), there will usually be a strong tendency for the density profile to adopt an $r^{-3/2}$ distribution: if the rate of injection of material into the accretion stream is not changing rapidly with time, the quantity $4\pi r^2 \rho v_r$ should be approximately independent of radius. The Shu model prediction for the density profile deep inside the infalling region may be written as:

$$\rho(r) = \frac{a_{\rm eff}^2}{\pi\sqrt{32}\,G r_{\rm inf}^{1/2}}\, r^{-\frac{3}{2}}, \tag{4.14}$$

where, as before, $r_{\rm inf} = a_{\rm eff} t$ is the infall radius, and $a_{\rm eff}$ is the effective sound speed. This may be written in terms of the molecular hydrogen number density, $n_{\rm H_2}$, using $n_{\rm H_2} = \rho/\mu$, where $\mu \simeq 2.8\, m_{\rm H}$ is the mean molecular mass:

$$n_{\rm H_2} \simeq 10^6 \left(\frac{a_{\rm eff}}{0.35\,{\rm km\,s^{-1}}}\right)^2 \cdot \left(\frac{r_{\rm inf}}{1000\,{\rm AU}}\right)^{-\frac{1}{2}} \cdot \left(\frac{r}{1000\,{\rm AU}}\right)^{-\frac{3}{2}} {\rm cm^{-3}}. \tag{4.15}$$

The exact Shu model density profile inside the whole infalling region is very well approximated by the following empirical formula:

$$\rho(r) = \frac{a_{\rm eff}^2}{2\pi G r_{\rm inf}^2}\left[0.35\left(\frac{r}{r_{\rm inf}}\right)^{-\frac{3}{2}} + 0.65\left(\frac{r}{r_{\rm inf}}\right)^{-0.64}\right]. \tag{4.16}$$

Writing this in terms of the molecular hydrogen number density, we find

$$n_{\rm H_2} = 2.9{\times}10^6 \left(\frac{a_{\rm eff}}{0.35\,{\rm km\,s^{-1}}}\right)^2 \cdot \left(\frac{r}{1000{\rm AU}}\right)^{-2} \left[0.35\left(\frac{r}{r_{\rm inf}}\right)^{-\frac{3}{2}} + 0.65\left(\frac{r}{r_{\rm inf}}\right)^{-0.64}\right] {\rm cm^{-3}}. \tag{4.17}$$

Outside the infall radius, the density profile is

$$\rho(r) = \frac{a_{\rm eff}^2}{2\pi G r^2}, \tag{4.18}$$

$$n_{\rm H_2} = 2.9 \times 10^6 \left(\frac{a_{\rm eff}}{0.35\,{\rm km\,s^{-1}}}\right)^2 \cdot \left(\frac{r}{1000{\rm AU}}\right)^{-2} {\rm cm^{-3}}. \tag{4.19}$$

There are several competing theoretical models which predict different forms of the density profiles at various stages in the contraction and collapse of a dense cloud core (e.g. Basu & Mouschovias 1994; Foster & Chevalier 1993). Once a central core has formed, however, and the collapse begins to evolve hydrodynamically, theoretically, there is a tendency for the *forms* of the density and velocity profiles to converge towards the Shu model forms, at least towards the centre of the collapsing regions (e.g.

Foster & Chevalier 1993). We therefore initially search for fits to our observations using density profiles of the form of Equation 4.17, although we do not require that the adopted density profile uses the same $r_{\rm inf}$ and $a_{\rm eff}$ as the Shu model form of the velocity profile. The values of $a_{\rm eff}$ and $r_{\rm inf}$ used in the model fits are simply adjustable parameters, and do not necessarily carry the physical meaning given to them by the Shu model.

4.1.4 The kinetic temperature profile

The temperature of the gas in an infalling protostellar envelope is determined by the balance of heating and cooling processes. The heating processes include line-absorption of dust-continuum photons followed by collisional de-excitation; compressional heating due to the converging gas motion; and gas-grain collisions (when the dust temperature is higher than the gas temperature). Cooling processes include line emission and gas-grain collisions (when the dust temperature is lower than the gas temperature). Ceccarelli, Hollenbach & Tielens (1996) modelled all of these processes, as well as chemical evolution and grain mantle desorption, to derive the temperature profile in protostellar envelopes with density and velocity profiles given by the Shu (1977) model, and a central embedded heating source. They found that in all the cases studied, the gas temperature profile stays within $\sim 30\%$ of the dust temperature, usually lying slightly below the dust temperature. In the following it is assumed that the gas temperature is well coupled to the dust temperature, which is primarily determined by the balance of absorbed and emitted continuum radiation. This assumption may be significantly in error, however, for hydrogen number densities below $\sim 10^4\,{\rm cm}^{-3}$.

An approximate expression for the dust temperature profile in a spherical protostellar envelope in the optically thin limit may be obtained as follows. We first of all assume that the wavelength dependence of the dust opacity over the range of peak wavelengths of the dust emission in the envelope, is given by

$$\kappa_d(\lambda) \propto \lambda^{-\beta}, \tag{4.20}$$

where β is a constant, and typically has a value between 1 and 2. We will later adopt the canonical value of 1.5 suggested by submillimetre dust continuum observations of Class 0 envelopes (e.g. André, Ward-Thompson & Barsony 1993). If the emitted radiation reaching the optically thin part of the envelope peaks at the wavelength $\lambda_\star$, then a representative grain of dust at the radius r will be heated by radiation at a rate approximately given by

$$\Gamma_g(r) \propto \frac{L_\star}{4\pi r^2}\lambda_\star^{-\beta}, \tag{4.21}$$

where $L_\star$ is the luminosity of the central source. If $T_d(r)$ is the grain temperature at the radius r, then the grain cooling rate approximately satisfies

$$\Lambda_g(r) \propto \sigma T_d(r)^4 \lambda_d(r)^{-\beta} \tag{4.22}$$

$$\propto \sigma T_d(r)^{4+\beta}, \tag{4.23}$$

where $\lambda_d(r)$ is the wavelength at which the dust emission peaks. In radiative equilibrium, $\Lambda_g(r) = \Gamma_g(r)$, which finally gives

$$T_d(r) \propto \left(\frac{L_\star}{r^2\lambda_\star^\beta}\right)^{1/(4+\beta)}. \tag{4.24}$$

The value of $\lambda_\star$ depends on the details of the dust radiative transfer through the optically thick inner region (i.e. how the material in this region is distributed). Kenyon et al. (1993) used the diffusion approximation in the optically thick region to estimate the value of $\lambda_\star$. For a density profile of the form $\rho(r) = \rho_0 r^{-q}$ this gives:

$$\lambda_\star \propto \left[\frac{{\rho_0}^{2/(q-1)}}{L}\right]^{1/(4+4\beta)}. \tag{4.25}$$

Substituting this expression into equation 4.24, and setting $\beta = 1.5$ and $q = 1.5$ (appropriate for a hydrodynamically collapsing region), we find

$$T_d(r) \propto \rho_0^{-0.055} L_\star^{0.21} r^{-0.36}. \tag{4.26}$$

The temperature profile in the optically thin part of the envelope is therefore only weakly dependent on the density normalisation and the luminosity. An expression for the accretion luminosity of the central protostar may be derived if the standard Shu model is correct. The mass accretion rate predicted by the Shu model is:

$$\dot{M}_\star \simeq \frac{a^3}{G}. \tag{4.27}$$

If the infalling gas falls directly onto the surface of the protostar, with radius $R_\star$, the accretion luminosity may be written as:

$$L_\star = \frac{GM_\star \dot{M}_\star}{R_\star} = \frac{Ma^3}{R_\star}, \tag{4.28}$$

$$\simeq 100 \left(\frac{M_\star}{\mathrm{M}_\odot}\right) \left(\frac{a}{0.35\,\mathrm{km\,s^{-1}}}\right)^3 \left(\frac{R_\star}{3\mathrm{R}_\odot}\right)^{-1} \mathrm{L}_\odot. \tag{4.29}$$

Model calculations for the central hydrostatic protostar indicate that the protostellar radius, $R_\star$, is a function of the mass accretion rate, the protostellar mass, and the deuterium abundance, but for masses below $1\,\mathrm{M}_\odot$ this radius is confined to the range 1.5–$6\,\mathrm{R}_\odot$, and has a typical value of around $3\,\mathrm{R}_\odot$ (Stahler 1988). The accretion luminosity could be considerably less than the value given by Equation 4.29, however, if the mechanical luminosity of the outflow accounts for a significant fraction of the accretion energy (Henriksen, André & Bontemps 1997).

Despite the approximations used in the above derivation, the predicted dependence of the temperature profile on the various quantities agrees well with the results of detailed dust radiative transfer calculations (e.g. Butner et al. 1990; Kenyon, Calvet & Hartmann 1993). Equation 4.26 only applies to the optically thin region of the envelope, however. Inside the radius at which the envelope becomes optically thick to its own radiation (typically $<\sim 100\,\mathrm{AU}$), the temperature profile steepens, to a $\sim r^{-5/7}$ power law (Adams & Shu; Kenyon et al. 1993). For the objects modelled in this chapter, the optically thick region is expected to be very much smaller than the beam size of the observations. and is comparable to the inner shell radius used in the radiative transfer models. At sufficiently large radii, the gas temperature will approach the ambient temperature of the larger scale cloud. We therefore adopt the temperature profile appropriate to the optically thin limit ($T \propto r^s$; $s = -0.33$–0.4) in the inner region, and switch to a flat profile at the radius where the power law inner profile falls below the ambient cloud temperature.

4.1.5 The abundance profile

The profiles of CS and HCO^+ relative abundance in an infalling protostellar envelope are governed by time dependent chemistry and the transfer of molecules between the gas phase and the ice mantles surrounding dust grains. This problem has been studied by Rawlings et al. (1992) and Willacy, Rawlings & Williams (1994) in the case of isothermal collapsing clouds. The objects studied in this thesis, contain internal stellar heating sources, and are unlikely to be well described by an isothermal model. The chemistry of internally heated infalling protostellar envelopes has been studied by Ceccarelli, Hollenbach & Tielens (1996), who included HCO^+ in their list of chemical species.

The principal formation mechanism of HCO+ in dense cloud environments is through the reaction of CO with H_3^+:

$$H_3^+ + CO \rightarrow HCO^+ + H_2. \tag{4.30}$$

H_3^+ is formed following the ionisation of molecular hydrogen hydrogen by cosmic rays (CR):

$$H_2 + CR \rightarrow H^+ + H + e^-, \tag{4.31}$$

$$H^+ + H_2 \rightarrow H_3^+. \tag{4.32}$$

The principal destruction mechanisms of HCO^+ are

$$HCO^+ + e^- \rightarrow CO + H, \tag{4.33}$$

$$HCO^+ + H_2O \rightarrow H_3O^+ + CO, \tag{4.34}$$

$$HCO^+ + CS \rightarrow HCS^+ + CO. \tag{4.35}$$

$$\tag{4.36}$$

The second of these reactions only becomes significant when H_2O ice evaporates from dust grain mantles at $T_d \geq 100$K. This introduces a qualitative difference between chemical models of HCO^+ in isothermal and internally heated envelope models. In the isothermal models, the abundance of HCO^+ increases in the inner regions, as a

result of the greater depletion of H_2O onto dust grains with increasing gas density (Rawlings et al. 1992). Conversely, internally heated models may warm the innermost regions sufficiently to *release* H_2O from grain mantles into the gas phase, causing a substantial *drop* in the HCO^+ abundance in the inner regions (Ceccarelli et al. 1996). The HCO^+ abundance profile has more than just an observational significance, since HCO^+ is one of the principal ionic species through which the cloud is coupled to the magnetic field, and chemical processes in the envelope may have *dynamical* consequences.

The main production mechanisms for CS include the following reactions (Prasad & Huntress 1982):

$$CH + S \rightarrow CS + H, \tag{4.37}$$

$$SO + C \rightarrow CS + O, \tag{4.38}$$

$$HCS^+ + e^- \rightarrow CS + H. \tag{4.39}$$

The first reaction only takes place in low density regions where CH is abundant. CS is difficult to destroy, since the main destruction mechanism of CS produces HCS^+, which leads directly back to CS. If sufficient carbon atoms remain available after formation of CO, all gas-phase sulphur should eventually be processed into CS in quiescent clouds (Swade 1989).

Given the theoretical uncertainties regarding the radial profiles of the tracer molecule fractional abundances, and the requirement to limit the parameter space, we used flat abundance profiles in our modelling. The fractional abundances of CS and HCO^+ measured in dense molecular gas cores occupy similar ranges, typically between 10^{-9} and 10^{-8} (e.g. Irvine et al 1987; McMullin, Mundy & Blake 1994; Blake et al. 1995). The measured values of $[^{12}C/^{13}C]$ at the galactocentric radius of the sun (which applies to all our observed objects) lie in the range 50–100 (Wilson & Rood 1994). We therefore restrict the abundances used in the modelling to these ranges of values.

4.2 Parameter study of infall profiles

4.2.1 The canonical infall model

It is useful to define a specific infalling envelope model, with plausible physical parameters, which may be used to investigate some general properties of infall spectral line profiles. We use the Shu model density and velocity profiles (equations 4.17 and 4.3) at the stage when a mass $M_\odot/2$ has already accreted onto the central protostar, and a further $\simeq M_\odot/2$ of envelope gas is infalling towards it. If we choose an effective sound speed for use in the Shu model formulae of $a_{\rm eff} = 0.35\,{\rm km\,s^{-1}}$, then an infall radius of $\simeq 3700\,{\rm AU}$ is implied. We therefore use the following Shu model relations for the systemic velocity and hydrogen number density profiles:

$$v_r(r) = \left[-0.49\left(\frac{r}{3700\,{\rm AU}}\right)^{-\frac{1}{2}} + 0.49\left(\frac{r}{3700\,{\rm AU}}\right)^{0.15}\right]\ {\rm km\,s^{-1}}, \quad (4.40)$$

$$n_{\rm H_2}(r) = 2.0\times10^5\left[0.35\left(\frac{r}{3700\,{\rm AU}}\right)^{-\frac{3}{2}} + 0.65\left(\frac{r}{3700\,{\rm AU}}\right)^{-0.64}\right]\ {\rm cm^{-3}}. \quad (4.41)$$

$$(4.42)$$

Outside the infall radius, the systematic velocity is set to zero, and the density profile is given by

$$n_{\rm H_2}(r) = 2.0\times10^5\left(\frac{r}{3700\,{\rm AU}}\right)^{-2}. \quad (4.43)$$

We truncate the density profile at an outer radius of 10000 AU, which encloses a total mass of $2.75\,M_\odot$. This corresponds to the typical radius at which dense cores merge with the more diffuse gas in the ambient molecular cloud. As we shall see, the data do not favour the Shu model over other forms of collapse.

The adopted microturbulent velocity dispersion is $\sigma_{\rm tb} = 0.3\,{\rm km\,s^{-1}}$, which is assumed to be spatially constant. Although there is little empirical or physical justification for a flat turbulent velocity profile, (see the discussion in the previous section), we make this assumption as a zeroth order approximation, in the absence of any clear consensus as to the correct description of turbulence in infalling envelopes.

As discussed above, the kinetic temperature profile (assumed to be equal to the dust temperature profile) in the optically thin part of the envelope is expected to be fairly insensitive to the luminosity of the central source. We choose a canonical temperature profile of

$$T(r) = 20 \left(\frac{r}{1000\mathrm{AU}} \right)^{-0.36} \mathrm{K}, \tag{4.44}$$

The normalisation of the temperature profile was fixed using the dust temperature profile calculated by Kenyon, Calvet & Hartmann (1993), for a source luminosity of $\sim 15 L_{\odot}$. The varying kinetic temperature in the envelope is not strictly consistent with the assumption of constant a_{eff} implied by the Shu model, where $a_{\mathrm{eff}}^2 = \sigma_{\mathrm{tb}}^2 + kT/\bar{m}$. Our primary concern is not to investigate the Shu model solution in detail however, but rather to investigate the essential features of line formation in infalling envelopes, whether the infall is described by the Shu model or not.

We set both the CS and HCO^+ relative abundances to 5.0×10^{-9}, and assume a $[H^{12}CO^+]/[H^{13}CO^+]$ isotopic ratio of 60. The set of molecular constants used in the radiative transfer modelling are listed in Table 4.2.1. The data are taken from the JPL spectral line catalogue (Poynter & Pickett 1985).

Molecule	Mass (10^{-27}kg)	μ (10^{-30}C m)	B_{rot} (GHz)	hB_{rot}/k (K)
HCO^+	48.16	12.2	44.59	2.14
$H^{13}CO^+$	49.81	13.0	43.38	2.08
CS	73.02	6.54	24.50	3.50

Table 4.1: Assumed physical constants of the molecules modelled. μ denotes the permanent molecular dipole moment.

4.2.2 The origin of the infall profile

We now use the radiative transfer code described in Chapter 2 to simulate JCMT spectral line observations of the canonical infall model, and investigate how the predicted

line profiles depend on a number of different model parameters.

Figure 4.1 shows the predicted HCO^+ , $H^{13}CO^+$ and CS line profiles for the canonical infall model described above. The model cloud was assumed to lie at a distance of 200 pc, which is approximately the median distance of our sample of sources, and the appropriate JCMT beam sizes for each transition were used when carrying out the beam convolution (see Chapter 3).
Double-peaked, blue-asymmetric line profiles are seen in all of the main isotope transitions, apart from the $CS(J = 7 \rightarrow 6)$ line, which is nevertheless skewed slightly bluewards of the systemic velocity. The minima between the peaks of the double-peaked profiles lie close to the systemic velocity. The $HCO^+(J = 3 \rightarrow 2)$ line shows a stronger self-reversal than the $HCO^+(J = 4 \rightarrow 3)$ line, and in both these lines the self-reversal is stronger than the $CS(J = 5 \rightarrow 4)$ line. The two single-peaked $H^{13}CO^+$ lines peak very close to the systemic velocity, coinciding with the minima in the main line profiles. Low level high-velocity wings are visible in all of the main line profiles, and appear to be stronger in the higher rotational transitions of both molecules.

To illustrate how the asymmetries in line profiles arise, we show in Figure 4.2 the separate contributions of the front and rear portions of the envelope to the line profiles for the $HCO^+(J = 4 \rightarrow 3)$ and $CS(J = 5 \rightarrow 4)$ transitions. The front hemisphere of the envelope (in which the systematic velocity is red-shifted) is seen to be mostly responsible for the red-shifted peak in the line profile, as expected. More surprising, however, is the observation that the front hemisphere also dominates the emission at velocities well into the blue-shifted side of the line profile, and contributes significantly to the blue-shifted peak. Emission from the rear hemisphere only becomes dominant in the most blue-shifted part of the line. It is interesting to note that the contribution of the rear hemisphere to the blue peak is no greater than the contribution of the front hemisphere to the red peak, and it is the extra contribution of the *front* hemisphere to the *blue*-shifted emission which produces the blue asymmetry. This contrasts with the explanation usually given for the infall asymmetry, in which it is argued that the optical depth to the warm dense blue-shifted gas just beyond the central protostar is

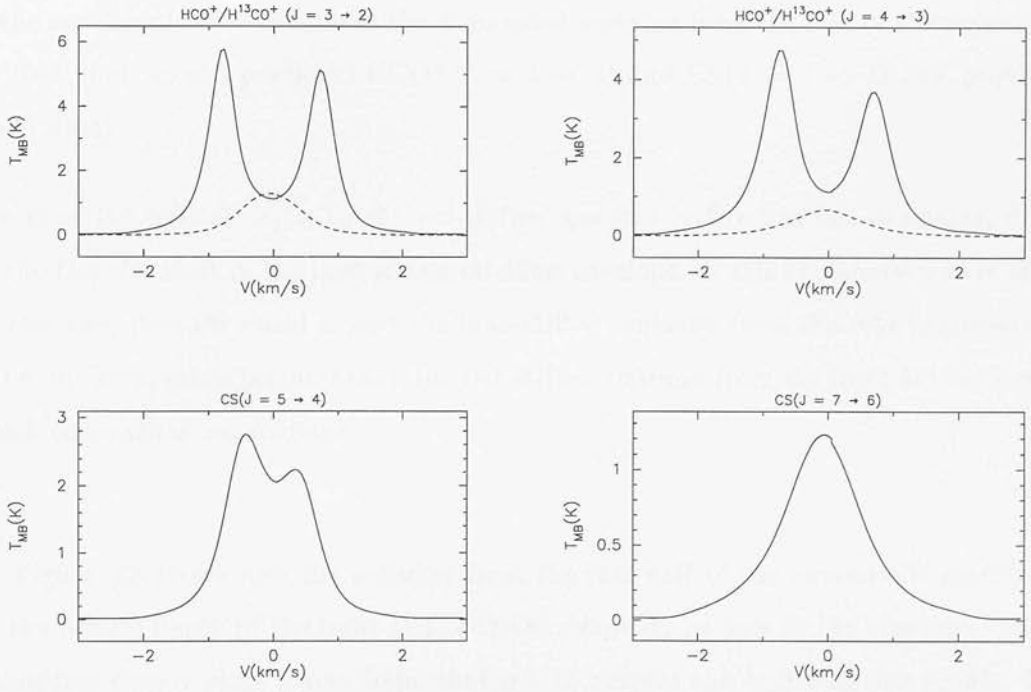

Figure 4.1: Predicted JCMT line profiles for the canonical infall model, for an assumed distance of 200 pc. The isotopic lines are plotted as dashed lines in the top panels.

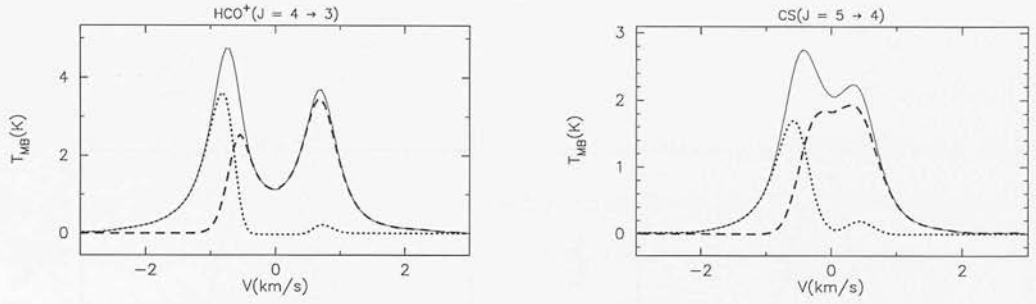

Figure 4.2: Plots showing the contribution of the emission from the front hemisphere of the envelope (dashed line) and the attenuated emission from the rear of the envelope (dotted line), to the predicted $HCO^+(J = 4 \rightarrow 3)$ and $CS(J = 5 \rightarrow 4)$ line profiles (solid lines).

less than the optical depth to the red-shifted gas just in front of the protostar, due to the Doppler shift of the intervening infalling envelope. If this explanation were the correct one, then we would expect the blue-shifted emission from the rear hemisphere to be, by itself, much brighter than the red-shifted emission from the front hemisphere, which contradicts our findings.

Figure 4.3 shows how the emission from the rear half of the envelope is modified by the optical depth of the front half of the envelope on its way to the observer. Self-absorption clearly plays a very important role in shaping the emergent line profile. In Figure 4.4 the contribution of the beam-averaged optical depths through the front and rear hemispheres of the envelope for both $CS(J = 5 \rightarrow 4)$ and $HCO^+(J = 4 \rightarrow 3)$ are plotted. The total optical depth of the $HCO^+(J = 4 \rightarrow 3)$ line is much greater than the $CS(J = 5 \rightarrow 4)$ line, which accounts for the stronger self-absorption features in the HCO^+ line. As expected, there is a separation in velocity of the peaks of the optical depth profiles from the front and rear hemispheres, although this is rather small ($\sim 0.2\,\mathrm{km\,s^{-1}}$).

To shed further light on how the asymmetric infall profiles are formed, we show in Figure 4.5 how the $HCO^+(J = 4 \rightarrow 3)$ line profile changes as successive 'layers'

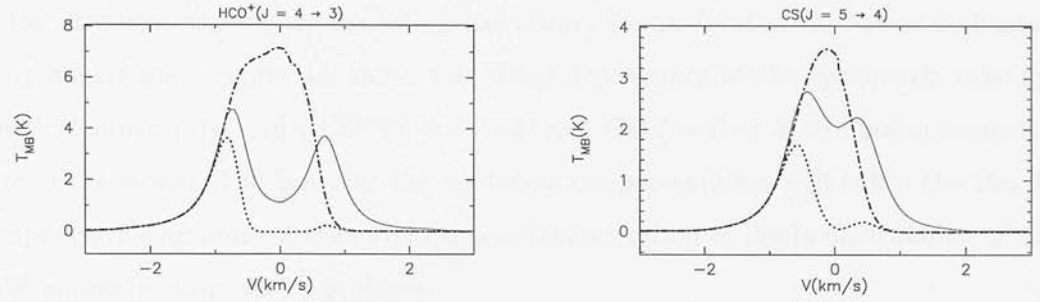

Figure 4.3: Plots showing the *unattenuated* emission from rear half of the model envelope (dot-dashed line) in the $HCO^+(J = 4 \rightarrow 3)$ and $CS(J = 5 \rightarrow 4)$ lines. The full line profile (solid line) and the attenuated emission from the rear (dotted line) are shown for comparison.

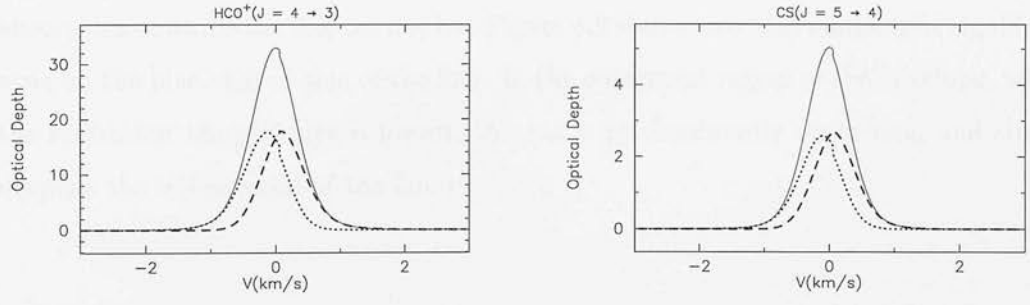

Figure 4.4: Plots showing the contribution to the total beam-averaged optical depth through the envelope (solid line) from the front and rear hemispheres of the canonical infall model (dashed and dotted lines respectively), in the $HCO^+(J = 4 \rightarrow 3)$ and $CS(J = 5 \rightarrow 4)$ lines.

of the model envelope are included, from the rear edge of the envelope forwards. For all the 'slice planes' in the rear of the envelope (left hand panel of Figure 4.5), the predicted profiles are single peaked. This is explained by the fact that in the rear half of the envelope, the higher excitation gas always lies in front of the lower excitation temperature gas. Figure 4.6 shows the radial dependence of the systematic velocity, kinetic temperature, and $HCO^+(J = 4 \rightarrow 3)$ and $CS(J = 5 \rightarrow 4)$ excitation temperature in the model. The fact that the excitation temperature lies well below the kinetic temperature over most of the envelope is a demonstration of the inapplicability of the LTE approximation to this problem.

As successive layers of the front half of the envelope are included in the line profile calculation (right hand panel of Figure 4.5), there is a reduction in the intensity in the core of the line. This is due to the fact that in the front half of the cloud, lower excitation temperature gas lies in the foreground, and absorbs the emission from the higher excitation gas behind it. Nevertheless, the *emission* of this gas is also very important in determining the form of the emergent line profile. The emission from gas near the centre, in the front of half of the envelope, is seen in Figure 4.5 to produce an increase in the line intensity at strongly red-shifted velocities. The contribution of this gas to the emission at lower velocities is obscured in the figure by the dominating effect of absorption towards the line centre, but Figure 4.2 shows that this emission is significant even on the blue-shifted side of the line. In the outermost region of the envelope, where the excitation temperature is lowest, the gas is predominantly absorbing, and simply deepens the self-reversal of the line profile.

4.2.3 Dependence on impact parameter and beam size

Figure 4.7 illustrates how the predicted $HCO^+(J = 4 \rightarrow 3)$ and $CS(J = 5 \rightarrow 4)$ line profiles depend on the impact parameter of the line of sight. As expected, the strength of the lines diminish with increasing impact parameter, as the beam samples increasingly less dense and lower temperature gas. The degree of asymmetry in the line

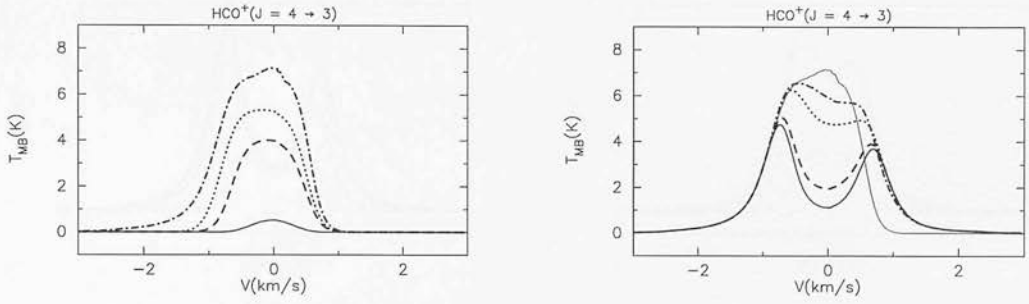

Figure 4.5: Plots illustrating how the $HCO^+(J = 4 \rightarrow 3)$ evolves as progressively more of the cloud is included in the line profile calculation. The profiles represent different 'slices' through the model cloud, where the slice planes are perpendicular to the line of sight and only the part of the cloud which lies behind the slice plane is included. The left hand plot shows profiles obtained for slice planes at various positions in the rear half of the cloud. The distances of the slice planes from the cloud centre along the line of sight are: 5000 AU (solid line); 2000 AU (dashed line); 1000 AU (dotted line); and 0 AU (dot-dashed line). The right hand plot shows the profiles obtained for slice planes lying in the front half of the cloud. The distances of the planes from the cloud centre are 0 AU (solid line); 1000 AU (dot-dashed line); 2000 AU (dotted line); 5000 AU (dashed line); and 10000 AU (double-peaked solid line). The radius of the cloud is 10000 AU.

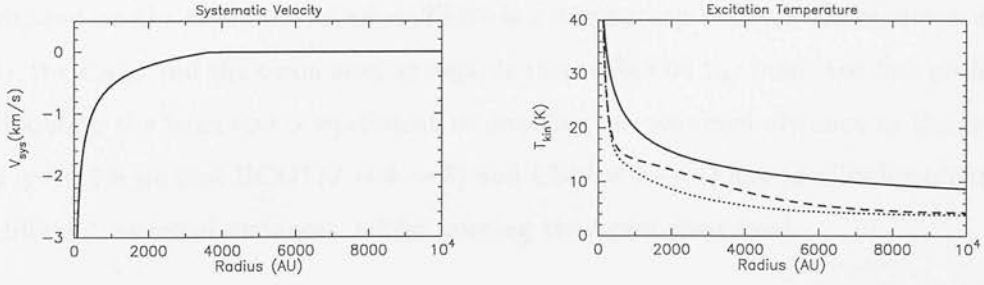

Figure 4.6: The left hand panel shows the radial profile of systematic velocity for the canonical infall model. In the right hand panel, the solution for the excitation temperatures of the $HCO^+(J = 4 \rightarrow 3)$ (dashed line) and $CS(J = 5 \rightarrow 4)$ (dotted line) transitions are plotted. The kinetic temperature profile (solid line) is also plotted for comparison.

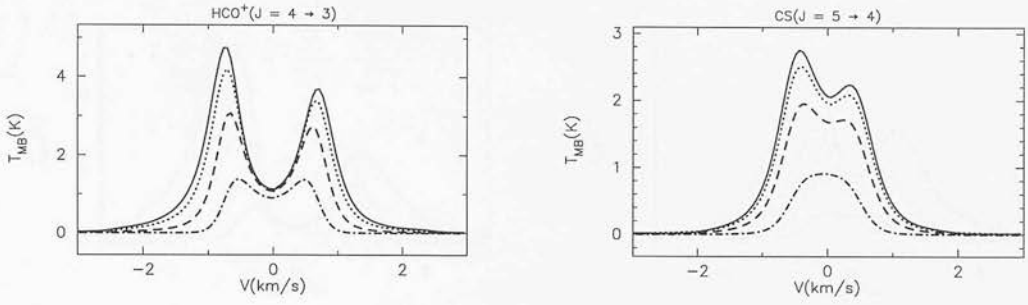

Figure 4.7: Plot showing the dependence of the line profiles on the impact parameter of the beam direction relative to the centre of the cloud. The solid lines show the on-source line profiles, and the line profiles for impact parameters of 1000 AU (dotted line), 2000 AU (dashed line), and 4000 AU (dot-dashed line) are also plotted. The assumed distance to the cloud is 200 pc.

profiles decrease with increasing impact parameter, partly because of the lower infall velocities at larger radii, and partly because of the lower column densities, and hence optical depth, along the line of sight. The lines also become narrower with increasing impact parameter, as a result of the decreasing infall velocity with radius.

The distances to many nearby protostellar objects are often only known to an accuracy of $\sim$50%, so it is important to examine how sensitively the predicted line profiles depend on the assumed distance. There is a degeneracy between the assumed distance to the cloud and the beam size, as regards their effect on the predicted line profiles: i.e. doubling the beamsize is equivalent to doubling the assumed distance to the cloud. In Figure 4.8 we plot $HCO^+(J = 4 \rightarrow 3)$ and $CS(J = 5 \rightarrow 4)$ line profiles for a number of different assumed distances, whilst keeping the beam sizes fixed.

The peak line temperatures increase approximately as the inverse of the assumed distance (or beam size). The increase in the strength of the line wings depends approximately on the inverse square of the assumed distance, which suggests that the line wing flux originates from a region on the source much smaller than the beam size. This is the explained by the fact that in the velocity profile we have adopted, the highest

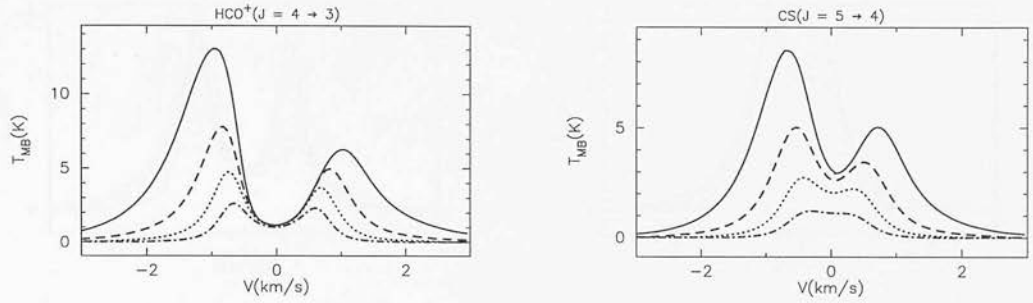

Figure 4.8: Plots showing the dependence of the predicted line profiles on the assumed distance to the cloud. Spectra are plotted for distances of 50 pc (solid lines), 100 pc (dashed lines), 200 pc (dotted lines), and 400 pc (dot-dashed lines).

infall velocities lie at the smallest radii, and therefore the high velocity wings of the line profile are formed in a very small region around the centre of the cloud. The different dependence of the line core and line wings on distance produces increasingly broad profiles with decreasing distance and beam size.

We conclude that distance uncertainties may contribute significantly to the overall uncertainty in the radiative transfer modelling of protostellar envelopes. Gregersen et al. (1997) analysed HCO^+ observations of a large sample of Class 0 sources using a model cloud at a single 'representative distance'. This approach will not give reliable results when the scatter in the distances of the objects in the sample is large.

4.2.4 Dependence on the infall velocity

In Figure 4.9 line profiles are plotted for a number of different infall radii (only the velocity profile is varied, according to Equation 4.3. and the density profile remains fixed as for the canonical model). For increasing values of the infall radius, larger fractions of the envelope take part in the infall motion, and the collapse speed at a given radius increases approximately as $r_{\rm inf}^{1/2}$. The line profiles become more strongly skewed towards blue velocities with increasing infall velocity, mainly as a result of the

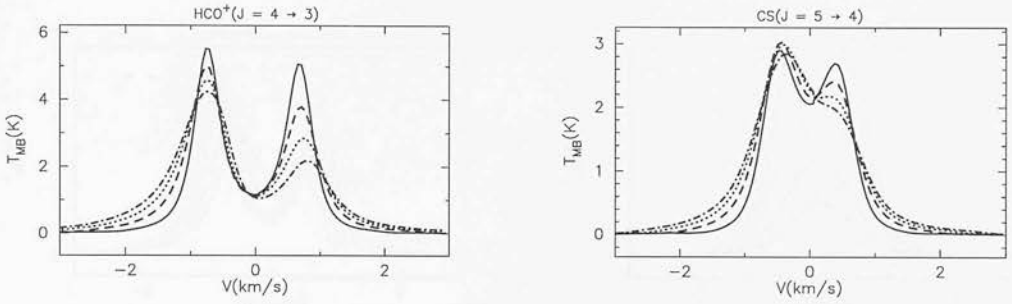

Figure 4.9: Plots illustrating the dependence of the line profiles on infall velocity. The infall velocity profiles were calculated using the Shu model relation (Equation 4.3), for infall radii of 2000 AU (solid lines), 4000 AU (dashed lines), 6000 AU (dotted lines) and 8000 AU (dot-dashed lines). The canonical values were used for all other model parameters.

diminishing intensity of the red-shifted peak. The actual velocities of the two peaks show remarkably little variation over range of infall velocities considered. Predictably, the models with the the highest infall velocities produce the strongest emission in the line wings. In actual observations, however, this infall signature will usually be obscured by emission from the outflow.

4.2.5 Dependence on tracer molecule abundance

Figure 4.10 shows how the predicted line profiles vary with the assumed relative abundance of CS and HCO^+ in the envelope. The relative abundance of the tracer molecule largely determines the optical depth through the envelope in the observed line, and is therefore a very important parameter in deciding the overall appearance of the line profile. This is apparent from the figure, where the intensities and shapes of the line profiles are seen to vary significantly over the factor of 10 range of relative abundances covered. As expected, the lowest values of the relative abundance (and hence optical depth) produce the weakest infall asymmetries. The progression of line shapes with increasing optical depth is from a single-peaked gaussian, to a single-peaked blue-skewed profile, to a profile with a blue-shifted peak and red-shifted 'shoulder' (or 'red knee'), to a double-peaked profile with a stronger blue-shifted peak. As the abundance and opti-

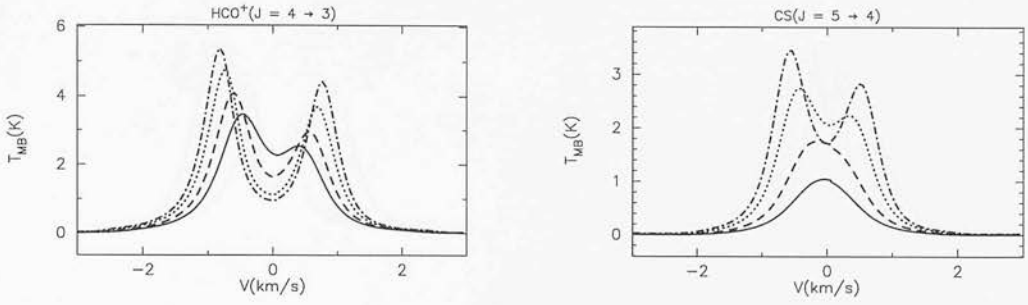

Figure 4.10: Plots showing the dependence of the predicted line profile on the constant relative abundance of the tracer molecule. Spectra are plotted for HCO^+/CS abundances (relative to molecular hydrogen) of 1×10^{-9} (solid lines), 2×10^{-9} (dashed lines), 5×10^{-9} (dotted lines), and 1.0×10^{-8} (dot-dashed lines).

cal depth increase further, the absorption dip deepens, the line peaks become stronger and their separation increases.

4.2.6 The effect of turbulence on the line profiles

Figure 4.11 shows how the line profiles depend on the value of the turbulent velocity dispersion, $\sigma_{\rm tb}$, when it is assumed to be uniform throughout the envelope. As the turbulence velocity dispersion increases, the most apparent effect on the line profiles is to increase the velocity separation between the two peaks, as a result of the broadening of the absorption profile of the foreground envelope. The total integrated flux in the line tends to increase with the turbulent velocity dispersion. This is because the peak optical depth of the foreground absorbing gas is reduced as the molecules are spread over a wider range of velocities, and the similar reduction in the optical of the strongly emitting gas in the centre of the cloud allows more of the emission to escape. Comparing the $HCO^+(J = 4 \rightarrow 3)$ and $CS(J = 5 \rightarrow 4)$ profiles in the figure, we find that the effect of changing the value of the turbulent velocity dispersion on the line profile depends quite strongly on the peak optical depth in the transition. When the optical depth is small, increasing the turbulence tends to 'smear out' the double-peaked profile, whereas for very optically thick lines the double-peaked structure remains just

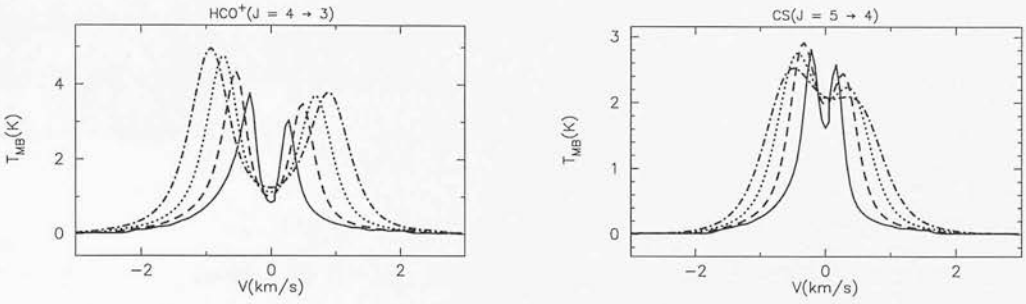

Figure 4.11: Plots showing the dependence of the predicted line profiles on the magnitude of the turbulent velocity dispersion, assumed in this case to be constant throughout the envelope. Spectra are plotted for turbulent velocity dispersions of $0.1\,\mathrm{km\,s^{-1}}$(solid lines), $0.2\,\mathrm{km\,s^{-1}}$(dashed lines), $0.3\,\mathrm{km\,s^{-1}}$(dotted lines) and $0.4\,\mathrm{km\,s^{-1}}$(dot-dashed lines). The equivalent FWHM turbulent velocity widths are found by multiplying these numbers by 2.35.

as promiment as the velocity gap between the two peaks increases.

Figure 4.12 illustrates how the line profiles vary with the exponent in the assumed power-law relation between the turbulent velocity and the density. Guided by the discussion on turbulence in the previous section, we investigate turbulent velocity laws of the form $\sigma_{\rm tb} \propto \rho^{1/4}$ and $\sigma_{\rm tb} \propto \rho^{1/2}$ (as found in the numerical simulations of Vásquez-Semadeni et al. 1997), and $\sigma_{\rm tb} \propto \rho^{-1/2}$ (derived using Larson's Laws). For comparison we also plot the profile produced by the canonical model, which assumes a flat turbulent velocity profile.

The profiles are clearly quite sensitive to the form of the turbulent velocity law. The profiles obtained using the $\sigma_{\rm tb} \propto \rho^{-1/2}$ law (dashed lines in the figure) are appreciably narrower than the other profiles, which is particularly evident in the cores of the $\mathrm{H^{13}CO^{+}}(J = 4 \rightarrow 3)$ and $\mathrm{CS}(J = 7 \rightarrow 6)$ lines. This arises because the $\rho^{-1/2}$ law assigns the lowest turbulent velocity dispersion to the hot, dense, inner regions of the cloud, where most of the line emission takes place. These profiles also tend to show the strongest emission in the close to the line centre, mainly arising from the lower optical

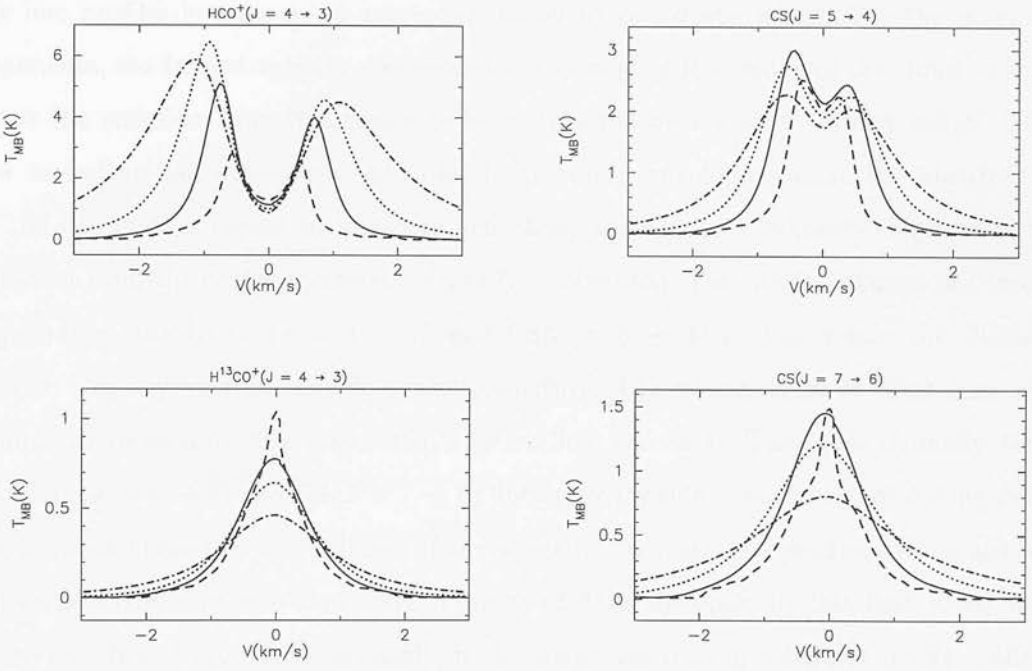

Figure 4.12: Plots showing the predicted line profiles for different forms of the microturbulent velocity profile. The adopted relations between the turbulent velocity dispersion, $\sigma_{\rm tb}$, and the gas density, ρ, were: $\sigma_{\rm tb}$ =constant (solid line); $\sigma_{\rm tb} \propto \rho^{-1/2}$ (dashed line); $\sigma_{\rm tb} \propto \rho^{1/4}$ (dotted line); and $\sigma_{\rm tb} \propto \rho^{1/2}$ (dot-dashed line). Each profile was normalised such that the FWHM turbulent velocity width ($= 2.35\sigma_{\rm tb}$) at the half-radius of the cloud (5000 AU) has a value of $0.3\,{\rm km\,s^{-1}}$.

depth of the outer envelope due to the enhanced velocity dispersion there, although in the case of the $H^{13}CO^+(J = 4 \rightarrow 3)$ and possibly the $CS(J = 7 \rightarrow 6)$ lines, it is due to the increased optical depth in the centre of the cloud, as these lines are not completely optically thick.

As the exponent s in the $\sigma_{tb} \propto \rho^s$ relation increases from -0.5 through to +0.5, the line profiles become much more dominated by broad line wings. For the positive exponents, the largest velocity dispersions are located in the centre of the cloud, which cause the emission from this region to be distributed over a wide velocity range. The low turbulent and systematic velocities in the outer envelope confine the absorption of the gas in this region to line core velocities, allowing the enhanced high velocity emission from the centre to remain virtually unobscured. Despite the change in overall appearance, the $HCO^+(J = 4 \rightarrow 3)$ and $CS(J = 5 \rightarrow 4)$ profiles retain the characteristic blue-asymmetric, double-peaked structure. The strong wings of these lines are similar to those normally associated with outflow emission. The more optically thin $H^{13}CO^+(J = 4 \rightarrow 3)$ and $CS(J = 7 \rightarrow 6)$ lines may provide some means of distinguishing between these two possibilities. If the wings in the main line profiles are caused by enhanced turbulence near the centre of the cloud, then the optically thin lines sould also show very broad profiles. Conversely, if the wings are tracing a bipolar outflow, then the optically thin line profiles, which are expected to be dominated by the envelope, should be narrower.

4.2.7 Solid-body rotation

Figure 4.13 shows how the predicted line profiles change when a solid-body rotation is superposed on the infall velocity field. This velocity field is not physically realistic however, since angular momentum conservation will tend to cause the angular velocity of the gas to increase as it falls inwards, even in the presence of magnetic braking (e.g. Mouschovias 1994), and we use this example simply to illustrate some of the qualitative effects of rotation on line profiles. A proper treatment of differential rotation

would require a two-dimensional radiative transfer analysis, which is computationally a very large step from the one-dimensional problem.

The on-source line profiles are least affected by the rotation, only showing a small decrease in the height of the double peaks, and a very slight broadening of the line as a whole. For differential Keplerian ($\Omega \sin i \sim r^{-3/2}$) rotation, the on-source profile would probably be more strongly affected, since the largest rotational velocities would then lie closest to the centre.

The off-centre line profiles are more affected by solid-body rotation than the on-source profiles. As expected, the shifts in the centroid velocity of the line profiles follow the rotational velocity gradient. As well as shifting the centroid, the rotation also significantly distorts the shape of the off-centre line profiles. On the blue-shifted side of the rotational velocity gradient, the rotation produces an enhanced blue-asymmetry in the line profiles, in addition to the blue-asymmetry produced by the infall. At the positions on the red-shifted side of the rotational velocity gradient, the blue infall-asymmetry is completely reversed by the rotation. This behaviour is in qualitative agreement with the spatial variation of the profile shapes across a number of the spectral line maps of protostellar envelopes presented in Chapter 3. It is difficult, however, to reproduce some of the very strongly red-skewed line profiles seen in a few of the maps (e.g. the $HCO^+(J = 4 \rightarrow 3)$ map of NGC1333-IRAS2) using this model.

Figures 4.14 and 4.15 show $HCO^+(J = 4 \rightarrow 3)$ and $CS(J = 5 \rightarrow 4)$ centroid velocity contour plots from the canonical infall model for projected rotational angular velocities of $\Omega \sin i$=0 and $30\,\mathrm{km\,s^{-1}\,pc^{-1}}$ respectively. The non-rotating, infalling model produces circularly symmetric negative centroid velocity contours, which reach a minimum at the central position. The solid body rotation tends to produce approximately parallel contours of centroid velocity, aligned with the axis of rotation. Due to the infall, however, the contours are distorted towards bluer velocities close to the centre of the cloud, producing a 'blue-bulge' in the centroid velocity contour plot, which encroaches

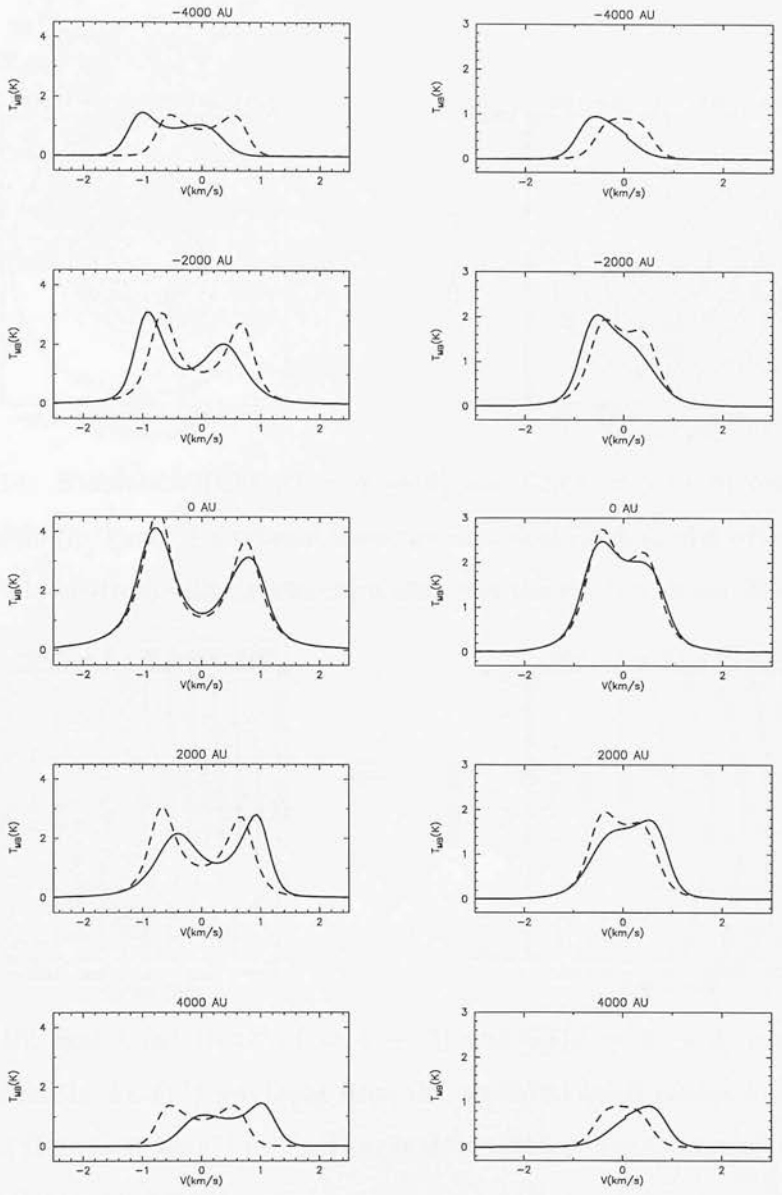

Figure 4.13: Plot showing the effect of solid-body rotation on infall line profiles. $HCO^+(J = 4 \rightarrow 3)$ and $CS(J = 5 \rightarrow 4)$ line profiles are plotted in the left and right hand columns respectively. The solid lines show the predicted line profiles for the canonical infall model and a projected angular velocity of solid-body rotation of $\Omega \sin i$=30 km s^{-1} pc^{-1}, where i is the inclination angle of the rotation axis to the line of sight. The lines are plotted for several impact parameters which are displaced from the centre of the cloud along the perpendicular to the rotation axis in the plane of the sky, by the distance given in the title of each plot. Impact parameters with positive displacements lie on the red-shifted side of the rotational velocity gradient. The dashed lines show the predicted line profiles in the absence of rotation, for comparison.

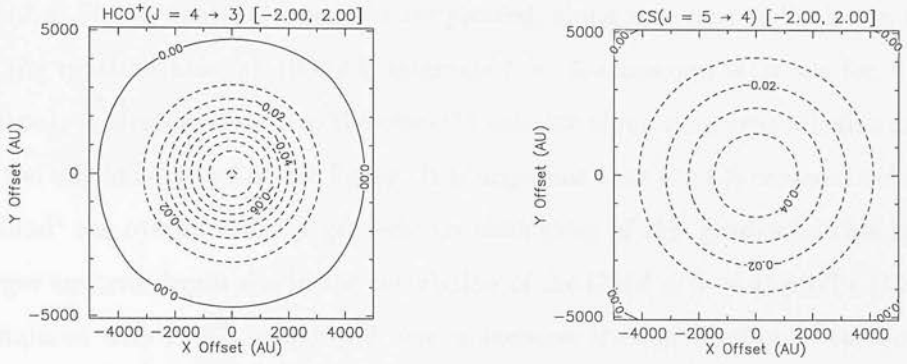

Figure 4.14: Simulated $HCO^+(J = 4 \rightarrow 3)$ and $CS(J = 5 \rightarrow 4)$ centroid velocity contour plots (in $km\,s^{-1}$) produced from the canonical infall model with no solid body rotation. The centroid velocity was calculated over the velocity range -2.0 to 2.0 $km\,s^{-1}$.

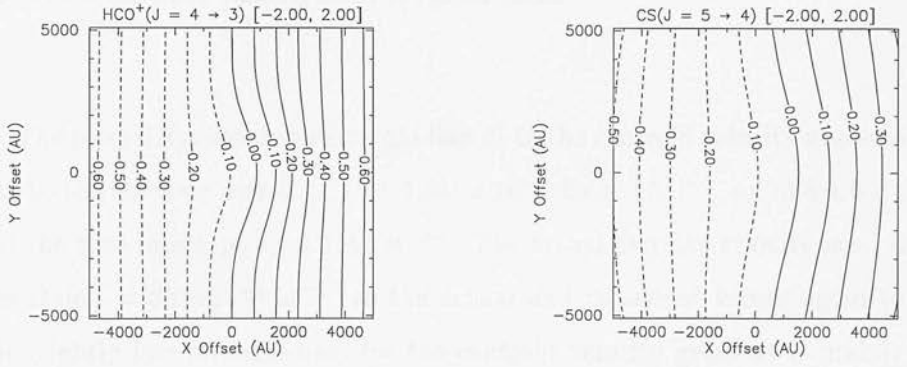

Figure 4.15: Simulated $HCO^+(J = 4 \rightarrow 3)$ and $CS(J = 5 \rightarrow 4)$ centroid velocity contour plots (in $km\,s^{-1}$) produced from the canonical infall model with a solid body rotation of $\Omega \sin i$=30 $km\,s^{-1}\,pc^{-1}$. The centroid velocity was calculated over the velocity range -2.0 to 2.0 $km\,s^{-1}$.

into the red-shifted half of the rotational velocity gradient. This behaviour was first noted by Walker, Narayanan & Boss (1994), who argued that centroid velocity plots provide a more robust signature of infall than the line profile shapes themselves.

In Chapter 3, we used measurements of the centroid velocity gradient across our spectral line maps of protostellar envelopes to place limits on the rotation rate of these envelopes. As a check on this procedure, we now carry out a similar analysis on the line profiles produced by the STENHOLM radiative code for the rotating envelope model used to produce Figure 4.13. In Figure 4.16 the calculated $HCO^+(J = 4 \rightarrow 3)$ and

CS($J = 5 \rightarrow 4$) centroid velocities are plotted, along axes perpendicular to and parallel to the rotation axis, at 1000 AU intervals (i.e. 5 arcsecond intervals for a distance of 200 pc). A straight line fit to the centroid velocity along the perpendicular axis is shown in the left hand panel of the figure. It is apparent that the CS centroid velocities 'drag behind' the overall velocity gradient on both sides of this gradient. This is due to the larger assumed beam size in the calculation of the CS($J = 5 \rightarrow 4$) profile (19.3′ FWHM compared with 13.6″), which will tend to increase the contribution of the brighter inner regions (which have lower rotational velocities) to the line profile. The centroid velocity along the axis parallel to the rotation axis in the right hand panel clearly shows the 'blue-bulge' signature discussed previously, although in this case the magnitude of the associated centroid velocity shift is rather small.

The formal least-squares straight line fit to the centroid velocity gradient perpendicular to the rotation axis is $(1.14 \pm 0.33) \times 10^{-4}$ km s^{-1}AU^{-1}, or 23.5 ± 6.8 km s^{-1} pc^{-1}, and the zero intercept is -0.018 km s^{-1}. The actual angular velocity used in the model was $\Omega \sin i = 30$ km s^{-1} pc^{-1}, so the actual and measured values agree to within 1σ. The slightly low measurement for the centroid velocity gradient is mainly due to the 'dragging behind' of the CS centroid velocities mentioned above, as can be seen from the figure. Nevertheless, this example shows that the centroid velocity gradient gives a reasonable estimate of the actual projected velocity gradient across a cloud, at least for the case of solid body rotation.

4.3 Comparison with observations

In this section we use the STENHOLM code to carry out radiative transfer modelling of two of the objects identified in Chapter 3 as strong infall candidates: NGC 1333-IRAS2 and Serpens SMM4.

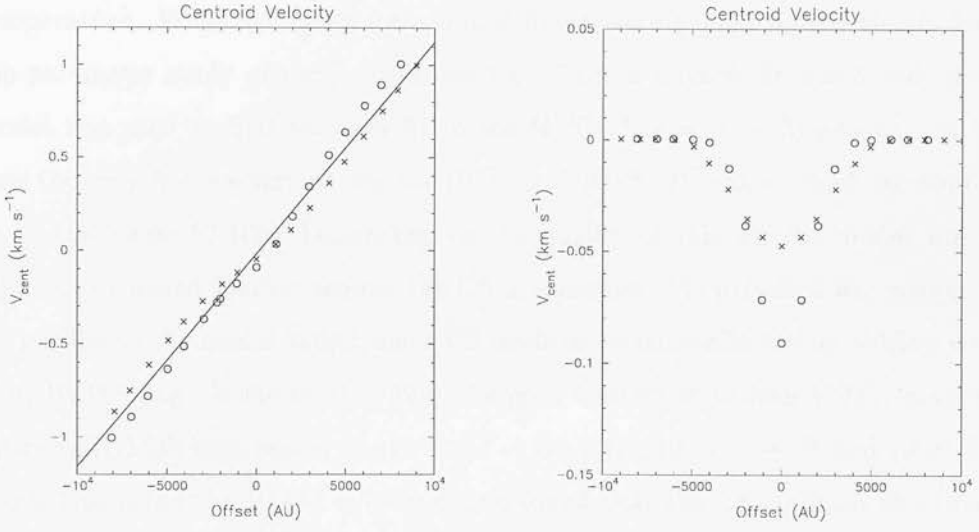

Figure 4.16: Centroid velocity measurements of the predicted $HCO^+(J = 4 \rightarrow 3)$ (open circles) and $CS(J = 5 \rightarrow 4)$ (crosses) line profiles for the canonical infall model with a solid body rotation of $\Omega \sin i$=30 km s^{-1} pc^{-1}. The left hand panel shows a least-squares straight line fit to the centroid velocities measured along the axis perpendicular to the rotation axis (i.e. in the direction of maximum rotational velocity gradient) passing through the centre of the cloud. See text for details of the line fit. The right hand panel shows the measured centroid velocities at positions along the rotation axis.

4.3.1 NGC 1333-IRAS 2

Figure 4.17 shows our best model fit to the HCO^+ and CS line profiles observed towards NGC1333-IRAS2. We approached the modelling by first searching for a fit to the $HCO^+(J = 4 \rightarrow 3)$ profile, choosing physical parameters lying within the constraints given in Section 4.1. We aimed to achieve consistency in our model fits with previously determined properties of the objects, such as the envelope mass and ambient gas temperature. When searching for a model fit we were guided by the trends found in the parameter study of the previous section. Once a suitable fit was found, the same model was used to find the best fit to the $H^{13}CO^+(J = 4 \rightarrow 3)$ profile, but in this case the only free parameter was the $[H^{12}CO^+]/[H^{13}CO^+]$ ratio, which we required to lie in the range 50-100. Depending on the quality of this fit, the model was either rejected, or tested further against the CS line profiles. We attached less weight to the CS profiles in the model fitting, since CS tends to be more affected by outflow emission than HCO^+ (e.g. Blake et al. 1995). Langer, Castets & Lefloch (1996) mapped the entire NGC1333 core region in the $CS(J = 5 \rightarrow 4)$, $(J = 3 \rightarrow 2)$ and $(J = 2 \rightarrow 1)$ transitions using the IRAM telescope, and found that the CS emission extended over a very wide area. The CS profiles may therefore be significantly affected by emission and absorption from the gas in the foreground core. Furthermore, the JCMT spectral line receiver RxA2, which was used to observe the $CS(J = 5 \rightarrow 4)$ line, was at the time of the observations known to be susceptible to unpredictable fluctuations in intrinsic broadening, affecting the shapes of and peak intensities of the observed line profiles.

The parameters used in the model fit were as follows:

$$v_r(r < 6000\,\mathrm{AU}) = \left[-0.29\left(\frac{r}{6000\,\mathrm{AU}}\right)^{-\frac{1}{2}} + 0.29\left(\frac{r}{6000\,\mathrm{AU}}\right)^{0.15}\right]\ \mathrm{km\,s^{-1}}, \quad (4.45)$$

$$v_r(r > 6000\,\mathrm{AU}) = 0\,\mathrm{km\,s^{-1}}, \quad (4.46)$$

$$n_{H_2}(r < 900\,\mathrm{AU}) = 2.46 \times 10^6\left[0.35\left(\frac{r}{900\,\mathrm{AU}}\right)^{-\frac{3}{2}} + 0.65\left(\frac{r}{900\,\mathrm{AU}}\right)^{-0.64}\right]\ \mathrm{cm^{-3}}, \quad (4.47)$$

$$n_{H_2}(r > 900\,\mathrm{AU}) = 2.46 \times 10^6\left(\frac{r}{900\,\mathrm{AU}}\right)^{-2}\ \mathrm{cm^{-3}}, \quad (4.48)$$

$$T(r < 2400\,\mathrm{AU}) = 17\left(\frac{r}{2400\mathrm{AU}}\right)^{-0.4}\ \mathrm{K}, \quad (4.49)$$

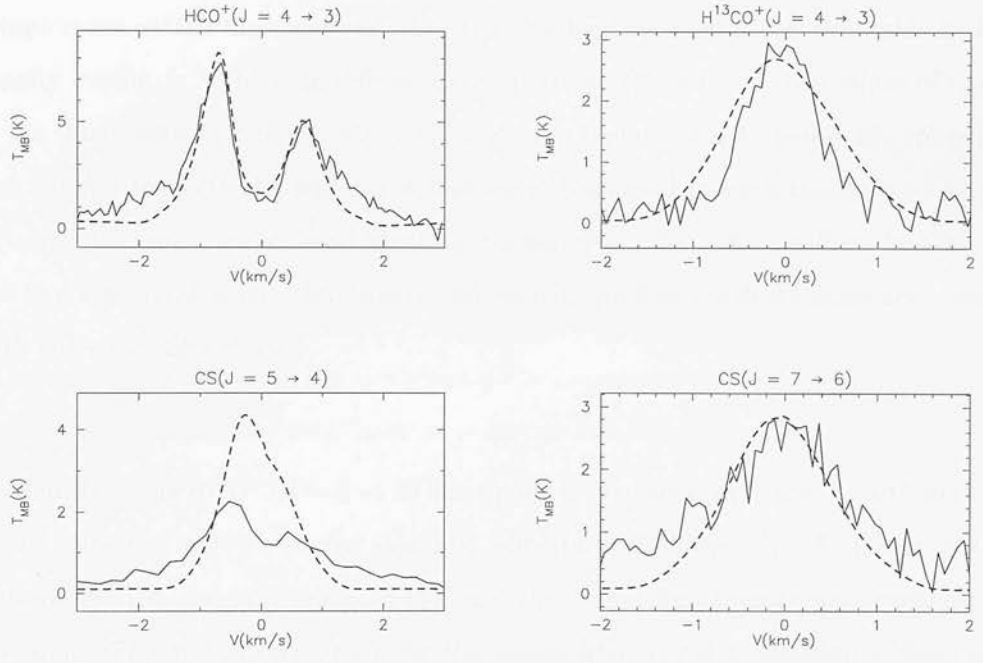

Figure 4.17: Model fits (dashed lines) to the on-source spectra (solid lines) observed towards NGC 1333-IRAS 2. The assumed systemic velocity is $7.75\,\mathrm{km\,s^{-1}}$, which has been subtracted from the velocities in the observed spectra. See the text for details.

$$T(r > 2400\,\mathrm{AU}) = 17\,\mathrm{K}, \tag{4.50}$$

$$\Delta v_{\mathrm{tb}}(\mathrm{FWHM}) = 0.60\,\mathrm{km\,s^{-1}}, \tag{4.51}$$

$$X_{\mathrm{HCO+}} = 6.0 \times 10^{-9}, \tag{4.52}$$

$$X_{\mathrm{CS}} = 6.0 \times 10^{-9}, \tag{4.53}$$

$$[\mathrm{H^{12}CO^{+}}]/[\mathrm{H^{13}CO^{+}}] = 90. \tag{4.54}$$

The outer radius of the cloud was set at 10 000 AU, and an inner shell radius of 15 AU was used. A distance to the cloud of 220 pc was assumed (Cernis 1990). The total envelope mass within the outer radius of the cloud inferred from the molecular hydrogen density profile, is $3.7\,\mathrm{M_{\odot}}$. In reference to Equations 4.3 and 4.17, the values of r_{inf} used in the infall velocity and density profiles above (Equations 4.45 and 4.47) are 6000 AU and 900 AU respectively, and $a_{\mathrm{eff}} = 0.29\,\mathrm{km\,s^{-1}}$was used in both cases. No acceptable fit could be found which used identical values of r_{inf} for both profiles, i.e. we could not find a solution where the density and velocity profiles taken together are consistent with the exact Shu model.

The fit to the $\mathrm{HCO^{+}}(J = 4 \rightarrow 3)$ line profile is very good between -1 and $1\,\mathrm{km\,s^{-1}}$(we quote velocities relative to the systemic velocity of $7.75\,\mathrm{km\,s^{-1}}$). At larger velocities in both the red and blue wings of the line, the model significantly underestimates the emission. The most likely origin for the excess high velocity emission is from one or both of the bipolar outflows associated with this source (see Chapter 3). The clear break in the slope of the observed line profile at $\simeq 1.3\,\mathrm{km\,s^{-1}}$also suggests a separate origin for the high velocity emission. We have not tried to estimate how much the outflow contributes to the line profile at lower velocities, however, and this is another source of uncertainty in the model fit.

The $\mathrm{H^{13}CO^{+}}(J = 4 \rightarrow 3)$ model fit agrees well with the peak velocity and intensity in the observed line. The model profile has overestimated the line width, however. The width of the $\mathrm{H^{13}CO^{+}}(J = 4 \rightarrow 3)$ line in the model is mostly determined by the systematic and turbulent velocities near the centre of the cloud, since the warm dense gas in this region has the strongest intrinsic emission, and for an optically thin tracer

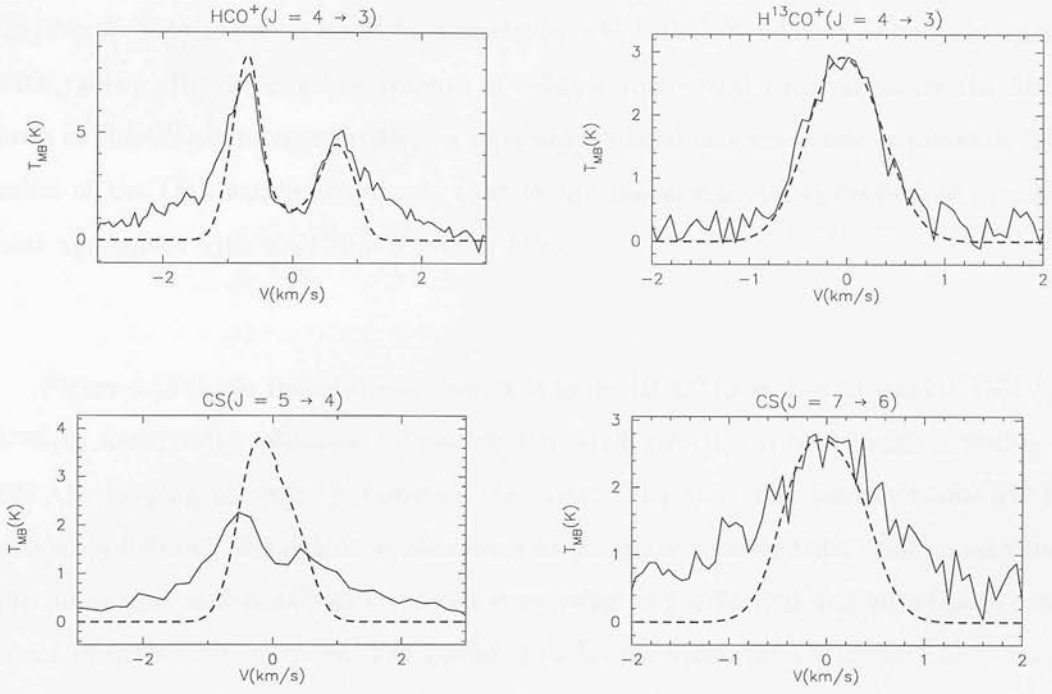

Figure 4.18: Model fits using the same model parameters as in Figure 4.17, but with the infall velocity set to zero inside a radius of 800 AU, and a factor of 4 reduction in the CS relative abundance.

this emission is unattenuated by the outer envelope on its way to the observer. The asymmetry in the main line profile is mainly sensitive to the systematic and turbulent velocities at larger radii. If the infall velocity at large radii is chosen to produce agreement with the asymmetry in the $HCO^+(J = 4 \rightarrow 3)$ profile, then the inferred velocity at small radii always produces too much broadening in the $H^{13}CO^+(J = 4 \rightarrow 3)$ line, as a result of the $v \propto r^{-1/2}$ velocity law.

The largest discrepancy between the observations and the model is in the $CS(J = 5 \rightarrow 4)$ line, where the model predicts a substantially higher intensity in the line core than is observed. Better fits to the overall intensity of the CS line (but not the line shape) could be found by reducing the CS relative abundance, however this would then underestimate the intensity of the $CS(J = 7 \rightarrow 6)$ line. The variable intrinsic broadening of RxA2 mentioned above may account for the factor of two discrepancy

in the CS($J = 5 \rightarrow 4$) intensity. It is possible that both the CS($J = 7 \rightarrow 6$) and CS($J = 5 \rightarrow 4$) could be fitted by a model in which the CS relative abundance varies with radius. However in the absence of reliable theoretical constraints on the likely form of the CS abundance profile, we have not pursued this extra free parameter. The value of the CS relative abundance used in the model fits was optimised to give the best agreement with the CS($J = 7 \rightarrow 6$) line.

Figure 4.18 shows the improved overall fit to the $HCO^+(J = 4 \rightarrow 3)$ and $H^{13}CO^+(J = 4 \rightarrow 3)$ line profiles obtained by setting the infall velocity to zero inside a radius of 800 AU, keeping all other parameters the same. The main line profile is affected remarkably little by this dramatic alteration to the inner velocity field, which underlines the point that each observed transition constrains only a limited domain of parameter space in the model envelope. The CS line profiles (in which the CS relative abundance has been lowered by a factor of 4 relative to the original model fit) are still not well fitted by this model. In both Figures 4.17 and 4.18, the predicted $H^{13}CO^+(J = 4 \rightarrow 3)$ and CS($J = 7 \rightarrow 6$) line profiles are almost identical to each other, and we could not produce simultaneous fits to the velocity widths of both observed profiles. Since CS emission shows a greater tendency for contamination by the outflow, we are inclined to attribute the larger velocity width on the CS($J = 7 \rightarrow 6$) line to the outflow, and tentatively suggest that the infall velocity is retarded, relative to the freefall relation, close to the centre of the cloud.

One possible explanation for this is centrifugal braking, if the infalling material has non-zero specific angular momentum (i.e. the initial collapsing cloud is rotating). The radius at which centrifugal effects are typically expected to become important is only $\sim$ 200 AU or less, however (Bodenheimer 1995), and broadening due to the rotational motion will tend to compensate for the retarded infall velocity. The situation becomes more complicated, however, if, as is argued below, NGC1333-IRAS2 contains a protobinary system. On a more speculative level, the ionising radiation responsible for the free-free emission associated with most Class 0 sources, usually attributed to the accretion shock or the interaction of a jet or outflow with ambient material (Neufeld

& Hollenbach, 1996), may increase the ionisation fraction in the infalling gas near to the centre of the cloud, and recouple it to the magnetic field, which could conceivably bring about a retardation in the infall velocity.

Before resorting to such explanations, however, further observational confirmation of this result is needed. We should also point out that the resolution of the problem may lie with some of the other assumptions we made to limit the volume of parameter space in which to search for a model fit, such as flat turbulent velocity and relative abundance profiles. Another possible explanation for the narrowness of the $H^{13}CO^+(J = 4 \rightarrow 3)$ line may be, for example, that in the innermost regions of the envelope, where the infall velocity is highest, the HCO^+ molecules are strongly depleted. HCO^+ may be depleted through reactions with H_2O, which is released from the ice mantles of dust grains when the dust grain temperature approaches 100 K (Ceccarelli et al. 1996; Section4.1). In our model fit, however, the temperature drops below 100 K at a radius of only > 80 AU. This radius appears to be too small to produce the required result.

In Figure 4.19, we compare the off-centre $HCO^+(J = 4 \rightarrow 3)$ line profiles with the model predictions. Because of the assumption of spherical symmetry, the predicted line profiles depend only on the impact parameter of the line of sight relative to the origin, and not on its direction. The decrease in line intensity with increasing impact parameter is reasonably well matched by the model. However the line *shapes* at the off-centre positions show less agreement. With the exception of the spectrum at the (0,15) position, the off-source line profiles are all skewed towards the blue. The model profiles are much more symmetric, as a result of the fall off in infall velocity at large radius, which is again a consequence of the $v \propto r^{-1/2}$ infall velocity law. It is very difficult to accommodate the strong high velocity emission seen in several of the off-source positions, most prominently at (0,15) and (15,-15), within a plausible infall model, particularly given the highly asymmetric distribution of the high velocity emission in both position and velocity, which could never be fitted by a spherically symmetric model.

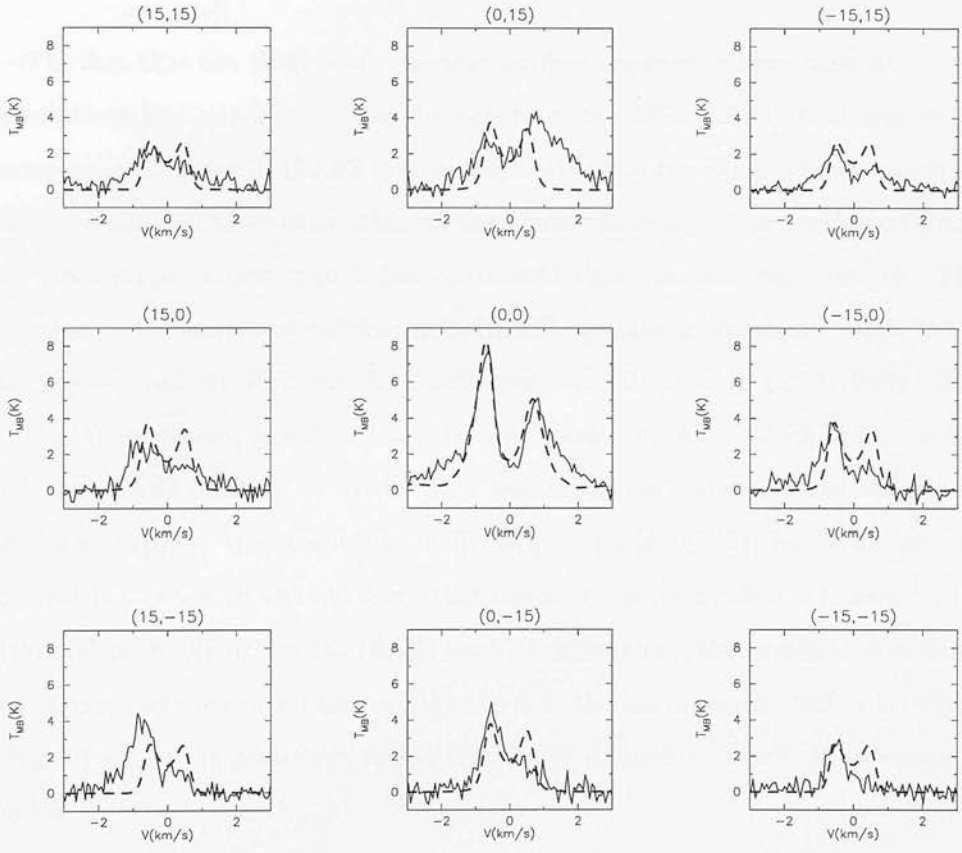

Figure 4.19: Comparison of the off-centre $HCO^+(J = 4 \rightarrow 3)$ line profiles observed towards NGC1333-IRAS2 (solid lines) with the model predictions (dashed lines). The Right Ascension and Declination offsets (in arcseconds) from the IRAS2 position are given in the title of each plot.

In Chapter 3 we explored the possibility that the centroid velocity gradient measured across the NGC1333-IRAS2 envelope using $HCO^+(J = 4 \rightarrow 3)$ and $CS(J = 5 \rightarrow 4)$ spectral line maps could be explained by rotation, and concluded that although rotation could not be ruled out, outflow was the more likely explanation. On the basis of the results presented here, we assert with greater confidence that the north-south bipolar outflow, and not rotation, is responsible for the centroid velocity gradient.

The fact that the north-south bipolar outflow appears to have been detected in our observations has implications for the nature of the NGC1333-IRAS2 system. As was discussed in Chapter 3, IRAS2 is associated with two bipolar outflows, which are very nearly perpendicular to each other on the plane of the sky. The north-south outflow is older, has larger extent, and is less collimated than the east-west outflow. The identification of the east-west outflow with IRAS2 appears to be secure, since the outflow axis passes precisely through the IRAS2 position (Hodapp & Ladd 1995). Sandell et al. (1994) suggested, however, that the north-south outflow, which is less well aligned with the IRAS2 position, is driven by a well separated, more evolved object. Our observations support the conclusion of Hodapp & Ladd (1995), based on near-infrared observations of the IRAS2 outflows, that the north-south outflow is indeed well aligned with, and probably driven by, IRAS2 itself. Furthermore, the presence of outflow emission so close to the central source suggests that the north-south outflow is still actively being driven by the protostar, rather than being a 'fossil remnant' of an earlier outflow episode.

This argues against the possibility that the two perpendicular outflows originate from a single driving source, where the outflow underwent a sudden change in direction from north-south to east-west on the sky about 10^4 years ago. The most likely situation, as far as can be ascertained from the current observational evidence, is that NGC1333-IRAS2 is a close protobinary source, surrounded by a common protostellar envelope. Both binary members drive bipolar outflows, which are probably very poorly aligned. If the outflows were nearly aligned, then to appear perpendicular to each other in the plane of the sky, both would have to be very highly inclined from the plane of

the sky. Outflow inclination angles are notoriously difficult to estimate, however the collimation of the east-west outflow (e.g. Sandell et al. 1994; Langer, Castets & Lefloch 1996) argues against such a high inclination angle. Therefore the true angle between the two outflows must be quite large.

The mass of the central protostars can be approximately estimated from the infall velocity profile used in the model fit, applying the freefall equation $M_\star = rv^2/2G$ to the inner part of the profile. Using this relation we obtain an estimate of $\simeq 0.3 M_\odot$. This must be regarded as rather uncertain, however, since a velocity profile which drops to zero in the innermost part of the cloud actually gives a better overall fit to the HCO^+ and $H^{13}CO^+$ data, as shown by Figure 4.18.

The presence of two non-aligned bipolar outflows originating from within the IRAS2 protostellar envelope is clearly difficult to reconcile with our perfectly spherically symmetric, radially infalling envelope model. It is possible that the contribution of the bipolar outflows to the low velocity emission in the line profiles could mimic some of the signatures of infall. We therefore do not claim that the interpretation of our observations in terms of infall is unique. However for the outflows to mimic exactly infall profiles in the way we have seen, seems unlikely. We have shown that they are reasonably consistent with an infall interpretation for reasonable choices of the model parameters.

The density and velocity profiles adopted in the best fit model are inconsistent with the Shu model, despite individually having the Shu model forms. The infall radius used in the velocity profile is a factor of ~ 7 greater than the infall radius used in the density profile, indicating that the infall is more well developed than a Shu model envelope with a similar density profile. As discussed in Chapter 1, the initial condition assumed by the Shu model is the static singular isothermal sphere. Hydrodynamical (e.g. Foster & Chevalier 1993) and Magnetohydrodynamical (e.g. Ciolek & Mouschovias 1994) simulations of the evolution of dense cloud cores during the pre-stellar phase predict,

however, that by the time the density profile approximates closely to a singular distribution, substantial infall velocities have already developed. Notwithstanding the uncertainties in our model fit, our results support this picture of a non-static initial condition for collapse.

In conclusion, we believe our data are consistent with the interpretation that IRAS2 is binary protostar surrounded by an infalling protostellar envelope and powering two non-aligned bipolar outflows.

4.3.2 Serpens SMM4

Figure 4.20 shows the model fits to the CS and HCO^+ on-source spectra observed towards Serpens SMM4. The approach to the modelling was similar to that used for NGC1333-IRAS2, starting with the $HCO^+(J = 4 \rightarrow 3)$ line, and then making adjustments to produce the optimal agreement with the remaining lines. To produce a fit to the $HCO^+(J = 4 \rightarrow 3)$ line required the infall radius in the Shu model form of the velocity profile to be set well beyond the outer radius of the cloud, i.e. the entire protostellar envelope must be infalling. If the infall radius was set inside the outer radius of the cloud, then absorption from the static gas beyond this radius tended to produce an absorption dip close to the systemic velocity, in disagreement with the observed profile. As the Shu model velocity profile is inappropriate in this case, we used a simple $r^{-1/2}$ power law, which is the asymptotic form of the inner part of the Shu model profile, to model the velocity profile instead.

The parameters used in the model were as follows:

$$v_r(r) = -1.95 \left(\frac{r}{1000\,\mathrm{AU}}\right)^{-\frac{1}{2}} \mathrm{km\,s^{-1}}, \tag{4.55}$$

$$n_{\mathrm{H_2}}(r < 2000\mathrm{AU}) = 1.48 \times 10^6 \left[0.35 \left(\frac{r}{2000\,\mathrm{AU}}\right)^{-\frac{3}{2}} + 0.65 \left(\frac{r}{2000\,\mathrm{AU}}\right)^{-0.64}\right] \mathrm{cm^{-3}}, \tag{4.56}$$

$$n_{\mathrm{H_2}}(r > 2000\,\mathrm{AU}) = 1.48 \times 10^6 \left(\frac{r}{2000\,\mathrm{AU}}\right)^{-2} \mathrm{cm^{-3}}, \tag{4.57}$$

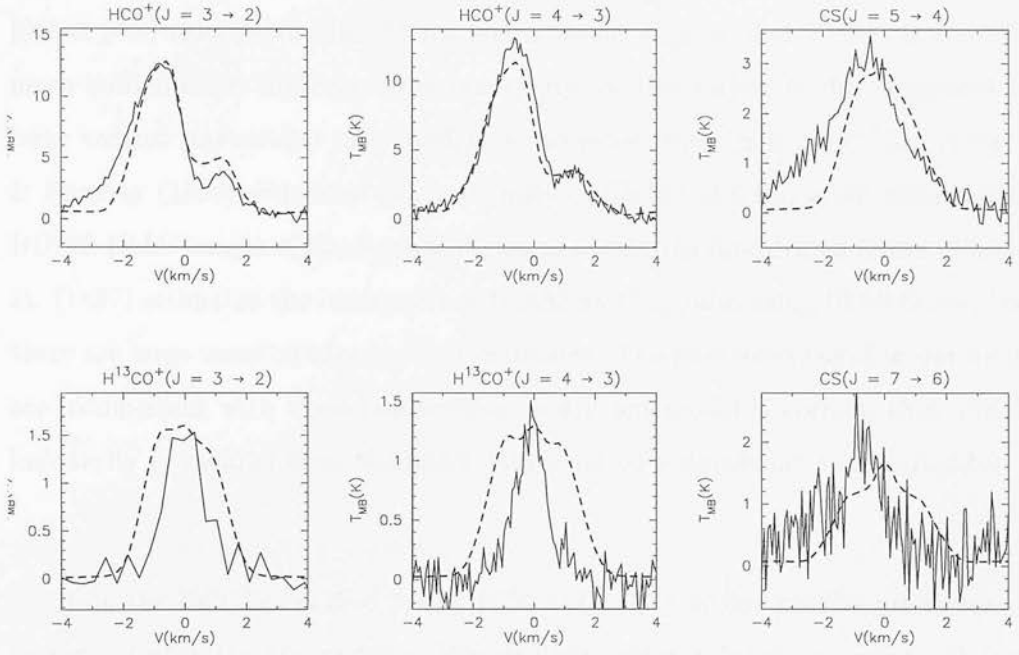

Figure 4.20:

$$T(r < 3800\,\mathrm{AU}) = 25\left(\frac{r}{3800\mathrm{AU}}\right)^{-0.4}\ \mathrm{K}, \tag{4.58}$$

$$T(r > 3800\,\mathrm{AU}) = 25\,\mathrm{K}, \tag{4.59}$$

$$\Delta v_{\mathrm{tb}}(\mathrm{FWHM}) = 0.80\,\mathrm{km\,s^{-1}}, \tag{4.60}$$

$$X_{\mathrm{HCO+}} = 3.5 \times 10^{-9}, \tag{4.61}$$

$$X_{\mathrm{CS}} = 3.5 \times 10^{-9}, \tag{4.62}$$

$$[\mathrm{H^{12}CO^+}]/[\mathrm{H^{13}CO^+}] = 90. \tag{4.63}$$

The outer radius of the model envelope was taken as 10 000 AU, and we used an inner shell radius of 62 AU. The assumed distance to the source was 300 pc. The total envelope mass implied by the model is $5.1\,\mathrm{M}_\odot$, consistent with the estimate of $3\,\mathrm{M}_\odot$ derived from the IRAS fluxes by Hurt & Barsony (1996).

As with NGC1333-IRAS2, the infall velocities in the model fit are much greater than would be predicted by the Shu model given the density profile. From the infall velocity profile we estimate the mass of the central protostellar system to be

$M_\star = rv^2/2G = 2.1 M_\odot$. The temperature profile is normalised at a considerably higher level than in the IRAS2 fit, which would suggest that SMM4 is considerably more luminous. A high accretion luminosity for this object is also suggested by the large central protostellar mass and mass accretion rate ($\simeq 6 \times 10^{-5} M_\odot \, yr^{-1}$). Hurt & Barsony (1996) estimated the luminosity of SMM4 at $9 L_\odot$, after deconvolving the HIRES IRAS images of the Serpens region to obtain the far-infrared fluxes. Jennings et al. (1987) estimated the luminosity of IRAS2 at $17 L_\odot$, also using IRAS fluxes, however there are large uncertainties on these estimates. The parameters used in our model fits are inconsistent with these luminosities, and if our model is correct, then the SMM4 luminosity calculated from the IRAS data must be a significant underestimate.

Both the $HCO^+(J = 3 \rightarrow 2)$ and $HCO^+(J = 4 \rightarrow 3)$ line profiles are in reasonable agreement with the observations. We see little evidence for emission from the outflow in these profiles, as was found in the $HCO^+(J = 4 \rightarrow 3)$ spectrum of NGC1333-IRAS2, and we can largely accommodate the high velocity wings in the observed line within our infall model. In Chapter three, we similarly concluded that the outflow contributes very little to the $HCO^+(J = 4 \rightarrow 3)$ emission observed towards Serpens SMM4, after comparing the morphology and velocity gradients seen in CO outflow maps with the corresponding properties in our $HCO^+(J = 4 \rightarrow 3)$ map.

The predicted $H^{13}CO^+$ linewidths are considerably broader than the observations, as we found with NGC1333-IRAS2, although the peak intensities are in very good agreement. Again, we suggest this may be indicating deviations of the infall velocity profile below the $r^{-1/2}$ free-fall profile in the centre of the cloud. We found in Chapter 3 that the SMM4 envelope shows strong evidence for rotation ($\Omega \sin i \simeq 28 \ km \, s^{-1} \, pc^{-1}$), and suggested that the flattening seen in the spatial distribution of integrated $HCO^+(J = 4 \rightarrow 3)$ emission may be caused by centrifugal support of the outer envelope. This gives some credence to the suggestion that centrifugal braking may retard the infall velocity near to the centre of the cloud.

The calculated CS($J = 5 \rightarrow 4$) and CS($J = 7 \rightarrow 6$) line profiles match the observed line intensities reasonably well, but their peak velocities of the calculated profiles are less red-shifted than the observations . The enhanced blue-shifted wings seen in both of the observed CS spectra strongly suggest that outflow contributes to the emission in these lines. As has been discussed, CS is believed to be enhanced relative to HCO^+ in bipolar outflows (Blake et al. 1995).

Figure 4.21 shows the fits to the off-centre $HCO^+(J = 4 \rightarrow 3)$ line profiles towards SMM4 from our best-fit model. We included a solid body rotation of $28\,\mathrm{km\,s^{-1}\,pc^{-1}}$ in the model (assuming the rotation axis is in the plane of the sky), consistent with the centroid velocity gradient measured across SMM4 in Chapter 3. Since the $HCO^+(J = 4 \rightarrow 3)$ spectra at the (0,0) and (0,7) positions have approximately equal intensities, we assumed that the centre of the cloud lies at the offset (0,3.5). Although the model profiles consistently underestimate the observed lines, we are encouraged by the overall agreement of the trends in the observed lineshapes across the envelope. It is likely that a better fit to the line intensities could be found by a continued search of the parameter space, however this may require a shallower density profile than the predicted by the Shu model. In contrast to IRAS2, we again find little evidence for outflow emission in the off-centre line profiles, and essentially all of the high velocity emission can be accounted for by the infall. We consider these results, when combined with the results presented in Chapter 3, to provide convincing evidence that both infall and rotation are taking place in the the Serpens SMM4 envelope. The magnitude of the rotational velocity is large enough for centrifugal effects to have a significant influence on the gas dynamics.

4.4 Summary

We have discussed the physical constraints which can be used to limit the number and range of parameters needed to define the spherically symmetric models in the STEN-

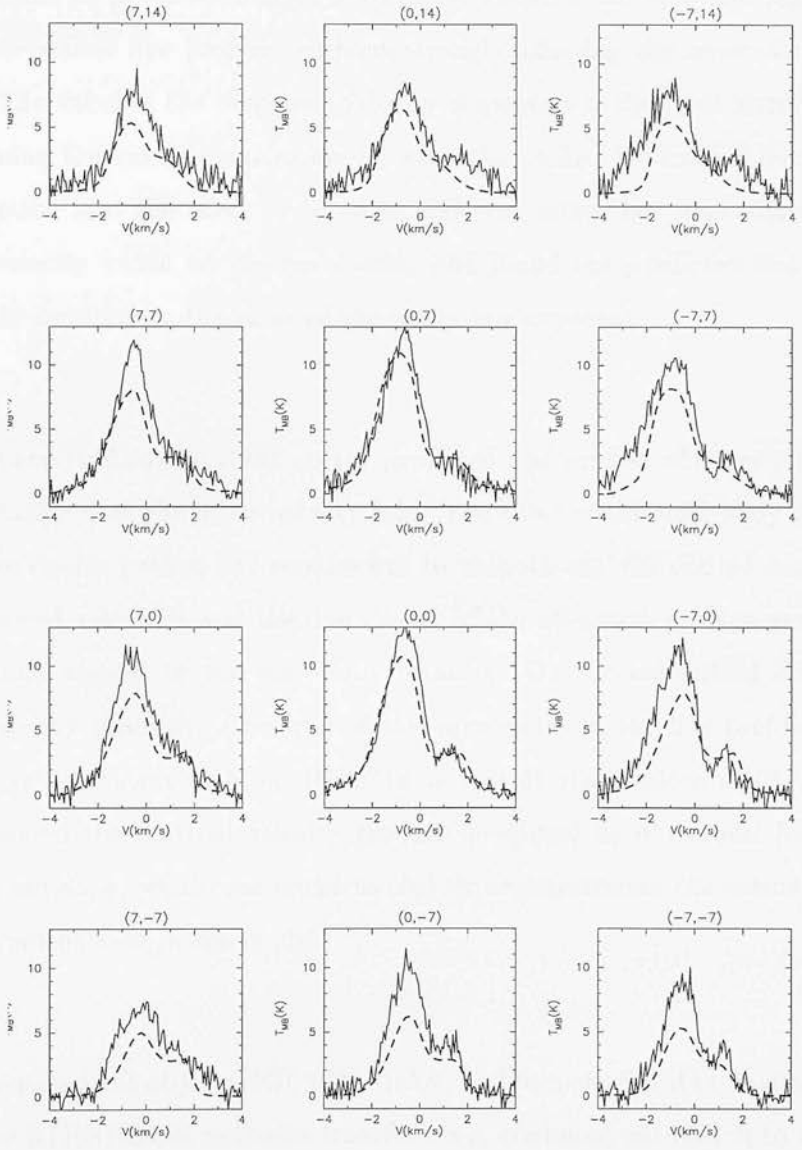

Figure 4.21: Comparison of the off-centre $HCO^+(J = 4 \rightarrow 3)$ line profiles observed towards Serpens SMM4 (solid lines) with the model predictions (dashed lines). The Right Ascension and Declination offsets (in arcseconds) from the IRAS2 position are given in the title of each plot. In the model spectra we have included a solid body rotation of 28 $\mathrm{km\,s^{-1}\,pc^{-1}}$, about an axis passing through the centre of the cloud at a position angle of +40°, as derived in in Chapter 3. The centre of the cloud was assumed to lie at the offset (0,3.5).

HOLM radiative transfer code. We have studied the dependence of the predicted line profiles on a number of model parameters. Increasing the infall velocities in the envelope tends to produce stronger asymmetry between the blue and red-shifted peaks of double-peaked line profiles, without strongly affecting the separation between the peaks. The value of the turbulent velocity dispersion is the most significant factor in determining the velocity separation between the peaks. We carried out a preliminary investigation into the effect of adopting different power law dependences of the turbulent velocity width on the gas density and found the predicted line profiles to be extremely sensitive to the value of the power law exponent.

We have studied the effect on the predicted line profiles of superimposing a solid-body rotation onto the infall velocity field. The effect of the solid-body rotation on the on-source double-peaked line profiles was to 'smooth out' the double peaked structure, The centroid velocities and the line shapes of the off-centre profiles were found to be significantly altered by the solid-body rotation. On the red-shifted side of the rotational velocity gradient, a reversal of the asymmetry in the line profiles was seen, in qualitative agreement with our $HCO^+(J = 4 \rightarrow 3)$ observations of IRAS 16293-2422. We measured the centroid velocity gradient predicted by our model for a solid body rotating envelope, which was found to slightly underestimate the actual rotational velocity gradient used in the model.

We selected the objects NGC1333-IRAS2 and Serpens SMM4 for detailed modelling using the STENHOLM radiative transfer code, confining our search to the Shu model forms for the density and velocity profiles in the modelling, although we did not require these profiles to use the same Shu model parameters in the models. Our best model fits to both the NGC1333-IRAS2 and Serpens SMM4 data used velocity profiles which were more strongly developed than the Shu model would predict, given the fit to the density profile. This is consistent with theoretical predictions that at the instant a central protostar is formed, the gas in the envelope has already accelerated to substantial velocities (e.g. Foster & Chevalier 1993), which contrasts with the static initial state assumed by the Shu model, and is one of the principal distinguishing features between

the Shu model and other collapse models.

Our fits to the $H^{13}CO^+$ line profile observations of both objects consistently overestimated the profile widths. We could produce better fits to these lines by lowering the infall velocity in the centre of the cloud, without significantly affecting the fits to the main line profile. The infall velocity may therefore be retarded from the $r^{-1/2}$ free-fall relation towards the centre of the cloud, possibly by centrifugal braking. Alternatively our assumption of a flat turbulent velocity profile may be incorrect.

In the case of IRAS2, the discrepancies between the model predictions and the observations for the off-source profiles could not possibly be accommodated within a plausible model of infall and rotation, and we attribute them to the outflow. This resolves the debate about whether IRAS2 contains the driving source of the north-south in its vicinity. IRAS2 has thus been unambiguously identified as the driving source of a collimated east-west outflow, and we conclude therefore that IRAS2 is a protobinary.

The model fits to the off-centre $HCO^+(J = 4 \rightarrow 3)$ line profiles of Serpens SMM4 included the solid-body rotation inferred from the $HCO^+(J = 4 \rightarrow 3)$ centroid velocity gradient in the calculation. The predicted and observed profiles showed good agreement in the overall line shape although the model consistently underestimated the line intensities. Since we found no evidence for excess emission from the outflow at the off-centre positions, we therefore concluded that Serpens SMM4 is an infalling and rotating protostar.

4.5 References

Adams F. C., Shu F. H., 1985, ApJ, 296, 655

André P., Ward-Thompson D., Barsony M., 1993, 406, 122

Basu S., Mouschovias T., 1994, ApJ, 265, 824

Blake G. A., Sandell G., van Dishoeck E. F., Groesbeck T. D., Mundy L. G., Aspin C., 1995, ApJ, 441, 689

Bodenheimer P., 1995, ARA&A, 33, 199

Butner H. M., Evans N. J., II, Harvey P. M., Mundy L. G., Natta A., Randich M. S., 1990, ApJ, 364, 164

Caselli P., Myers P. C., 1995, ApJ, 446, 665

Ceccarelli C., Hollenbach D. J., Tielens A. G. G. M., 1996, ApJ, 471, 400

Cernis K., 1990, Ap&SS, 166, 315

Ciolek G. E., Mouschovias T. Ch., 1994, ApJ, 425, 142

Foster P. N., Chevalier R. A., 1993, ApJ, 416, 303

Gregersen E. M., Evans N. J., II, Zhou S., Choi M., 1997, ApJ, 484, 256

Henriksen R., André P., Bontemps S., 1997, A&A, 323 549

Hodapp K.-W., Ladd E. F., 1995, ApJ, 453, 715

Hunter C., 1977, ApJ, 218, 834

Hurt R. L., Barsony M., 1996, ApJ, 460, L45

Irvine W. M., Goldsmith P. F., Hjalmarson A., 1987, in Hollenbach D. J., Thronson H. A., eds, Interstellar Processes, Dordrecht, Reidel

Jennings R. E., Cameron D. H. M., Cudlip W., Hirst C. J., 1987, MNRAS, 226, 461

Kenyon S. J., Calvet N., Hartmann L., 1993, ApJ, 414, 676

Langer W. D., Castets A., Lefloch B., 1996, ApJ, 471, L111

Larson R. B., 1969, MNRAS, 145, 271

Larson R. B., 1981, MNRAS, 194, 809

Lizano S., Shu F., 1989, ApJ, 342, 834

McKee C. F., Zweibel E. G., 1995, ApJ, 440, 686

McLaughlin D. E., Pudritz R. E., 1996, ApJ, 469, 194

McMullin J. P., Mundy L. G., Blake G. A., 1994, ApJ, 437, 305

Mouschovias T. Ch., 1994, in Clemens D. P., Barvainis R., eds, Clouds, Cores and Low Mass Stars, ASP Conference Series Vol 65, p. 134

Myers P. C., 1983, ApJ, 270, 105

Neufeld D. A., Hollenbach D. J., 1996, ApJ, 471, L45

Park Y.-S., Hong S. S., 1995, A&A, 300, 890

Poynter R. L. Pickett H. M., 1985, Applied Optics, 24, 2235

Prasad S. S., Huntress W. W., Jr. 1982, ApJ, 260, 590

Rawlings J. M. C., Hartquist T. W., Menten K. M., Williams D. A., MNRAS, 1992, 255, 471

Sandell G., Knee L. B. G., Aspin C., Robson I. E., Russell A. P. G., 1994, A&A, 285, L1

Shu F. H., 1977, ApJ, 214, 488

Stahler S. W., 1988, ApJ, 332, 804

Swade D. A., 1989, ApJ, 345, 828

Terebey S., Shu F. H., Cassen P., 1984, ApJ, 286, 529

Vásquez-Semadeni E., Cantó J., Lizano S., 1997, ApJ, preprint

Walker C. K., Naraynan G., Boss A. P., 1994, ApJ, 431, 767

Willacy K., Rawlings J. M. C., Williams D. A., 1994, MNRAS, 269, 921

Wilson T. L., Rood R. T., 1994, ARA&A, 32, 191

Zhou S., 1992, ApJ, 394, 204

Chapter 5

Conclusions

In this thesis we have studied the problem of how to identify, and measure the properties of, infalling protostellar envelopes, through radiative transfer modelling of submillimetre spectral line observations. This is a timely project, since the principal theoretical star formation models are beginning to make distinguishing predictions concerning the evolution of the velocities and densities of the gas in protostellar envelopes. Since spectral lines carry information about the velocities and densities of the gas in which they are formed, they may potentially be used to discriminate between these models. Our aim in this thesis was first to assess critically the use of spectral line modelling to investigate protostellar infall, and secondly to identify and study new infall candidates.

The main conclusions of this thesis are that we have found observational evidence which tends to support the assertion that SMM4, NGC1333-IRAS2 and IRAS 16293 are undergoing a phase of significant infall. The model fits that we have found to the observations of SMM4 and IRAS2 lead us to believe that this is a very plausible conclusion. We may not have proved this beyond doubt, but believe the balance of evidence is in its favour.

5.1 Observations

We carried out a submillimetre spectral line survey using the James Clerk Maxwell Telescope, of a sample of objects representing the earliest known stages of protostellar evolution. The objects studied were L1448-IRS3, NGC1333-IRAS2, VLA 1623, L1689S-IRS67, IRAS 16293-2422, L483, and Serpens SMM1, SMM2, SMM3 and SMM4. These are all Class 0 sources, apart from L1689-IRS67, which is a Class I source, and L483, which appears to be borderline Class 0/Class I. Of the objects in our sample, IRAS 16293-2422 and L483 had previously been suggested as infall candidates.

Our study has revealed a complicated mixture of infall, rotation and outflow motions. Of the ten objects included in our sample, five showed qualitative signatures of infall (i.e. blue-skewed line profiles) in the high critical density tracers, CS and HCO^+ . Of the remaining objects, four showed either no signature of infall or conflicting signatures in different tracers, and one (L483) showed red-skewed line profiles, in direct conflict with the infall expectation. We examined the evidence that the line profiles of the HCO^+ and CS transitions observed towards each of the objects were confused by emission from outflows, by comparing the morphology and centroid velocity gradients found in maps of these transitions with CO outflow maps, wherever possible. A strong conclusion of this study is that the CS and HCO^+ submillimetre transitions, which are usually thought of as good tracers of protostellar envelopes by virtue of their large critical densities, are often significantly contaminated by outflow emission. There appears to be no molecular tracer which is uniquely sensitive to the protostellar envelope. The other molecule commonly used to probe protostellar envelope gas is H_2CO (e.g. Zhou et al. 1993), but this too is thought to be enhanced in bipolar outflows (Blake et al. 1995). Overall our observations indicate that HCO^+ is less susceptible to contamination from the outflow than CS.

5.2 Candidate infalling protostars

We identify two objects from the five infall candidates in our sample, Serpens SMM4 and IRAS 16293-2422, for which we find little or no evidence of contamination by outflows in the HCO^+ and CS data. Both these objects show strong evidence for rotation ($\Omega \sin i \simeq 28$ and 66 $\mathrm{km\,s^{-1}\,pc^{-1}}$ respectively), and appear elongated perpendicular to the rotation axis in maps of integrated $HCO^+(J = 4 \rightarrow 3)$ emission. This may provide evidence that centrifugal support is significant in the outer region of the envelope. We identify NGC1333-IRAS2 as a third strong infall candidate, although in this object the HCO^+ and CS spectra show evidence of contributions from the outflow.

5.3 The model code

The modelling in this thesis was carried out using a modified version of the STENHOLM radiative transfer code developed by Matthews, Little and Gibb at the University of Kent (Matthews 1986). The code employs the Λ-iteration method to solve the spectral line radiative transfer problem in the rotational transitions of linear molecules, using the assumption of spherical symmetry. The model cloud is defined by specifying radial profiles of systematic velocity, temperature, density, tracer molecule abundance and micro-turbulent velocity dispersion. Once the model has converged, a simulated telescope observation on the cloud is carried out.

We have confirmed the viability of the STENHOLM code as a practical tool for the analysis of submillimetre spectral line profiles. We have shown that the code performs convincingly when tested against both simple analytical LTE predictions, and independent non-LTE radiative transfer calculations. The Λ-iteration method is often criticised because for certain problems it can take a prohibitively long time for full convergence to be achieved, particularly when the optical depths in the problem are large. Using a reliable estimator of the convergence, however, the most optically thick

models tested were typically found to converge in less than one hour of CPU time on a fast workstation.

5.4 Infall parameters

We have examined the physical constraints which can be used to limit the number and range of parameters used in the spherically symmetric model fits. The parameters which are of most relevance to the theoretical models are the velocity and density profiles. The shapes and intensities of the observed line profiles are also influenced by the temperature, relative abundance, and turbulent velocity profiles. Of these, the abundance and turbulent velocity profiles are the least well understood. In the modelling of the data, we have assumed flat profiles for these two parameters as a practical measure, since otherwise the parameter space would be too large to search in a reasonable time. The uncertain validity of these assumptions, and the assumption of spherical symmetry itself, are the largest sources of uncertainty in the modelling.

We have studied the dependence of the predicted line profiles on a number of model parameters, and identified the following trends. Increasing the infall velocity tends to produce an stronger asymmetry between the blue and red-shifted peaks in double-peaked line profiles, without strongly affecting the separation between the peaks. The value of the turbulent velocity dispersion, when assumed to be spatially uniform, is the most significant factor in determining the velocity separation between the peaks in the double-peaked profiles. The turbulent velocity dispersion was not found to have a significant effect on the degree of asymmetry of the line profile however. We carried out a preliminary investigation into the effect of adopting different power law dependences of the turbulent velocity width on the gas density, and found the predicted line profiles to be extremely sensitive to the value of the power law exponent. The uncertainty in the correct form of the turbulent velocity profile is a limiting factor in the accuracy of the model fits to the infall velocity profile.

The relative abundance of the tracer molecule, by determining the overall optical depth through the cloud, plays a central role in determing the appearance of line profiles. Changing the value of the tracer molecule abundances over their empirical observational ranges, the predicted line profile can change from a single gaussian profile to a strongly double-peaked asymmetric line profile. Since the *absolute* tracer molecule abundance is proportional to the gas density, the uncertainty in the relative abundance is an important source of uncertainty in the density profiles of the model fits.

5.5 Rotation

We have studied the effect on the predicted line profiles of superimposing a solid-body rotation onto the infall velocity field. This does not introduce any departure from spherical symmetry, as far as the Λ-iteration calculation is concerned, since the radiation field in the frame co-moving with the rotation remains unaltered if the rotation is solid-body (apart from the relativistic corrections to the radiation field of order v^2/c^2, and the inconsequential doppler shift of the background continuum radiation). The effect of the solid-body rotation on the on-source line profiles was simply to 'smooth out' the double peaked structure, but for plausible values of the angular velocity this effect was found to be small. Both the centroid velocities and the line shapes of the off-centre profiles were found to be significantly altered by the solid-body rotation however. On the red-shifted side of the rotational velocity gradient, a reversal of the asymmetry in the line profiles was seen, in qualitative agreement with our $HCO^+(J = 4 \rightarrow 3)$ observations of IRAS 16293-2422. We measured the centroid velocity gradient predicted by our model for a solid body rotating envelope, which was found to slightly underestimate the actual rotational velocity gradient used in the model. The measured centroid velocity gradient across observed spectral line maps should therefore be treated as lower limits to the actual line of sight velocity gradient in the cloud. The degree to which it is an underestimate depends on the beam size of the transition, the degree of central

concentration of the emission, and size of the region over which the velocity gradient is observed.

5.6 Specific cases studied

We selected the objects NGC1333-IRAS2 and Serpens SMM4 for detailed modelling using the STENHOLM radiative transfer code. We were able to produce reasonable fits to most of the data, and we believe them to be sufficiently well constrained, within the range of parameter space we have chosen to explore, to draw some preliminary conclusions from the results.

We confined ourselves to the Shu model forms for the density and velocity profiles in the modelling, both of which are defined by just two parameters: the infall radius and the effective sound speed. In an attempt to explore alternative descriptions of protostellar collapse, however, we did not require the density and velocity profiles to have the same values for these parameters in our fits. This still left open the possibility that the exact Shu model could provide the best fit to the data.

Our best model fits to both the NGC1333-IRAS2 and Serpens SMM4 data used velocity profiles which were more strongly developed than the Shu model would predict, given the fit to the density profile. This is consistent with theoretical predictions that at the instant a central protostar is formed, the gas in the envelope has already accelerated to substantial velocities (e.g. Foster & Chevalier 1993), which contrasts with the static initial state assumed by the Shu model, and is one of the principal distinguishing features between the Shu model and other collapse models. In the subsequent evolution the infall velocities and mass infall rates are predicted to be higher than in the Shu model.

Our fits to the $H^{13}CO^+$ line profile observations of both objects consistently overestimated the profile widths. We could produce better fits to these lines by lowering the infall velocity in the centre of the cloud, without significantly affecting the fits to the main line profile. The infall velocity may therefore be retarded from the $r^{-1/2}$ free-fall relation towards the centre of the cloud, possibly by centrifugal braking. Alternatively our assumption of a flat turbulent velocity profile may be incorrect.

The model predictions for the off centre $HCO^+(J = 4 \rightarrow 3)$ line profiles showed greater discrepancies with the observed profiles. In the case of IRAS2, these discrepancies could not possibly be accommodated within a plausible model of infall and rotation, and we attribute them to the outflow. This resolves the debate about whether IRAS2 contains the driving source of the north-south outflow in its vicinity. IRAS2 has also been unambiguously identified as the driving source of a collimated east-west outflow, and we conclude therefore that IRAS2 is a protobinary.

The model fits to the off-centre $HCO^+(J = 4 \rightarrow 3)$ line profiles of Serpens SMM4 included the solid-body rotation inferred from the $HCO^+(J = 4 \rightarrow 3)$ centroid velocity gradient in the calculation. The predicted and observed profiles showed good agreement in the overall line shape although the model consistently underestimated the line intensities. In particular, the distortion of the model profiles caused by the solid-body rotation represented the data well. Since we found no evidence for excess emission from the outflow at the off-centre positions, we therefore concluded that Serpens SMM4 is an infalling and rotating protostar.

5.7 Future work

In this thesis we have made a number of approximations to facilitate the analysis of our spectral line observations, including the assumption of spherical symmetry, the microturbulent approximation, the complete redistribution approximation, and assumptions concerning the forms of the radial profiles of the different physical parameters. To take

the work carried out in this thesis forward, the following considerations need to be addressed:

- **Spherical Symmetry:** The assumption of spherical symmetry was used in this thesis to make the computational radiative transfer problem tractable in a reasonable length of time. Significant deviations from spherical symmetry are found in actual observations of protostellar envelopes, however, including clumpiness and flattened structures, and therefore spherically symmetric analyses can only be expected to have limited accuracy. The problem is not only a computational one, since increasing the dimensionality of the models also significantly increases the parameter space in which model fits have to be constrained by the data. It is essential that the parameter space be constrained within manageable limits if meaningful results are to be obtained. Structure on smaller scales than our beam play an important role. Forthcoming submillimetre interferometer arrays will assist with this problem.

- **Turbulence:** Turbulence plays a central role in determining the appearance of infall line profiles, but theoretical models are only just beginning to examine the behaviour of turbulence in the protostellar environment. The turbulence in protostellar envelopes may either be driven from larger scales, through a Kolmogorov cascade starting with the differential rotation about the galactic centre of an entire molecular cloud, and from smaller scales, through the perturbing effect of bipolar outflows, jets and stellar winds. The uncertain nature of turbulence is a major limiting factor in the accurate determination of the systematic velocity in protostellar envelopes.

- **Abundance:** The abundances of the tracer molecules are crucial in shaping the appearance of line profiles, and again are only poorly understood. The chemical abundances in protostellar envelopes depend not only on the current physical state of the gas, but also depend in general on its history. The transfer of molecules

between grain mantles and the gas phase is an added complication. The uncertainties in chemical abundances are a major limiting factor in the ability to determine envelope densities reliably.

- **Outflows:** The molecular outflows commonly associated with the earliest stages of protostellar evolution can contribute significantly to the line profiles observed towards protostellar envelopes, even for the molecules which are usually thought of as good tracers of the protostellar envelope. There is no reliable tracer which is sensitive only to the protostellar envelope and not the outflow. This means that the possible effect of outflow on the observed line profiles must be evaluated before a claim that infall is taking place can be reliably made. It is unclear what factors are important in determining whether the outflow contributes strongly to the line profiles, although the inclination angle of the outflow is probably important. Because blue-shifted outflow lobes are always situated on the near side of the protostellar envelope to the observer, and red-shifted lobes are situated on the far side, there will be a tendency for blue-shifted emission from the outflow to be less absorbed by the envelope than the red-shifted emission. This asymmetry works in the same direction as the infall asymmetry, and could conceivably lead to a misidentification of infall. The problem of the interaction of jets and outflows with the protostellar envelope is a complicated one, but is clearly important in over half of all potential infall candidates.

Notwithstanding the above caveats, this thesis has shown that significant progress can be made even with relatively simple assumptions.

5.8 References

Blake G. A., Sandell G., van Dishoeck E. F., Groesbeck T. D., Mundy L. G., Aspin C., 1995, ApJ, 441, 689

Foster P. N., Chevalier R. A., 1993, ApJ, 416, 303

Matthews N., 1986, PhD thesis, University of Kent

Zhou S., Evans N. J., II, Kompe C., Walmsley C. M., 1993, ApJ, 404, 232